

B_1^+ -mapping and B_1^+ inhomogeneity correction at high field

THÈSE N° 6582 (2015)

PRÉSENTÉE LE 1^{ER} MAI 2015

À LA FACULTÉ DES SCIENCES DE BASE

LABORATOIRE LEENAARDS-JEANTET D'IMAGERIE FONCTIONNELLE ET MÉTABOLIQUE

PROGRAMME DOCTORAL EN PHYSIQUE

ÉCOLE POLYTECHNIQUE FÉDÉRALE DE LAUSANNE

POUR L'OBTENTION DU GRADE DE DOCTEUR ÈS SCIENCES

PAR

Florent EGGENSCHWILER

acceptée sur proposition du jury:

Prof. G. Meylan, président du jury
Prof. R. Gruetter, directeur de thèse
Prof. O. Bieri, rapporteur
Prof. S. Malik, rapporteur
Prof. J.-Ph. Thiran, rapporteur



ÉCOLE POLYTECHNIQUE
FÉDÉRALE DE LAUSANNE

Suisse
2015

Abstract

Magnetic resonance imaging is a modern imaging technique that allows anatomical images used in many medical diagnosis to be acquired in a completely non-invasive way. MR images acquired at the highest strength of the main magnetic field B_0 are of interest since they highly benefit from the increased signal to noise ratio which is proportional to B_0 . At ultra high field strengths ($B_0 \geq 7$ Tesla) images with more contrast and higher resolution can thus be obtained, opening new insights into the understanding of organ structures and disease evolutions.

One of the main challenges of ultra high field magnetic resonance imaging is that the wavelength of magnetic resonance radiations, which is inversely proportional to B_0 starts to be equal to or shorter than the typical organs of interest. At such wavelength, the transmit magnetic field B_1^+ used to manipulate the magnetization in magnetic resonance imaging is subject to constructive and destructive interferences and becomes position dependent. This inhomogeneity in the B_1^+ field leads to signal and contrast variations in the anatomical images which are prone to misinterpretation. The B_1^+ inhomogeneity can be so intense that regions void of signal are observed where structural information is lost.

This thesis is about measuring and correcting the inhomogeneous B_1^+ field at 7 Tesla.

To be able to correct the B_1^+ inhomogeneity, it is necessary to measure it first. An appropriate B_1^+ -mapping sequence should provide accurate measurements in a wide range of B_1^+ values in a short amount of time since the acquisition of the B_1^+ distribution can be considered as an adjustment step before the acquisition of anatomical images. Moreover, parallel transmission, a promising tool providing more flexibility for the B_1^+ inhomogeneity correction, requires the acquisition of an individual B_1^+ profile for each element of an N channel array. Those profiles show large variations with intense B_1^+ values close to the transmitting elements and low values further distant. The acquisition of such profiles justifies the needs for a fast mapping sequence providing accurate measurements over a large range of B_1^+ values. According to these criteria, the SA2RAGE sequence, which is based on the combination of two three-dimensional gradient echo images, was developed. The sequence parameters were optimized in order to provide the largest range where the B_1^+ field is measured precisely. A typical three-dimensional $64 \times 64 \times 48$ with $3 \times 3 \times 4 \text{ mm}^3$ B_1^+ map can be acquired in less than 2min with the SA2RAGE sequence.

The next challenge was to correct the B_1^+ inhomogeneity observed across the brain at 7 Tesla. RF shimming, where the amplitudes and phases of the different elements of a parallel transmit array are optimized to generate an homogeneous B_1^+ distribution over the region of interest, was used as a first approach. The B_1^+ inhomogeneity correction provided by the standard RF shimming process being rapidly limited, another approach, where a specific set of amplitudes and phases is optimized for different slices along the image, was investigated. Compared to standard RF shimming, the slice based approach provided a 21% improvement.

Despite the results obtained, the potential of RF shimming was not sufficient to mitigate the severe B_1^+ inhomogeneity across the brain at 7 Tesla. To obtain results of higher quality, pulse design where radiofrequency and gradient waveforms are optimized to generate the desired magnetization profile, was considered. Since they provide enough degrees of freedom for the B_1^+ inhomogeneity correction while remaining short in duration, k_T -point pulses which are made of hard sub-pulses of different amplitudes and phases separated by gradient blips, were used. It was already known that k_T -point pulses designed in the small tip angle approximation where the excitation profile corresponds to the Fourier transform of the radiofrequency pulse shape provided substantial B_1^+ inhomogeneity correction.

In this thesis, a methodology making use of the Cayleigh-Klein coefficients to express the Bloch equations in a linear form was developed for the design of k_T -point pulses beyond the low tip angle regime. Excitation, inversion and refocusing pulses were designed and significant improvements were observed in the resulting magnetization profiles when compared to those corresponding to the design of k_T -points in the small tip angle regime.

k_T -points were then designed for a turbo spin echo sequence with variable flip angles in order to remove the effect of the inhomogeneous B_1^+ distribution on T_2 -weighted imaging at 7 Tesla.

In the first approach, a k_T -point pulse was designed in the small tip angle regime to make the excitation profile as homogeneous as possible. By evaluating different types of k_T -points, it was demonstrated that a symmetric k_T -point pulse designed in the small tip angle regime still generates an homogeneous excitation profile for flip angles as high as 120° . Although they were designed to improve the homogeneity in the excitation profile, it was shown that symmetric k_T -points also perform well for the refocusing pathways.

A single symmetric k_T -point pulse was designed in the small tip angle regime and used to replace all the original hard pulses of a turbo spin echo sequence with the maximum flip angle right below 120° . This static design where the ratios of the k_T -point sub-pulses remain constant from one pulse to the next was conducted on both single channel and parallel transmit systems. This methodology provided a significant improvement in terms of signal and contrast homogeneity in T_2 -weighted images. When adding parallel transmission, anatomical images largely devoid of artifacts resulting from the common B_1^+ inhomogeneity at 7 Tesla were acquired.

To be able to acquire T_2 -weighted images with a good signal and contrast homogeneity by using a more efficient turbo spin echo sequence protocol, e.g. with a shorter RF pulse duration such that images are less sensitive to B_0 variations, the design of dynamic k_T -point pulse was developed in this thesis. A dynamic design means that a specific k_T -point waveform is optimized for each pulse of the turbo spin echo sequence, implying that the relationships between the sub-pulse vary from one pulse to the next. Since the magnetization states along the echo train have to be taken into account in the optimization process, the k_T -point pulses of the sequence were designed according to a cost function comparing the theoretical signal over several echoes and the one simulated thanks to the spatially resolved extended phase

graph formalism.

It was demonstrated that, although at a cost of an increase of the specific absorption rate, the dynamic outperforms the static k_T -point design in terms of signal and contrast homogeneity obtained in the acquired T_2 -weighted images. This also means that if the image quality is maintained, the dynamic k_T -point design allows more efficient protocols to be used.

In conclusion, a fast sequence providing reliable measurements over a wide range of B_1^+ values and therefore well adapted for parallel transmission applications was developed. This tool provided the B_1^+ profiles required for the correction of the B_1^+ inhomogeneity at high field. Regarding clinical applications, promising T_2 -weighted anatomical images were obtained by designing static and dynamic k_T -point pulses for a turbo spin echo sequence.

Keywords:

B_1^+ -mapping, RF-shimming, RF pulse design, k_T -points, Parallel transmission, T_2 -weighted imaging, Spatially resolved extended phase graph, Turbo spin echo sequence.

Résumé

L'imagerie par résonance magnétique nucléaire est une technique fascinante permettant une acquisition non-invasive d'images anatomiques utilisées dans de nombreux diagnostics médicaux.

Un intérêt particulier est observé concernant l'acquisition d'images réalisée à des valeurs du champ principal B_0 élevées, le rapport signal sur bruit étant effectivement proportionnel à B_0 . À ultra haut champ ($B_0 \geq 7$ Tesla), des images avec un meilleur contraste et une résolution plus élevée peuvent ainsi être obtenues, ouvrant la porte à une compréhension plus profonde de la structure des organes ainsi qu'à l'évolution de maladies.

Un des principaux désavantages de l'imagerie par résonance magnétique à ultra haut champ est que la longueur d'onde des radiations, inversement proportionnelle à B_0 devient égale ou plus courte que la plupart des organes à imager. À de telles longueurs d'onde, le champ magnétique transmit B_1^+ utilisé pour manipuler la magnétisation en imagerie par résonance magnétique est affecté par des interférences constructives et destructives, le rendant variable spatialement. Cette inhomogénéité du champ B_1^+ engendre des uniformités du signal et du contraste dans les images anatomiques, pouvant donner lieu à de mauvaises interprétations. L'inhomogénéité du champ B_1^+ peut être si intense qu'elle génère des régions dépourvues de signal dans l'image où l'information structurelle est perdue.

Cette thèse concerne la mesure et la correction de l'inhomogénéité du champ B_1^+ à 7 Tesla. Afin de corriger l'inhomogénéité du champ B_1^+ , il est nécessaire de la mesurer en premier lieu. Une séquence permettant de cartographier le champ B_1^+ devrait fournir des mesures précises dans une large plage de valeurs de B_1^+ et de façon rapide puisque l'acquisition du profil du champ B_1^+ est considérée comme une étape d'ajustement avant l'acquisition d'images anatomiques. De plus, la transmission parallèle, un outil prometteur permettant plus de flexibilité pour la correction de l'inhomogénéité du champ B_1^+ , requiert l'acquisition d'un profil individuel de champ B_1^+ pour chaque élément d'une antenne à N canaux. Ces profils présentent d'importantes variations avec des valeurs intenses de B_1^+ proche des éléments émettant les radiations et de faibles valeurs dans les régions plus éloignées. L'acquisition de tels profils justifie les besoins d'une séquence de cartographie rapide et produisant des mesures précises B_1^+ dans une plage de valeurs étendue.

En accord avec ces critères, la séquence SA2RAGE, qui est basée sur l'acquisition de deux images d'écho de gradient tri-dimensionnelles, a été développée. Les paramètres de la séquence ont été optimisés afin de pouvoir mesurer le champ B_1^+ de manière précise dans l'intervalle le plus étendu possible. La séquence SA2RAGE permet la cartographie d'un profil tri-dimensionnel de champ B_1^+ avec une taille de matrice $64 \times 64 \times 48$ et une résolution de $3 \times 3 \times 4 \text{ mm}^3$ en moins de 2min.

Le défi suivant était de corriger l'inhomogénéité du champ B_1^+ observée à travers le cerveau à 7 Tesla. En première approche, la méthode dite de RF shimming où les amplitudes et phases des différents éléments d'une antenne de transmission parallèle sont optimisées de

façon à générer une distribution homogène du champ B_1^+ dans la région d'intérêt a été utilisée. La correction de l'inhomogénéité du champ B_1^+ accessible à l'aide de la procédure standard de RF shimming étant rapidement limitée, une autre approche où l'optimisation des amplitudes et phases des différents éléments de l'antenne est réalisée pour différentes coupes le long de l'image a été étudiée. En comparaison avec le RF shimming standard, l'approche basée sur les coupes permet une amélioration de 21% en moyenne sur 4 sujets. En dépit des résultats obtenus, le potentiel de RF shimming était insuffisant pour corriger de manière significative l'intense inhomogénéité du champ B_1^+ observée à 7 Tesla. Afin d'obtenir des résultats de meilleure qualité la technique de pulse design a été considérée. Cette méthode cherche à optimiser les formes d'ondes radiofréquence et de gradient afin de générer le profile de magnétisation désiré. Puisqu'ils fournissent suffisamment de degrés de liberté pour la correction de l'inhomogénéité du champ B_1^+ tout en restant courts temporellement, les pulses k_T -points composés de sous-pulses rectangulaires avec amplitudes et phases différentes séparés par des impulsions de gradient ont été considérés. Il avait déjà été montré que les pulses k_T -points optimisés dans l'approximation des petits angles où le profile d'excitation correspond à la transformée de Fourier de la forme du pulse radiofréquence généraient une correction significative de l'inhomogénéité du champ B_1^+ . Dans cette thèse, une méthodologie faisant appel aux coefficients Cayleigh-Klein pour exprimer les équations de Bloch sous forme linéaire a été développée afin d'optimiser des pulses k_T -points au-delà du régime des petits angles. Des pulses d'excitation, inversion et refocalisant ont été optimisés et d'importantes améliorations ont été observées dans les profiles de magnétisation résultants, en comparaison avec ceux obtenus avec l'optimisation de pulses k_T -points dans le régime des petits angles. Des pulses k_T -points ont ensuite été calculés pour une séquence turbo spin écho avec angles de bascule variables dans le but d'annihiler l'effet de la distribution inhomogène du champ B_1^+ sur les images pondérées en T_2 à 7 Tesla. Dans la première approche, un pulse k_T -point est optimisé dans le régime des petits angles pour rendre le profile d'excitation aussi homogène que possible. En évaluant différents types de pulses k_T -points, il a été démontré qu'un pulse k_T -point symétrique créé dans le régime des petits angles génère encore une profile d'excitation homogène pour des angles de bascule aussi élevés que 120° . Bien qu'ils aient été construits pour améliorer l'homogénéité dans le profile d'excitation, il a été montré que les pulse k_T -points symétriques sont également adaptés pour la refocalisation de la magnétisation. L'approche utilisée était d'optimiser un unique pulse k_T -point symétrique dans le régime des petits angles et de l'utiliser pour remplacer tous les pulses rectangulaires originaux de la séquence turbo spin écho dont l'angle de bascule maximal était juste inférieur à 120° . Ce design statique où les rapports entre les sous-pulses des k_T -points restent constants d'un pulse de la séquence à l'autre a été appliqué pour les systèmes à un canal et à transmission parallèle. Il a été démontré qu'en utilisant cette méthodologie, une amélioration significatives en termes d'homogénéité du signal et du contrast dans les images pondérées en T_2 pouvait

être obtenue. En ajoutant la composante de transmission parallèle, des images anatomiques entièrement dépourvues des artefacts résultants de l'inhomogénéité du champ B_1^+ à 7 Tesla ont été acquises.

Afin de pouvoir acquérir des images pondérées en T_2 avec une bonne homogénéité du signal et du contraste en utilisant un protocole de la séquence turbo spin écho plus efficace, par exemple avec une durée de pulse plus courte de façon à ce que les images soient moins sensibles aux variations du champ B_0 , les k_T -points dynamiques ont été développés dans cette thèse. Un design dynamique signifie que pour chaque pulse de la séquence turbo spin écho, un k_T -point pulse spécifique est optimisé, ce qui implique que les rapports entre les sous-pulses varient d'un pulse à l'autre. Puisque les états de la magnétisation au long du train d'échos doivent être considérés dans le processus d'optimisation, les pulses k_T -points de la séquence ont été calculés selon une fonction de coût comparant le signal théorique de plusieurs échos et celui simulé à l'aide du formalisme de diagramme de phase étendu et spatialement résolu.

Malgré une augmentation du taux d'absorption spécifique, il a été démontré que les pulses k_T -points dynamiques surpassent les statiques en termes d'homogénéités du signal et du contraste obtenues dans les images pondérées en T_2 acquises. Cela signifie également que pour une qualité d'image similaire, les pulses k_T -points dynamiques permettent l'utilisation d'un protocole plus efficace.

En conclusion, une séquence rapide produisant des mesures fiables sur une large plage de valeurs du champ B_1^+ et donc bien adaptée pour les applications de transmission parallèle a été développée. Cet outil a été utilisé pour acquérir les profils de champs B_1^+ nécessaires pour la correction de l'inhomogénéité du champ transmit observée à haut champ B_0 . Concernant les applications cliniques, de prometteuses images anatomiques pondérées en T_2 ont été obtenues en optimisant des pulses k_T -points statiques et dynamiques pour une séquence turbo spin écho.

Mots-clés:

Cartographie B_1^+ , RF-shimming, Optimisation de pulses RF, K_T -points, Transmission parallèle, Image pondérée en T_2 , Diagramme de phase étendu et spatialement résolu, Séquence turbo spin écho.

"The beautiful thing about learning is that no one can take it away from you."

B.B. King

"Learn from yesterday, live for today, hope for tomorrow. The important thing is not to stop questioning."

A. Einstein

Contents

Abstract	iii
Résumé	vi
Table of Contents	xiii
List of Figures	xvii
1. Scope of the thesis	1
2. Background	5
2.1. Historical background	5
2.2. Physics of NMR	9
2.2.1. Description with quantum mechanics	9
2.2.2. Classical description	12
2.2.3. Gradients and slice selection	26
2.2.4. Gradient echo	29
2.2.5. Spin echo, Hahn echo and stimulated echo	30
2.2.6. Phase Graph	34
2.3. Magnetic Resonance Imaging (MRI)	45
2.3.1. The signal equation and its Fourier interpretation	45
2.3.2. Field of view and spatial resolution	48
2.3.3. Artifacts	53
2.3.4. Image weightings and sequences	53
2.4. Hardware, the basics	63
2.4.1. Magnets	63
2.4.2. Gradients	65
2.4.3. RF system	67
2.5. Safety considerations and SAR	73
2.5.1. B_0 effects	73
2.5.2. Gradient effects	73
2.5.3. RF effects	73

3. RF pulse design and fighting B_1^+ inhomogeneity	77
3.1. General RF pulse design	77
3.1.1. Design at small tip angle	78
3.1.2. Design at high tip angle	81
3.2. RF pulse design to correct B_1^+ inhomogeneity	86
3.2.1. B_1^+ -mapping and the unit transformation	87
3.2.2. Spokes and k_T -points	88
3.3. Parallel transmission	91
3.3.1. Superposition principle	92
3.3.2. Time efficient methods for B_1^+ -mapping	93
3.3.3. RF Shimming	97
3.3.4. Transmit SENSE and spatial domain method for the design of RF pulses in PTx	102
4. B_1^+-mapping with the SA2RAGE sequence	105
4.1. SA2RAGE sequence	106
4.1.1. Introduction	106
4.1.2. Methods	108
4.1.3. Results	111
4.1.4. Discussion	115
4.1.5. Conclusions	117
4.1.6. Appendix A	117
4.1.7. Appendix B	119
5. T_2-weighted imaging with static k_T-points	125
5.1. Improvement in T_2 -weighted imaging through the use of k_T -points	126
5.1.1. Introduction	126
5.1.2. Methods	127
5.1.3. Results	133
5.1.4. Discussion	139
5.1.5. Conclusions	141
6. K_T-point design in the HTA regime	
&	
T_2-weighted imaging with dynamic k_T-points	143
6.1. K_T -points described by Cayleigh-Klein coefficients	143
6.1.1. Introduction	143
6.1.2. Methods	144
6.1.3. Results and discussion	148
6.1.4. Conclusion	150

6.2. Dynamic k_T -points: a new concept to improve T_2 -weighted imaging at high field	151
6.2.1. Introduction	151
6.2.2. Methods	152
6.2.3. Results	157
6.2.4. Discussion	159
6.2.5. Conclusions	161
7. General Conclusion and outlook	163
7.1. Main conclusions	163
7.2. Outlook	164
List of Symbols	167
List of Abbreviations	169
References	180
Publications	181
Curriculum vitae	183
Acknowledgments	185

List of Figures

2.1. The nucleus and its spin	9
2.2. Spins in up and down states	11
2.3. Macroscopic magnetization formed by the sum of spins	12
2.4. Gyroscope illustrating the precession motion	14
2.5. Precession of a magnetic moment	15
2.6. Rotating frame	16
2.7. Excitation in the lab frame	18
2.8. Excitation in the rotating frame	19
2.9. Hard pulse	19
2.10. B_0 inhomogeneity	20
2.11. Dephasing of nuclei moments	21
2.12. Relaxation curves	22
2.13. Magnetization recovery	25
2.14. Free Induction Decay	26
2.15. Magnetic field gradient	27
2.16. Slice selection	28
2.17. RF pulse and gradient involved in slice selection	28
2.18. Gradient echo	30
2.19. Spin echo	31
2.20. Hahn echo	32
2.21. Stimulated echo	33
2.22. States in phase graph formalism	35
2.23. Phase graph steps	37
2.24. Phase graph	40
2.25. Readout and phase encoding for k-space filling	46
2.26. From pulse sequence to k-space filling	49
2.27. K-space and image space	50
2.28. Fourier pairs	50
2.29. Gradient characteristics and echo sampling	51
2.30. Spin echo sequence illustrating ρ , T_1 and T_2 contrasts	54
2.31. T_1 and T_2 contrasts based on sequence parameters	55

2.32. TSE sequence with 180° refocusing pulses	57
2.33. Isochromat evolution for a sequence $90_{x'}^\circ - 180_{x'}^\circ - 180_{x'}^\circ$	58
2.34. Isochromat evolution for a sequence $90_{x'}^\circ - 180_{y'}^\circ - 180_{y'}^\circ$	59
2.35. Effect of the 90° phase shift between excitation and refocusing pulses in TSE sequences	60
2.36. Phase graphs of TSE sequence with 180° and variable refocusing pulses	61
2.37. TSE signal for 180° and 60° refocusing pulses	61
2.38. Flip angle and signal evolutions for 3 different TSE schemes	62
2.39. Sinc (2D) versus hard pulses (3D) in TSE	63
2.40. Structure of an MR scanner	64
2.41. Maxwell and Golay coil configurations	65
2.42. Trapezoidal gradients with and without correction	66
2.43. One loop with linear polarization	68
2.44. Two loops with circular polarization	68
2.45. Birdcage coil	69
2.46. Parallel transmit system	71
2.47. Reception line	72
3.1. Trajectory along k_z depending on the slice-selective gradient	81
3.2. Piece-wise constant sinc pulse for the SLR algorithm	83
3.3. Comparison of the size of the human wavelength becomes shorter when B_0 increases	87
3.4. Spoke pulse	89
3.5. K_T -point pulse	91
3.6. Superposition principle in parallel transmission	93
3.7. From B_1^+ profiles of the modes to individuals	97
3.8. RF shimming over the entire brain	99
3.9. Standard vs. slab-base RF shimming	100
3.10. Slab-based RF shimming	101
4.1. SA2RAGE sequence	108
4.2. Lookup table and CNR curve	109
4.3. Maps of CNR_{width}	111
4.4. Error introduced on the B_1^+ estimations when considering different T_1 s	112
4.5. B_1^+ maps as a function of RF voltage	113
4.6. SA2RAGE brain images leading to B_1^+ profiles	114
4.8. Effect of RF spoiling on the SA2RAGE sequence	121
4.9. B_1^+ mapping vs RF voltage for different RF spoiling schemes	122
4.10. Effect of RF spoiling on in-vivo B_1^+ maps	123
5.1. Hard pulse and different types of k_T -points	129

5.2. Evolution of the excitation profiles of short and extended k_T -points as a function of the flip angle	133
5.3. SR-EPG simulations for different types of k_T -points	134
5.4. Deviations generated by different types of k_T -point pulses	135
5.5. Excitation profiles and T_2 -weighted images with and without k_T -points on the single channel system	137
5.6. Excitation profiles and T_2 -weighted images with and without k_T -points on the parallel transmit system	138
6.1. Symmetric k_T -point	144
6.2. Targeted and initial excitation profiles	146
6.3. High tip angle k_T -point workflow	147
6.4. High tip angle excitation k_T -point pulse	148
6.5. Algorithm convergence for the excitation k_T -point pulse	149
6.6. High tip angle inversion k_T -point pulse	149
6.7. Algorithm convergence for the inversion k_T -point pulse	150
6.8. High tip angle refocusing k_T -point pulse	150
6.9. Algorithm convergence for the refocusing k_T -point pulse	151
6.10. Predefined TSE signal evolution and dynamic k_T -point illustration	153
6.11. Effect of random voxel selection on the accuracy of the simulations and the computation speed	158
6.12. Deviation between sequence echoes and theoretical signal	158
6.13. Difference maps calculated with and without k_T points from measured and simulated data	159
6.14. T_2 -weighted images acquired with and without k_T -points	159

Scope of the thesis

Since its discovery in the seventies, magnetic resonance imaging (MRI) rapidly became a widespread modality for the visualization of human anatomy and found a broad range of applications in medical diagnosis. One of the main advantages of MRI is that tissue structures and organs can be imaged in a non-invasive way.

The quality of MR images highly benefits from the increased signal to noise ratio (SNR) available at high strength of the main magnetic field B_0 . This implies that for the same signal intensity, images with a better resolution can be acquired. The acquisition of images at higher and higher B_0 strengths is thus of central interest.

The strength of the B_0 field is expressed in Tesla (T) unit. In this thesis, experiments were conducted on a 7T scanner which is considered as the lower limit of ultra high field strength MR systems. At those field strengths, interference effects due to the fact that the wavelength (inversely proportional to B_0) becomes equal to or smaller than the typical organ of interest, make the distribution of the transmit magnetic field B_1^+ used to manipulate the magnetization inhomogeneous. This inhomogeneity gives rise to signal and contrast variations in the acquired images which can mislead or prevent medical diagnosis.

This thesis is dedicated to the measurement and correction of the inhomogeneous B_1^+ field across the brain at 7T. The first challenge was to develop a B_1^+ -mapping sequence adapted to the requirements of parallel transmission where the B_1^+ profiles generated by the different transmitters of an array coil need to be quickly measured as a calibration step for applications dedicated to B_1^+ inhomogeneity correction.

The second challenge was to obtain anatomical brain images unaffected by the severe B_1^+ inhomogeneity observed at 7T. Since a multi channel system was available in the MR facility used in this thesis, the benefits provided by techniques involving parallel transmission such as RF shimming and transmit SENSE could be exploited. Since it was known that RF shimming cannot correct the B_1^+ inhomogeneity sufficiently to obtain MR images with uniform signal and contrast, more efforts were introduced on the development of RF pulse design methodologies.

K_T -point pulses which are made of hard sub-pulses of different amplitudes and phases sep-

arated by gradient blips are well adapted since they provide enough degrees of freedom for the B_1^+ inhomogeneity correction while remaining short in duration. It was already demonstrated that k_T -point pulses designed in the small tip angle approximation where the excitation profile corresponds to the Fourier transform of the RF pulse shape provided substantial B_1^+ inhomogeneity correction. Here, the aim was to propose new types of k_T -points in the small and high tip angle regimes in order to take advantage of the most adapted k_T -point pulse depending on the properties of the sequence of interest.

The greatest achievement of this thesis was to show that by designing k_T -point pulses for a turbo spin echo sequence with variable flip angles, T_2 -weighted anatomical images largely devoid of artifacts resulting from the common B_1^+ inhomogeneity at 7T could be acquired.

Outline of the thesis

Chapter 2 describes the physics and the main mathematical concepts behind nuclear magnetic resonance (NRM). The fundamental aspects based on quantum mechanics are explained first. The remaining concepts are introduced by using a classical description. Principles such as macroscopic magnetization, rotating frame, excitation, relaxation, signal detection, echo formation and phase graph are presented in order to set the basis required to understand how MRI, which is described in the second part of this chapter, can be performed. The main hardware elements used in MRI as well as safety aspects are presented at the end of the chapter.

Chapter 3 explains how the inhomogeneous distribution of the transmit magnetic field, characteristic in MRI performed at high B_0 field strengths can be corrected. One promising way is to design RF pulses taking the inhomogeneous profile of the B_1^+ field into account and generating a uniform excitation profile.

The small tip angle approximation and the Shinnar-Le Roux algorithm which are two well known techniques among the RF pulse design community are presented at the beginning of the chapter. Spoke and k_T -point RF pulses are then introduced since their use is perfectly adapted for the B_1^+ inhomogeneity correction.

The last part of the chapter deals with parallel transmission which offers a new degree of freedom for the B_1^+ inhomogeneity correction. The concept of RF shimming where the amplitudes and phases of a parallel transmit array are optimized to produce the most uniform B_1^+ profile over the region of interest is first presented. Transmit SENSE which combines the degrees of freedom provided by RF pulse design and parallel transmission is finally described.

Chapter 4 introduces the concept of B_1^+ -mapping. As B_1^+ inhomogeneity correction requires the knowledge of the B_1^+ profile over the region of interest, the SA2RAGE sequence was developed. This B_1^+ -mapping sequence is used throughout the thesis to acquire B_1^+

maps on the single channel and parallel transmit systems.

Chapter 5 describes the design of static k_T -points used to replace the original hard pulses of a turbo spin echo sequence in order to correct the signal and contrast inhomogeneities observed on T_2 -weighted images at $7T$. Static means that a single k_T -point pulse is designed in the small tip angle regime to replace both excitation and refocusing pulses of the turbo spin echo sequence. Different types of k_T -points are evaluated in the process and their validity beyond the small tip angle regime is investigated.

Chapter 6 introduces a new methodology for the design of excitation, inversion and refocusing k_T -point pulses in the high tip angle regime is subsequently introduced. It is then shown that T_2 -weighted images can be further improved by designing dynamic k_T -point pulses for the turbo spin echo sequence. Unlike the static design where a single k_T -point pulse is calculated in the small tip angle regime, the dynamic design combines the spatially resolved extended phase graph framework with a gradient descent algorithm to optimize a specific k_T -point pulse for all the pulses in the TSE sequence.

Chapter 7 presents an overall conclusion based on an overview of the main achievements of this thesis. An outlook concerning B_1^+ inhomogeneity correction at ultra high magnetic field is discussed.

2

Background

2.1 Historical background

NMR was born in the field of Chemistry where NMR spectroscopy proved to be extremely useful to determine the structure of molecules by studying the peaks of their associated spectra. The arrival of NMR Imaging combined with the continuous developments of instruments and techniques made NMR particularly suitable in Medicine. Thanks to its non-invasive character and the multiple tissue contrasts it provides, NMR Imaging became a routine procedure in radiology. NMR is not just a modality allowing anatomy and pathologies to be imaged but its potential has also been demonstrated in the investigation of organ operations, in the analysis of in vivo chemistry and even in the understanding of the brain functions.

To better understand how the NMR field was brought to what it is nowadays, the current section will go through the major discoveries related to NMR.

In the early 1920s, the existence of the electron angular momentum or spin was verified through several studies and in particular, the Stern-Gerlach experiment which demonstrated that a beam of silver atoms sent across an inhomogeneous magnetic field was deflected not into a continuum but in only two discretized directions.

Such a phenomenon was supported in 1928 by Dirac's formalism which predicts that, resulting from its charge, the electron spin can be either in up or down state.

In the meanwhile, the spin principle was foreseen for the atomic nuclei by analyzing atomic spectra and in 1924, Pauli established the relationship linking the nuclear spin \vec{S} to the magnetic dipole moment $\vec{\mu}$ through the gyromagnetic ratio γ .

In 1939, Rabi's group having made major improvements in beam techniques followed Stern's experiment to show that a sodium beam passing through an inhomogeneous magnetic field would split into $2I+1$ components, I being the nuclear spin of sodium atoms.

Subsequently, the stream of sodium atoms was sent through an homogeneous constant mag-

netic field which was perpendicularly crossed by an electromagnetic radiation in the radio-frequency (RF) range. At a well defined radiation frequency (called the Larmor frequency), a small but measurable deflection of the beam was observed, meaning that when absorbing a specific amount of energy, sodium atoms change their nuclear magnetic moment. This was the first observation of NMR, and in 1944 Rabi was awarded the Nobel Prize in Physics.

In 1946, Felix Bloch from Stanford and Edward Purcell from Harvard Universities independently announced the discovery of NMR in bulk materials. Bloch expected that applying an RF radiation on the sample could tip the macroscopic magnetization away from its equilibrium state and make it precess about the main magnetic field at a well-defined frequency. Bloch thought that this time varying magnetization would induce an electric signal in a copper wire loop. Bloch, Hansen and Packard managed to validate the phenomenon using a sample of liquid water [1].

On the other side, Purcell, Torrey and Pound demonstrated the same physical properties while studying a block of paraffin [2]. In 1952, Bloch and Purcell shared the Nobel Prize in Physics for their discovery of NMR in condensed matter and the developments brought to it.

The fundamental mechanism of nuclear relaxation was established in 1948 by Bloembergen, Purcell and Pound [3].

In 1950, the relationship linking the signal frequency with the main magnetic field and the gyromagnetic ratio was well known and it was expected that at a given magnetic field strength, this frequency would be fixed for a specific nucleus, independently of its chemical surrounding. However, variations in the resonance frequency were observed when investigating ^{19}F and ^{31}P signals. Initially, the chemical shift was considered as a limitation to the precision in the measurement of the gyromagnetic ratio of the different nuclei but soon it was realized that this new feature resulted from the magnetic properties of the electrons surrounding the nucleus and could have a crucial role in the analysis of the molecular structure. NMR spectroscopy was born.

Up to that point, the standard way of acquiring the resonances of the compound of interest consisted in sweeping the electromagnetic radiation frequency or, more commonly, the current throughout the magnet in order to change the resonance condition and measure the intensity of the energy absorptions. This technique was named continuous-wave (CW) spectroscopy since the RF radiation was maintained during the entire experiment. One limitation of CW spectroscopy was that several minutes were required to acquire all the desired resonance lines of the sample which could be made inaccurate due to the random drift of the field produced by the magnet.

While many efforts were brought to make the magnetic fields more stable, new concepts fundamentally changed the way NMR spectroscopy was performed. Bloch suggested that

instead of using a continuous radiation, the sample could be excited with a short RF pulse instead.

Following this idea, Hahn observed that an oscillating decaying signal with well-defined frequency components (called "Free Induction Decay" or FID) could be acquired after such an excitation. He then demonstrated that applying a second RF pulse at time τ after the excitation pulse would rebuild the decaying signal at a time 2τ . This fundamental technique in NMR was named a spin echo or Hahn echo.

Ernst and Anderson showed in 1966 that an FID signal could be decomposed into its frequency components by using the Fourier transform formalism [4].

Together, the concepts of spin echo, short RF pulses exciting a broad range of frequencies and spectral analysis of the FID signal represented a drastic improvement in NMR spectroscopy.

In 1974, Ernst's group presented the first practical use of 2D NMR spectroscopy [5], where a new time variable is added in a sequence of pulses in order to establish a spectrum with two frequency dimensions. The analysis of such a 2D spectrum is more convenient when studying large and complex molecules for which many overlap would have been observed with one-dimensional NMR. Moreover, supplementary information such as coupling or distance between nuclei can be easily deduced from a 2D NMR spectroscopy experiment.

In 1991, Ernst was awarded the Nobel Prize in Chemistry for his contribution in the introduction of the Fourier transform formalism in NMR spectroscopy and for his impact on the development of multi-dimensional NMR methods.

On the hardware side, magnets with improved field stability and homogeneity were built. Regarding the demand for higher magnetic field strengths leading to superior SNR, superconducting magnets became of great interest since iron-core electromagnets had shown their physical limitations. Those instrumental improvements allowed the investigation of more and more complex molecules.

In the early 1980s, Wüthrich's group used multi-dimensional NMR spectroscopy to measure spectra of proteins in water. Based on this methodology, the same group showed for the first time in 1985 the complete 3D structure of a protein in solution [6]. Wüthrich received the Nobel Prize in Chemistry in 2002 "for his development of nuclear magnetic resonance spectroscopy for determining the three-dimensional structure of biological macromolecules in solution".

Another breakthrough was brought in 1973 when Lauterbur showed that the origin of the signal acquired during an NMR experiment could be determined when linear magnetic field gradients are applied across the sample. By measuring several 1D profiles with gradients imposed in different directions, a two dimensional image is reconstructed [7]. This was the

beginning of NMR imaging later renamed MRI to avoid the 'Nuclear' term.

In the same year, Mansfield's group demonstrated that the acquired MR signal could be mathematically interpreted and converted into a useful image [8]. For their contributions in the development of MRI, Lauterbur and Mansfield shared the 2003 Nobel Prize in Physiology or Medicine.

Garroway showed in 1974 that combining a short RF pulse with a magnetic field gradient leads to the excitation of a single slice of the sample of interest [9].

Meanwhile, Damadian reported in 1971 that different NMR signals were measured for tumors and normal tissues [10]. This was explained by the fact that cancerous and healthy tissues have much different relaxation times, a concept still in use nowadays in cancer detection.

After having attended one of Lauterbur's conference in 1974, Ernst realized that orthogonal linear gradients could be applied to the sample such that the spatial image can be reconstructed by performing a two- or three-dimensional Fourier transform. This led to the publication by Kumar, Welti and Ernst in 1975 establishing the fundamentals for MRI reconstruction [11], although the practical implementation was shown by Edelstein known as spin wrap imaging [12].

MRI became one of the most widely used technique in medicine regarding the investigation of the body anatomy since different tissues produce signals depending on their water content and relaxation times.

One of the last remarkable discovery in the NMR field called functional MRI or fMRI was made by Seiji Ogawa in 1990. He observed that the MRI signal changes on brain regions depending on their concentration of oxy- and deoxy-hemoglobin [13]. When brain neurons are activated, the oxygen consumption required to activate brain regions leads to measurable variations in the MRI signal. This concept was used to map brain regions responding to various stimulations e.g. visual, auditory or sensory.

NMR was therefore tremendously developed over the last century and still represents a field with a huge research interest. Ultra-high field NMR is now sought in order to take advantage of the higher SNR available, providing better resolution which is desired in both NMR spectroscopy (better peak discrimination) and MRI (observation of sub-millimeter structures). Many efforts are currently made to perform deeper analysis in structural biology, to improve image quality and to study tissue properties and metabolic functions in a more comprehensive way.

2.2 Physics of NMR

An overview of the striking events happening across the last century and bringing NMR to what it is nowadays was given in the previous section. The current one will focus on the physics behind NMR. At first, the description will be made at a quantum level by presenting the concepts of nuclear spin and angular momentum and how nuclei behave when they are placed in a magnetic field. In a second step, we will show that by introducing the macroscopic magnetization \vec{M} , a semi-classical model can be used to describe the spin physics. The different elements interacting with \vec{M} will be brought into the description and the way they are used to produce the NMR signal will be explained. Basic pulse sequences and phase graph, a tool allowing the analysis of more complex sequences will finally be presented.

2.2.1 Description with quantum mechanics

2.2.1.1 Nuclear spin and magnetic moment

Every atom is composed of the fundamental particles, i.e. electrons orbiting a nuclei made of protons and neutrons. Each particle possesses an intrinsic property called spin and can therefore be seen as rotating around its own axis. As its name indicates it, NMR deals with the nuclear part of the atom.

Protons and neutrons are spin $\frac{1}{2}$ particles (fermions), what means, following Pauli's formalism [14], that they can be in only two spin states.

For each type of atom, the overall spin I of the nuclei is given by the number of protons and neutrons involved. As in the case of electrons in atomic orbitals, protons and neutrons pair up such that an even number of those two particles in the nuclei will lead to $I = 0$. Now if the numbers of protons and neutrons are both odd, the remaining uncoupled proton and neutron will remain in parallel spin states since this minimizes their potential energy without infringing the Pauli exclusion principle. An integer I will result from this kind of nucleus configuration. On the other hand, an even number of protons and an odd number of neutrons or vice versa gives rise to a semi integer I value.

A nucleus having a non-zero spin I can be represented as a spinning charge sphere (Fig. 2.1). Analogous to the angular momentum associated with a spinning object in classical mechan-



Figure 2.1: Geometrical representation of a nucleus and its spin. Similarly as the angular momentum \vec{L} in classical mechanics, the spin angular momentum \vec{S} is used in quantum mechanics.

ics, the spin angular momentum \vec{S} can be linked to a nucleus of spin I . From electrodynamic laws, a spinning charge gives rise to a loop current creating a magnetic moment $\vec{\mu}$. \vec{S} and $\vec{\mu}$ are linked by the gyromagnetic ratio γ specific to each nucleus through

$$\vec{\mu} = \gamma \vec{S} \quad (2.1)$$

In the absence of magnetic field, \vec{S} can take any random orientation. A key element to produce the NMR effect is the strong magnetic field, the B_0 field, which is applied by convention in the z direction. When this field is on, \vec{S} can be in $2I + 1$ states with its component parallel to B_0 quantized to

$$S_z = \hbar m \quad (2.2)$$

where $m \in [-I, -I+1, \dots, I-1, I]$ and \hbar is the Planck's constant ($h = 6.626 \cdot 10^{-34} m^2 kg / s$) divided by 2π . Having a nuclear spin being necessary to produce a NMR signal, atoms with $I = 0$ cannot be detected. Unlike spin $\frac{1}{2}$ nuclei for which the charge distribution can be considered as symmetric, nuclei with $I \geq \frac{1}{2}$ possess a charge distribution shaped as an oblate or prolate spheroid (rugby ball shape). This asymmetry creates interactions between the nucleus and surrounding electrons leading to a hardly measurable signal. Indeed, the stronger the nucleus-electron interaction, the shorter the atom stays in an observable state. The category of spin $\frac{1}{2}$ nuclei is therefore the most suited for NMR studies. 1H having a high sensitivity due to its large γ factor and the natural abundance of water (70-90% of tissues is H_2O), proton is the most commonly used atom in human NMR experiments. Atoms as ^{13}C , ^{31}P and ^{23}Na are also under investigation since they provide useful metabolic information. Although a general formalism will be kept throughout, this thesis deals with proton NMR. Proton is a spin $\frac{1}{2}$ nuclei and its gyromagnetic ratio $\gamma^{1H} = 42.58 \text{ MHz/T}$. Numerical examples for 1H will thus go along with the general formula derived in the next sections.

2.2.1.2 Energy levels and Boltzmann statistics

As mentioned in the previous section, nuclei can be in $2I+1$ states when the main magnetic field B_0 is applied. For a spin $\frac{1}{2}$ nucleus, only 2 states corresponding to $m = \pm \frac{1}{2}$ exist. This implies that $\vec{\mu}$ can have two possible orientations. From quantum mechanics, the energy of a magnetic moment $\vec{\mu}$ in an external field \vec{B} is given by

$$E = -\vec{\mu} \cdot \vec{B} \quad (2.3)$$

The minus sign takes into account the fact that the energy of the nucleus is minimum when $\vec{\mu}$ and \vec{B} are parallel and maximum when they are anti-parallel. By combining equations (2.1) to (2.3) and considering that the B_0 field is applied in the z direction, the energy level of each state is

$$E_{m=\pm\frac{1}{2}} = -\mu_z B_0 = -\gamma S_z B_0 = \mp \frac{1}{2} \gamma \hbar B_0 \quad (2.4)$$

Independently of the state they are in, the magnetic moments are not completely aligned with \vec{B}_0 , S_z being the projection of \vec{S} on the z axis. This is illustrated in Fig. 2.2 with the "spin-up" state corresponding to $m = \frac{1}{2}$ where \vec{S} is almost aligned with \vec{B}_0 and the "spin-down" state ($m = -\frac{1}{2}$) where \vec{S} is almost anti-parallel to \vec{B}_0 . Transitions of nuclei from one

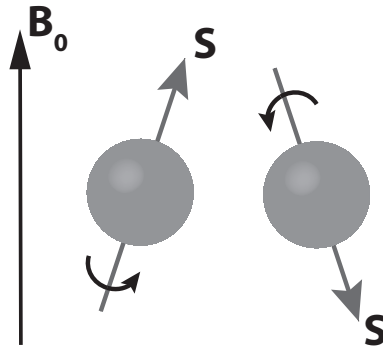


Figure 2.2: Spin states of a spin $\frac{1}{2}$ nucleus in a magnetic field \vec{B}_0 . For $I=\frac{1}{2}$, the nuclei can be either in up (left) or down (right) states.

state to the other occur with the absorption or emission of a certain amount of energy which is simply given by the difference

$$\Delta E = E_{m=-\frac{1}{2}} - E_{m=\frac{1}{2}} = \gamma\hbar B_0 \quad (2.5)$$

Planck's equation $E = \hbar\omega$ involves that an electromagnetic radiation of frequency

$$\omega_0 = \gamma B_0 \quad (2.6)$$

creates transitions between the two states. This specific value called the Larmor frequency thus depends on the nucleus gyromagnetic ratio as well as the strength of the magnetic field \vec{B}_0 . At $B_0 = 7\text{T}$, this frequency is equal to $42.58 \cdot 10^6 \cdot 7 \approx 297\text{MHz}$ for ^1H atoms. Following the principle of minimum energy, most of the nuclei should occupy the spin-up state. However, at room temperature, both states are almost equally populated since thermal energy is order of magnitude higher than ΔE . For a large number of nuclei, the ratio between populations in spin-up n_+ and spin-down n_- states is described by Boltzmann's statistic

$$\frac{n_-}{n_+} = e^{-\Delta E/k_B T} \quad (2.7)$$

where k_B is the Boltzmann's constant ($k_B = 1.38 \cdot 10^{-23}$ J/K) and T the temperature. For protons in a 7T B_0 field and at room temperature ($T = 300\text{K}$), $n_-/n_+ = 0.999992$. This means that out of one million nuclei, there are eight more in the n_+ population than in the n_- . The NMR signal is directly proportional to such a tiny discrepancy. A few protons out of one million taking part to the signal creation implies that NMR is not a very sensitive technique.

However human tissues contain about 10^{22} protons per ml which is sufficient to produce a detectable signal.

2.2.2 Classical description

2.2.2.1 Macroscopic magnetization

As mentioned previously, under the effect of the B_0 field, only two spin states are possible for the proton nuclei. The macroscopic magnetization \vec{M} corresponds to the sum over all

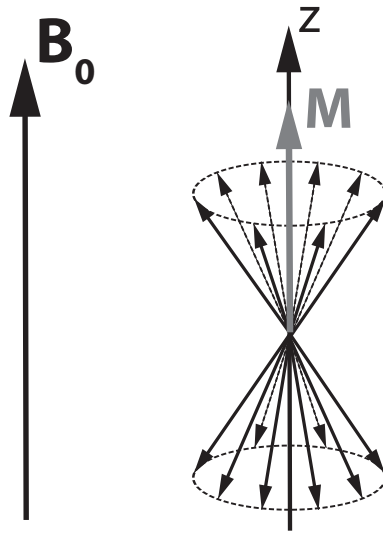


Figure 2.3: Macroscopic magnetization \vec{M} (gray arrow) formed by the sum of every magnetic moments (black arrows). The density of nuclei being huge, the transverse components of their angular momentum which lie on the dashed circles average out. As there is slightly more nuclei in the up than in the down state, \vec{M} points in the same sense as \vec{B}_0 .

the $\vec{\mu}'$ s

$$\vec{M} = \sum \vec{\mu} \quad (2.8)$$

Assuming a random distribution of the magnetic moment phases, each $\vec{\mu}$ component perpendicular to z has a paired one oriented in the opposite direction. After summation only the z component of \vec{M} is nonzero (Fig. 2.3). As it was demonstrated beforehand, n_+ state is slightly more populated than n_- . The difference $n_+ - n_-$ thus corresponds to the number of magnetic moments in the spin-up state that create \vec{M} which is therefore pointing in the same direction as B_0 (Fig. 2.3). At equilibrium, \vec{M} has the following form

$$\vec{M} = \begin{pmatrix} 0 \\ 0 \\ M_0 \end{pmatrix} \quad (2.9)$$

The maximum detectable NMR signal is proportional to the equilibrium magnetization M_0 . As it is built by the excess of nuclei in the spin-up state, it can be expressed as

$$M_0 = (n_+ - n_-)\mu_z \quad (2.10)$$

By considering that $\gamma\hbar B_0 \ll k_B T$, $n_+ \approx n_- \approx N_{tot}/2$ ($N_{tot} = n_+ + n_-$) and by combining (2.1) and (2.2) to find that $\mu_z = \frac{1}{2}\gamma\hbar$, the previous expression becomes

$$M_0 = n_+ \left(1 - \frac{n_-}{n_+}\right) \frac{1}{2}\gamma\hbar \approx n_+ \left(1 - \left(1 - \frac{\Delta E}{k_B T}\right)\right) \frac{1}{2}\gamma\hbar \approx \frac{N_{tot}}{2} \frac{\gamma\hbar B_0}{k_B T} \frac{1}{2}\gamma\hbar \quad (2.11)$$

Replacing N_{tot} by the number of proton per unit volume ρ leads to

$$M_0 = \frac{\rho}{2} \frac{\gamma\hbar B_0}{k_B T} \frac{1}{2}\gamma\hbar \quad (2.12)$$

For a given nuclei, the amount of available magnetization is thus proportional to B_0 and $1/T$. This explains why NMR at high field strength is of central interest. No real advantage is provided from the temperature dependence since this is constrained for in-vivo studies. At 7T and 310K, one gram of water ($H_2O \approx 18\text{g/mol}$) corresponding to $6.8 \cdot 10^{26} \text{ } ^1\text{H atoms/m}^3$ generates a nuclear magnetization $M_0 \approx 8.6 \cdot 10^{-2} \text{ A/m}$ (the conversion $\text{J/T} = \text{Am}^2$ was used throughout the calculations), which is small, but detectable.

2.2.2.2 Precession and rotating frame

The description of a gyroscopic motion is well established by the laws of classical mechanics. A spinning disc with angular momentum \vec{L} in a gyroscope (Fig. 2.4) creates a circular motion with frequency $\vec{\Omega}_{gyro}$ around the z axis. This type of motion induced by a spinning object is called precession. From Newton's second law, the angular momentum variation is equal to the torque $\vec{\tau}$ applied on the object

$$\frac{d\vec{L}}{dt} = \vec{\tau} \quad (2.13)$$

For the gyroscope, the torque results from the gravity leading to a counterclockwise precession in the configuration shown in Fig. 2.4. Rotation kinematics shows that the variation in position of an object describing a circular motion with frequency ω about an axis is described by

$$\frac{d\vec{r}}{dt} = \vec{\omega} \times \vec{r} \quad (2.14)$$

where \vec{r} describes the position of the object in respect to the axis of rotation. In this last equation, the vector \vec{r} can be replaced by any vectorial entity, as long as it is describing a circular motion with frequency $\vec{\omega}$ around the axis of rotation. For the gyroscope, the following

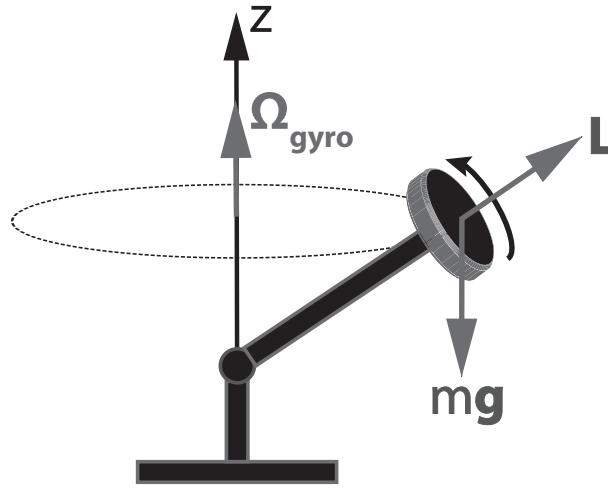


Figure 2.4: Gyroscope made of a spinning disk on a rod that can rotate in any direction. The torque created by the gravitational force modifies the direction of the angular momentum \vec{L} giving rise to a precession motion about the z axis with frequency $\vec{\Omega}_{gyro}$. The behavior of a nuclei in a magnetic field can be thought of as a gyroscope where \vec{B}_0 and \vec{S} respectively replace the gravitational force and the angular momentum.

expression can thus be set for the angular momentum

$$\frac{d\vec{L}}{dt} = \vec{\Omega}_{gyro} \times \vec{L} \quad (2.15)$$

A nuclei with spin angular momentum \vec{S} in a magnetic field \vec{B} behaves quite similarly as the gyroscope in the gravitational field (Fig. 2.4). From electromagnetism, when placed in the \vec{B} field, a magnetic moment $\vec{\mu}$ undergoes a torque given by

$$\vec{\tau} = \vec{\mu} \times \vec{B} \quad (2.16)$$

Equation (2.13) can be rewritten for the spin angular momentum

$$\frac{d\vec{S}}{dt} = \vec{\mu} \times \vec{B} \quad (2.17)$$

Multiplying each side by γ and considering equation (2.1) as well as the identity $\vec{a} \times \vec{b} = -\vec{b} \times \vec{a}$, the previous expression becomes

$$\frac{d\vec{\mu}}{dt} = -\gamma \vec{B} \times \vec{\mu} \quad (2.18)$$

By analogy with equation (2.15) μ precesses around \vec{B} at a frequency $\vec{\omega} = -\gamma \vec{B}$. When considering nuclei in the main magnetic field \vec{B}_0 , a clockwise precession occurs (Fig. 2.5) at the

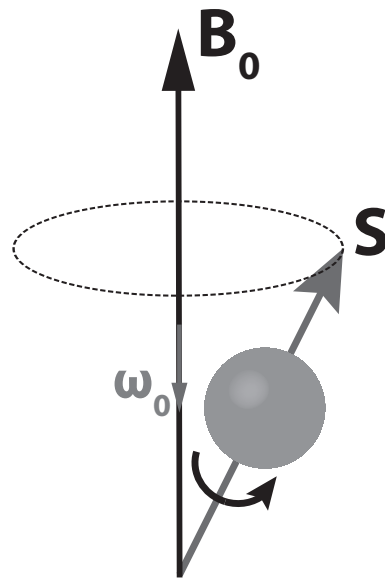


Figure 2.5: Magnetic moment in the magnetic field \vec{B}_0 . As it is spinning about its own axis, the magnetic moment describes a precession motion about \vec{B}_0 , similarly to a gyroscope in the gravitational field.

specific angular frequency

$$\vec{\omega}_0 = -\gamma \vec{B}_0 \quad (2.19)$$

This last expression corresponds to the Larmor frequency found in (2.6) while using the approach with quantum mechanics. Interestingly, the frequency at which the nuclei precess around the \vec{B}_0 field is the same as the one required for an electromagnetic radiation to create transitions between the two spin states. Summing over the magnetic moments on both sides of equation (2.18) gives rise to

$$\frac{d\vec{M}}{dt} = -\gamma \vec{B} \times \vec{M} \quad (2.20)$$

This implies that if not parallel to the z axis, the macroscopic magnetization precesses about the \vec{B}_0 field at the Larmor frequency $\vec{\omega}_0$. It will be explained later how \vec{M} can end up with components perpendicular to \vec{B}_0 . In a frame rotating about \vec{B}_0 at $\vec{\omega}_0$, \vec{M} becomes stationary. Such a rotating reference frame will be particularly helpful to simplify the representation of the magnetization evolution when RF pulses and relaxation mechanisms will be included in the description. To the x and y coordinates in the lab (fixed) frame correspond the x' and y' ones in the rotating frame (Fig. 2.6). Since the rotation is about the z axis, z and z' are identical. Mathematically, the relationship between the lab and rotating frames is given by

$$\left(\frac{d\vec{M}}{dt} \right)_{rot} = \left(\frac{d\vec{M}}{dt} \right)_{lab} - \vec{\omega} \times \vec{M} \quad (2.21)$$

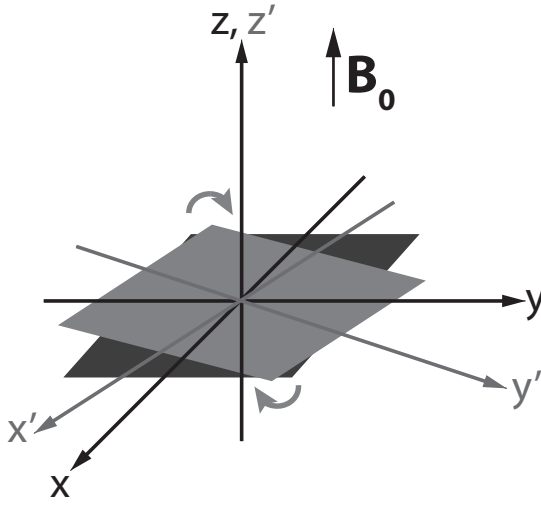


Figure 2.6: Lab (black) and rotating (gray) reference frames. The x , y and z coordinates in the lab frame become x' , y' and z' in the rotating frame. In a frame rotating at the Larmor frequency, the transverse components of \vec{M} are stationary.

with $\vec{\omega}$ the rotating frame frequency which in our case is equal to $-\gamma B_0 \cdot \vec{e}_z$. Taking equation (2.20) as $(d\vec{M}/dt)_{lab}$, a general expression for the temporal variation of \vec{M} in the rotating frame can be derived

$$\left(\frac{d\vec{M}}{dt}\right)_{rot} = -\gamma B \times \vec{M} - \vec{\omega} \times \vec{M} = -\gamma(\vec{B} + \frac{\vec{\omega}}{\gamma}) \times \vec{M} = -\gamma \vec{B}_{eff} \times \vec{M} \quad (2.22)$$

The last term into brackets corresponds to the effective magnetic field \vec{B}_{eff} applied to \vec{M} with the fictitious field term $\vec{\omega}/\gamma$ resulting from the rotation of the frame. An expression similar to equation (2.20) was obtained by introducing an additional magnetic field term in the description. In the same way, other fields related to RF pulses and gradients will be considered later by adding terms to \vec{B}_{eff} . In the particular case where only \vec{B}_0 is applied and with $\vec{\omega} = -\gamma \vec{B}_0$, the motion of \vec{M} becomes

$$\left(\frac{d\vec{M}}{dt}\right)_{rot} = -\gamma(\vec{B}_0 + \frac{-\gamma \vec{B}_0}{\gamma}) \times \vec{M} = \vec{0} \quad (2.23)$$

This result is null independently of the magnetization orientation which means that in the rotating frame at the Larmor frequency, in the absence of relaxation and when only \vec{B}_0 is applied, \vec{M} remains stationary.

2.2.2.3 Main magnetic field \vec{B}_0

As mentioned earlier in the text, the orientation of the main magnetic field B_0 is along z also called the longitudinal direction. This field is permanent and its strength is usually given

in Tesla units (1T = 10'000 Gauss(G)). From now on, the following convention will be used concerning the magnitude of the \vec{B}_0 field

$$|\vec{B}_0| \equiv B_0 \quad (2.24)$$

As shown in equation (2.12), the amount of magnetization giving rise to the NMR signal increases linearly with B_0 . Nowadays, typical clinical scanners are in the 1.5 - 3T range. Higher field magnets are more commonly used in research. In this thesis all the measurements were performed at 7T. For comparison purposes, the strength of Earth's magnetic field ranges from 25 to 65 μT (0.25-0.65G). Besides strength, the other important aspect of the \vec{B}_0 field is its homogeneity. Indeed, a constant value of B_0 is desired over the entire sample of interest. Manufacturers can now achieve a field homogeneity over a sphere of radius $r=20\text{cm}$ of a few ppm when no patient is present. This means that the fields experienced by nuclei located at two opposite points on the surface of the sphere differ by a few millionth of Tesla. In terms of frequencies, the precession difference of the two nuclei is on the Hz order as compared to the MHz order of the Larmor frequency. For in-vivo NMR and especially MRI, the issue is that field distortions occur at interfaces between tissues with different magnetic properties or even worse at air-tissue boundaries. Many improvements have been achieved in B_0 inhomogeneity correction also called B_0 -shimming but with the desire for higher field magnets where B_0 homogeneity is harder to reach, this topic remains an active research area.

2.2.2.4 Radiofrequency field B_1

At equilibrium \vec{M}_0 which is on the μT order cannot be distinguished from the \vec{B}_0 field since it is aligned with it. At this stage, the idea is to bring the magnetization in the xy plane, also called the transverse plane, such that it can be measured by a detector only acquiring magnetic fields perpendicular to the z direction. The magnetization can be tipped away from the longitudinal direction by applying a new magnetic field, called \vec{B}_1 in the transverse plane. From equation (2.20) the effect of this \vec{B}_1 field would be to induce a rotation of \vec{M} in the plane defined by the z axis and the direction perpendicular to \vec{B}_1 in the transverse plane. However, as soon as \vec{M} tips away from the z axis, it starts to have a nonzero component perpendicular to \vec{B}_0 which according to equation (2.20) will precess about z at the Larmor frequency (Fig. 2.7). Therefore, the rotation of the magnetization towards the transverse plane continues if the \vec{B}_1 field follows the precession of \vec{M} , i.e. it has to rotate with a frequency close to ω_0 about z. By sending 90° out of phase RF radiations of frequency ω and amplitude B_1 with two orthogonal RF transmitters, the following B_1 field is created

$$\vec{B}_{1,xy}(t) = B_1(t)(\cos(\omega t) \cdot \hat{x} - \sin(\omega t) \cdot \hat{y}) \quad (2.25)$$

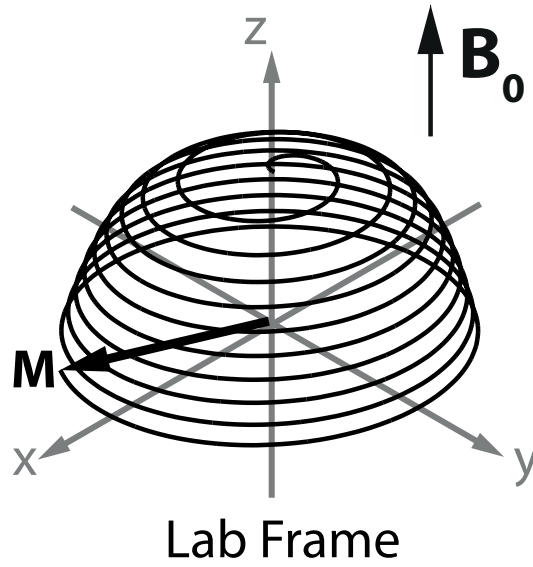


Figure 2.7: Magnetization evolution under the effect of a \vec{B}_1 field applied in the transverse plane and rotating at the Larmor frequency. As soon as \vec{M} has a component perpendicular to the main \vec{B}_0 field, it starts to precess about it according to equation (2.20).

By tuning ω to the Larmor frequency, this field will follow the precession of \vec{M} and thus bring it gradually towards the transverse plane (Fig. 2.7). The description is much simpler in the rotating reference frame where $\vec{B}_1(t)$ is stationary in the transverse plane, e.g. in the x' direction. In this frame, the expression of \vec{B}_{eff} in equation (2.22) becomes

$$\vec{B}_{eff} = B_1(t) \cdot \hat{x}' + \left(B_0 + \frac{\omega_0}{\gamma} \right) \cdot \hat{z} = B_1(t) \cdot \hat{x}' \quad (2.26)$$

The evolution of \vec{M} is thus given by

$$\left(\frac{d\vec{M}}{dt} \right)_{rot} = -\gamma \begin{pmatrix} B_1(t) \\ 0 \\ 0 \end{pmatrix} \times \vec{M} \quad (2.27)$$

The spiral motion of \vec{M} in the lab frame becomes a simple rotation about \vec{B}_1 in the rotating frame (Fig. 2.8). More generally, for any \vec{B}_1 field stationary in the transverse plane, the rotation of \vec{M} would be described by

$$\left(\frac{d\vec{M}}{dt} \right)_{rot} = -\gamma \vec{B}_1 \times \vec{M} \quad (2.28)$$

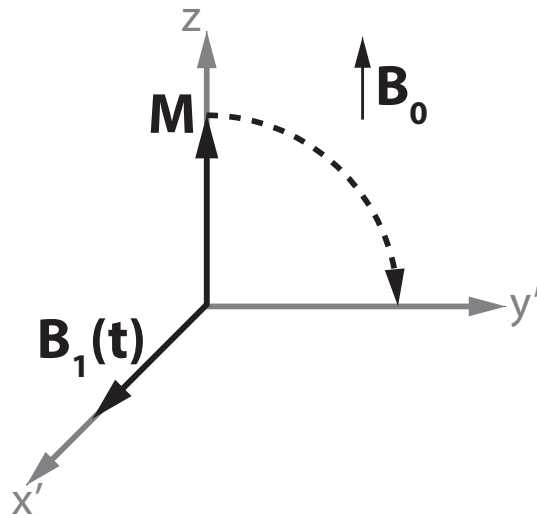


Figure 2.8: In the frame rotating at Larmor frequency ω_0 , the \vec{B}_1 field (also rotating at ω_0) is static in the transverse plane. The precession of the magnetization about \vec{B}_0 is unnoticeable in the rotating frame and therefore, the motion of \vec{M} is reduced to a rotation about \vec{B}_1 .

As the shape of this last expression is similar to equation (2.20), the angular frequency of \vec{M} about \vec{B}_1 can be written as

$$\vec{\omega}_1(t) = -\gamma \vec{B}_1(t) \quad (2.29)$$

A \vec{B}_1 field with constant amplitude B_1 applied in the x' direction for a duration τ and then switched off is called a hard pulse (Fig. 2.9). The angle α with which the magnetization was

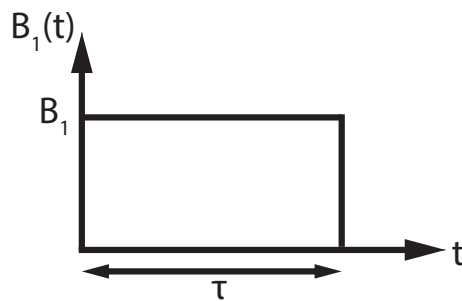


Figure 2.9: Hard pulse of duration τ and amplitude B_1 . The induced flip angle is proportional to the area under the pulse $B_1 \cdot \tau$.

tilted at the end of an RF pulse of duration τ can be calculated in a general way as

$$\alpha = \int_0^\tau \vec{\omega}_1(t) dt = \gamma \int_0^\tau \vec{B}_1(t) dt \quad (2.30)$$

For the hard pulse, this integral can be simplified to

$$\alpha = \gamma \int_0^\tau B_1 dt = \gamma B_1 \tau \quad (2.31)$$

An RF pulse bringing \vec{M} from the z direction to the transverse plane is called a 90° pulse. Following the same logic, a 180° pulse flips \vec{M} with a 180° angle. Following on with the hard pulse example, a 90° flip angle can be achieved in 0.5ms if $B_1 = 11\mu T$ which is way below the strength of the B_0 field.

The hard pulse described previously was a particular case where \vec{B}_1 was applied along the x' direction corresponding to a null phase. RF pulses used to manipulate \vec{M} can have time varying amplitudes and phases. These types of pulses will be analyzed later on in this thesis.

2.2.2.5 Relaxation times T_1 , T_2 and T_2^*

In the previous section, the process of bringing \vec{M} into the transverse plane called excitation, was described. After the RF pulse, two relaxation mechanisms take place. The transverse component of the magnetization M_{xy} decays away while the longitudinal component M_z returns to its equilibrium state M_0 . The physical interactions explaining those mechanisms are diverse and complex. In this text, only dipole-dipole interactions which are the most relevant in human tissues will be taken into account in the description of relaxation. To describe the decay of M_{xy} , it is important to recall that \vec{M} corresponds to the sum of many magnetic moments. Right after the excitation pulse, those moments are all in phase meaning that they point in the same direction and are precessing about \vec{B}_0 at Larmor frequency. Under those conditions, M_{xy} is maximal. In living tissues atoms are rotating, vibrating and translating in

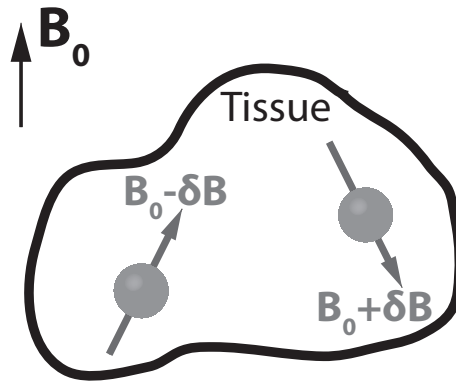


Figure 2.10: Dipole-dipole interaction leading to varying magnetic fields experienced by the involved nuclei. Indeed, the nuclei on the left is affected by B_0 minus the small magnetic field δB generated by the nuclei on the right. Its precession frequency is thus lower than γB_0 . The opposite situation occurs for the nuclei on the right side of the figure, which precesses at a higher frequency.

random ways (Brownian motion). When two nuclei become close to each other, their magnetic moment adds up to \vec{B}_0 , changing their respective precession frequencies (Fig. 2.10). In

the rotating frame, such magnetic moments will start to rotate clockwise if their new precession frequency is higher than ω_0 and anticlockwise if it is smaller. When nuclei move away from each other, this dipole-dipole or spin-spin interaction stops and they precess again at ω_0 but they are now dephased in respect to their original position (Fig. 2.11). Many interac-

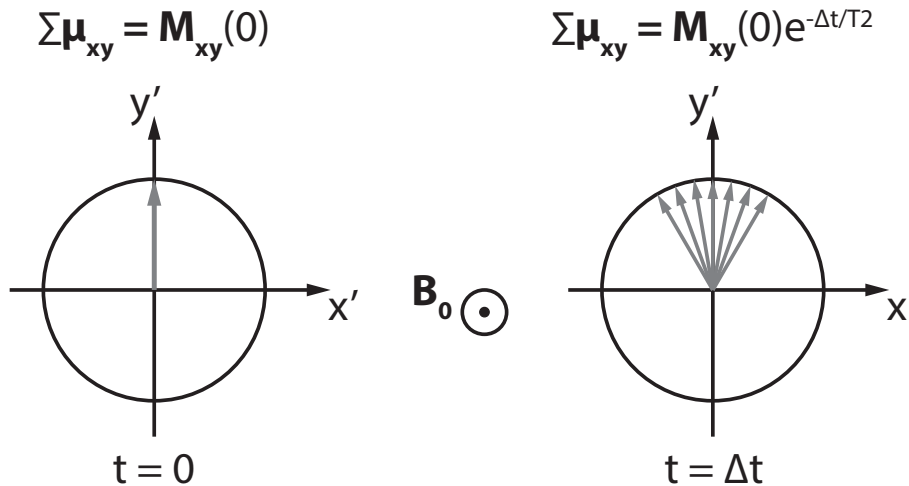


Figure 2.11: After an RF pulse, all the magnetic moments brought in the transverse plane are aligned ($t=0$). Due to dipole-dipole interactions, the magnetic moments see different precession frequencies, leading to a loss of coherence over a period of time Δt .

tions of this type occur over time increasing the dephasing between the magnetic moments what finally ends up in a complete loss of coherence in the transverse plane. According to this mechanism, the evolution of M_{xy} over an infinitesimal duration dt is given by

$$\frac{dM_{xy}}{dt} = -\frac{M_{xy}}{T_2} \quad (2.32)$$

After integration between 0 and t , the transverse magnetization follows an exponential decay characterized by the relaxation time T_2

$$M_{xy}(t) = M_{xy}(0)e^{-\frac{t}{T_2}} \quad (2.33)$$

where $M_{xy}(0)$ is the initial transverse magnetization, e.g. after the excitation pulse (Fig. 2.12a). At time T_2 , 37% of $M_{xy}(0)$ can still be detected. Different T_2 values are found in human tissues depending on how fast the protons are tumbling. When ^1H atoms are tumbling quickly, a particular nuclei will experience a rapidly fluctuating magnetic field of which average value is close to B_0 . Under this condition, the magnetic moments are maintained in a coherent state for a longer period what corresponds to a long T_2 value. Cerebrospinal fluids (CSF) for example is a tissue with a long T_2 relaxation as compared to other tissues found in the human brain. On the other hand, for slowly tumbling atoms fluctuations cannot be averaged out and the loss of coherence will occur much faster, leading to a short T_2 .

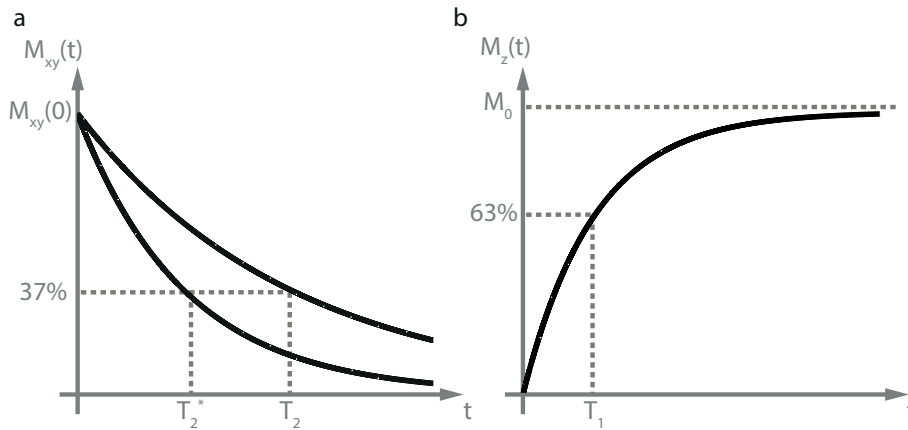


Figure 2.12: (a) T_2 (top) and T_2^* (bottom) decay curves. The characteristic times T_2 and T_2^* correspond to a 63% coherence loss in respect to the initial state $M_{xy}(0)$. (b) T_1 -recovery curve. The characteristic time T_1 corresponds to a 63% recovery of the equilibrium magnetization after a 90° excitation (assuming $M_z = M_0$ before the pulse).

Typical T_2 values found in human tissues are on the tens of ms order.

When applying the excitation pulse to bring \vec{M} into the transverse plane a certain amount of energy is absorbed by the system of nuclei. During transverse relaxation or T_2 -decay, a loss of coherence between the magnetic moments occurs but the net energy of the system is unchanged. Longitudinal relaxation or T_1 -recovery describes how the z components of the magnetization returns to equilibrium. During excitation, the absorbed energy created the transfer of nuclei from spin-down to spin-up states. This energy has to be released to the surrounding environment or lattice such that the system of nuclei returns to its original state. Protons promoted in spin-up state are in a stable position and therefore, their transition back to the spin-down state does not occur spontaneously. The return of nuclei in their initial state is stimulated by the randomly fluctuating magnetic fields resulting from the tumbling dipoles belonging to the lattice. Such fields contain a broad range of orientations and frequencies but only those perpendicular to \vec{B}_0 and rotating at ω_0 can induce transitions between states. According to this mechanism, the evolution of M_z over an infinitesimal duration dt is given by

$$\frac{dM_z}{dt} = -\frac{M_z - M_0}{T_1} \quad (2.34)$$

After integration between 0 and t , the longitudinal magnetization follows an exponential recovery characterized by the relaxation time T_1

$$M_z(t) = M_0 + (M_z(0) - M_0)e^{-\frac{t}{T_1}} \quad (2.35)$$

where $M_z(0)$ is the initial longitudinal magnetization. After a 90° excitation pulse $M_z(0) = 0$. At time T_1 , 63% of M_0 is back in the longitudinal direction (Fig. 2.12b). Human tissues have different T_1 values depending on the density of atoms tumbling at Larmor frequency. The higher it is the more favored transitions are, what corresponds to a short T_1 . For ex-

ample, the density of water molecules tumbling at ω_0 being low in CSF, the longitudinal relaxation process is slow and therefore T_1^{CSF} is long. For any given tissue, a higher density of molecules tumbles at low frequency than at high. If B_0 increases so does ω_0 and thus less protons will be tumbling at the new Larmor frequency making the T_1 relaxation longer at high field. Typical T_1 values found in human tissues are on the order of a hundred to a thousand of ms, i.e. T_1 recovery is a much longer process than T_2 decay.

When describing the mechanism of transverse relaxation, dipole-dipole interactions were considered at the microscopic level. The loss of coherence between magnetic moments can also arise from the unavoidable inhomogeneity of the main magnetic field particularly pronounced at tissue interfaces, air-tissue boundaries or regions of high iron concentration. This field fluctuation $\Delta B_0(\vec{r})$ involves that nuclei at different spatial positions will not precess at ω_0 leading to a faster dephasing between them. The transverse relaxation taking \vec{B}_0 inhomogeneities into account is characterized by

$$\frac{1}{T_2^*} = \frac{1}{T_2} + \gamma \Delta B_0 \quad (2.36)$$

T_2^* being $\leq T_2$, a faster decay of M_{xy} occurs when nuclei are affected by ΔB_0 . Most of the contrasts obtained in MRI result from the fact that body tissues have different T_1 , T_2 or T_2^* relaxation times. The methodology used to acquire images with specific contrasts will be described in section 2.3.4.1.

2.2.2.6 Bloch equations

Adding the relaxation components (2.32) and (2.34) to equation (2.20) provides

$$\frac{d\vec{M}}{dt} = -\gamma \vec{B} \times \vec{M} - \frac{M_x \cdot \vec{e}_x + M_y \cdot \vec{e}_y}{T_2} - \frac{(M_z - M_0) \cdot \vec{e}_z}{T_1} \quad (2.37)$$

This system represents the Bloch equations which correspond to the general description of the magnetization evolution in the classical mechanics framework. Those equations taking the precession and relaxation mechanisms into account are very useful to predict the magnetization state after a series of RF pulses, what consists in a valuable tool in pulse sequence development. With the \vec{B}_1 field given by equation (2.25) and the static \vec{B}_0 field along the z direction, \vec{B} in the previous expression is given by

$$\vec{B} = B_1(t)(\cos(\omega t) \cdot \vec{e}_x - \sin(\omega t) \cdot \vec{e}_y) + B_0 \cdot \vec{e}_z \quad (2.38)$$

Rewriting the equation of each component one by one leads to

$$\begin{aligned}
 \frac{dM_x}{dt} &= \gamma [M_y B_0 + M_z B_1 \sin(\omega t)] - \frac{M_x}{T_2} \\
 \frac{dM_y}{dt} &= \gamma [-M_x B_0 + M_z B_1 \cos(\omega t)] - \frac{M_y}{T_2} \\
 \frac{dM_z}{dt} &= \gamma [M_x B_1 \sin(\omega t) - M_y B_1 \cos(\omega t)] - \frac{M_z - M_0}{T_1}
 \end{aligned} \tag{2.39}$$

The evolution of the system, for example after an RF pulse (absence of B_1), can be obtained simply by solving the previous differential equations. The transverse terms being decoupled from the longitudinal ones in this particular case, $M_x(t)$ and $M_y(t)$ can be obtained by solving the matrix system

$$\frac{d}{dt} \begin{pmatrix} M_x \\ M_y \end{pmatrix} = \begin{bmatrix} -\frac{1}{T_2} & \omega_0 \\ -\omega_0 & -\frac{1}{T_2} \end{bmatrix} \begin{pmatrix} M_x \\ M_y \end{pmatrix} \tag{2.40}$$

Calculating the eigenvalues of the 2 by 2 matrix $\lambda_{1,2} = -1/T_2 \pm i\omega_0$ and setting $M_x(0)$ and $M_y(0)$ as initial conditions, the solutions can be written as

$$\begin{aligned}
 M_x(t) &= [M_x(0)\cos(\omega_0 t) + M_y(0)\sin(\omega_0 t)]e^{-\frac{t}{T_2}} \\
 M_y(t) &= [M_y(0)\cos(\omega_0 t) - M_x(0)\sin(\omega_0 t)]e^{-\frac{t}{T_2}}
 \end{aligned} \tag{2.41}$$

For the longitudinal component, the solution is simply obtained by integrating on both sides and with the initial condition $M_z(0)$

$$M_z(t) = M_z(0)e^{-\frac{t}{T_1}} + M_0(1 - e^{-\frac{t}{T_1}}) \tag{2.42}$$

In the particular case where a 90° pulse is applied in the $+x'$ direction when the system is at equilibrium, the state of the magnetization after the pulse is $M_x(0) = M_z(0) = 0$ and $M_y(0) = M_0$, and the magnetization evolution in the lab frame follows

$$\begin{aligned}
 M_x(t) &= M_0 \sin(\omega_0 t) e^{-\frac{t}{T_2}} \\
 M_y(t) &= M_0 \cos(\omega_0 t) e^{-\frac{t}{T_2}} \\
 M_z(t) &= M_0 (1 - e^{-\frac{t}{T_1}})
 \end{aligned} \tag{2.43}$$

where it was assumed that at time $t=0$, the x and x' axes coincide. The rotation and decay of transverse components combined with the recovery of M_z gives rise to a spiral shaped motion of \vec{M} when returning back to equilibrium (Fig. 2.13). Although they are entirely based on classical mechanics, Bloch equations can be used to describe most of MRI concepts. Some applications where Bloch equations have a central role will be presented afterwards.

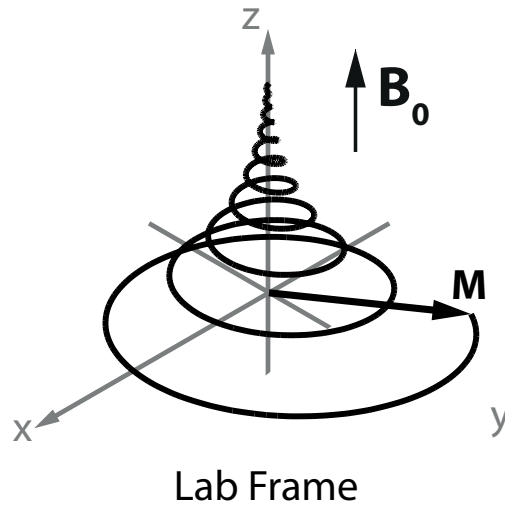


Figure 2.13: Return of magnetization back to equilibrium in the lab frame of reference. T_2 or T_2^* relaxation is responsible for the decay of the transverse magnetization whereas M_z increases due to T_1 -recovery.

2.2.2.7 Signal detection

It was explained earlier in the text that after an excitation pulse, part of or even the whole (for a 90° pulse) of \vec{M} is brought into the xy plane. The reason for this desire to have magnetization in the transverse plane is because it is rotating about \vec{B}_0 . From Faraday's law of induction, a time varying magnetic field flux $d\Phi_B/dt$ induces an electromotive force ε (or voltage) in a conductor loop placed nearby.

$$\varepsilon = -\frac{d\Phi_B}{dt} \quad (2.44)$$

Starting from simple wire loops, the devices used to detect the NMR signal, called RF coils, have become more and more sophisticated in order to lose as less signal as possible during the reception process. Once the excitation pulse is off, as \vec{M}_{xy} is rotating in the transverse plane, a signal oscillating at ω_0 will be induced in the RF coil (Fig. 2.14). Due to T_2^* -decay, an exponential envelope is observed on the signal shape $S(t)$. The mathematical expression for $S(t)$ after an excitation pulse with flip angle α is

$$S(t) = RX(\vec{r})e^{-\frac{t}{T_2^*}}e^{-i\omega_0 t}\sin(\alpha)M_z(0) \quad (2.45)$$

with $M_z(0)$ the longitudinal magnetization before the pulse and $RX(\vec{r})$ the coil sensitivity which, as discussed later for simple loops, decreases with the distance \vec{r} between the coil and the sample. This type of decaying signal is called Free Induction Decay (FID).

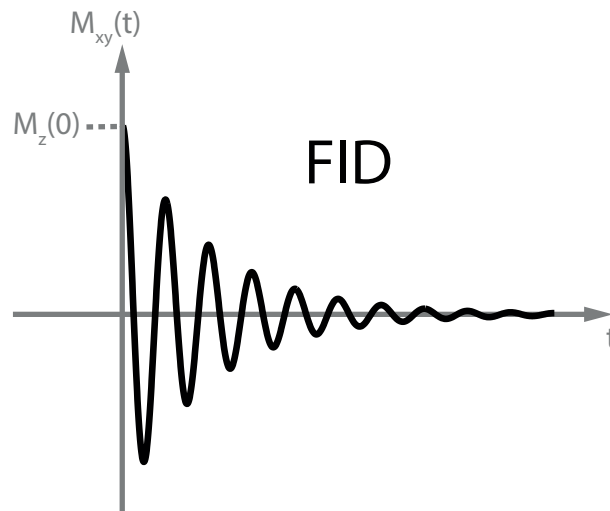


Figure 2.14: MR signal generated by the magnetization brought in the transverse plane by an RF pulse. The fast oscillating component results from the fact that M_{xy} precesses at ω_0 . T_2 or T_2^* relaxation occurs over time leading to an exponential decay of M_{xy} (cf. Fig. 2.12a).

2.2.3 Gradients and slice selection

So far, if inhomogeneities in the \vec{B}_0 field are neglected, \vec{M} was only precessing about z at ω_0 . This means that after excitation, every magnetic moments throughout a region of interest are precessing with the same frequency. In this case, it is not possible to deduce which position within the subject the signal is coming from. In the process of obtaining spatial localization which was first explored by both Lauterbur and Mansfield, linearly varying gradient fields are applied in x, y and z directions. A gradient field in one particular direction means that depending on the position an extra term will be added to the \vec{B}_0 field. The gradients in the three orthogonal directions can be expressed as

$$G_i = \frac{\partial B_z}{\partial i} \quad i \in [x, y, z] \quad (2.46)$$

Magnetic field gradients are usually given in mT/m and, as will be described in section 2.4 they are produced by three sets of gradient coils located in the magnet walls. In the case where G_x is applied, the B_z field varies along the x direction according to

$$B_z(x) = B_0 + G_x \cdot x \quad (2.47)$$

This implies that the frequency at which each nuclei precesses becomes position dependent (Fig. 2.15). The expression for the precession frequency at location x is simply obtained by multiplying the previous equation by γ

$$\omega(x) = \omega_0 + \gamma G_x \cdot x \quad (2.48)$$

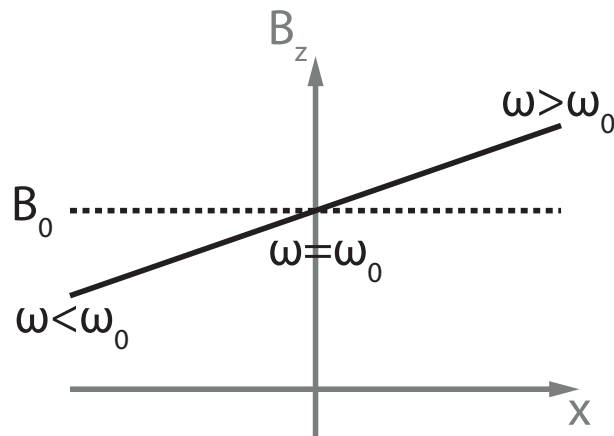


Figure 2.15: Linear evolution of B_z under the effect of a gradient $G_x = dB_z/dx$ in the x direction. A positive gradient provides a precession frequency ω smaller than ω_0 for $x < 0$ and higher for $x > 0$. The opposite effect would be observed for $G_x < 0$.

Spatial information can thus be encoded by applying gradients in two or three directions such that protons at different locations emit signals with position dependent frequencies. This will be explained in more details in section 2.3.1.

A linear gradient is also required to perform slice selection, i.e. to excite only the nuclei belonging to a specific two-dimensional slab of the sample. To perform slice selection along z , the excitation pulse has to be applied in the presence of a gradient along z , G_z . The condition on the excitation pulse is that it has a narrow bandwidth $\Delta\omega$ centered at Larmor frequency. Indeed, it was explained in section 2.2.2.4 that if \vec{M} precesses about \vec{B}_0 at ω_0 , \vec{B}_1 must rotate at ω_0 to bring the magnetization towards the transverse plane. Now that the nuclei precess with ω depending on their z position, only those with frequencies belonging to $[\omega_0 - \Delta\omega/2, \omega_0 + \Delta\omega/2]$ will be excited. Usually, sinc shaped RF pulses of the form $\sin(\pi\Delta\omega \cdot t)/(\pi\Delta\omega \cdot t)$ are good candidates for slice selection since in the small tip angle regime, their frequency profile is a rectangle of bandwidth $\Delta\omega$ (Fig. 2.16). Positions along the z axis where nuclei precess at frequencies outside the bandwidth of the RF pulse $B_1(t)$ remain unexcited. By changing the RF pulse carrier frequency, the position of the selected slice can be varied. Indeed, the positions of nuclei on resonance with the new range of frequencies will be different. Δz can be controlled either by changing the RF pulse bandwidth, $\Delta\omega$, or by varying the gradient strength, G_z . A thinner slice is thus obtained by increasing G_z since the slope of the line in figure 2.16 becomes steeper or by reducing the pulse bandwidth leading to a longer pulse duration. At the end of the slice selection process performed by using a sinc RF pulse (Fig. 2.17), a refocusing gradient lobe with half the duration of the first one is applied. This negative lobe is required because at the end of the RF excitation, the magnetic moments in the Δz slab are out of phase since they were all precessing at different frequencies during the excitation and therefore ended up with orientations spread in the xy plane. Mathematically, the transverse magnetization at each position z within the selected

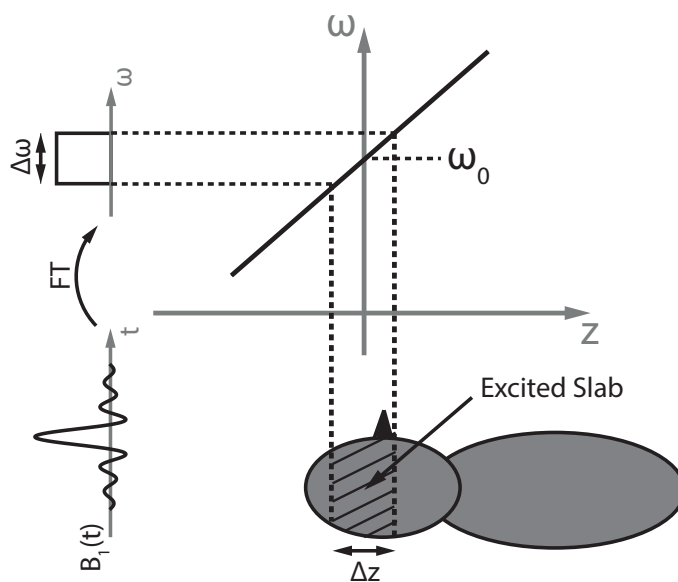


Figure 2.16: Slice or slab of width Δz excited by a sinc pulse of bandwidth $\Delta\omega$. Only magnetic moments at positions located in the region where the precession frequencies correspond to $\Delta\omega$ will be affected by the pulse. The slab position can be modified by changing the pulse carrier frequency ω_0 whereas Δz varies accordingly to the pulse bandwidth $\Delta\omega$ or the gradient strength G_z . It will be shown in section 3.2 that in the small tip angle regime, the excited slice profile is the Fourier transform of the RF pulse shape. Under this condition, the magnetization in a Δz interval is excited uniformly by a sinc pulse.

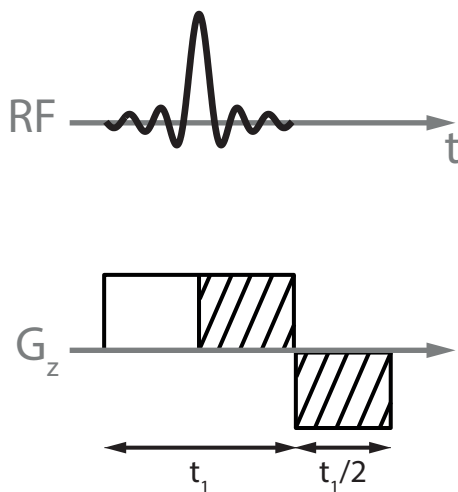


Figure 2.17: Slice-selection process where the RF pulse and gradient are combined to excite the magnetization in a slab of width Δz . As it is assumed that \vec{M} experiences the pulse effect when its central part is applied, the magnetic moments at different z positions are dephased by the G_z gradient over a period of time $t_1/2$. Such that every magnetic moments are in phase at the end of the slice selection process, a gradient lobe of duration $t_1/2$ is applied after the first one but with the opposite polarity.

slice is multiplied by a phase term given by

$$e^{i\gamma G_z z \frac{t_1}{2}} \tag{2.49}$$

As it is proportional to the integral over the z positions in the Δz interval, the measured signal would be weak at this stage since destructive interferences occur when adding up the magnetic moments throughout the slice. The role of the gradient with negative polarity is to unwind the linear phase accrued during the sinc excitation pulse. A negative gradient with the same amplitude as the first one and duration $t_1/2$ would create the following phase factor

$$e^{-i\gamma G_z z \frac{t_1}{2}} \quad (2.50)$$

which cancels the phase dispersion associated to equation (2.49), meaning that after the negative gradient, the magnetic moments in the selected slice are all aligned in the same direction and no phase cancellation occurs anymore.

In equation (2.49), only half of the pulse duration $t_1/2$ was considered. This is because physically, the magnetization is mainly flipped when the central lobe of the sinc pulse is applied, i.e. at time $t_1/2$. This means that the phase dispersion occurs during the second half of the pulse and therefore maximum refocusing is obtained if the duration of the negative gradient is $t_1/2$.

2.2.4 Gradient echo

Echo formation is a very important concept in MR. Echoes can be generated either by using gradients or RF pulses. The gradient echo mechanism will be presented in this subsection while the spin echo and the stimulated echo will be described in the next one. Without generality loss, the case where the magnetic moments are all along y' after a 90° RF pulse applied in the x' direction will be considered as a starting condition (Fig. 2.18b). The first element in the gradient echo creation is a negative gradient applied immediately after the excitation pulse (Fig. 2.18a), e.g. along the x direction. As explained in the previous section, magnetic moments at different x locations will start to dephase (Fig. 2.18c). Nuclei become out of phase in a much faster way than during T_2^* -decay process. A positive gradient is then applied, inverting the slope sign of the $B_z(x)$ line. Magnetic moments at positions where ω was faster, now become slower and vice versa (Fig. 2.18d). At the point where the positive lobe reaches the area of the negative lobe, all magnetic moments are back in phase along the y' direction (Fig. 2.18e). During the whole process, dephasing due to dipole-dipole interactions as well as B_0 inhomogeneities also occur. Since the positive gradient only refocuses the phase shift created by the negative lobe, the maximum gradient echo signal S_{GE} will be

$$S_{GE}(TE) = S_0 e^{-\frac{TE}{T_2^*}} \quad (2.51)$$

where S_0 is the maximum signal available after the excitation pulse. For a 90° pulse and the magnetization at thermal equilibrium before it, $S_0 = M_0$ whereas for a flip angle α , $S_0 = M_0 \sin(\alpha)$. As T_2^* -decay evolves during the time TE , the phase losses due to local field inhomogeneities cannot be removed by the positive gradient. Applying the gradients as

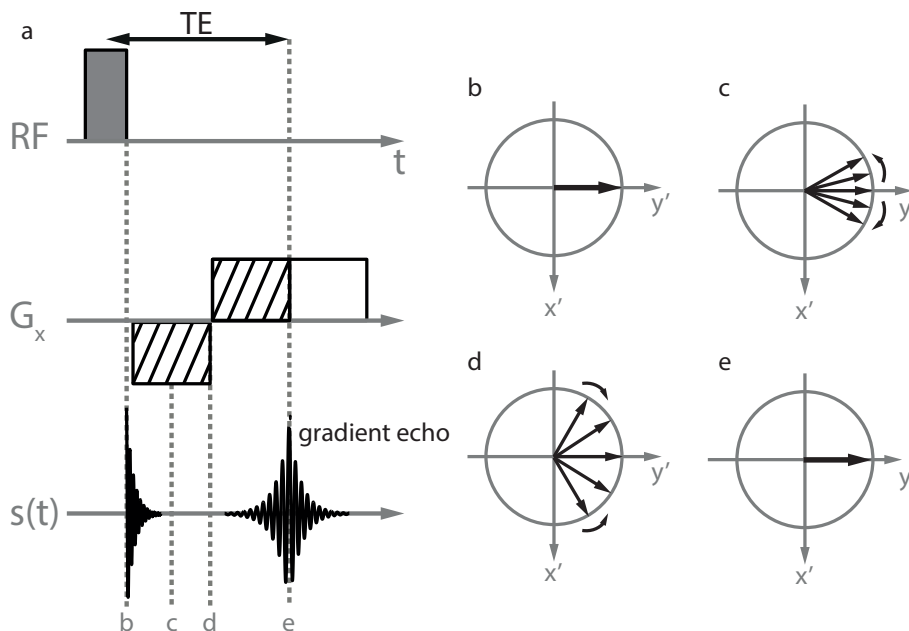


Figure 2.18: (a) Diagram illustrating the gradient echo formation. (b) After the pulse applied in the x' direction, \vec{M} is along y' . (c) Under the effect of the dephasing $-G_x$ gradient, magnetic moments at different locations become out of phase. (d) After the dephasing period, a refocusing gradient with the opposite polarity is applied in order to rephase the magnetic moments together. (e) A gradient echo occurs when the dephasing and refocusing areas are equal, meaning that the magnetic moments are back in phase.

fast as possible in order to have the shortest TE minimizes this effect.

2.2.5 Spin echo, Hahn echo and stimulated echo

Another type of echo can be created by applying a 180° refocusing pulse after the excitation pulse (Fig. 2.19a). In the case of a 90° pulse applied in the x' direction, \vec{M} is brought along y' (Fig. 2.19b) and then magnetic moments become out of phase (Fig. 2.19c) due to dipole-dipole interaction and B_0 inhomogeneities. At time $TE/2$ after the excitation, the 180° pulse is applied along the y' axis. All the magnetic moments are thus flipped by 180° about the y' axis (Fig. 2.19d) meaning that after the pulse, the phase dispersion due to local field inhomogeneities decreases (Fig. 2.19e). It is important to note that unlike in the case of the gradient echo formation, the frequency of magnetic moments was not modified by the 180° pulse, i.e. the ones with $\omega > \omega_0$ are still rotating clockwise whereas those with $\omega < \omega_0$ keep their anticlockwise rotation in the rotating frame. As dephasing occurred during the $TE/2$ period between the two pulses, the same duration is required for the magnetic moments to come back in phase along y' and form the spin echo (Fig. 2.19f). When compared to gradient echo, the main advantage is that the B_0 inhomogeneities do not affect the spin echo signal. Indeed, a nuclei precessing slower or faster than ω_0 due to ΔB_0 will accumulate a phase

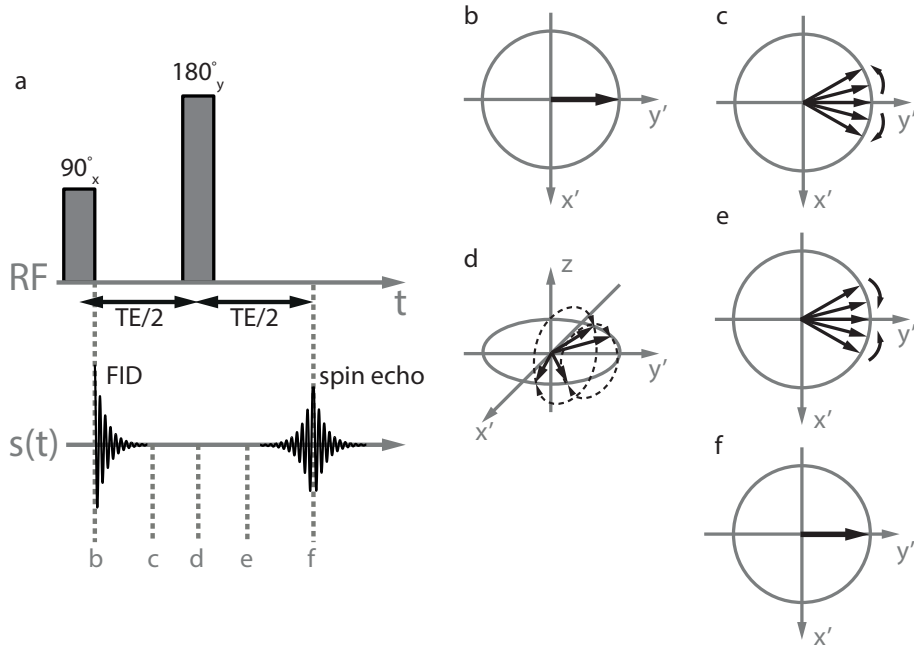


Figure 2.19: (a) Diagram illustrating the spin echo formation. (b) The 90°_x pulse brings \vec{M} along the y' axis. (c) Magnetic moments dephase due to dipole-dipole interactions and \vec{B}_0 inhomogeneities. (d) At time $TE/2$ after the 90° pulse, magnetic moments experience a rotation caused by the refocusing pulse. (e) Since they are still precessing with the same frequency, the magnetic moments are coming back in phase. (f) At time $TE/2$ after the 180° pulse, \vec{M} is in a coherent state giving rise to the spin echo.

shift for a time $TE/2$. The existing signal for t in the $[0, TE/2]$ interval is given by

$$S(t) = S_0 e^{i\gamma\Delta B_0 t} e^{-\frac{t}{T_2^*}} \quad (2.52)$$

where the first exponential term takes the dephasing due to B_0 inhomogeneities into account. Once the 180° pulse has been applied, the phase created by ΔB_0 evolves in the opposite direction. For $t > TE/2$, the signal expression becomes

$$S(t) = S_0 e^{i\gamma\Delta B_0 TE/2} e^{-\frac{TE}{2T_2^*}} e^{-i\gamma\Delta B_0 t} e^{-\frac{t}{T_2^*}} \quad (2.53)$$

At time TE after the 90° pulse, the phase shifts accrued due to ΔB_0 before and after the refocusing pulse will thus exactly compensate each other. On the other hand, the 180° pulse does not refocus the phase dispersion caused by spin-spin interactions due to its random character (the phase shifts before and after the pulse are not identical). T_2 -decay thus occurs during the whole process what means that the expression for the maximum spin echo signal S_{SE} is

$$S_{SE} = S_0 e^{-\frac{TE}{T_2}} \quad (2.54)$$

A 90° pulse followed by a 180° one is not the only way of obtaining a spin echo. Actually

2 Background

any combination of two pulses with any flip angles α_1 and α_2 can be used. Spin echoes that are not resulting from the 90° - 180° pair are usually called Hahn echoes [15]. The process for a pair of 90° pulses applied along x' will be depicted here. Magnetic moments that were all along y' after the first pulse dephase for a period $TE/2$ (Fig. 2.20a-c). To better

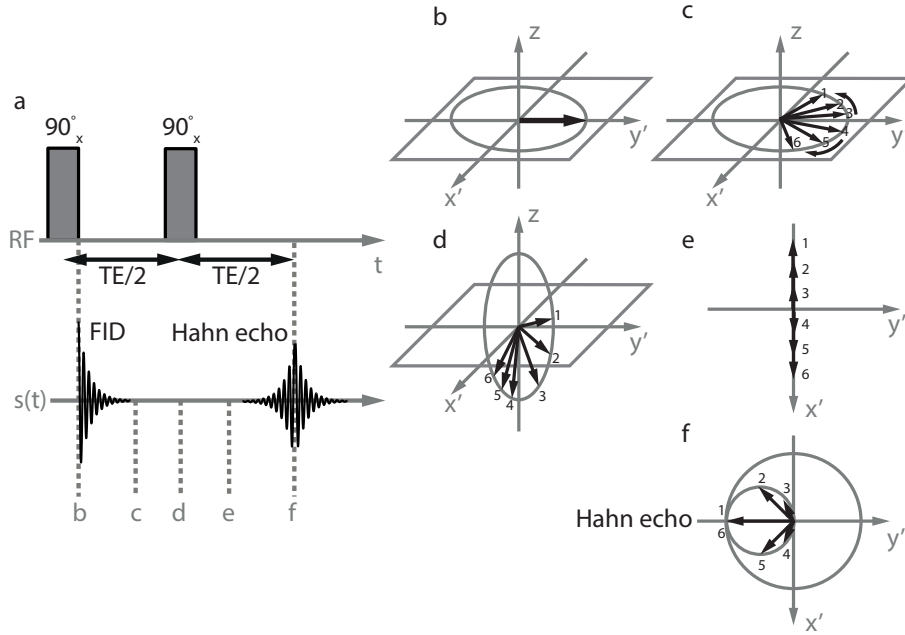


Figure 2.20: (a) Diagram illustrating the Hahn echo formation. (b) \vec{M} is brought along y' by the first 90°_x pulse. (c) Magnetic moments with different precession frequencies lead to coherence loss. (d) The second 90°_x pulse brings the magnetic moments in the $x'z$ plane. (e) For the Hahn echo formation, the longitudinal components are not considered. On the other side, the transverse components continue their rotation towards the $-y'$ direction. (f) As they possess different precession frequencies, the magnetic moments do not come back in phase on the $-y'$ axis at the same time. The maximum coherence occurs at time $TE/2$ after the second pulse, when the magnetic moments lie on a circle.

explain the Hahn echo formation, the evolution of magnetic moments $\vec{\mu}_{1-6}$ is depicted on illustrations. $\vec{\mu}_{1-3}$ are precessing slower than ω_0 ($\omega_{\vec{\mu}_1} < \omega_{\vec{\mu}_2} < \omega_{\vec{\mu}_3}$) whereas $\vec{\mu}_{4-6}$ are precessing faster ($\omega_{\vec{\mu}_6} > \omega_{\vec{\mu}_5} > \omega_{\vec{\mu}_4}$). The second 90° pulse flips every magnetic moments in the $x'z$ plane (Fig. 2.20d). From this point, the z components of $\vec{\mu}_{1-6}$ are unimportant since they will not take part in the Hahn echo formation (they will play a role in the stimulated echo process) and therefore only transverse components of the magnetic moments can be considered (Fig. 2.20e). After the second pulse, magnetic moments start to come back in phase towards the $-y'$ direction. As $\vec{\mu}_1$ and $\vec{\mu}_6$ have the extreme precession frequencies, they come back in phase on the $-y$ axis before any other magnetic moments. The maximum phase coherence is reached at time $TE/2$ after the second pulse when the magnetic moments lie on a circle (Fig. 2.20a,f). This incomplete refocusing implies that the Hahn echo amplitude is smaller than the spin echo one. More generally, the amplitude S_{HE} for a Hahn echo resulting

from a pair of pulses α_1 and α_2 is given by

$$S_{HE} = S_0 e^{-\frac{TE}{T_2}} \sin(\alpha_1) \sin^2\left(\frac{\alpha_2}{2}\right) \quad (2.55)$$

For the 90° - 90° pair, the Hahn echo amplitude is thus half the one of a full spin echo.

Another type of echo can be produced by applying three pulses with flip angles α_1 , α_2 , α_3 : the stimulated echo. 90° pulses will be considered again to explain the mechanism in its simplest form. As for the Hahn echo, magnetic moments that were all along y' after the first pulse dephase for a period $TE/2$ (Fig. 2.21a-c). In this example the evolution

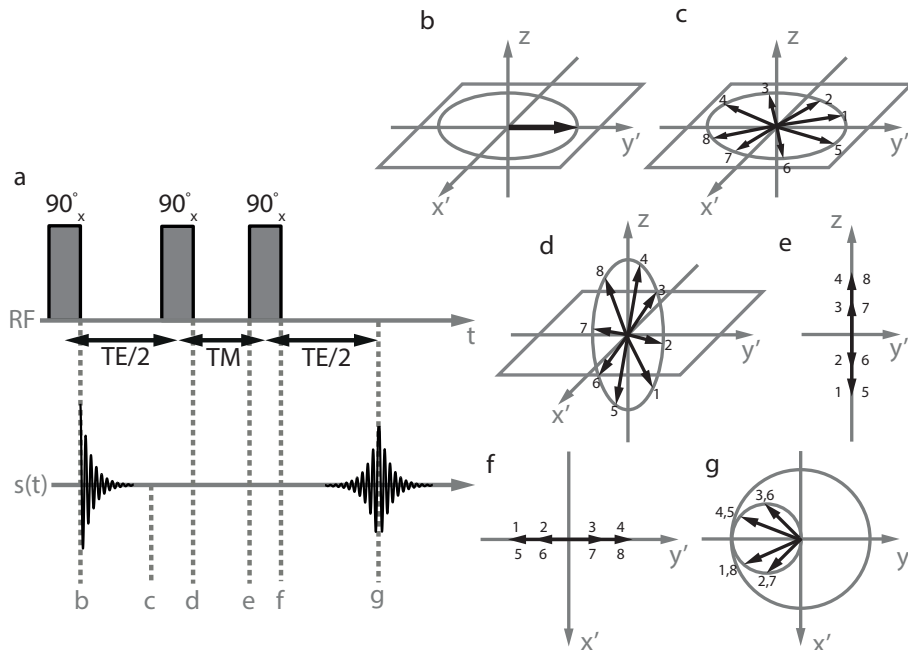


Figure 2.21: (a) Diagram illustrating the stimulated echo formation. (b) \vec{M} is brought along y' by the first 90°_x RF pulse. (c) Magnetic moments with different precession frequencies lead to coherence loss. (d) The second 90°_x pulse brings the magnetic moments in the $x'z$ plane. (e) The longitudinal components that were unimportant in the Hahn echo formation are responsible for the stimulated echo. The transverse components are now left apart. (f) The third 90°_x pulse brings the longitudinal components along the y' axis. (g) As they correspond to the slowly rotating magnetic moments of (b), the components along $-y'$ do not dephase too much while the fast components go from the $+y'$ side to $-y'$. Similarly as for the Hahn echo, a maximum coherence state, the stimulated echo, is reached at time $TE/2$ after the third pulse when the magnetic moments lie on a circle.

of eight magnetic moments $\vec{\mu}_{1-8}$ will be depicted. $\vec{\mu}_{1-4}$ are precessing slower than ω_0 ($\omega_{\vec{\mu}_1} > \omega_{\vec{\mu}_2} > \omega_{\vec{\mu}_3} > \omega_{\vec{\mu}_4}$) whereas $\vec{\mu}_{5-8}$ are precessing faster ($\omega_{\vec{\mu}_8} > \omega_{\vec{\mu}_7} > \omega_{\vec{\mu}_6} > \omega_{\vec{\mu}_5}$). As during the Hahn echo formation, the second 90° pulse flips every magnetic moments in the $x'z$ plane (Fig. 2.21d). This time, the transverse components of $\vec{\mu}_{1-8}$ which precess about z and produce the Hahn echo described earlier are unimportant and the focus is kept on the longitudinal components (Fig. 2.21e). Practically, the unwanted transverse components are suppressed either by choosing $TM \gg T_2$ or by applying a strong dephasing gradient

in order to create a complete loss of phase coherence. The longitudinal components will undergo T_1 -recovery for the TM period (Fig. 2.21a). The third RF pulse then flips those μ_z components into the $x'y'$ plane such that the slowly dephasing magnetic moments ($\vec{\mu}_{1,2,5,6}$) lie along $-y'$ whereas quick ones ($\vec{\mu}_{3,4,7,8}$) point towards $+y'$ (Fig. 2.21f). At this point components on both sides of the y axis are canceling each other and no signal can be detected. As they are quickly precessing about z , the y components of $\vec{\mu}_{3,4,7,8}$ rapidly become negative while $\vec{\mu}_{1,2,5,6}$ are still on the $-y'$ side since they dephase in a slower way. Similarly as for the Hahn echo formation, the coherence between magnetic moments therefore gradually increases until it reaches a maximum at time $TE/2$ after the third pulse (Fig. 2.21a), when the magnetic moments lie on a circle along the $-y'$ axis (Fig. 2.21g). Of course the magnetic moments are not completely in phase at this moment meaning that the stimulated echo amplitude S_{STE} is smaller than the spin echo one. Longitudinal relaxation affects the magnetization when it is stored in the z direction during the period TM whereas transverse relaxation occurs during the two $TE/2$ intervals. S_{STE} therefore depends on both T_1 and T_2 relaxation times. In the general case with three pulses α_1 , α_2 and α_3 the stimulated echo amplitude is given by

$$S_{STE} = \frac{1}{2} S_0 \sin(\alpha_1) \sin(\alpha_2) \sin(\alpha_3) e^{-\frac{TM}{T_1}} e^{-\frac{TE}{T_2}} \quad (2.56)$$

For a specific S_0 signal and assuming TE and TM short as compared to relaxation times such that exponential terms can be neglected, the maximum amplitude of the stimulated echo produced by three 90° pulses is half the one of a full spin echo. Stimulated echoes formed by three 90° pulses are often used in MR spectroscopy where the signal coming from a small volume of interest is targeted. In this case, RF pulses with slice selective gradients in different directions generate a stimulated echo signal coming only from protons belonging to the volume defined by the intersection of the three selected slices. For both Hahn and stimulated echoes, visualizing their formation for flip angles different from 90° becomes less intuitive. The framework presented in the next section will allow the prediction of the echoes as well as their amplitudes throughout any particular series of RF pulses. For example, it will be shown that three pulses with flip angles α_1 , α_2 and α_3 can create up to five echoes (four Hahn echoes and one stimulated echo).

2.2.6 Phase Graph

The evolution of \vec{M} can be calculated with precision using Bloch equations, but requires simulations over a large number of isochromats (microscopic groups of magnetic moments) precessing at different frequencies ω . The magnetization at a certain point of the pulse sequence is obtained by performing the vector sum over all isochromats. In order to get a precise solution, several thousands of isochromats should be considered in simulations, what is quite demanding in terms of computation. Moreover, the distribution of isochro-

mats becomes really complex when several pulses are involved and information about echo formation is not trivial.

The phase graph is an elegant tool that deals with groups of isochromats, what facilitates the understanding of the echo positions and amplitudes for a sequence of consecutive equally spaced RF pulses. To explain how phase graph works the basis will be set by revisiting the Hahn and stimulated echoes where the concept of configuration states will be introduced. In multipulse experiments, dephasing occurs between RF pulses. As explained previously, the loss of coherence between magnetic moments arises from multiple effects such as gradients, spin-spin interactions and B_0 inhomogeneities.

The concept of configuration states F and Z , which is central in the phase graph description can be explained by considering the dephasing produced by a gradient along z (G_z) on a set of isochromats initially in phase (Fig. 2.22). The phase accrued by an isochromat of

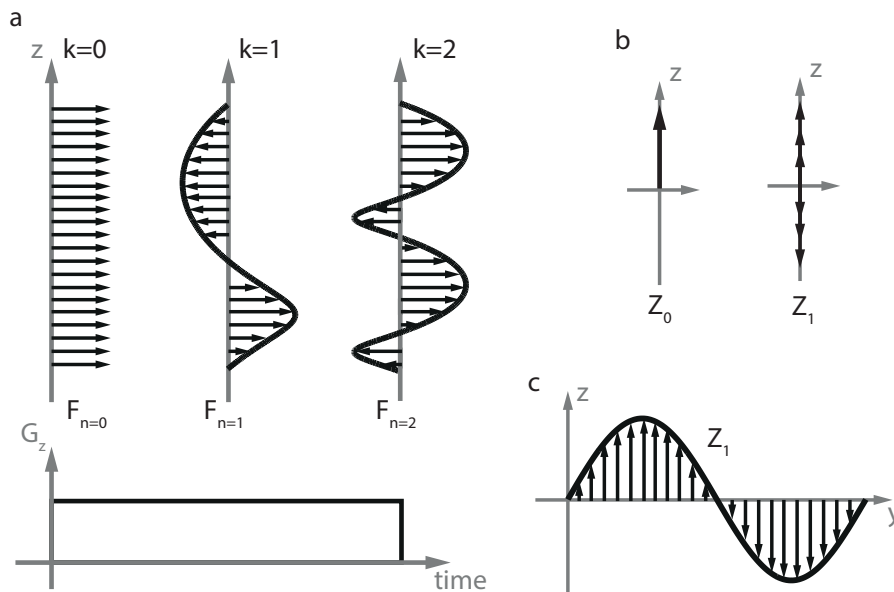


Figure 2.22: (a) A set of in phase isochromats corresponds to an F_0 state. A gradient leads to different precession frequencies according to the position of the isochromats. The dephasing unit k describes by how much isochromats are dephased by a gradient over a time period. If $k=1$, this means that a 2π dephasing is generated by the gradient from the slowest to the fastest isochromat. A gradient with $k=1$ thus transforms an F_0 state into F_1 which corresponds to an helix with 2π pitch. If the gradient is maintained for the same period, F_1 becomes F_2 (helix with π pitch). (b) The longitudinal components of isochromats are represented by Z_n states. Z_0 corresponds to the situation where every isochromats point towards $+z$. Under the effect of an RF pulse, nonzero components will be created from the F_1 state in the longitudinal direction, which correspond to a Z_1 state. (c) Sinusoidal Z_1 state resulting from the rotation of an F_1 state created by a gradient in the y direction.

magnitude M at position z over a period t is

$$\theta = \gamma G_z \cdot z \cdot t \quad (2.57)$$

Although in this expression the gradient is considered as the only source bringing the isochromats out of phase, some other components such as B_0 inhomogeneities, $\Delta B_0(\vec{r})$ could also be taken into account. At time t , the transverse components of isochromats are defined by

$$\begin{aligned} M_x(z, t) &= M \cos(\gamma G_z \cdot z \cdot t) \\ M_y(z, t) &= M \sin(\gamma G_z \cdot z \cdot t) \end{aligned} \quad (2.58)$$

Those equations define an helix for which, according to equation (2.57), the pitch decreases if θ increases (Fig. 2.22). The same analysis can be performed for gradients applied along x or y . More generally, for a gradient \vec{G} having components in every spatial direction, equation (2.57) becomes

$$\theta = \gamma \vec{G} \cdot \vec{r} \cdot t \quad (2.59)$$

what means that potentially, various helices with different pitches could be found along x , y and z .

For common sequences which are regular and periodic, isochromats are dephased in a similar way between almost every pulses. The shortest dephasing period of the sequence, T , can thus be considered as the reference and the dephasing unit $k=1$ can be associated to a dephasing of $\gamma \vec{G} \vec{r} T$. It can be assumed that a set of isochromats originally in phase will be transformed in an helix $F_{n=1}$ which has a 2π pitch (one turn from bottom to top) by a $k=1$ dephasing period (Fig. 2.22). As every other dephasing periods of the sequence can be expressed as multiples of the reference period, only helices with integer number of turns will be generated. A left-handed helix with n turns ($n \in \mathbb{N}$) made of components in the transverse plane is called a configuration state F_n (Fig. 2.22). On the other hand a right-handed helix on which isochromats are dephased in the opposite direction corresponds to an F_{-n} state. Those states are usually pictured from the top as disks of radius depending on the isochromat magnitudes and with a circular arrow indicating the helix chirality (Fig. 2.23).

Z_n states describe modulated longitudinal magnetization and are represented by a series of arrows (longitudinal components of isochromats) in the z direction (Fig. 2.22b). A Z_0 state corresponds to the situation where the z components of the isochromats are pointing towards $+z$ with no spatial modulation. A Z_n state is created under the effect of an RF pulse transferring F states into the longitudinal direction. As shown in equation (2.58), helices are made of sine and cosine evolutions of M_x and M_y . Therefore, a Z state will also have a sinusoidal shape along the axis where dephasing occurred in the transverse plane. For example, an F_1 state created by a dephasing in the y direction will produce a Z_1 state of sinusoidal shape with the same spatial frequency (Fig. 2.22c). Accordingly, a Z_2 state is π periodic.

To illustrate how the states evolve in a phase graph, the effect of three RF pulses with flip angles $\alpha_1, \alpha_2, \alpha_3$ and identical dephasing durations between them (Fig. 2.23) will be studied. The mathematical expressions of F and Z states before and after each pulse will be presented during the description. The formalism required to establish those equations will be detailed

after this pictorial example.

Assuming an initial equilibrium state, the magnetization flipped towards the transverse

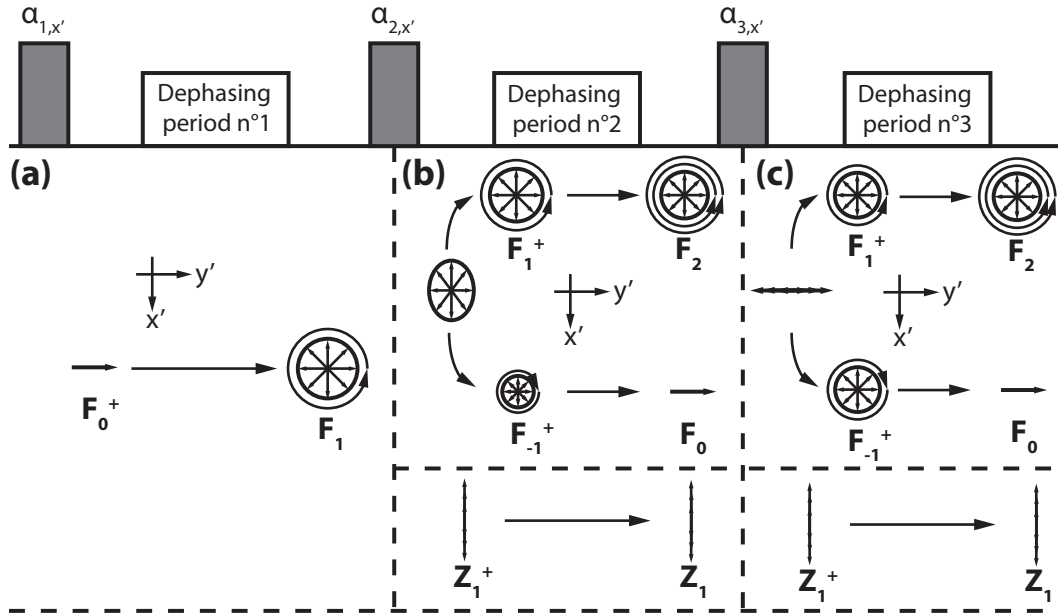


Figure 2.23: Effects of three RF pulses with flip angles α_1 , α_2 and α_3 on the F_n , F_{-n} and Z_n states. (a) Assuming the magnetization at equilibrium before the first pulse (Z_0 state), F_0^+ is created right after. In this example, $k=1$ dephasing periods are considered. Between the first and second RF pulses, F_0^+ thus evolves towards F_1 . The circular arrows surrounding the states indicate if the corresponding helix is left or right-handed. The number of arrows is related to the pitch of the helix. A π periodic helix is thus represented by two arrows. (b) The second pulse rotates the F_1 state into a tilted disk that can be decomposed as an ellipse and a series of vectors pointing along $+z$ and $-z$. The ellipse can be seen as the sum of two helices with opposite orientations and different radii F_1^+ and F_{-1}^+ . As it results from an F_1 state the series of vectors in the longitudinal direction corresponds to a Z_1^+ state. During the dephasing period, F_1^+ and F_{-1}^+ respectively evolve towards F_2 and F_0 (Hahn echo) whereas Z_1^+ , which does not undergo dephasing evolves towards Z_1 . (c) The third pulse tilts the Z_1 state into the $y'z$ plane. The resulting configuration can be decomposed into a Z_1^+ state and a series of vectors lying on the $+y$ and $-y$ directions. The sum of an F_1^+ and F_{-1}^+ states with the same radii reproduces this set of vectors along y . Again, during the dephasing period, F_1^+ and F_{-1}^+ respectively evolve towards F_2 and F_0 whereas Z_1^+ becomes Z_1 .

plane by an RF pulse of flip angle α_1 applied along x' can be characterized by the states F_0 and Z_0 since M_{xy} is along y' and M_z in the $+z$ direction. Their mathematical expressions are given by

$$\begin{aligned} F_0^+ &= -iM_0 \sin(\alpha_1) \\ Z_0^+ &= M_0 \cos(\alpha_1) \end{aligned} \quad (2.60)$$

In the phase graph formalism the F_0 state which describes in phase magnetization thus corresponds to FIDs or echo formations.

Magnetic moments then loose their phase coherence during the period between α_1 and α_2 (Fig. 2.23a). As the dispersion periods are identical from one RF pulse to the other, they can

all be associated to $k=1$. Therefore, between the first and second RF pulses, transverse components of isochromats will be brought from state F_0^+ to F_1 . At this point, they are evenly distributed in the $x'y'$ plane meaning that no signal can be detected. Considering T_2 -decay occurring over the inter pulse duration T_I , F_1 is given by

$$F_1 = -iM_0 \sin(\alpha_1) e^{-\frac{T_I}{T_2}} \quad (2.61)$$

The second pulse tilts the disk of transverse magnetization by an angle α_2 about x' . This tilted disk can be seen as an ellipse in the $x'y'$ plane and a series of vectors pointing in $+z$ or $-z$ in the longitudinal direction (Fig. 2.23b).

As it results from the F_1 state, the longitudinal configuration corresponds to a Z_1^+ state. The ellipse can be seen as the sum of two dephased states F_1^+ and F_{-1}^+ which have the same phase dispersion but in opposite directions, i.e. the y' component of a vector in F_1^+ state has the opposite sign in F_{-1}^+ . The $+$ sign in F_1^+ and F_{-1}^+ indicates that those are states right after an RF pulse. To form an ellipse, the radius of F_1^+ and F_{-1}^+ should be different (Fig. 2.23b) otherwise their sum corresponds to a series of vectors along y' (Fig. 2.23c). The radii of F states depend on how they are populated. It will be shown later that the state populations can be precisely calculated throughout the sequence. The expressions of the F_1^+ , F_{-1}^+ and Z_1^+ states created by the second RF pulse from F_1 are

$$\begin{aligned} F_1^+ &= -iM_0 \sin(\alpha_1) \cos^2\left(\frac{\alpha_2}{2}\right) e^{-\frac{T_I}{T_2}} \\ F_{-1}^+ &= -iM_0 \sin(\alpha_1) \sin^2\left(\frac{\alpha_2}{2}\right) e^{-\frac{T_I}{T_2}} \\ Z_1^+ &= -\frac{1}{2} M_0 \sin(\alpha_1) \sin(\alpha_2) e^{-\frac{T_I}{T_2}} \end{aligned} \quad (2.62)$$

During the dephasing period following the second RF pulse, F_1 becomes an F_2 state (assuming $k=1$) and, as it has the opposite phase dispersion, F_{-1} evolves towards F_0 and therefore produces an echo. This corresponds to the Hahn echo described for the two pulses example in section 2.2.5. The longitudinal magnetization being only experiencing T_1 -recovery between the pulses, the Z_1^+ state becomes Z_1 which is given by

$$Z_1 = -\frac{1}{2} M_0 \sin(\alpha_1) \sin(\alpha_2) e^{-\frac{T_I}{T_2}} e^{-\frac{T_I}{T_1}} \quad (2.63)$$

This transition corresponds to the longitudinal magnetization storage that was already discussed in the description of the stimulated echo.

The third RF pulse (also assumed along x') then tilts Z_1 into the $y'z$ plane creating another Z_1^+ configuration and a transversal part lying in $+y'$ and $-y'$ (Fig. 2.23c). This part can be seen again as the sum of F_1^+ and F_{-1}^+ states but this time with the same radius. The expressions

of the F_1^+ , F_{-1}^+ and Z_1^+ states generated by the third pulse from Z_1 are

$$\begin{aligned} F_1^+ &= \frac{i}{2} M_0 \sin(\alpha_1) \sin(\alpha_2) \sin(\alpha_3) e^{-\frac{T_1}{T_2}} e^{-\frac{T_1}{T_1}} \\ F_{-1}^+ &= -\frac{i}{2} M_0 \sin(\alpha_1) \sin(\alpha_2) \sin(\alpha_3) e^{-\frac{T_1}{T_2}} e^{-\frac{T_1}{T_1}} \\ Z_1^+ &= -\frac{1}{2} M_0 \sin(\alpha_1) \sin(\alpha_2) \cos(\alpha_3) e^{-\frac{T_1}{T_2}} e^{-\frac{T_1}{T_1}} \end{aligned} \quad (2.64)$$

During the dephasing period ($k=1$), F_1^+ becomes F_2 and F_{-1}^+ evolves towards F_0 giving rise to a stimulated echo since it corresponds to the refocusing of the magnetization stored in the longitudinal direction. Right before the third pulse, F_0 and F_2 states existed. For sake of simplicity, they were not considered anymore since the effect of the second pulse on the F_1 state was already described and can be easily extended to those states. From this simple example, the following rules can be set for F_n , F_{-n} and Z_n in the phase graph formalism :

1. When an RF pulse is applied, every existing states with dephasing index n generates the F_n^+ , F_{-n}^+ and Z_n^+ states with the initial population redistributed among them.
2. For a dephasing period of unit $+k$, F_n^+ and F_{-n}^+ states respectively evolve towards F_{n+k} and F_{-n+k} while experiencing T_2 -decay whereas Z_n^+ becomes Z_n and is only affected by T_1 -recovery.

2.2.6.1 Phase Graph: a pictorial view

The evolution of F_n^+ , F_{-n}^+ and Z_n^+ states can be illustrated in a two-dimensional phase graph where the states are displayed in the vertical axis and the time in the horizontal one. An example is presented for a sequence of three pulses α_1 , α_2 and α_3 with unequal dephasing periods after each pulse (Fig. 2.24). The F_0^+ and Z_0^+ states created by the first pulse evolve into F_1 and Z_0 (Z_n evolution are represented by dashed lines) since it is assumed that the reference dispersion period ($k=1$) occurs between the first and second RF pulses.

The second RF pulse gives rise to F_1^+ , F_{-1}^+ , Z_1^+ , F_0^+ and Z_0^+ states. As $k=3$ for the second dephasing period, the F_{-1}^+ state becomes an F_2 state right before the third RF pulse. As the line representing this evolution crosses the horizontal axis, the magnetization goes through an F_0 state, what corresponds to an echo formation. This is the Hahn echo generated by two pulses discussed in section 2.2.5.

In the diagram, echoes are represented by small circles on the time axis when an existing magnetization state crosses the F_0 line. At the end of the second dephasing period, F_4 , F_3 , F_2 , Z_1 , Z_0 states exist. From them, the third RF pulse creates 14 new states, 3·3, 1·2 and 1·3. Indeed, each transverse and longitudinal with $n \neq 0$ state generates three different states, whereas states with $n=0$ generate only F_0^+ and Z_0^+ . As four transverse states with $n < 0$ exist, four echoes can be formed in the period after the third RF pulse. The first circle from the left corresponds to the stimulated echo discussed in section 2.2.5 with magnetization stored in

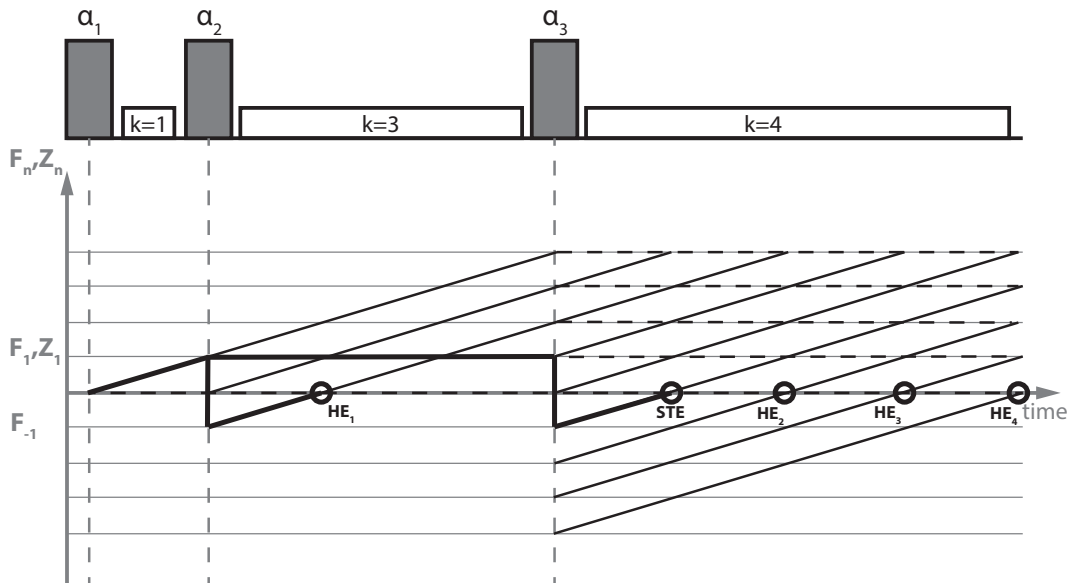


Figure 2.24: Phase graph diagram showing the pathways created by three pulses α_1 , α_2 and α_3 separated by unequal dephasing periods. On the diagram, the horizontal axis corresponds to the time whereas the different F and Z states are represented on the vertical axis. The first pulse creates the Z_0^+ and F_0^+ states which respectively evolve towards Z_0 and F_1 . From the F_1 state, the second pulse generates F_1^+ , F_{-1}^+ and Z_1^+ which respectively become F_4 , F_2 and Z_1 before the third pulse. The Z_0 state generates F_0^+ and Z_0^+ which evolve towards F_3 and Z_0 . From the third pulse, $F_{\pm 1}^+$, $F_{\pm 2}^+$, $F_{\pm 3}^+$, $F_{\pm 4}^+$, Z_1^+ , Z_2^+ , Z_3^+ and Z_4^+ are created. The different thin lines on the diagram show the evolutions of those states after the pulse. Echoes are represented by circles on the horizontal axis. The lines in bold indicate the pathways of the Hahn and stimulated echoes described in section 2.2.5.

the longitudinal direction. The second one results from the refocusing of the first Hahn echo by the third pulse whereas the last two circles are Hahn echoes generated respectively by the pair $\alpha_2 - \alpha_3$ and $\alpha_1 - \alpha_3$. The pathways for the Hahn and stimulated echoes described in section 2.2.5 are depicted with bold lines on figure 2.24.

This example demonstrates that five echoes can be generated by three RF pulses. When the dephasing periods between the pulses are identical (which is usually the case in MR sequences), the second and fourth echoes occur at the same time. Depending on the RF pulse phases, those echoes can sum up constructively or destructively. So far, only the position of echoes can be predicted but the information about their amplitudes is missing.

2.2.6.2 Phase Graph: the mathematical description

Hereafter, a mathematical formalism is presented such that the value of each state can be calculated from one pulse to the other. The phase Φ of RF pulses which had no particular consequence up to this point will be introduced in equations.

The phase $\psi = \psi(\vec{r})$ can be defined for an isochromat at position \vec{r} as the phase accumulated during the reference period ($k=1$) due to B_0 inhomogeneities and applied gradients. During dephasing periods, isochromats will thus experience multiples of ψ and magnetization

components can be expressed as a function of $\psi(\vec{r})$. To make the description simpler, the complex notation for the magnetization in the transverse plane will be used

$$M_{xy} = M_x + iM_y \quad (2.65)$$

Helices F_n describing a configuration of isochromats in the transverse plane can be considered as spatial harmonics indexed by the integer n representing how many times the magnetization experienced the reference dephasing $\psi(\vec{r})$. M_{xy} for isochromats at different positions can be expressed as a complex Fourier series

$$M_{xy}(\psi) = \sum_{n=-\infty}^{\infty} F_n \cdot e^{in\psi} \quad (2.66)$$

The complex elements F_n can be seen as Fourier coefficient with amplitude and phase respectively representing the populations of states (radius of helices) and their phase in the $x'y'$ plane. The conjugate form of the previous equation can be expressed as

$$M_{xy}^*(\psi) = \left(\sum_{n=-\infty}^{\infty} F_n \cdot e^{in\psi} \right)^* = \sum_{n=-\infty}^{\infty} F_n^* \cdot e^{-in\psi} = \sum_{n=-\infty}^{\infty} F_{-n}^* \cdot e^{in\psi} \quad (2.67)$$

where "*" denotes the complex conjugate and therefore $M_{xy}^* = M_x - iM_y$. Finally, a Fourier series can also be written for the longitudinal magnetization with Z_n states playing the role of spatial harmonics.

$$M_z(\psi) = \sum_{n=-\infty}^{\infty} Z_n \cdot e^{in\psi} \quad (2.68)$$

Three dimensional rotation matrices are commonly used to describe the motion of the magnetization experiencing an RF pulse of flip angle α and applied along a direction defined by an angle Φ in respect to the x' direction. The two rotation matrices

$$\mathbf{R}_{x'}(\alpha) = \begin{bmatrix} 1 & 0 & 0 \\ 0 & \cos\alpha & -\sin\alpha \\ 0 & \sin\alpha & \cos\alpha \end{bmatrix} \quad (2.69)$$

and

$$\mathbf{R}_z(\Phi) = \begin{bmatrix} \cos\Phi & -\sin\Phi & 0 \\ \sin\Phi & \cos\Phi & 0 \\ 0 & 0 & 1 \end{bmatrix} \quad (2.70)$$

respectively describe a rotation of angle α around the x' axis and a rotation of angle Φ around the z axis. Using matrix composition, the effect of an RF pulse with flip angle α and phase

Φ is represented by

$$\mathbf{R}_\Phi(\alpha) = \mathbf{R}_z(\Phi)\mathbf{R}_{x'}(\alpha)\mathbf{R}_z(-\Phi) = \begin{bmatrix} \cos^2\Phi + \cos\alpha\sin^2\Phi & \cos\Phi\sin\Phi(1 - \cos\alpha) & \sin\alpha\sin\Phi \\ \cos\Phi\sin\Phi(1 - \cos\alpha) & \sin^2\Phi + \cos\alpha\cos^2\Phi & -\sin\alpha\cos\Phi \\ -\sin\alpha\sin\Phi & \sin\alpha\cos\Phi & \cos\alpha \end{bmatrix} \quad (2.71)$$

This last matrix describes how an RF pulse transforms M_x , M_y and M_z vectors individually. Each component after the pulse is thus given by

$$\begin{bmatrix} M_x \\ M_y \\ M_z \end{bmatrix}^+ = \mathbf{R}_\Phi(\alpha) \begin{bmatrix} M_x \\ M_y \\ M_z \end{bmatrix}^- \quad (2.72)$$

where - and + signs refer to state before and after the pulse, respectively. Equations (2.66) to (2.68) were not set for the $[M_x; M_y; M_z]$ basis but for the $[M_{xy}; M_{xy}^*; M_z]$ one. The transition from one basis to the other can be obtained mathematically with the use of \mathbf{S} and \mathbf{S}^{-1} matrices of the form

$$\mathbf{S} = \begin{bmatrix} 1 & i & 0 \\ 1 & -i & 0 \\ 0 & 0 & 1 \end{bmatrix}; \quad \mathbf{S}^{-1} = \frac{1}{2} \begin{bmatrix} 1 & 1 & 0 \\ -i & i & 0 \\ 0 & 0 & 2 \end{bmatrix} \quad (2.73)$$

such that

$$\begin{bmatrix} M_x \\ M_y \\ M_z \end{bmatrix} \begin{matrix} \xleftarrow{\mathbf{S}} \\ \xrightarrow{\mathbf{S}^{-1}} \end{matrix} \begin{bmatrix} M_{xy} \\ M_{xy}^* \\ M_z \end{bmatrix} \quad (2.74)$$

It is known from linear algebra that a transformation represented by a matrix \mathbf{A} in a certain basis is transformed into another matrix given by $\mathbf{C}^{-1}\mathbf{A}\mathbf{C}$ in a new basis, where \mathbf{C} and \mathbf{C}^{-1} are matrices allowing the transitions between the two basis. $\mathbf{R}_{x'}(\alpha)$ and $\mathbf{R}_z(\Phi)$ rotations in the $[M_x; M_y; M_z]$ basis thus become $\mathbf{T}_{x'}(\alpha)$ and $\mathbf{T}_z(\Phi)$ in the $[M_{xy}; M_{xy}^*; M_z]$ basis under the following transformations

$$\mathbf{T}_{x'}(\alpha) = \mathbf{S}^{-1}\mathbf{R}_{x'}(\alpha)\mathbf{S} = \begin{bmatrix} \cos^2\frac{\alpha}{2} & \sin^2\frac{\alpha}{2} & -i\sin\alpha \\ \sin^2\frac{\alpha}{2} & \cos^2\frac{\alpha}{2} & i\sin\alpha \\ -\frac{i}{2}\sin\alpha & \frac{i}{2}\sin\alpha & \cos\alpha \end{bmatrix} \quad (2.75)$$

and

$$\mathbf{T}_z(\Phi) = \mathbf{S}^{-1}\mathbf{R}_z(\Phi)\mathbf{S} = \begin{bmatrix} e^{i\Phi} & 0 & 0 \\ 0 & e^{-i\Phi} & 0 \\ 0 & 0 & 1 \end{bmatrix} \quad (2.76)$$

In this basis, an RF pulse of flip angle α and phase Φ is represented by $\mathbf{T}_\Phi(\alpha) = \mathbf{T}_z(\Phi)\mathbf{T}_{x'}(\alpha)\mathbf{T}_z(-\Phi)$ or $\mathbf{S}^{-1}\mathbf{R}_\Phi(\alpha)\mathbf{S}$. In the basis with complex magnetization components, the transitions generated by an RF pulse are obtained from

$$\begin{bmatrix} M_{xy} \\ M_{xy}^* \\ M_z \end{bmatrix}^+ = \begin{bmatrix} \cos^2 \frac{\alpha}{2} & e^{2i\Phi} \sin^2 \frac{\alpha}{2} & -ie^{i\Phi} \sin \alpha \\ e^{-2i\Phi} \sin^2 \frac{\alpha}{2} & \cos^2 \frac{\alpha}{2} & ie^{i\Phi} \sin \alpha \\ -\frac{i}{2} e^{-i\Phi} \sin \alpha & \frac{i}{2} e^{i\Phi} \sin \alpha & \cos \alpha \end{bmatrix} \begin{bmatrix} M_{xy} \\ M_{xy}^* \\ M_z \end{bmatrix}^- \quad (2.77)$$

Equations (2.66) to (2.68) can now be introduced in the last system to produce

$$\begin{bmatrix} \sum_{n=-\infty}^{\infty} F_n \cdot e^{in\psi} \\ \sum_{n=-\infty}^{\infty} F_{-n}^* \cdot e^{in\psi} \\ \sum_{n=-\infty}^{\infty} Z_n \cdot e^{in\psi} \end{bmatrix}^+ = \begin{bmatrix} \cos^2 \frac{\alpha}{2} & e^{2i\Phi} \sin^2 \frac{\alpha}{2} & -ie^{i\Phi} \sin \alpha \\ e^{-2i\Phi} \sin^2 \frac{\alpha}{2} & \cos^2 \frac{\alpha}{2} & ie^{i\Phi} \sin \alpha \\ -\frac{i}{2} e^{-i\Phi} \sin \alpha & \frac{i}{2} e^{i\Phi} \sin \alpha & \cos \alpha \end{bmatrix} \begin{bmatrix} \sum_{n=-\infty}^{\infty} F_n \cdot e^{in\psi} \\ \sum_{n=-\infty}^{\infty} F_{-n}^* \cdot e^{in\psi} \\ \sum_{n=-\infty}^{\infty} Z_n \cdot e^{in\psi} \end{bmatrix}^- \quad (2.78)$$

As the coefficients of the matrix describing the RF pulse do not explicitly depend on n , the following system can be established

$$\begin{bmatrix} F_n \\ F_{-n}^* \\ Z_n \end{bmatrix}^+ = \begin{bmatrix} \cos^2 \frac{\alpha}{2} & e^{2i\Phi} \sin^2 \frac{\alpha}{2} & -ie^{i\Phi} \sin \alpha \\ e^{-2i\Phi} \sin^2 \frac{\alpha}{2} & \cos^2 \frac{\alpha}{2} & ie^{i\Phi} \sin \alpha \\ -\frac{i}{2} e^{-i\Phi} \sin \alpha & \frac{i}{2} e^{i\Phi} \sin \alpha & \cos \alpha \end{bmatrix} \begin{bmatrix} F_n \\ F_{-n}^* \\ Z_n \end{bmatrix}^- \quad (2.79)$$

This expression describes the first rule of the phase graph formalism in a mathematical way, i.e. each state with index n generates F_n , F_{-n} and Z_n with populations defined by the $\mathbf{T}_\Phi(\alpha)$ transformation. The second rule can be characterized by the operators \mathbf{E} and \mathbf{R} which respectively represent the evolution and relaxation of F and Z states between pulses. During a dephasing period with any arbitrary k , the states F_n^+ , F_{-n}^+ and Z_n^+ evolve according to

$$\mathbf{E}(k) : \quad F_n^+ \rightarrow F_{n+k} \quad Z_n^+ \rightarrow Z_n \quad (2.80)$$

Assuming the RF pulses to be short enough such that relaxation mechanisms can be neglected while they are applied, T_1 -recovery and T_2 -decay for a period τ between two pulses are described by

$$\mathbf{R}(\tau, T_1, T_2) = \begin{bmatrix} E_2 & 0 & 0 \\ 0 & E_2 & 0 \\ 0 & 0 & E_1 \end{bmatrix} \quad (2.81)$$

where $E_{1,2} = e^{-\tau/T_{1,2}}$. This operator is valid for states with $n \neq 0$. In the case where $n=0$, the following relation has to be used in order to include the recovery towards thermal equilibrium

$$\begin{bmatrix} F_n \\ F_{-n}^* \\ Z_n \end{bmatrix}^+ = \begin{bmatrix} E_2 & 0 & 0 \\ 0 & E_2 & 0 \\ 0 & 0 & E_1 \end{bmatrix} \begin{bmatrix} F_n \\ F_{-n}^* \\ Z_n \end{bmatrix}^- + \begin{bmatrix} 0 \\ 0 \\ M_0(1 - E_1) \end{bmatrix} \quad (2.82)$$

The evolution of states F_n^+ , F_{-n}^+ and Z_n^+ experiencing an RF pulse with flip angle α and phase Φ followed by a dephasing period of duration τ and arbitrary k is described by the matrix composition $\mathbf{E}(k)\mathbf{R}(\tau, T_1, T_2)\mathbf{T}_\Phi(\alpha)$.

The expressions for the Hahn and stimulated echo amplitudes will now be derived from the phase graph formalism by considering an arbitrary sequence with three pulses of flip angles α_1 , α_2 and α_3 and dephasing periods with $k_1=1(\tau_1)$, $k_2(\tau_2)$ and $k_3(\tau_3)$. For the sake of simplicity it is assumed that the pulses are applied along x' ($\Phi = 0$). Considering that the magnetization is at thermal equilibrium $[0, 0, M_0]^T$ before the first RF pulse, the value of F_0 after it can be obtained from equation (2.79)

$$F_0^+ = -iM_0\sin\alpha_1 \quad (2.83)$$

This state becomes an F_1 state before the second RF pulse and following equation (2.82) its value is given by

$$F_1 = -iM_0\sin\alpha_1 e^{-\frac{\tau_1}{T_2}} \quad (2.84)$$

From this state, the second RF pulse generates three new states given by (at this stage F_{-1}^- and Z_1^- do not exist)

$$\begin{aligned} F_1^+ &= -iM_0\sin\alpha_1 \cos^2 \frac{\alpha_2}{2} e^{-\frac{\tau_1}{T_2}} \\ (F_{-1}^*)^+ &= -iM_0\sin\alpha_1 \sin^2 \frac{\alpha_2}{2} e^{-\frac{\tau_1}{T_2}} \\ Z_1^+ &= -\frac{1}{2}M_0\sin\alpha_1 \sin\alpha_2 e^{-\frac{\tau_1}{T_2}} \end{aligned} \quad (2.85)$$

During the second dephasing period, F_{-1}^* becomes an F_0 state expressed as

$$F_0 = -iM_0\sin\alpha_1 \sin^2 \frac{\alpha_2}{2} e^{-\frac{\tau_1}{T_2}} e^{-\frac{\tau_2}{T_2}} \quad (2.86)$$

Assuming that the dephasing amplitude is similar on both side of the second RF pulse, the duration τ_1 appears in the second exponential term since the duration it takes for the F_{-1}^* state to be refocused into an echo is identical to the one required to bring F_0^+ into F_1 . Setting $TE = 2\tau_1$, the amplitude of the last result corresponds to the signal presented in equation (2.55) for the Hahn echo. After the second RF pulse, Z_1^+ evolves into Z_1 and according to equation (2.81)

$$Z_1 = -\frac{1}{2}M_0\sin\alpha_1 \sin\alpha_2 e^{-\frac{\tau_1}{T_2}} e^{-\frac{\tau_2}{T_1}} \quad (2.87)$$

From this state, the third RF pulse will generate an $(F_{-1}^*)^+$ state given by

$$(F_{-1}^*)^+ = -i\frac{1}{2}M_0\sin\alpha_1 \sin\alpha_2 \sin\alpha_3 e^{-\frac{\tau_1}{T_2}} e^{-\frac{\tau_2}{T_1}} \quad (2.88)$$

Similarly as for the Hahn echo, this F_{-1} state becomes F_0 at time τ_1 after the third pulse. The expression for the formed echo at this point is obtained by taking T_2 relaxation into account from the last equation

$$F_0 = -i\frac{1}{2}M_0\sin\alpha_1\sin\alpha_2\sin\alpha_3e^{-\frac{\tau_1}{T_2}}e^{-\frac{\tau_2}{T_1}}e^{-\frac{\tau_1}{T_2}} \quad (2.89)$$

By considering the magnitude of this state and setting $TE = 2\tau_1$ and $TM = \tau_2$, the relation given in equation (2.56) for the stimulated echo signal comes out.

2.3 Magnetic Resonance Imaging (MRI)

In the previous section, the main NMR concepts were described. It will be shown in the current section how gradients can be used to encode the spatial information in the detected signal. A simple sequence with RF pulses and gradients will be analyzed in order to establish the relationship between the acquired signal and the magnetization profile $m(x,y)$ across a selected slice. It will be explained that the acquired data is represented in a spatial frequency domain called k-space. The links between k-space sampling, k-space width, image field of view and spatial resolution will be subsequently discussed. Image artifacts resulting from insufficient sampling frequency or k-space coverage will also be presented. The main types of contrasts obtained on MR images and a more advanced sequence taking advantage of tissue specific relaxation times and providing anatomical profiles currently used for clinical diagnosis will finally be described.

2.3.1 The signal equation and its Fourier interpretation

During the acquisition process, the receiving coil collects the MR signal from every x and y positions of the excited slice. Spatial information can be encoded in the signal by applying gradients in the x and y directions after slice selection (Fig. 2.25a). As explained in section 2.2.4 the other role of the G_x gradient is to generate an echo at time TE after the RF pulse. Without loss of generality, thermal equilibrium magnetization before the application of a 90° excitation will be considered. After the pulse the \vec{B} field in equation (2.37) is given by

$$\vec{B}(x, y, t) = [B_0 + G_x(t)x + G_y(t)y] \vec{e}_z \quad (2.90)$$

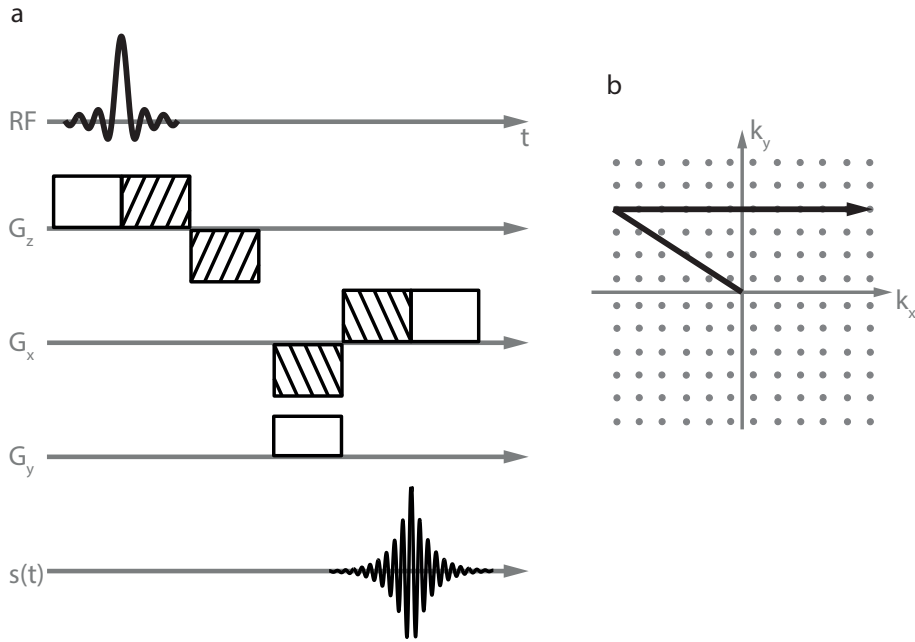


Figure 2.25: (a) Gradient echo where besides its role in the echo formation, G_x is used to encode a range of k_x positions. The G_y gradient defines the k_y coordinate in k-space. (b) Trajectory in k-space corresponding to the $G_x - G_y$ gradient pair in (a).

This expression assumes a perfectly uniform B_0 field. Writing the Bloch equations for each component, it reads

$$\begin{aligned} \frac{dM_x}{dt} &= \gamma [B_0 + G_x(t)x + G_y(t)y] M_y - \frac{M_x}{T_2} \\ \frac{dM_y}{dt} &= -\gamma [B_0 + G_x(t)x + G_y(t)y] M_x - \frac{M_y}{T_2} \\ \frac{dM_z}{dt} &= -\frac{M_z - M_0}{T_1} \end{aligned} \quad (2.91)$$

As the recorded signal is proportional to the amount of magnetization in the transverse plane, the notation involving $M_{xy} = M_x + iM_y$ is more adapted here. From the previous set of equations, the following relation can be established

$$\frac{dM_{xy}}{dt} = \frac{dM_x}{dt} + i\frac{dM_y}{dt} = -i\gamma [B_0 + G_x(t)x + G_y(t)y] M_{xy} - \frac{M_{xy}}{T_2} \quad (2.92)$$

The solution to this equation is obtained by considering the initial condition $M_{xy}(t = 0) = M_0(x, y)$

$$M_{xy}(x, y, t) = M_0(x, y) e^{-\frac{t}{T_2}} e^{-i\omega_0 t} e^{-i\gamma \int_0^t [G_x(\tau)x + G_y(\tau)y] d\tau} \quad (2.93)$$

where $M_0(x, y)$ represents the thermal equilibrium magnetization. $T_2(x, y)$ and $M_0(x, y)$ are position dependent since they vary as a function of the tissue they come from. Assuming a

receiver coil with homogeneous sensitivity over the excited slice, the acquired signal will be

$$s_r(t) = \int_x \int_y M_{xy}(x, y, t) dx dy = \int_x \int_y M_0(x, y) e^{-\frac{t}{T_2}} e^{-i\omega_0 t} e^{-i\gamma \int_0^t [G_x(\tau)x + G_y(\tau)y] d\tau} dx dy \quad (2.94)$$

$s_r(t)$ is thus the temporal signal generated by all the transverse components of isochromats precessing in the selected slice. This signal is demodulated by making use of a mixer and a low pass filter (cf. section 2.4) in order to remove the carrier frequency ω_0 such that only the envelope $s(t) = s_r(t) e^{i\omega_0 t}$ remains. Assuming transverse relaxation can be ignored over the echo formation period ($TE \ll T_2$), the expression for $s(t)$ becomes

$$s(t) = \int_x \int_y M_0(x, y) e^{-i\gamma \int_0^t [G_x(\tau)x + G_y(\tau)y] d\tau} dx dy \quad (2.95)$$

At this point, the two following spatial frequencies defining the k-space coordinates can be defined

$$\begin{aligned} k_x &= \frac{\gamma}{2\pi} \int_0^t G_x(\tau) d\tau \\ k_y &= \frac{\gamma}{2\pi} \int_0^t G_y(\tau) d\tau \end{aligned} \quad (2.96)$$

With these new quantities, the expression for $s(t)$ which is called the signal equation now becomes

$$s(t) = S(k_x, k_y) = \int_x \int_y M_0(x, y) e^{-2\pi i [k_x x + k_y y]} dx dy \quad (2.97)$$

When gradients are applied in the x and y directions, the acquired echo signal $s(t)$ comes from the magnetization in every spatial positions $M_0(x, y)$ modulated by the spatial frequencies defined by the integrals over time involved in $k_x(t)$ and $k_y(t)$. The time varying gradients applied in x and y directions thus define a trajectory in the k-space (Fig. 2.25b). It comes out from the signal equation that the magnetization profile $M_0(x, y)$ can be retrieved by applying a 2D Fourier transform to $S(k_x, k_y)$.

A sufficient coverage of the k-space is required to obtain a decent representation of the magnetization profile from $S(k_x, k_y)$ when performing the Fourier transform. The target is to acquire an appropriate set of time signals such that the best approximation of $M_0(x, y)$ can be reconstructed. The sequence is thus repeated with gradients varied such that different k-space coordinates are visited. In its simplest form, the coverage is performed by acquiring one line of the k-space after the other, at equally spaced distances along k_y , defining a Cartesian trajectory. Usually, the gradient shape in the x direction does not vary from one repetition to the other such that $k_x(t)$ involved in the echo signal corresponds to the filling of one k-space line (Fig. 2.25b).

The negative lobe of the G_x gradient provides a k-space crossing starting from $-k_{x,max}$ instead of 0 (Fig. 2.25b). G_y , called the phase encoding gradient, is then varied at each

repetition of the sequence in order to acquire k-space lines with different k_y coordinates (Fig. 2.25b). The k-space coverage is defined by $k_{x,max}$ and $k_{y,max}$ which will be described in more details in the next section. Ideally, the entire infinite k-space should be acquired such that its Fourier transform exactly reproduces $M_0(x, y)$. This cannot be performed practically because acquisition time and gradient strength are limited. However, anatomical images of human organs with a decent spatial resolution can still be acquired with a limited extent of the k-space filling.

Other strategies were developed to fill up the k-space. For example, oscillating gradients in both G_x and G_y can be used to obtain a spiral trajectory instead of Cartesian.

2.3.2 Field of view and spatial resolution

In the previous section, the relationship between the acquired signal and the spatial magnetization $M_0(x, y)$ was established. What was not explained is that during acquisition, the signal is not continuously acquired but sampled at every Δt intervals. The height of the G_y gradient is also varied in discret steps from one repetition to the other meaning that only k-space points separated by Δk_x horizontally and Δk_y vertically are actually acquired (Fig. 2.26). For a k-space sampled with Δk_x and Δk_y and acquired up to $k_{x,max}$ and $k_{y,max}$, the signal equation has to be rewritten as

$$\hat{S}(k_x, k_y) = S(k_x, k_y) \frac{1}{\Delta k_x \Delta k_y} \cdot {}^2\text{III}\left(\frac{k_x}{\Delta k_x}, \frac{k_y}{\Delta k_y}\right) \cdot {}^2\Pi\left(\frac{k_x}{W_{k_x}}, \frac{k_y}{W_{k_y}}\right) \quad (2.98)$$

where W_{k_x} and W_{k_y} represent the widths of the acquired k-space in both x and y directions (Fig. 2.27a) and their expressions are

$$\begin{aligned} W_{k_x} &= 2 \left(k_{x,max} + \frac{\Delta k_x}{2} \right) \\ W_{k_y} &= 2 \left(k_{y,max} + \frac{\Delta k_y}{2} \right) \end{aligned} \quad (2.99)$$

The two-dimensional Dirac comb ${}^2\text{III}$ and rectangular function ${}^2\Pi$ in equation 2.98 respectively represent the k-space sampling and truncation operations. As a reminder the one-dimensional forms of those functions and their Fourier transforms are given by

$$\begin{aligned} \frac{1}{\Delta} \text{III}\left(\frac{x}{\Delta}\right) &= \sum_{n=-\infty}^{\infty} \delta(x - n\Delta) & \xrightarrow{\text{FT}} & \text{III}(\Delta \cdot k_x) = \frac{1}{\Delta} \sum_{n=-\infty}^{\infty} \delta(k_x - \frac{n}{\Delta}) \\ \text{II}\left(\frac{x}{W}\right) &= \begin{cases} 1, & \text{if } -\frac{W}{2} \leq x \leq \frac{W}{2} \\ 0, & \text{otherwise} \end{cases} & \xrightarrow{\text{FT}} & W \text{sinc}(W \cdot k_x) = \frac{\sin(\pi W \cdot k_x)}{\pi k_x} \end{aligned} \quad (2.100)$$

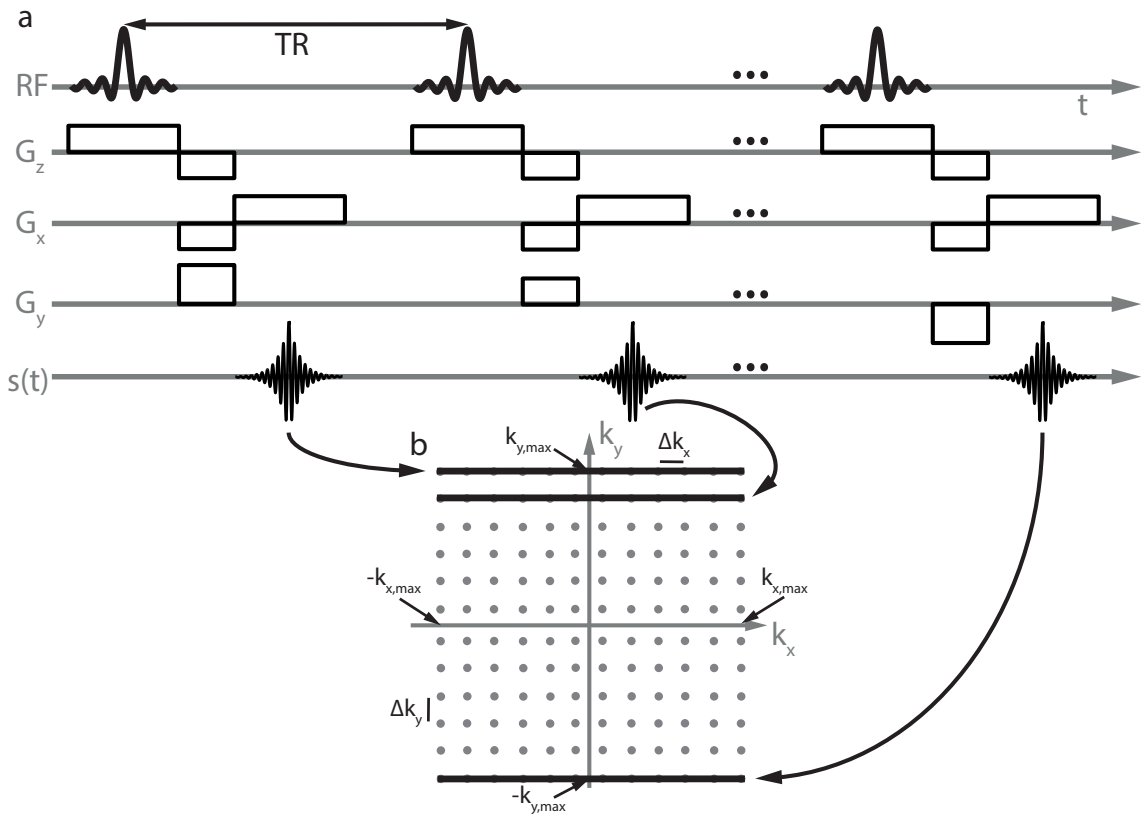


Figure 2.26: (a) Slice-selective gradient echo sequence with G_x and G_y gradients used to encode spatial information. (b) Cartesian k -space filling related to the sequence in (a). $k_{x,max}$ and $k_{y,max}$ define the k -space coverage whereas Δk_x and Δk_y correspond to the sampling rates in x and y directions.

where $\delta(x)$ represents the Dirac's distribution. The Fourier transform of a Dirac comb with Δ intervals is another Dirac comb with $1/\Delta$ steps (Fig. 2.28). On the other hand, the Fourier transform of a rectangular function of width W is a sinc of bandwidth $2/W$. As a product in one space becomes a convolution (denoted by the $*$ symbol hereafter) in its Fourier domain, the measured magnetization profile $\hat{m}(x, y)$ has the form

$$\hat{m}(k_x, k_y) = FT \{ \hat{S}(k_x, k_y) \} = m(x, y) *^2 \text{III}(\Delta k_x x, \Delta k_y y) * W_{k_x} W_{k_y} \text{sinc}(W_{k_x} x) \text{sinc}(W_{k_y} y) \quad (2.101)$$

This equation shows that the true magnetization profile $m(x, y)$ is convolved with a two-dimensional Dirac comb with $1/\Delta k_x$ and $1/\Delta k_y$ intervals and a sinc function in both x and y dimensions with $2/W_{k_x}$ and $2/W_{k_y}$ bandwidths. The convolution by the Dirac comb means that the $m(x, y)$ will be replicated along x and y directions every $1/\Delta k_x$ and $1/\Delta k_y$ steps (Fig. 2.27b). The convolution by the sinc functions gives rise to 2D blurring on the acquired image which limits the ability to resolve detailed structures. This will be further explained in the next section. The field of view in x and y directions FOV_x and FOV_y determine the distances at which the next replication of $m(x, y)$ will be observed. As the distance between

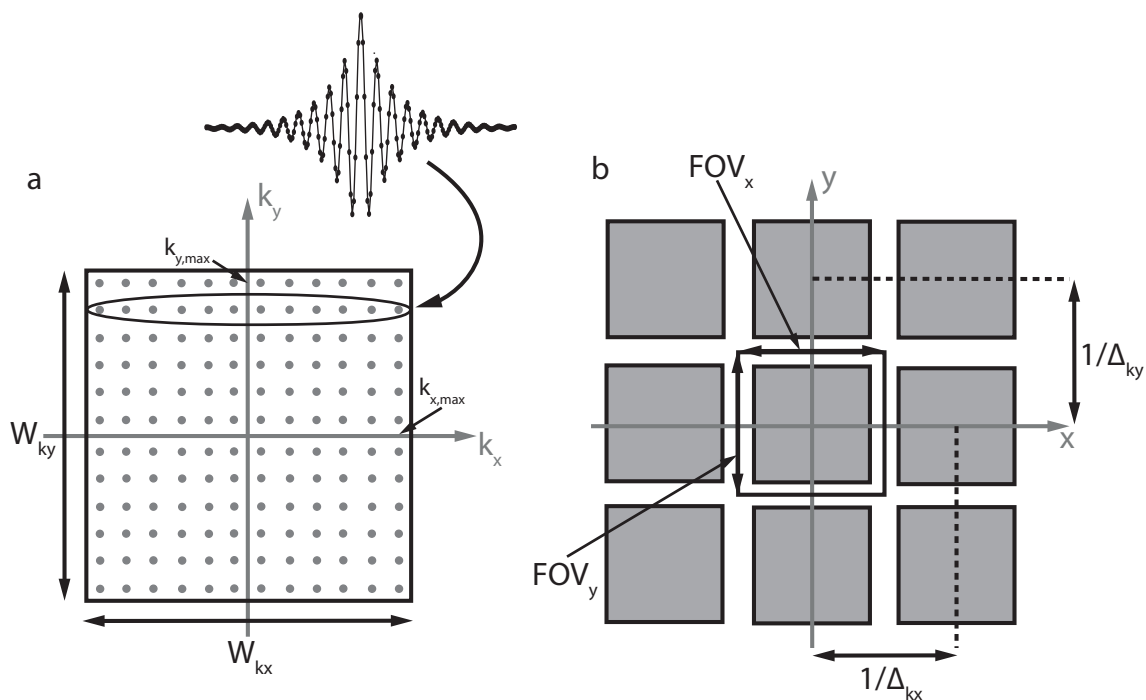


Figure 2.27: (a) Discret k -space resulting from the signal sampling at every Δt intervals. W_{kx} and W_{ky} define the widths of the acquired k -space in x and y directions. (b) Image space with replicated islands of the $M_0(x, y)$ profile resulting from the k -space sampling with Δk_x and Δk_y intervals. In this example, Δk_x and Δk_y are small enough such that the replicated versions of $M_0(x, y)$ do not overlap.

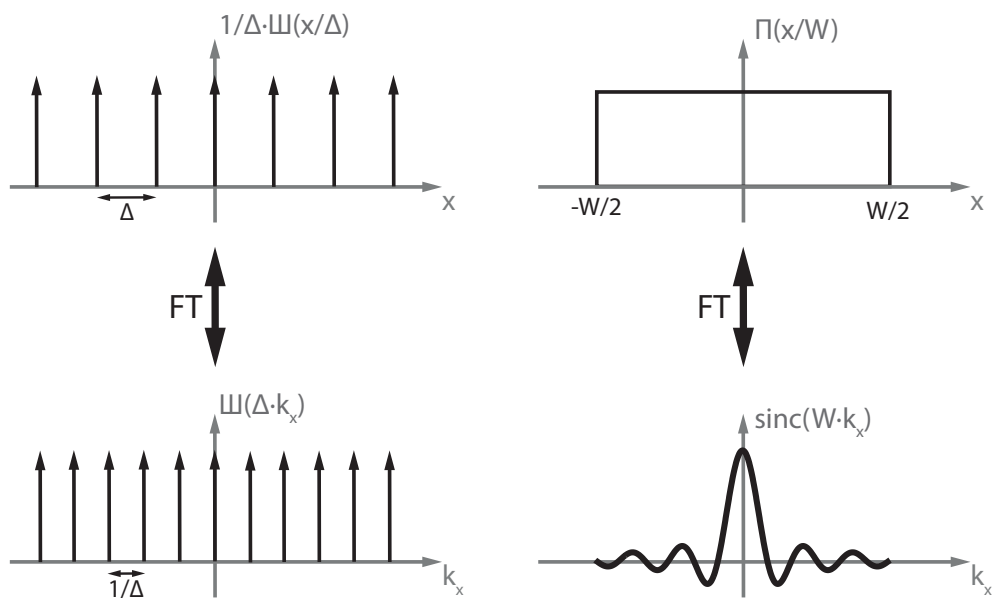


Figure 2.28: Fourier transforms of Dirac comb and rectangular function representing k -space sampling and truncation operations.

two side-by-side replicated versions of $m(x,y)$ is given by $1/\Delta k_x$ or $1/\Delta k_y$ (Fig. 2.27b), FOV_x and FOV_y follow the relations

$$\begin{aligned} FOV_x &= \frac{1}{\Delta k_x} \\ FOV_y &= \frac{1}{\Delta k_y} \end{aligned} \quad (2.102)$$

Zooming in the spatial encoding gradient of figure 2.26, it comes out that Δk_x and Δk_y correspond to the incremental areas of G_x and G_y gradients (Fig. 2.29).

Defining $G_{x,max}$ and $G_{y,max}$ as the maximum amplitudes of G_x and G_y , τ_x and τ_y their dura-

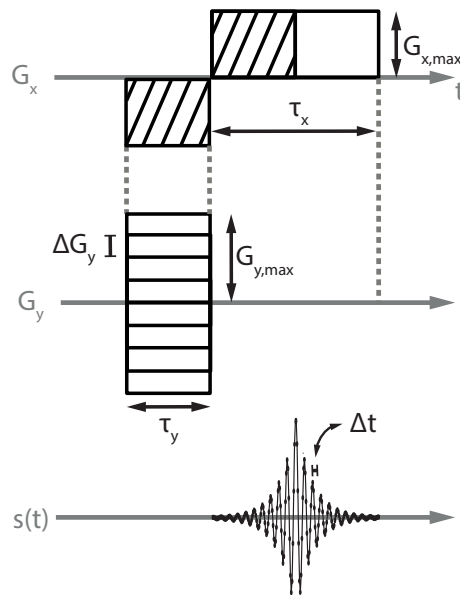


Figure 2.29: Encoding gradient parameters involved in the calculation of the image FOV and resolution.

tions (Fig. 2.29), then using equation (2.96), Δk_x and Δk_y can be expressed as

$$\begin{aligned} \Delta k_x &= \frac{\gamma}{2\pi} G_{x,max} \Delta t \\ \Delta k_y &= \frac{\gamma}{2\pi} \Delta G_y \tau_y \end{aligned} \quad (2.103)$$

where Δt and ΔG_y represent the interval between two data samples and the G_y gradient increment from one repetition to the other (Fig. 2.29), respectively. If the echo signal is sampled N_x times and N_y increments of ΔG_y are used to sample the k -space in the y direction,

spatial resolutions δ_x and δ_y are given by

$$\begin{aligned}\delta_x &= \frac{FOV_x}{N_x} = \frac{1}{\Delta k_x N_x} = \frac{1}{W_{k_x}} \\ \delta_y &= \frac{FOV_y}{N_y} = \frac{1}{\Delta k_y N_y} = \frac{1}{W_{k_y}}\end{aligned}\quad (2.104)$$

For each dimension, the second and third equality were set by considering equation 2.102 and figure 2.27. As shown in equation (2.99), W_{k_x} and W_{k_y} involve $k_{x,max}$ and $k_{y,max}$ of which values can be deduced from figure 2.29

$$\begin{aligned}k_{x,max} &= \frac{\gamma}{2\pi} G_{x,max} \frac{\tau_x}{2} \\ k_{y,max} &= \frac{\gamma}{2\pi} G_{y,max} \tau_y\end{aligned}\quad (2.105)$$

Combining equations (2.99), (2.103), (2.104) and (2.105) gives rise to the following expressions for the spatial resolutions

$$\begin{aligned}\delta_x &= \frac{1}{2k_{x,max} + \Delta k_x} = \frac{1}{\frac{\gamma}{2\pi} G_{x,max} \tau_x + \frac{\gamma}{2\pi} G_{x,max} \Delta t} = \frac{1}{\frac{\gamma}{2\pi} G_{x,max} (\tau_x + \Delta t)} \\ \delta_y &= \frac{1}{2k_{y,max} + \Delta k_y} = \frac{1}{\frac{\gamma}{2\pi} 2G_{y,max} \tau_y + \frac{\gamma}{2\pi} \Delta G_y \tau_y} = \frac{1}{\frac{\gamma}{2\pi} (2G_{y,max} + \Delta G_y) \tau_y}\end{aligned}\quad (2.106)$$

In most cases, N_x and N_y are large (>100) and therefore $W_{k_x} \approx 2k_{x,max}$ and $W_{k_y} \approx 2k_{y,max}$, what leads to

$$\begin{aligned}\delta_x &\approx \frac{1}{2k_{x,max}} = \frac{1}{\frac{\gamma}{2\pi} G_{x,max} \tau_x} \\ \delta_y &\approx \frac{1}{2k_{y,max}} = \frac{1}{\frac{\gamma}{2\pi} 2G_{y,max} \tau_y}\end{aligned}\quad (2.107)$$

In figures 2.26 and 2.29 the gradients were referred to as G_x , G_y and G_z . From now on, the term "phase encoding" (G_{PE}) will be used for the gradient incremented at each repetition. Indeed, a phase shift depending on their positions was accrued by the isochromats at the end of this gradient. The "frequency encoding" gradient (G_{FE}) provides the acquisition of one entire line of k-space frequencies during a repetition. As its name indicates it, the "slice selection" gradient (G_{SS}) is involved in the process of selecting the slice of interest. Since the slice of interest is not always in the xy plane, the notation G_{SS} , G_{PE} and G_{FE} is preferred to the one with physical coordinates G_x , G_y and G_z .

2.3.3 Artifacts

It was shown in the last section that due to k-space sampling and truncation, the magnetization profile actually acquired was a convolution of the true $m(x,y)$ with a two-dimensional Dirac comb and sinc functions. The convolution by the Dirac comb involves replications of $m(x,y)$ every $1/\Delta k_x$ and $1/\Delta k_y$ intervals which also correspond to the FOV_x and FOV_y (Fig. 2.27). This means that if $1/\Delta k_x < FOV_x$ or $1/\Delta k_y < FOV_y$, the replicated versions will start to overlap. For example, if $1/\Delta k_x$ corresponds to a field of view smaller than the head in a brain scan, the exceeding part will appear overlapping on the reconstructed image. This artifact called aliasing can be avoided by reducing Δk_x and Δk_y .

From equation (2.103), aliasing in the y direction can be avoided by reducing the incremental area under the G_y gradient, i.e. by diminishing the product $\Delta G_y \cdot \tau_y$. If the k-space coverage in the y direction is maintained, more encoding steps are required, resulting in an increase of the acquisition time. In the x direction, aliasing is usually avoided by increasing the sampling rate, i.e. reducing Δt .

As mentioned earlier, the convolutions by sinc functions in equation (2.101) coming from k-space truncation create blurring in the final image. This artifact results from the loss of the information coming from the non acquired high k-space frequencies which provide image details. Mathematically, an infinite extent of W_{k_x} and W_{k_y} would transform the sinc functions into Dirac's distributions, what would suppress the artifact. As an infinite k-space acquisition is not feasible in practice, following equation (2.105), the parameters $G_{x,max}$, $G_{y,max}$, τ_x and τ_y providing the maximal W_{k_x} and W_{k_y} values are selected such that the desired resolution is obtained.

2.3.4 Image weightings and sequences

2.3.4.1 Proton density, T_1 and T_2 weighted imaging

Different types of contrast can be obtained in MRI by varying the sequence parameters. Since biological tissues have different proton densities ρ as well as relaxation times T_1 and T_2 , the signal they generate can be manipulated in several ways. To illustrate how images with contrasts depending more on ρ , T_1 or T_2 can be obtained, a spin echo imaging sequence with echo time TE and repetition time TR will be considered (Fig. 2.30). To analyze how the image contrast is affected by the sequence parameters, the equation of the echo signal will be derived. As the sequence is repeated many times to fill up the k-space, at some point, a steady-state is reached, i.e. the state of the magnetization at the end of each repetition (right before a new 90° pulse) is identical. It can be assumed that $TE \ll TR$ what means that at the end of a repetition, the transverse magnetization is entirely out of phase ($M_{xy} = 0$). It results that the steady-state magnetization $m_{z,ss}$ is purely longitudinal. For a tissue with proton density ρ and relaxation times T_1 and T_2 , the state of the magnetization after the 90°

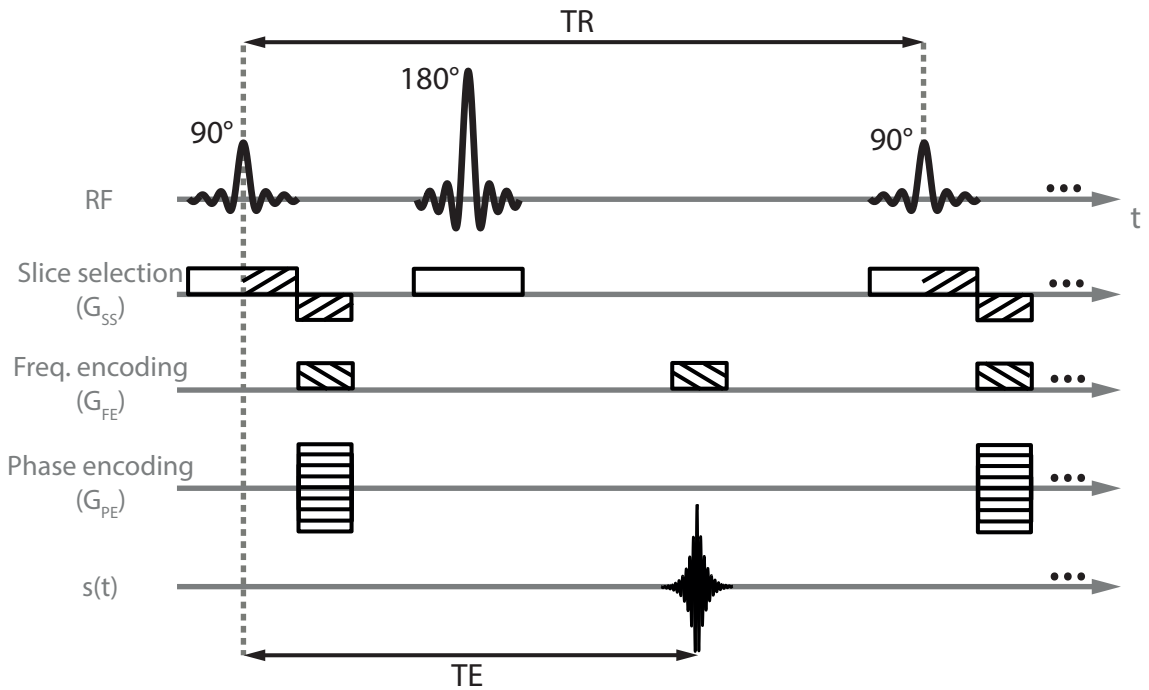


Figure 2.30: Spin echo sequence where the echo time (TE) and repetition time (TR) play a crucial role in the image contrast are displayed.

pulse considered as the $t=0$ position is

$$\begin{aligned} M_{xy}(0) &= m_{z,ss} \sin(90^\circ) = m_{z,ss} \\ M_z(0) &= m_{z,ss} \cos(90^\circ) = 0 \end{aligned} \quad (2.108)$$

Following equation (2.35), the longitudinal magnetization at time TR, which reaches the steady-state again is given by

$$M_z(TR) = m_{z,ss} = M_0 \left(1 - e^{-\frac{TR}{T_1}} \right) \quad (2.109)$$

As explained in section 2.2.5, B_0 inhomogeneities are refocused by the 180° pulse and therefore the spin echo signal can be expressed as a function of TE and TR

$$S(TE, TR) \propto \rho \left(1 - e^{-\frac{TR}{T_1}} \right) e^{-\frac{TE}{T_2}} \quad (2.110)$$

where ρ which is proportional to M_0 was introduced. The echo signal is thus determined by three components : ρ , the term into brackets and e^{-TE/T_2} . The evolutions of $1-e^{-TR/T_1}$ and e^{-TE/T_2} as a function of TR and TE for 3 different tissues are displayed on figure 2.31. The curves presented were simulated using T_1 and T_2 values of the main brain tissues at 7T provided by [16–18]

	T_1 [ms]	T_2 [ms]
CSF	3400	100*
GM	1939	50*
WM	1126	28

CSF, GM and WM respectively stand for Cerebro Spinal Fluids, Gray and White Matter. The stars mean that the T_2 values could not be found in the literature and therefore were roughly approximated. Although T_1 measurements for brain tissues at 7T performed by several groups are in accordance with each others, there is still high variations in the results found for the measurement of T_2 . Nevertheless, the following analysis remains valid for T_1 and T_2 values slightly different than those presented in the previous table.

If TR is made long (right line on Fig. 2.31a) and TE short (left line on Fig. 2.31b), the bracketed and e^{-TE/T_2} terms become close to one, leaving the echo signal mainly proportional to ρ . The result is a so-called proton density (PD) weighted image. In this type of images, tis-

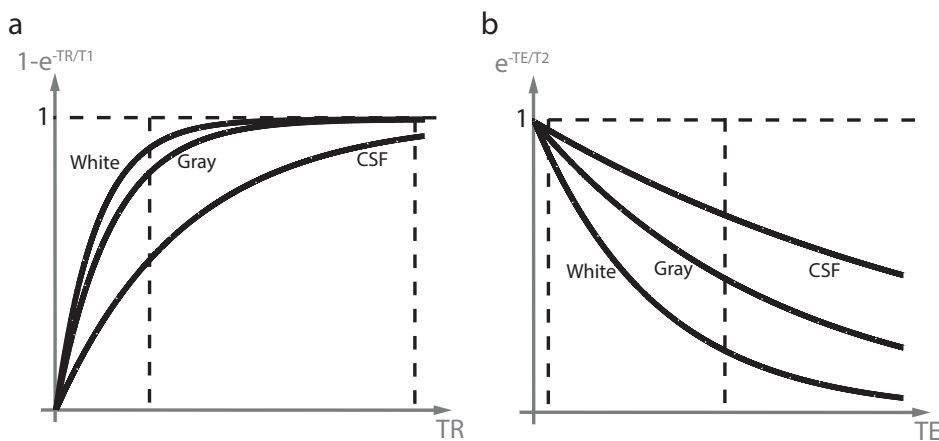


Figure 2.31: (a) T_1 -recovery curves for the main brain tissues. The vertical dashed lines highlight the contrast obtained when using a short (left) or long (right) TR. (b) T_2 -decay curves for the same tissues as in (a). The vertical lines highlight the contrast obtained when using a short (left) or long (right) TE.

sues with higher ρ such as CSF or fat will provide more signal and therefore appear brighter. Nevertheless the contrast between tissues in PD-weighted imaging is poor since their ρ values are rather similar. Keeping the TR long but setting TE to a value in the order of the average T_2 over the tissues (right line on Fig. 2.31b) involves that the signal is dominated by the e^{-TE/T_2} term, providing an image with a contrast based on the differences in T_2 . In such T_2 -weighted images, CSF having a much higher T_2 value than other tissues, appear very bright. Abnormal fluids or tumors also present intense signal as compared to darker healthy tissues. That makes T_2 -weighted imaging a suitable tool in pathology detection.

In order to have an echo signal dominated by the term in brackets in equation (2.110), TE is set at its shortest value (left line on Fig. 2.31b) while a TR in the order of the average T_1 is

used (left line on Fig. 2.31a) to maximize the T_1 difference between tissues (T_1 -weighting). As their T_1 value is high, CSF are dark on T_1 -weighted images whereas other tissues appear brighter. A lot of anatomical information can be obtained from this type of images where tissue boundaries are clearly delineated.

The analysis of this simple sequence shows that different types of contrasts can be obtained on MR images by varying TR and TE. The equation of the echo signal is very useful to understand how the variation of a specific parameter affects the resulting image. For more complex sequences, a mathematical expression of the measured signal is even more important to know how the image contrast varies since besides TE and TR, additional parameters are involved.

2.3.4.2 Turbo Spin Echo sequence

In the spin echo sequence shown in figure 2.30 only one k-space line is acquired per repetition while not all the transverse magnetization has relaxed. As $TR \gg TE$, a lot of time is still available from the echo to the application of the next excitation. By adding another 180° pulse, M_{xy} can be refocused giving rise to a second echo. In a turbo spin echo (TSE) sequence, a 90° pulse is followed by several 180° pulses creating a train of echoes. The TSE sequence is also known as fast spin echo (FSE) or rapid acquisition with relaxation enhancement (RARE) sequence. By adapting the phase encoding gradient between the pulses, multiple k-space lines can be acquired in a TR interval (Fig. 2.32). The acquisition time required to acquire a slice with the spin echo sequence is given by

$$TA_{SE} = N_{PE} \cdot TR \quad (2.111)$$

where N_{PE} is the number of k-space points in the phase encoding direction. For a TSE sequence with an echo train length ETL, the acquisition time is lowered to

$$TA_{TSE} = \frac{TA_{SE}}{ETL} \quad (2.112)$$

It would thus take 12min to acquire an image with $N_{PE} = 256$ by using a spin echo sequence with $TR = 3s$ whereas only 40s are required for a TSE sequence with $ETL = 16$.

The echo spacing (ES) which also corresponds to the interval between 180° pulses is twice the duration between the 90° and the first refocusing pulse (Fig. 2.32). The first sequence with this pulse configuration was proposed by Carr and Purcell in 1954 [19]. ETL is limited since T_2 -decay occurs from one echo to the next.

The phase between the 90° and the refocusing pulses plays a crucial role in TSE sequences. Figure 2.33 shows the evolution of isochromats until the second echo when all pulses are applied along x' . Assuming imperfect 180° pulses inducing a rotation slightly smaller than half a turn, after the first refocusing pulse (Fig. 2.33c), isochromats have a nonzero component towards $-z$. The second refocusing pulse (Fig. 2.33f) amplifies this error since it generates

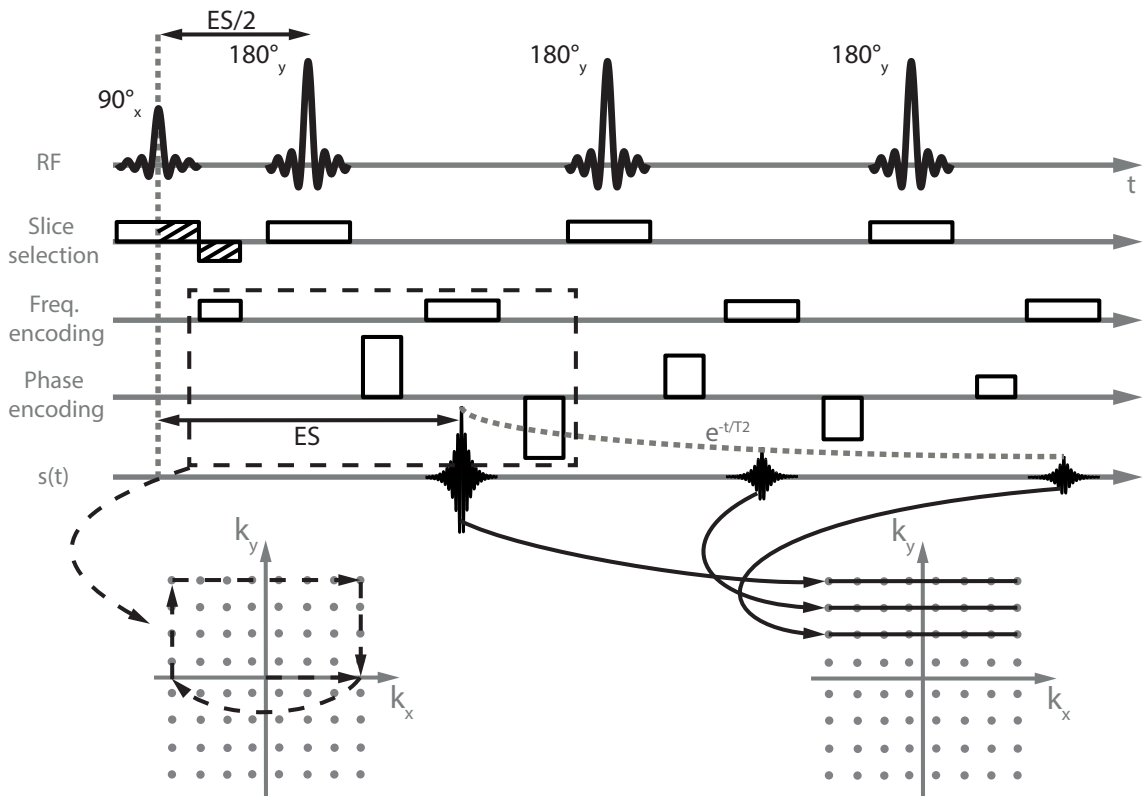


Figure 2.32: Turbo spin echo sequence where the phase encoding gradient is set in a way that different echoes correspond to different k -space lines. The trajectory defined by the gradients in the dashed box is depicted on the k -space in the bottom left side. T_2 relaxation can be observed from one echo to the next.

another rotation $< 180^\circ$ about the x' axis. Such a cumulative effect rapidly degrades the train of echoes.

The situation changes if the phases of the excitation and refocusing pulses are shifted by 90° . Figure 2.34 depicts the situation for a 90° pulse applied along x' and refocusing pulses along y' .

With this configuration, an imperfect 180° pulse produces isochromats with nonzero components along $+z$ in the $-x'y'$ quadrant and $-z$ in the $x'y'$ one. The echo formation then occurs and dephasing brings isochromats with $+z$ components in the $x'y'$ quadrant whereas the ones with $-z$ components end up in the $-x'y'$ quadrant right before the next RF pulse (assuming a dephasing as presented in Fig. 2.34). As the first refocusing pulse, the second one will induce a rotation smaller than 180° , bringing isochromats with $\pm z$ components exactly on the $x'y'$ plane. In this way, the error created by an imperfect refocusing pulse is corrected by the following one.

The advantage of having or not the 90° phase shift between the excitation and the refocusing pulses is obvious on figure 2.35. The curves were simulated using the EPG formalism by considering imperfect refocusing pulses of flip angle 160° and relaxation effects where

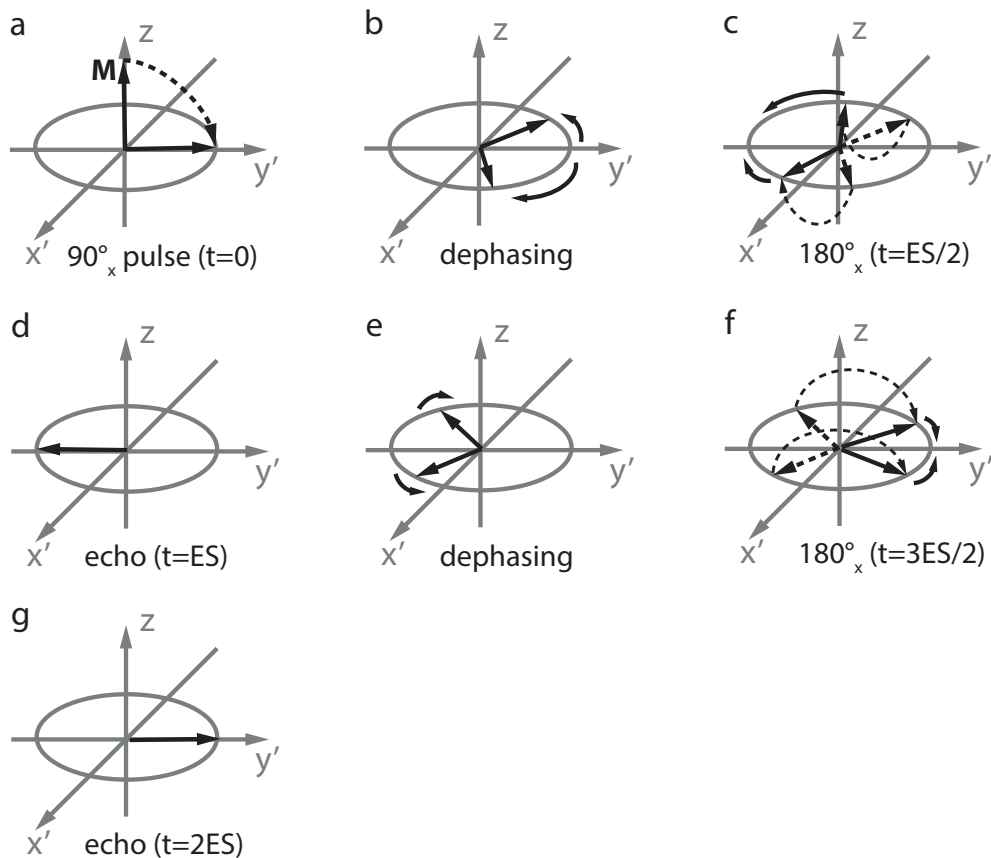


Figure 2.33: Evolution of isochromats until the second echo generated by the TSE sequence with every pulses applied in the x' direction. The drawings assume that the 180° refocusing pulses are perfect. The description for imperfect pulses is done in the text. (a) The 90° pulse excites \vec{M} towards the y' direction. (b) Isochromat dephasing. (c) First refocusing pulse inducing a 180° rotation about the x' axis. (d) First echo along the $-y'$ direction. (e) Isochromat dephasing. (f) Second refocusing pulse inducing a 180° rotation about the x' axis. (g) Second echo along the y' direction.

neglected. This figure shows that the error created by imperfect refocusing pulses does not propagate across the echo train when the 90° phase shift is set between the excitation and the refocusing pulses. On the other hand, when all the pulses are applied in the same direction, the echo signal decreases rapidly.

The importance of the 90° phase shift between the excitation and refocusing pulses in a TSE sequence was established by Meiboom and Gill in 1958 [20]. This requirement combined with the necessity of having an interval between the 180° pulses twice as long as the gap from the excitation to the first refocusing pulse are known as the CPMG (Carr - Purcell - Meiboom - Gill) conditions.

The duration from the beginning of the sequence to the point where the k-space center line is acquired is called the effective TE (TE_{eff}). The phase encoding scheme can be modified such that the central k-space segment is acquired earlier (short TE_{eff}) or later (long TE_{eff}) in the sequence. As for the TE parameter in the spin echo sequence, the contrast on a TSE image

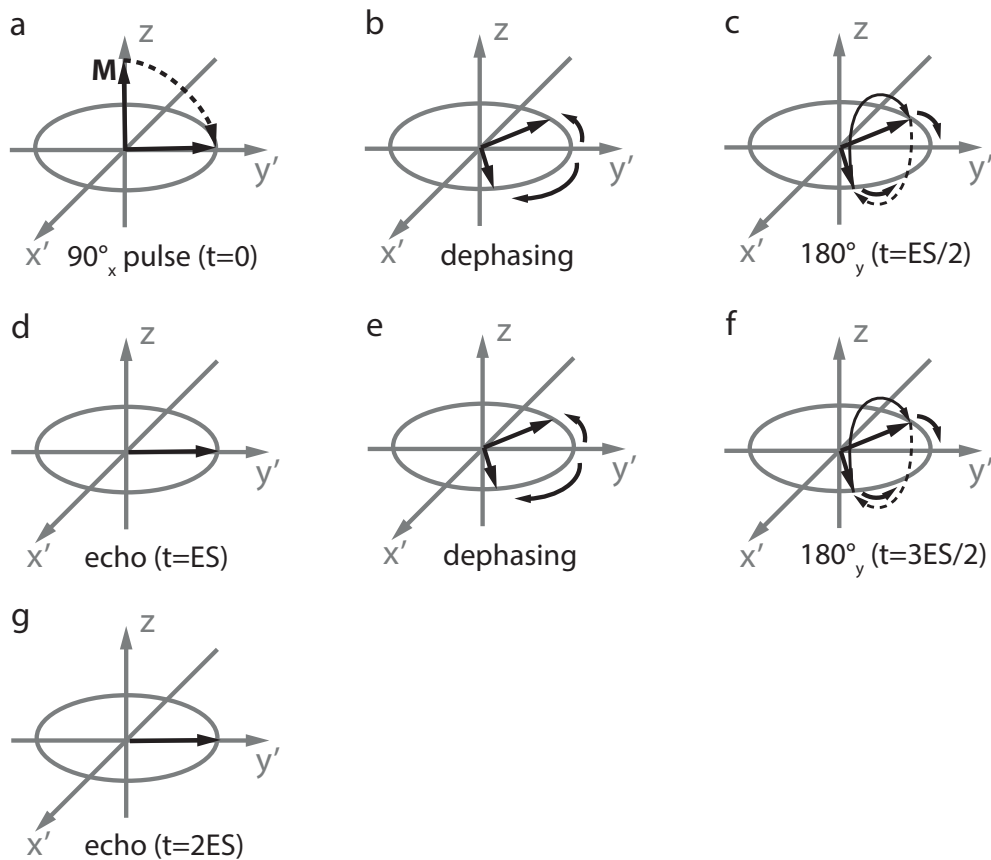


Figure 2.34: Evolution of isochromats until the second echo generated by the TSE sequence with a 90° phase shift between the excitation and the refocusing pulses. (a) The 90° pulse excites \vec{M} towards the y' direction. (b) Isochromat dephasing. (c) First refocusing pulse inducing a 180° rotation about the y' axis. (d) First echo along the y' direction. (e) Isochromat dephasing. (f) Second refocusing pulse inducing a 180° rotation about the y' axis. (g) Second echo along the y' direction.

highly depends on TE_{eff} . Therefore, proton density, T_1 and T_2 -weighted imaging can also be performed with TSE sequences. The contrast information is primarily determined by the central segments (low frequency components) whereas details about tissue boundaries and finer structures are provided by outer k-space lines (high frequency components). As seen on figure 2.32, echoes in the train are affected by T_2 -decay. The central segments are thus generally attributed to echoes at the beginning of the train which have a higher amplitude such that the main part of the image is associated to the acquisitions with the highest signal. In respect to a signal that would be constant from one echo to the next, T_2 -decay involves the multiplication of the k-space data by a decaying exponential corresponding to a convolution with a Lorentzian in the image space, what gives rise to blurring in the final image. This artifact is also increased when long echo trains are used. However by choosing carefully the TSE sequence parameters, images comparable to the ones provided by the spin echo sequence can be obtained in a much shorter acquisition time.

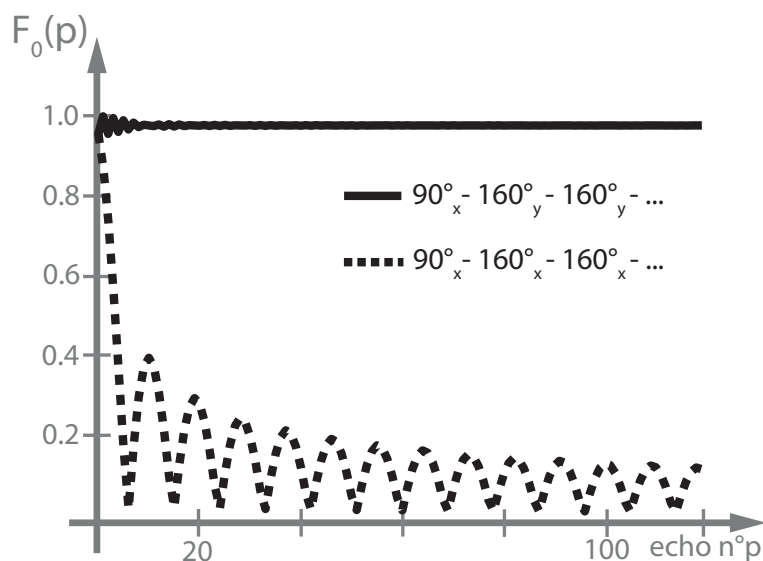


Figure 2.35: EPG simulations of the signal amplitudes throughout the echo train generated by a TSE sequence with 160° refocusing pulses. When the excitation and refocusing pulses are 90° phase shifted, the loss of magnetization due to the imperfect refocusing pulses is corrected every two echoes, leading to a tiny difference as compared to the case with perfect 180° pulses (solid curve). On the other hand, when all the pulses are applied in the same direction, the error generated by the imperfect refocusing propagates from one echo to the next and the signal decreases rapidly (dashed curve).

Besides blurring, another drawback of the sequence presented in figure 2.32 is that a significant amount of RF energy is deposited on the sample since several 180° pulses are applied in a short period of time. The energy deposition can be significantly reduced by using a TSE sequence with refocusing pulses smaller than 180° [21]. In this case, the signal not only depends on spin (Hahn) echoes but also on stimulated echoes. This is obvious when comparing the phase graph pathways of the TSE using 180° pulses and the one with lower flip angles (Fig. 2.36).

As explained in section 2.2.5 magnetization stored in the z direction is involved in the stimulated echo mechanism. Maintaining some part of the magnetization along z, affected by T_1 relaxation rather than T_2 , allows echoes with sufficient amplitudes to be acquired over a longer period and therefore enables higher ETL values to be used. To illustrate it, the phase graph formalism was used to simulate the amplitude of echo signals (F_0 states) throughout TSE sequences with refocusing pulses of flip angles 180° and 60° (Fig. 2.37). With every other sequence parameters the same, the train length can be extended by reducing the flip angles from 180° to 60° .

Since it involves stimulated echoes, the image acquired using a TSE sequence with refocusing pulses $<180^\circ$ presents a contrast which depends both on T_1 and T_2 -weightings. It was discovered that instead of keeping the refocusing pulses constant throughout the sequence, trains of variable flip angles could be optimized to reach a certain signal evolution.

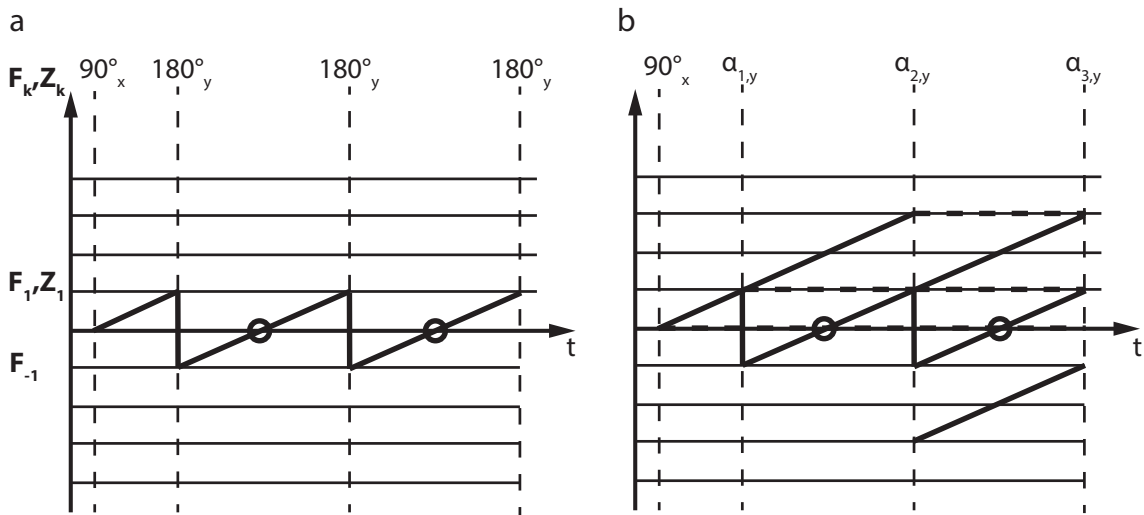


Figure 2.36: Phase graphs for the TSE sequence with 180° refocusing pulses only (a) and variable flip angles (b). A certain amount of magnetization is stored in the longitudinal direction as soon as refocusing pulses with flip angles smaller than 180° are applied as shown by the horizontal dashed lines in (b).

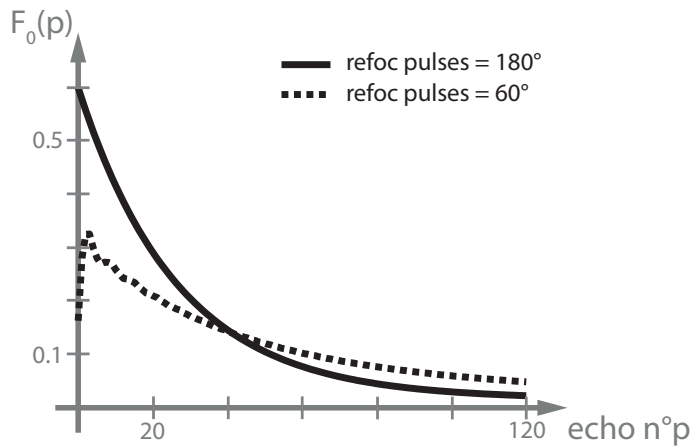


Figure 2.37: Comparison of echo trains for TSE sequences with 180° (solid) and 60° (dashed) refocusing pulses. Although the signal intensity is smaller at the beginning of the echo train for the sequence with 60° pulses, the advantage is that the period where echoes with sufficient amplitudes exist is extended, meaning that longer ETL values can be used with this pulse configuration. Moreover, the exponential decay associated to blurring in the final image is less pronounced when smaller flip angles are used.

In particular, Alsop demonstrated that an appropriate ramp made of pulses with higher flip angles applied at the beginning of the sequence brings the magnetization into a static pseudo steady state (sPSS) where the stability of echo signals is quite robust versus flip angle variations [22]. It was then proposed to also vary the flip angles after the ramp bringing \vec{M} into sPSS such that the ETL can be further increased [23–25].

Figure 2.38 compares the signal evolutions associated with a sequence of constant flip angles and a train where refocusing pulses were optimized such that a constant echo amplitude is reached over the largest time period for a specific tissue. Both sequences have the same av-

verage flip angle of 84° .

With variable flip angles, echo trains can be maintained up to 1s or longer, meaning that

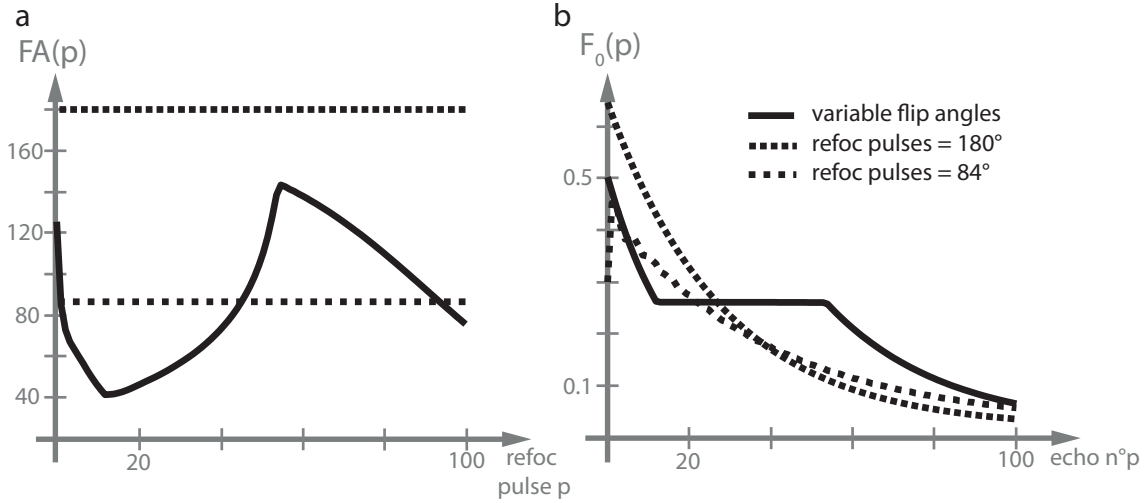


Figure 2.38: (a) Train of flip angles for TSE sequences with 180° (tight dashes), 84° (spaced dashes) and variable (solid) refocusing pulses. (b) Echo trains corresponding to the flip angle evolutions in (a).

with an echo spacing of 4ms, several hundreds of echoes can be collected in one TR. Very long trains are of particular interest for three-dimensional TSE sequences where the acquisition time given by equations (2.111) and (2.112) becomes

$$TA_{TSE,3D} = \frac{N_{PE} \cdot N_{PE,2} \cdot TR}{ETL} \quad (2.113)$$

where N_{PE2} corresponds to the number of points acquired in the second phase encoding direction. One of the main challenges when acquiring large 3D volumes is to make it in a clinically reasonable amount of time. Acquiring the volume of interest using a 3D instead of 2D acquisitions by replacing the slice-selective sinc pulses by non-selective hard pulses (Fig. 2.39) is advantageous. Indeed, using hard pulses shorter than sinc allows ES to be reduced and therefore, more echoes can be acquired over the period where a sufficient signal exists. Since isochromats in the entire volume are affected by hard pulses applied without slice-selective gradient, a phase encoding gradient $G_{PE,2}$ similar to G_{PE} is applied in the formerly named slice-selection direction (Fig. 2.39).

ES can be further reduced by recording the k-space lines in a shorter amount of time. This is possible by making use of the maximal sampling bandwidth BW during the acquisition process.

The scan time can also be reduced by using parallel imaging which will not be described in this thesis. Briefly, the idea is to skip the acquisition of a predefined number of k-space lines and use the sensitivity profiles of the different receiving coil elements to recover the missing information. In this way, the acquisition time can be reduced by a factor of almost 2 if every

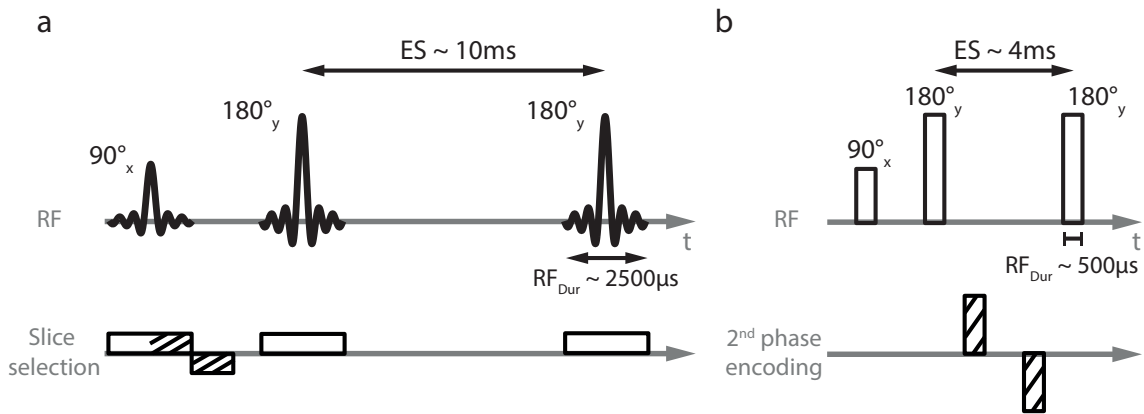


Figure 2.39: (a) TSE sequence with slice-selective sinc pulses. (b) TSE sequence with non-selective hard pulses exciting a 3D volume. The advantage of using hard pulses is that their duration (RF_{Dur}) can be made much shorter than sinc pulses and therefore, ES can be reduced as well. The slice selection direction in (a) is now referred to as the second phase encoding direction where gradients similar to those used in the first phase encoding direction (cf. Fig. 2.32) were introduced such that echoes corresponding to different positions in a 3D k -space can be acquired.

other k -space lines are skipped.

2.4 Hardware, the basics

So far, it was explained that when placed in the \vec{B}_0 field, magnetic moments of spin 1/2 molecules can lie in one of two distinct energy states with a certain probability, creating a macroscopic magnetization \vec{M} . It was also shown how \vec{M} can be manipulated by the RF field \vec{B}_1 and magnetic field gradients \vec{G} such that a signal can be detected by the receiver coil. In this section, the main hardware components involved in the image creation will be described.

2.4.1 Magnets

On modern scanners, the \vec{B}_0 field is created by a strong superconducting magnet. Niobium-titanium (NbTi) is usually used as the superconducting material in which the current creating the \vec{B}_0 field flows. NbTi microfilaments embedded in a copper core in order to facilitate their manipulation, form wires which are wound in a solenoid shape such that the electric current passing through creates a magnetic field in the z direction (Fig. 2.40). As NbTi becomes superconducting below 9.4K, the coils are immersed in a cryostat filled up with liquid helium (4K) to maintain the current circulating indefinitely.

When setting up the magnet, the homogeneity of the B_0 field degrades due to interactions with the surrounding environment. B_0 -shimming which is the process of making the main magnetic field more homogeneous is performed with two types of shim coils. A first set of superconducting shim coils is located inside the cryostat (Fig. 2.40). The coils are designed such that the current passing through generates magnetic fields associated with different

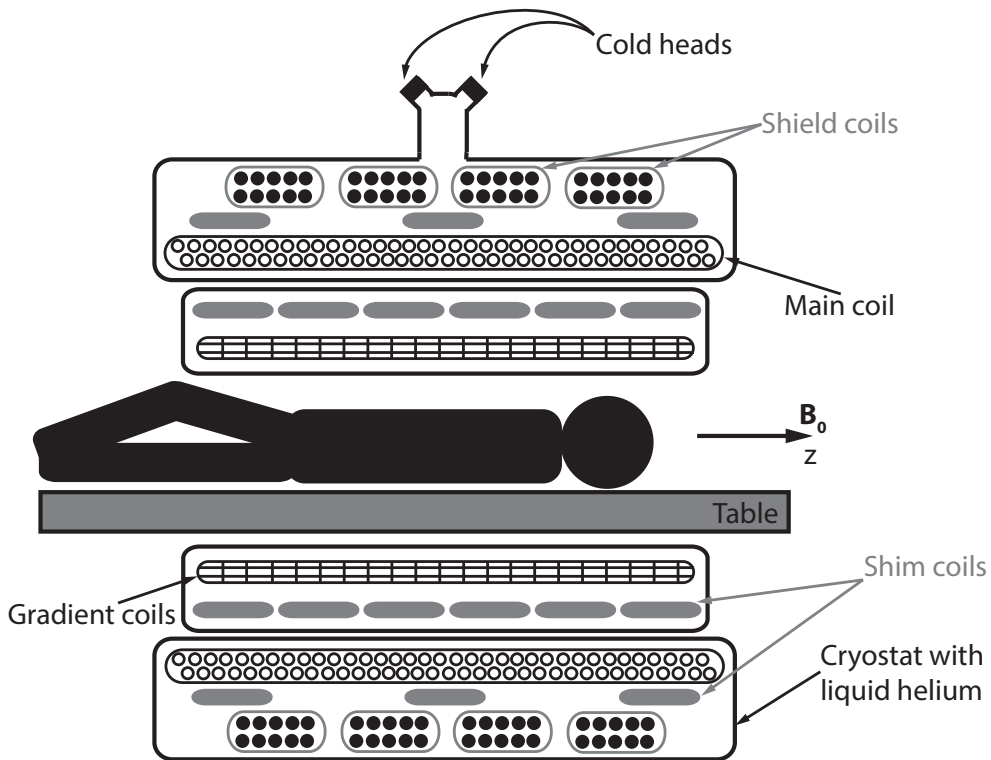


Figure 2.40: Structure of the main parts of the 7T MR device used in this thesis : the magnet and the gradient system. To maintain the NbTi filaments superconducting, the main coil is immersed in a cryostat filled up with liquid Helium. The shield coils used to decrease the fringe field outside of the magnet are also placed in the cryostat, as well as a set of shim coils calibrated during the installation such that the most homogeneous B_0 field is generated inside the empty magnet bore. Within the inner bore tube, the subject lies on a table that can be moved along the z direction and surrounded by the element containing the gradient and another set of shim coils used to perform B_0 shimming on a patient-by-patient basis. On the top part of the cryostat, two cold heads are used to get the boiled-off Helium back into its liquid phase.

spherical harmonics. The currents flowing through those coils are calculated using an iterative process at the magnet setup such that the most homogeneous \vec{B}_0 field is obtained inside the magnet bore when it is empty.

Another set of shim coils, which are resistive, is placed in the cylinder formed by the cryostat (Fig. 2.40). By measuring the B_0 field distribution over the region of interest at the beginning of an MR experiment, the current that should flow through each shim coil can be calculated such that the B_0 profile becomes as homogeneous as possible.

Unlike the shimming obtained with the coils placed inside the cryostat which is performed only once, the B_0 correction allowed by the resistive shim coils can be done on a patient-by-patient basis.

For safety and practical reasons, it is important to reduce the effects of the strong B_0 field outside the magnet bore. For the 7T system used in this thesis, this is performed by another set of coils in the cryostat (Fig. 2.40). Those shield coils generate a field designed to reduce the magnetic field outside the main coil thereby decreasing the fringe field of the magnet.

In the 7T system described here, boiling-off liquid Helium is collected and recondensed by

two cold heads (Fig. 2.40) which are Helium pumps creating a characteristic low-frequency background noise.

2.4.2 Gradients

As explained in sections 2.2.3 and 2.3.1, linear magnetic field gradients in x , y and z directions are required for slice selection and spatial localization. Gradients are generated by loops of wire mounted on a cylindrical shell placed in the tube formed by the cryostat (Fig. 2.40). In its simplest form, the linear gradient varying in the z direction $G_z = \frac{\partial B_z}{\partial z}$ is produced by a Maxwell pair (Fig. 2.41a). Two coils with counter-rotating currents generate

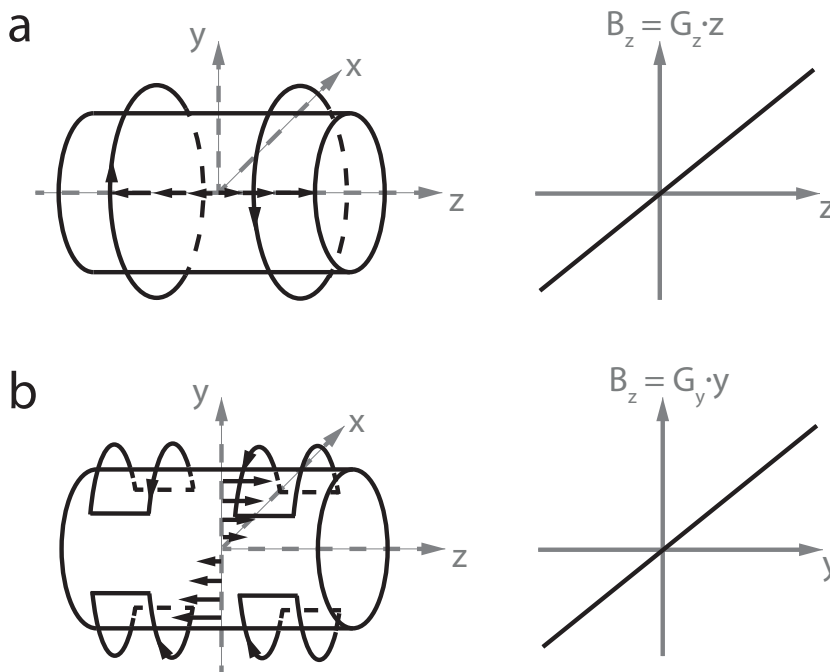


Figure 2.41: (a) Maxwell pair creating a linear magnetic field gradient along the z direction ($G_z = \partial B_z / \partial z$). (b) Goley coil configuration creating $G_y = \partial B_z / \partial y$. Rotating the set of Goley coils by 90° would result in the generation of the G_x gradient.

a magnetic field increasing or decreasing (depending on the current direction) as a function of z . The Goley coil configuration (Fig. 2.41b) represents the original design for the gradients in the other directions $G_x = \frac{\partial B_z}{\partial x}$ and $G_y = \frac{\partial B_z}{\partial y}$. Four saddle shaped loops are placed on the cylinder such that the desired field is generated by the inner arcs. The G_x and G_y gradients are thus only linear on the fraction of the magnet bore located between those arcs.

The location where $B_z = B_0$ corresponding to $x = y = z = 0$ is called the magnet isocenter. The strength of G_x , G_y and G_z which defines the slope of the lines showing B_z as a function of x , y or z on figure 2.41 is expressed in mT/m.

The highest values that the gradient system can produce $G_{x,max}$, $G_{y,max}$ and $G_{z,max}$ are of interest since they determine the highest k -space positions achievable, as shown in equation

(2.105). The acquired k-space lines are proportional to the area under the gradient shape given by $G(t)$. For the same area, a shorter duration can be used if a higher gradient amplitude is available which would result, to some extent, in a shorter echo time, reducing the total acquisition time as well as potential signal increase (less transverse relaxation). According to section 2.2.3, a higher $G_{z,max}$ would also result in a steeper slope of the $\omega(z)$ line (Fig. 2.16) allowing the selection of thinner slices for the same RF pulse duration. For conventional gradient systems, maximum values in the range of 10-80 mT/m can be reached for the gradient amplitude. With the gradient system used in this thesis, a maximal amplitude of 80 mT/m can be achieved.

So far, rectangular gradients were displayed on the pulse sequence illustrations. Actually most gradient pulses have a trapezoidal shape (Fig. 2.42a) since they cannot be turned on and off instantaneously. The duration required to reach the desired gradient amplitude or

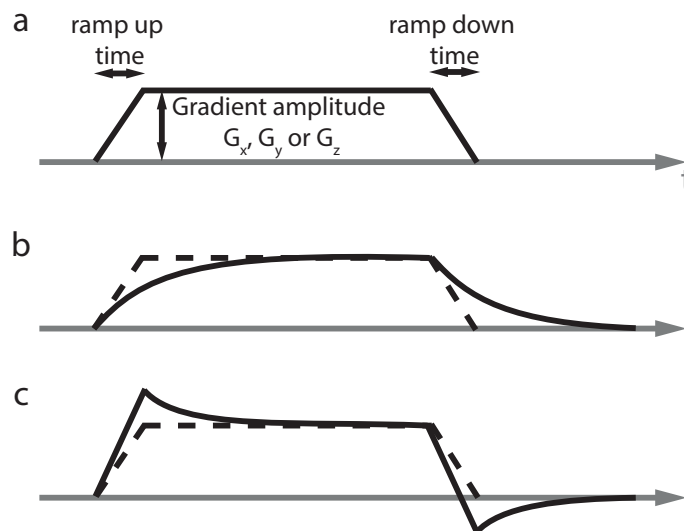


Figure 2.42: (a) Targeted trapezoidal gradient waveform. (b) Gradient shape actually applied due to the fields generated by eddy currents. (c) Gradient waveform compensating eddy current effects.

to return from it to zero is called ramp up or down time. The slew rate is given by the ratio between the gradient amplitude and the ramp up or down time and is expressed in T/m/s. Slew rates on the order of 20-350 T/m/s are typically found nowadays. For the experiments performed in this thesis, the maximum available slew rate was 333 T/m/s.

Switching the gradient from zero to its maximum value creates a time-varying magnetic field inducing eddy currents in the nearby conducting materials of the magnet e.g. the cryostat. As the field resulting from eddy currents is opposed to the gradient variation, the actual shape will be smaller during the ramp up and higher when ramping down (Fig. 2.42b). To correct for that, the gradient waveform is designed with more pronounced slopes and corrections going above the gradient amplitude at the beginning and below zero at the end (Fig. 2.42c).

During MR sequences, gradients are switched on and off very rapidly resulting in vibrations of the gradient coils. This gives rise to the disagreeable noise heard during MR experiments with a frequency that depends on how quickly the gradients are switched on and off and an amplitude proportional to the vibration modes of the gradient system.

2.4.3 RF system

The key element of the RF system is the RF coil which plays a crucial role in both the transmission of the \vec{B}_1 field and the reception of the MR signal. In this section, the transmission side will first be presented where the concepts of linear and circular polarization will be described. The birdcage coil and the arrays used for parallel transmission will be subsequently introduced. The section will end by describing the basic coil configurations used for the signal detection.

2.4.3.1 Transmission

As already presented, \vec{M} can be flipped by an angle α about a certain axis by applying an RF pulse with appropriate amplitude and phase. It was also shown that during the slice-selection process, the width of the slab excited by the RF pulse depends on its bandwidth $\Delta\omega$. It was finally explained that \vec{M} can be manipulated only if \vec{B}_1 rotates at the Larmor frequency.

Polarization

In the 1970's, the most common way to produce the desired rotating \vec{B}_1 field was to use wire loops with a current oscillating at ω_0 such that a linearly polarized field perpendicular to \vec{B}_0 is created. Figure 2.43 presents a single loop generating a linearly polarized \vec{B}_1 field that can be decomposed as the sum of two components, both rotating with frequency ω_0 but in opposite directions (gray and black thin arrows in figure 2.43b). The linearly polarized configuration is inefficient since the magnetization only experiences the effect of the component rotating at Larmor frequency (black arrow). The other component with $-\omega_0$ being ineffective, it only deposits unwanted RF energy in the sample, increasing the specific absorption rate (cf. section 2.5).

A purely rotating \vec{B}_1 field can be generated by adding a second loop in the orthogonal direction and driving them with sinusoidal currents 90° out of phase (Fig. 2.44a). With this configuration called circularly polarized, the components rotating with $-\omega_0$ frequency (gray arrows) cancel each other whereas the effective ones (black arrows) add up together producing a rotating \vec{B}_1 field (Fig. 2.44b). This configuration reduces significantly the amount of energy deposited in the sample since all the produced \vec{B}_1 is effectively used for the excitation.

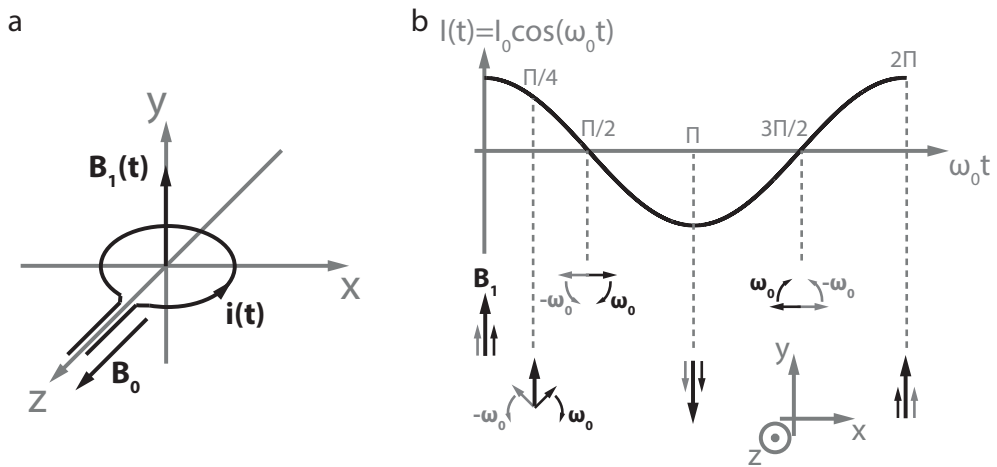


Figure 2.43: (a) Current oscillating at ω_0 frequency in a wire loop lying in the xz plane creating a time varying \vec{B}_1 field along the y direction. (b) \vec{B}_1 field generated by the wire loop at different time points. The \vec{B}_1 field can be seen as two counter rotating components, one with frequency ω_0 (black thin arrows), the other one with $-\omega_0$ (gray thin arrows).

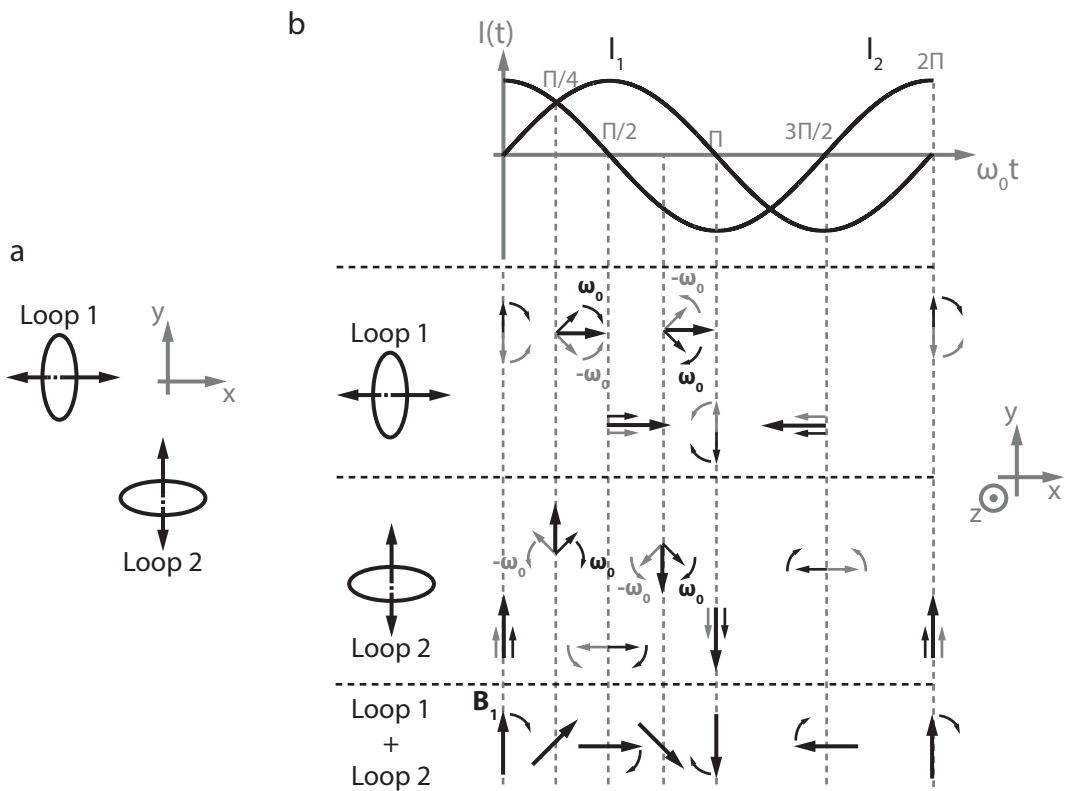


Figure 2.44: (a) Two orthogonal wire loops generating a rotating \vec{B}_1 field. (b) \vec{B}_1 fields generated by each loop at different time points (first and second rows). The last row correspond to the rotating field obtained when summing the contributions of the two loops. The \vec{B}_1 field generated by each loop is seen as two counter rotating components, one with frequency ω_0 (black thin arrows), the other one with $-\omega_0$ (gray thin arrows).

Birdcage Coil

When performing an MRI experiment, the \vec{B}_1 field generated by the RF coil should be as homogeneous as possible over the region of interest such that isochromats at different \vec{r} positions in the sample are manipulated in the expected way. Volume coils are designed according to this principle. From antenna theory, a perfectly homogeneous rotating field in the transverse plane can be created inside a conducting cylinder if the current distribution around its surface varies sinusoidally. A birdcage coil is one of the simplest type of volume coils that approximates the conducting cylinder. This coil is made of two circular loops linked by N straight conductors (Fig. 2.45a). An example of the fields generated in

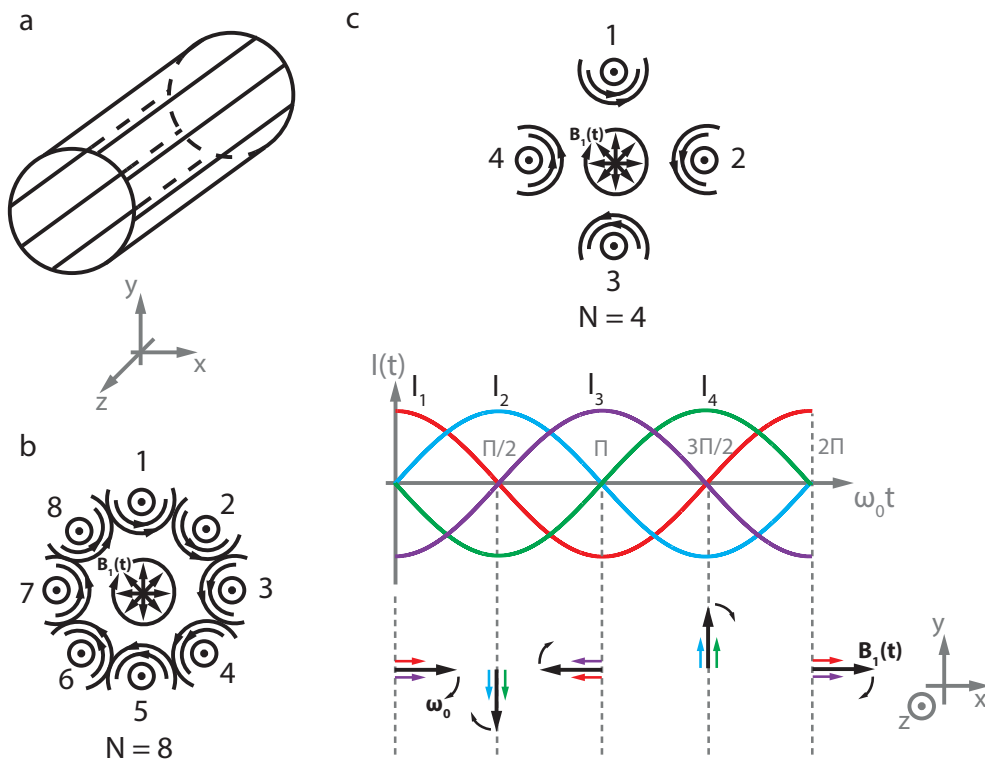


Figure 2.45: (a) Birdcage coil made of two loops linked with N straight conductors. To generate a CP mode, the currents have to be phase shifted by $2\pi/N$ radians from one wire to the next. (b) Magnetic field generated by the current flowing through each conductor of a birdcage coil with $N=8$ conductors. The resulting rotating \vec{B}_1 field is shown in the center. (c) Birdcage coil with $N=4$ conductors. The evolution of the currents are phase shifted by $2\pi/4 = \pi/2$ from one conductor to the next resulting in a rotating \vec{B}_1 field in the transverse plane.

the transverse plane by the current through the wires and the resulting rotating \vec{B}_1 field is illustrated in figure 2.45b for the case where $N=8$. In general, the current passing through each wire is phase shifted by $2\pi/N$ radians. To better understand how this current configuration generates a rotating \vec{B}_1 field, the case where $N=4$ straight conductors is considered in figure 2.45c.

Two opposite elements e.g. 1 and 3 generate field components adding up if the currents I_1

and I_3 are phase shifted by π . In the same way, this phase shift implies that the field components produced by elements 2 and 4 point in the same sense. With this configuration of the currents throughout the coil, a central rotating \vec{B}_1 field is generated over time. By extending this analysis to other positions in the transverse plane and considering a higher N value it can be shown that an RF field distribution close to the ideal one of the conducting cylinder can be obtained. This configuration of the coil producing a rotating \vec{B}_1 at every positions in the transverse plane is called the homogeneous mode or circularly polarized (CP) mode.

Parallel Transmit System and Arrays

At high B_0 strengths, the wavelength of the fields generated by the coil elements inside the object becomes equal to or smaller than its diameter. Constructive and destructive interferences occur, leading to an inhomogeneous \vec{B}_1 distribution with alternating bright and dark regions across the sample. Moreover, when a subject is inserted inside the magnet, tissue dielectric properties distort the B_1 profile. The CP mode provided by the birdcage coil in the absence of an object is not appropriate anymore for the acquisition of an image with an homogeneous and efficient B_1^+ field.

Parallel transmit arrays were developed such that the \vec{B}_1 distribution throughout the sample can be optimized. Each array element is individually controlled such that it generates its own \vec{B}_1 field. The sum over those individual entities corresponds to the net \vec{B}_1 field across the sample. The magnitude and phase of each element can be optimized such that the most homogeneous \vec{B}_1 distribution is produced. This will be described in more details in section 3.3.3.

In addition to the control of their amplitudes and phases (RF shimming), the individual array elements can run different RF waveforms. As will be discussed in sections 3.2 and 3.3, RF pulses can be designed for each element (Transmit SENSE) of the parallel transmit system (Fig. 2.46). To achieve this, each channel has a modulator that physically creates the designed individual waveforms which are then scaled up by the RF power amplifiers. Before reaching the array itself, the waveforms go through Transmit Antenna Level Sensor (TALES) units forming the online RF power monitoring system used by Siemens in parallel transmission. Each unit measures the forward going RF power through the corresponding channel. If the measured value is higher than a certain safety threshold (cf. section 2.5), the current measurement is stopped by the system.

As parallel transmit arrays are generally used for transmission and reception, a transmit-receive (T/R) switch is required on each channel. The role of this device is to protect the electronics involved in reception which is made to detect signals order of magnitude smaller than the transmitted signal. The principle of a T/R switch lies on the use of diodes and a $\lambda/4$ cable to prevent the transmit signal from going through the receive line and destroy components such as the expensive preamplifier used to amplify the weak measured signal.

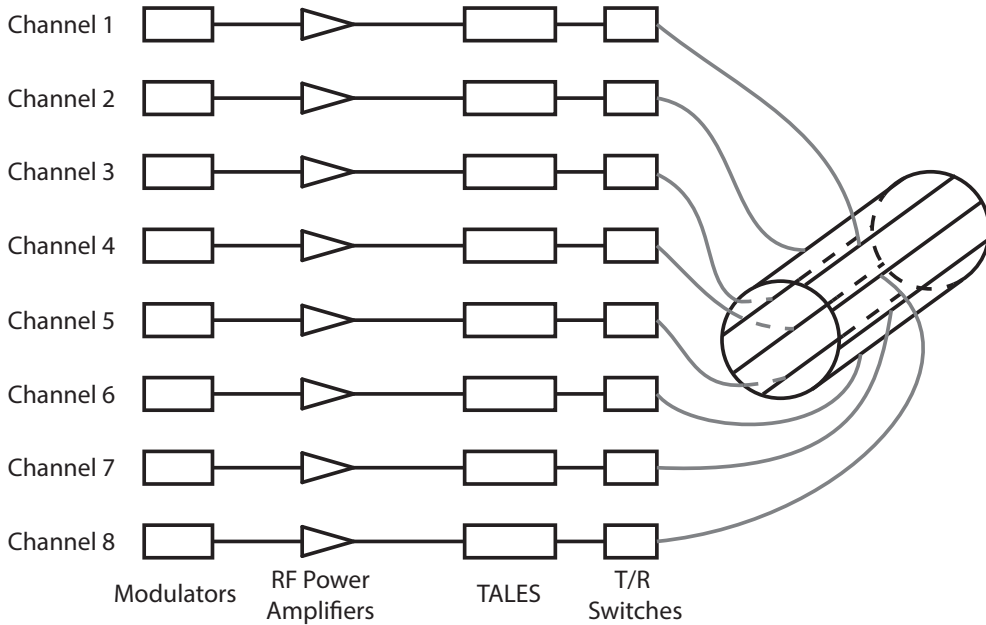


Figure 2.46: Eight channel parallel transmit system used in this thesis. Such a system offers the possibility of running RF pulses specifically tailored for each coil element in order to obtain the desired magnetization profile across the subject. The designed waveforms are physically created by the modulators and then scaled up by the RF power amplifiers. To make sure the designed sequences remain below the safety guidelines, RF power measuring units (TALES) calculate the forward going RF power for each channel. If a measured value is higher than the safety threshold, the sequence is stopped. Since the array coil is used for both transmission and reception, T/R switches are used to protect the receiving line from the RF radiations sent during the transmission phase.

2.4.3.2 Reception

On the receive side, the role of the coil is to acquire the highest percentage of the MR signal while minimizing the noise. This is performed by adjusting the coil dimensions as close as possible to the sample providing the signal. For birdcage coils or parallel transmit arrays which are usually used in both transmission and reception, the length and diameter is adapted depending on the sample size. For example, a torso coil will be larger than a head one.

It was shown in section 2.3.1 that the signal $s_r(t)$ produced by the magnetization excited in the transverse plane can be written as the product of the low frequency signal $s(t)$ containing the image information and the high frequency term $e^{-i\omega_0 t}$. The signal $s(t)$ can be expressed as a time varying complex quantity

$$s(t) = \alpha(t)e^{i\phi(t)} \quad (2.114)$$

with $\alpha(t)$ and $\phi(t)$ the time varying amplitude and phase of the useful signal. With this relation, $s_r(t)$ takes the form

$$s_r(t) = \alpha(t)e^{-i(\omega_0 t - \phi(t))} \quad (2.115)$$

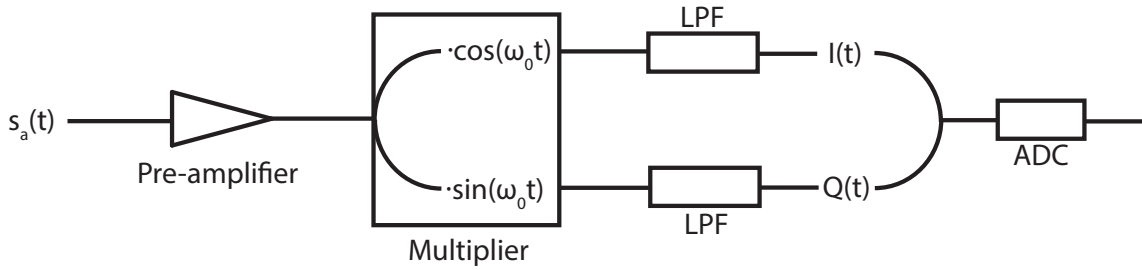


Figure 2.47: Reception line where the detected signal $s_a(t)$ is first amplified using a pre-amplifier and then demodulated via the multiplier and the low pass filters (LPF) in order to remove the high frequency oscillations which do not contain image information. The demodulated signal is finally digitized for further processing.

The main parts of the reception line are presented on figure 2.47. As soon as the tiny MR signal is detected (under the form of a voltage) it is amplified such that the highest amplitude is preserved in respect to the noise introduced by the detection line.

The next step is to get rid of the high frequency oscillations in the detected signal. It should be noted here that in practice, a real value is measured, what implies that the actual detected quantity is

$$s_a(t) = \text{Re}[s_r(t)] = \alpha(t)\cos(\omega_0 t - \phi(t)) \quad (2.116)$$

The demodulation of $s_a(t)$ down to $s(t)$ is performed by using a multiplier combined with low pass filters. The role of the multiplier is to multiply the $s_a(t)$ signal by $\cos(\omega_0 t)$ on one side and by $\sin(\omega_0 t)$ on the other side. The results of those operations are

$$s_a(t) \cdot \cos(\omega_0 t) = \alpha(t)\cos(\omega_0 t - \phi(t)) \cdot \cos(\omega_0 t) = \frac{1}{2}\alpha(t) [\cos(2\omega_0 t - \phi(t)) + \cos(-\phi(t))] \quad (2.117)$$

and

$$s_a(t) \cdot \sin(\omega_0 t) = \alpha(t)\cos(\omega_0 t - \phi(t)) \cdot \sin(\omega_0 t) = \frac{1}{2}\alpha(t) [\sin(2\omega_0 t - \phi(t)) - \sin(-\phi(t))] \quad (2.118)$$

Low pass filtering is then applied in order to filter out the high frequency terms $2\omega_0 t - \phi(t)$ and obtain $I(t)$ and $Q(t)$

$$\begin{aligned} I(t) &= \frac{1}{2}\alpha(t)\cos(\phi(t)) \\ Q(t) &= \frac{1}{2}\alpha(t)\sin(\phi(t)) \end{aligned} \quad (2.119)$$

Combining $I(t)$ and $Q(t)$ as

$$I(t) + iQ(t) = \frac{1}{2}\alpha(t)e^{i\phi(t)} \quad (2.120)$$

corresponds to the useful signal given in equation (2.114) with its amplitude halved.

Now that the carrier frequency was removed, the signal can be sampled more easily and this is performed by an analog to digital converter (ADC).

2.5 Safety considerations and SAR

During an MRI experiment, the subject is exposed to the main magnetic field B_0 , time varying gradients (G_x, G_y, G_z) and the RF field B_1 . The potential dangers that those different fields can create will be discussed hereafter.

2.5.1 B_0 effects

The main hazard regarding the B_0 field is the force exerted on ferromagnetic implants such as clips, stents or staples. Patients with cardiac pacemaker should also avoid MRI scans since the internal components of the device could be damaged by the B_0 effects.

Many subjects report sensory effects such as dizzy feeling, nausea and metallic taste when coming out of the MR scanner. Those mild effects which rapidly vanish when the subject is brought back outside the scanner are harmless.

Care is always adopted with patients and staff who are pregnant even if a link between magnetic field exposure and pregnancy issues has never been made. Some studies on women working with magnets reported that aspects as fertility and pregnancy are not affected by the magnetic field [26].

2.5.2 Gradient effects

The use of imaging sequences where gradients need to be quickly switched e.g. echo planar imaging (EPI) sequences, produces rapid field variations dB/dt that, from Faraday's law, generate electric currents in tissues. Above the threshold potential which is the critical value at which an action potential is initiated, the generated current will cause peripheral nerve stimulation (PNS) giving rise to a tingling feeling for the subject. The currents created by the dB/dt variation may also disturb the function of implanted medical devices.

On modern scanners the dB/dt is monitored throughout the sequence and must stay within the limits provided by IEC standards or FDA in order to minimize the degree of PNS.

2.5.3 RF effects

When applying an RF pulse to create the desired \vec{B}_1 field, energy is deposited in the tissues. When many pulses are applied in a short amount of time, tissue heating with potential physiological consequences can occur. Regarding this effect, particular care should be observed with heat-sensitive body parts which are poorly perfused such as eyes.

SAR

The specific absorption rate (SAR) is a measurement of the RF energy deposition caused by electric fields in the body and is commonly used in the domains of MRI and mobile

phones. The SAR has the unit of watts per kilogram and can be calculated using the relation

$$SAR = \int_{VOI} \frac{\sigma(\vec{r})|\vec{E}(\vec{r})|^2}{\rho(\vec{r})} d\vec{r} \quad (2.121)$$

where $\sigma(\vec{r})$ and $\rho(\vec{r})$ respectively represent the spatial electric conductivity and density distributions. The integration is performed over the volume of interest, VOI. Based on this equation, the SAR associated to an RF pulse can be calculated given that a simulation of the \vec{E} field generated by the coil was performed beforehand. Several types of body models with different $\sigma(\vec{r})$ and $\rho(\vec{r})$ can be used to estimate $\vec{E}(\vec{r})$ when the coil is loaded and have a higher confidence on the SAR deposition on a subject whose σ, ρ are unknown.

For a given sequence, the SAR must be below specific values established by the IEC 60601-2-33 standard or the FDA in the USA. For example the IEC guidelines state that the SAR, when imaging the head, should not exceed $3.2W \cdot kg^{-1}$ for a 6min duration. Knowing the maximum value SAR^{max} produced by the RF coil, it can be determined from TR and the shape of the pulses if running the sequence is allowed or not.

The SAR can be reduced in several ways. As explained in section 2.4.3.1, compared to the linear configuration, using a circularly polarized coil reduces the amount of energy deposited in the sample since it avoids the wasted \vec{B}_1 component to be created.

As it indicates how intensively RF pulses are applied during the sequence, the SAR can be lowered by increasing the TR since the fraction of the scan time where pulses are applied decreases.

When working with a TSE sequence, the SAR can be reduced by decreasing the number of pulses in the train or by reducing the flip angle of the refocusing pulses.

On standard systems, when performing the simulation of the SAR associated to an RF coil, the phase relationships between the RF waveforms generated by the different coil elements are known. As was explained in section 2.4.3.1, the RF coils are generally driven in quadrature mode. This means that the $\vec{E}_i(\vec{r})$ field profile generated by each coil element i can be precisely simulated (amplitude and phase) and therefore, the calculation of their interaction can be performed.

The task becomes more complicated when using a parallel transmit system where the amplitudes and phases of the different array elements can be manipulated.

As the phase of $\vec{E}_i(\vec{r})$ is unknown beforehand, it is impossible to determine if at a certain position, the fields generated by two different elements will add up or cancel each other unless simulations are done for each specific array configuration or RF pulse.

To calculate the SAR of a parallel transmit array, the worst case scenario assuming that the \vec{E} fields coming from different transmitters constructively interfere at every positions is often considered. A largely overestimated SAR of the coil results from this assumption, making the experiments harder to be kept under the SAR guidelines than on the normal system.

From the SAR simulations, three thresholds are generally calculated for the parallel trans-

mit system: (1) peak, (2) 10 seconds average and (3) 6 min average RF power. The power of an RF pulse must at any instant stay below (1) and while integrating over 10s or 6min, the power delivered by the sequence should remain smaller than (2) and (3).

As mentioned in section 2.4.3.1, on the parallel transmit system used in this thesis, the TALEs units monitor the forward going RF power of each channel. If the measured power exceeds one of the thresholds (1-3), the sequence is stopped.

A less restrictive way of calculating the SAR in parallel transmit systems remains an active field of research. An elegant method was proposed in [27] where spatially and time-dependent variables involved in SAR calculation are separated. Therefore, $\vec{E}_i(\vec{r})$, $\sigma(\vec{r})$ and $\rho(\vec{r})$ are expressed in the form of Q matrices calculated and stored in a database. The time-consuming simulations of those matrices are done beforehand based on the coil geometry and various body models. Once the subject is inserted inside the magnet, a real time SAR calculation can be performed since only the time dependent variables corresponding to the designed RF waveforms need to be added to the already computed Q matrices. In comparison to the worst case scenario, calculating the SAR using this approach provides a much higher flexibility in the choice of protocols on parallel transmit systems.

3

RF pulse design and fighting B_1^+ inhomogeneity

3.1 General RF pulse design

It was explained in section 2.2.3 that to select a slice of width Δz , a gradient in the z direction has to be combined with an RF pulse of bandwidth $\Delta\omega$. This requirement does not guarantee that every positions within the slice will experience the same excitation. Significant variations in the $M_{xy}(z)$ profile can be observed in the Δz interval for an inappropriate RF pulse shape. In section 3.1.1, the small tip angle (STA) approximation [28] upon which many RF pulse design techniques are based [29–38], will be introduced. It will be shown that in the range of flip angles where the approximation holds, the magnetization profile $M_{xy}(z)$ can be expressed as the Fourier transform of the RF shape $B_1(t)$. In this regime, a sinc pulse with bandwidth $\Delta\omega$ and flip angle α applied in the x direction would generate a rectangular distribution of $M_y(z)$ with height $M_0 \sin(\alpha)$ for positions within the Δz interval and zero outside. In a similar way as for the description of the MR signal acquisition, a spatial k -space was introduced in the description [39]. An RF pulse designed in the STA regime can thus be regarded as the deposition of RF energy across a trajectory in the excitation k -space.

Surprisingly, the STA approximation performs reasonably well for flip angles as high as $\sim 90^\circ$ [39, 40]. However, due to the non-linearity of Bloch equations, the Fourier relationship between $M_{xy}(z)$ and $B_1(t)$ is not valid anymore above a certain limit. For larger tip angles, the amplitude and phase of the RF shape has to be determined using a suited optimization method in order to obtain a uniform magnetization distribution within the selected slice. Moreover, when designing RF pulses for which the STA approximation is still valid, improved results are obtained by using high tip angle methodologies, at a cost of a more complex optimization process.

Several methods were proposed for the design of high flip angle RF pulses [41–44]. Among them, the Shinnar-Le Roux algorithm will be described in section 3.1.2 since it introduces the formalism involving the Cayleigh Klein coefficients on which the RF pulse design technique presented in section 6.1 is based.

3.1.1 Design at small tip angle

The small tip angle (STA) approximation will be detailed here since it makes the design of pulses in the low tip angle regime very simple and efficient, explaining why it is still widely spread among the pulse design society.

If the relaxation terms in equation (2.37) are neglected and for a \vec{B} field involving an arbitrary gradient field \vec{G}

$$\vec{B} = B_1(t)(\cos(\omega t) \cdot \vec{e}_x - \sin(\omega t) \cdot \vec{e}_y) + (B_0 + \vec{G} \cdot \vec{r}) \cdot \vec{e}_z \quad (3.1)$$

the Bloch equations in the rotating frame are given by

$$\dot{\vec{M}} = \vec{M} \times \gamma(B_{1,x'} \cdot \vec{e}_{x'} + B_{1,y'} \cdot \vec{e}_{y'} + (\vec{G} \cdot \vec{r}) \cdot \vec{e}_z) \quad (3.2)$$

This system of equations can also be expressed as

$$\dot{\vec{M}} = \gamma \begin{bmatrix} 0 & \vec{G} \cdot \vec{r} & -B_{1,y'} \\ -\vec{G} \cdot \vec{r} & 0 & B_{1,x'} \\ B_{1,y'} & -B_{1,x'} & 0 \end{bmatrix} \vec{M} \quad (3.3)$$

In the small tip angle (STA) regime, the longitudinal magnetization is considered to remain constant throughout the RF pulse and equal to the equilibrium state M_0 . This is justified by the fact that the flip angles involved are small ($\alpha < 30^\circ$). A constant M_z implies that dM_z/dt is null and therefore the previous system becomes

$$\begin{bmatrix} dM_{x'}/dt \\ dM_{y'}/dt \\ 0 \end{bmatrix} = \gamma \begin{bmatrix} 0 & \vec{G} \cdot \vec{r} & -B_{1,y'} \\ -\vec{G} \cdot \vec{r} & 0 & B_{1,x'} \\ B_{1,y'} & -B_{1,x'} & 0 \end{bmatrix} \begin{bmatrix} M_{x'} \\ M_{y'} \\ M_0 \end{bmatrix} \quad (3.4)$$

With this assumption, transverse components $M_{x'}$ and $M_{y'}$ are not coupled anymore with M_z . Using the notations $M_{xy} = M_{x'} + iM_{y'}$ and $B_{1,xy} = B_{1,x'} + iB_{1,y'}$, the two first equations can be merged together as

$$\begin{aligned} \frac{dM_{xy}}{dt} &= \frac{dM_{x'}}{dt} + i\frac{dM_{y'}}{dt} = \gamma\vec{G} \cdot \vec{r}[M_{y'} - iM_{x'}] + \gamma M_0[iB_{1,x'} - B_{1,y'}] \\ &= -i\gamma\vec{G} \cdot \vec{r}M_{xy} + i\gamma M_0 B_{1,xy} \end{aligned} \quad (3.5)$$

Replacing $\gamma\vec{G} \cdot \vec{r}$ by ω , the previous equation becomes

$$\dot{M}_{xy} = -i\omega M_{xy} + i\gamma M_0 B_{1,xy} \quad (3.6)$$

One way to solve this differential equation is to use the Laplace transform \mathcal{L} defined as

$$\mathcal{L}[f(x)] = \int_0^{\infty} e^{-sx} f(x) dx = F(s) \quad (3.7)$$

Two useful properties of the Laplace transform are

$$\begin{aligned} f(x) = e^{-ax} &\rightarrow \mathcal{L}[f(x)] = \frac{1}{s+a} \\ \mathcal{L}[f'(x)] &= s\mathcal{L}[f(x)] - f(0) \end{aligned} \quad (3.8)$$

Performing the Laplace transform on both sides of equation (3.6), it comes

$$s\mathcal{M}_{xy}(s) - M_{xy}(0) = -i\omega\mathcal{M}_{xy}(s) + iM_0\mathcal{B}_{1,xy}(s) \quad (3.9)$$

where $\mathcal{M}(s)$ and $\mathcal{B}_{1,xy}(s)$ are the Laplace transforms of $M_{xy}(t)$ and $\gamma B_{1,xy}(t)$, respectively. As the magnetization is considered as being initially at equilibrium, no transverse component exists at $t=0$ and therefore $M_{xy}(0) = 0$. Reordering the terms in the previous equation leads to

$$\mathcal{M}_{xy}(s) = iM_0 \frac{\mathcal{B}_{1,xy}(s)}{s + i\omega} \quad (3.10)$$

Now taking the inverse Laplace transform and considering the first relation of (3.8) and the fact that the Laplace transform of a product is the convolution of the Laplace transforms, the previous equation becomes

$$M_{xy}(t) = iM_0 \left[\gamma B_{1,xy}(t) * e^{-i\omega t} \right] \quad (3.11)$$

where $*$ denotes the convolution operator. As a reminder, the expression for two convoluted functions f and g is

$$(f * g)(t) = \int_{-\infty}^{\infty} f(\tau)g(t - \tau)d\tau \quad (3.12)$$

Using this identity, the expression for $M_{xy}(t)$ can be rewritten as

$$M_{xy}(t) = iM_0 \int_0^t \gamma B_{1,xy}(\tau) e^{-i\omega[t-\tau]} d\tau \quad (3.13)$$

In the general case where a time-varying gradient $\vec{G}(t)$ is applied, the ω term appearing in the exponential is not constant anymore. Therefore, the $\omega[t - \tau]$ part has to be changed as $\int_{\tau}^t \omega(t') dt' = \gamma \int_{\tau}^t \vec{G}(t') \cdot \vec{r} dt'$ what gives rise to

$$M_{xy}(t, \vec{r}) = iM_0 \int_0^t \gamma B_{1,xy}(\tau) e^{-i\gamma \int_{\tau}^t \vec{G}(t') \cdot \vec{r} dt'} d\tau \quad (3.14)$$

Finally, defining

$$\vec{k}(\tau) = \frac{\gamma}{2\pi} \int_{\tau}^t \vec{G}(t') dt' \quad (3.15)$$

equation (3.14) becomes

$$M_{xy}(t, \vec{r}) = iM_0 \int_0^t \gamma B_{1,xy}(\tau) e^{-2\pi i \vec{k}(\tau) \cdot \vec{r}} d\tau \quad (3.16)$$

This result shows the existence of a Fourier relationship between the RF waveform $B_{1,xy}(t)$ and the magnetization it excites in the transverse plane $M_{xy}(t)$. Having such an analytical solution between the RF pulse and the resulting magnetization significantly helps the pulse design process. Moreover, by discretizing over space and time dimensions, equation (3.16) can be written as

$$d(x, y) = iM_0 \sum_{t=1}^T \gamma B_{1,xy}(t) e^{-2\pi i (k_x(t)x + k_y(t)y)} \quad (3.17)$$

If d is expressed as a $M \times 1$ column vector with M the number of voxels in the region of interest, the previous relation can be transformed as the system of equations

$$\mathbf{d} = \mathbf{A}\mathbf{B} \quad (3.18)$$

where \mathbf{A} is an $M \times T$ matrix of which elements are given by

$$A_m^t = iM_0 e^{-2\pi i (k_x(t)x_m + k_y(t)y_m)} \quad (3.19)$$

and \mathbf{B} is a $T \times 1$ complex vector containing the amplitudes and phases of the $B_{1,xy}$ field at the different durations t . Equation (3.18) shows that the non-linear Bloch equations can be approximated by a linear system in the STA regime.

At this point it is important to consider the meaning of $\vec{k}(\tau)$ defined in equation (3.15). Similarly to the k -space definitions provided in (2.96), $\vec{k}(\tau)$ also corresponds to a position on a space named the "excitation k -space". Equation (3.16) can thus be interpreted as a weighted trajectory across the "excitation k -space". The displacement through the trajectory is described by $\vec{k}(\tau)$ whereas the RF weightings are represented by $B_{1,xy}(\tau)$.

One subtlety with the way the trajectory is visited lies in the integral limits of equation (3.15). Indeed, the integration is made from τ to t , implying that when $\tau = t$, i.e. at the end of the pulse, $\vec{k}(\tau) = 0$. This means that the last point of the trajectory is always the k -space center. At $\tau = 0$, the position in k -space is given by the integral over the complete gradient waveform. Figure 3.1 illustrates with two simple examples how the k -space trajectory changes when modifying the gradient shape. In the first case (Fig. 3.1a) the trajectory goes from the k_z position defined by the integral over the gradient shape to zero. As this example only considers a G_z gradient, the trajectory goes along the k_z direction. In the second case (Fig. 3.1b), the trajectory starts at $k_{z,1} > 0$ and the goes to $k_{z,2} = -k_{z,1}$ (since the dashed

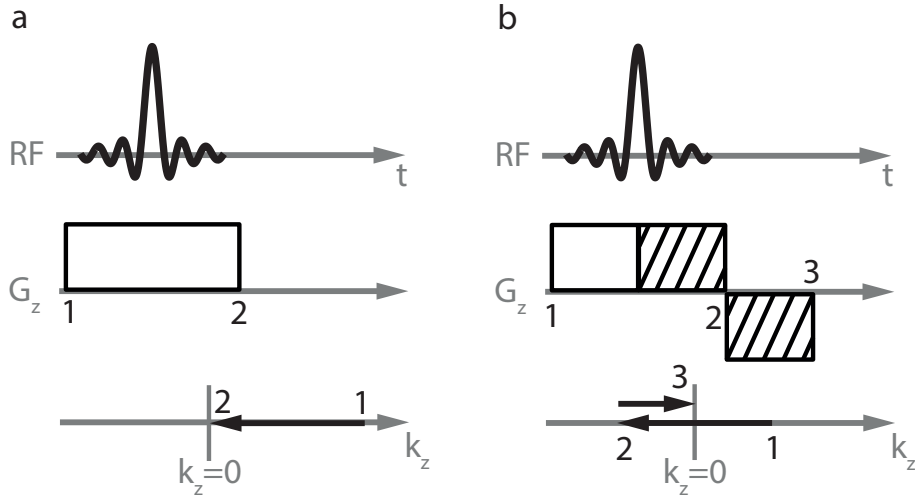


Figure 3.1: K-space trajectory as defined in equation (3.15). At $t=0$, the k -space position corresponds to the integral over the applied gradient waveform. On the other hand, the k -space trajectory always ends at the k -space center. (a) The trajectory starts at the $k_{z,a}$ position corresponding to the integral over the gradient shape and ends at $k_z = 0$. (b) the trajectory starts at $k_{z,b} = \frac{1}{2}k_{z,a}$, then goes to $k_{z,2} = -k_{z,b}$ and finishes at $k_z = 0$.

areas under the positive and negative lobes are identical) and finishes at $k_z = 0$. The second example illustrates a more symmetric k -space weighting from the sinc pulse.

3.1.2 Design at high tip angle

A very widespread method used to design slice selective RF pulses at high tip angle is the Shinnar-Le Roux algorithm proposed in 1989 [45]. Its principle will be explained hereafter. It was shown in section 2.2.6 that the effect of a gradient or an RF pulse can be described by 3×3 rotation matrices $\mathbf{T}_x(\alpha)$ and $\mathbf{T}_z(\Phi)$ such that the magnetization state after an RF pulse, \mathbf{M}^+ , can be expressed as a function of its state before the pulse, \mathbf{M}^- , as

$$\mathbf{M}^+ = \mathbf{R}\mathbf{M}^- \quad (3.20)$$

The rotation matrix \mathbf{R} representing the effect of n RF pulses and gradients is given by the product of individual matrices

$$\mathbf{R} = \mathbf{T}_x^n(\alpha)\mathbf{T}_z^n(\Phi)\dots\mathbf{T}_x^1(\alpha)\mathbf{T}_z^1(\Phi) \quad (3.21)$$

Following group theory [46], a three dimensional rotation can be represented by a 2×2 matrix \mathbf{Q} of which elements are called the Cayleigh-Klein parameters α and β

$$\mathbf{Q} = \begin{pmatrix} \alpha & -\beta^* \\ \beta & \alpha^* \end{pmatrix} \quad (3.22)$$

Similarly to \mathbf{T} matrices that act on 3D complex vectors, \mathbf{Q} matrices act on 2D complex vectors called spinors which are elements of the $SU(2)$ group (special unitary group of degree 2). Matrices belonging to this group are unitary and their determinant is 1, meaning that

$$\alpha\alpha^* + \beta\beta^* = 1 \quad (3.23)$$

This relationship guarantees that the length of the magnetization vector is preserved during a rotation.

According to the description made by Jaynes in [47], the Cayleigh-Klein parameters describing a rotation of angle ϕ about an axis defined by the direction $\vec{n} = (n_x, n_y, n_z)^T$ are given by

$$\begin{aligned} \alpha &= \cos(\phi/2) - in_z \sin(\phi/2) \\ \beta &= -i(n_x + in_y) \sin(\phi/2) \end{aligned} \quad (3.24)$$

If n rotations are involved, the total rotation is described by the \mathbf{Q}^{Tot} matrix

$$\mathbf{Q}^{Tot} = \begin{pmatrix} \alpha & -\beta^* \\ \beta & \alpha^* \end{pmatrix} = \mathbf{Q}_n \dots \mathbf{Q}_j \dots \mathbf{Q}_0 = \begin{pmatrix} \alpha_n & -\beta_n^* \\ \beta_n & \alpha_n^* \end{pmatrix} \dots \begin{pmatrix} \alpha_j & -\beta_j^* \\ \beta_j & \alpha_j^* \end{pmatrix} \dots \begin{pmatrix} \alpha_0 & -\beta_0^* \\ \beta_0 & \alpha_0^* \end{pmatrix} \quad (3.25)$$

Since the 2x2 matrices can be determined by the entries appearing on their first column (the second one is simply obtained by calculating the complex conjugate values of the first), no information loss occurs if the matrix-matrix products are replaced by matrix-vectors products

$$\begin{aligned} \begin{pmatrix} \alpha & -\beta^* \\ \beta & \alpha^* \end{pmatrix} &= \begin{pmatrix} \alpha_n & -\beta_n^* \\ \beta_n & \alpha_n^* \end{pmatrix} \dots \begin{pmatrix} \alpha_j & -\beta_j^* \\ \beta_j & \alpha_j^* \end{pmatrix} \dots \begin{pmatrix} \alpha_0 & -\beta_0^* \\ \beta_0 & \alpha_0^* \end{pmatrix} \equiv \\ &\begin{pmatrix} \alpha \\ \beta \end{pmatrix} = \begin{pmatrix} \alpha_n & -\beta_n^* \\ \beta_n & \alpha_n^* \end{pmatrix} \dots \begin{pmatrix} \alpha_j & -\beta_j^* \\ \beta_j & \alpha_j^* \end{pmatrix} \dots \begin{pmatrix} \alpha_0 \\ \beta_0 \end{pmatrix} \end{aligned} \quad (3.26)$$

Again considering the group theory, the matrix \mathbf{R}^{CK} including the Cayleigh-Klein coefficients α and β is given by

$$\mathbf{R}^{CK} = \begin{pmatrix} (\alpha^*)^2 & -\beta^2 & 2\alpha^*\beta \\ -(\beta^*)^2 & \alpha^2 & 2\alpha\beta^* \\ -\alpha^*\beta^* & -\alpha\beta & \alpha\alpha^* - \beta\beta^* \end{pmatrix} \quad (3.27)$$

With the knowledge of coefficients $(\alpha, \beta)^T$ the magnetization created by an RF pulse and its associated gradients is expressed as

$$\begin{pmatrix} M_{xy} \\ M_{xy}^* \\ M_z \end{pmatrix}^+ = \begin{pmatrix} (\alpha^*)^2 & -\beta^2 & 2\alpha^*\beta \\ -(\beta^*)^2 & \alpha^2 & 2\alpha\beta^* \\ -\alpha^*\beta^* & -\alpha\beta & \alpha\alpha^* - \beta\beta^* \end{pmatrix} \begin{pmatrix} M_{xy} \\ M_{xy}^* \\ M_z \end{pmatrix}^- \quad (3.28)$$

From this system, several particular cases can be observed. Assuming the initial magnetization is positioned along the z direction ($\vec{M}^- = (0, 0, M)^T$), the design of an excitation pulse consists in the optimization of the $2\alpha^*\beta$ term. For an inversion pulse the term $\alpha\alpha^* - \beta\beta^*$ bringing M_0 towards $-M_0$ is of interest. Assuming the magnetization is initially in the state $\mathbf{M}^- = (M_{xy}^-, M_{xy}^{*-}, 0)^T$ the refocusing pulse of a spin echo sequence would be designed by optimizing the $(\alpha^*)^2$ and $-\beta^2$ terms.

The calculation of the Cayleigh-Klein coefficients is thus central for the design of a particular type of RF pulse.

As described in section 2.2.3 the slice selection process is performed by applying an RF pulse simultaneously with a G_z gradient. One key assumption of the Shinnar-Le Roux algorithm is to consider the pulse shape as piece-wise constant over Δt intervals (Fig. 3.2). For a small

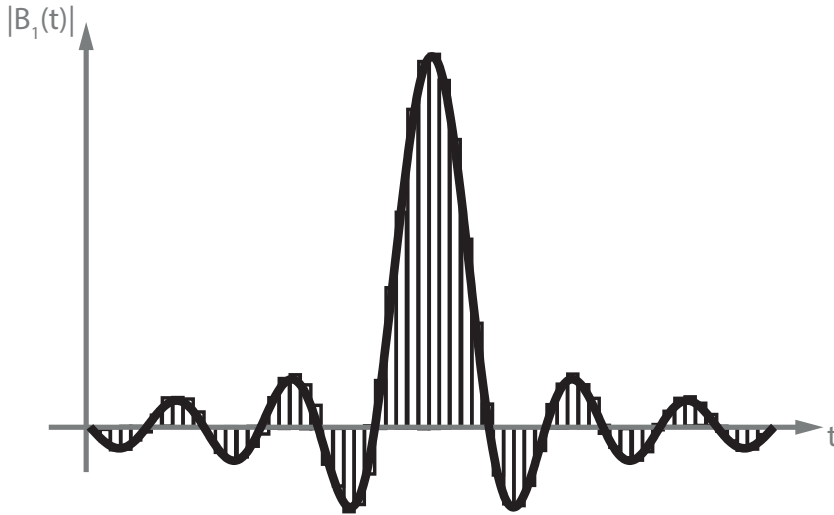


Figure 3.2: Sinc RF pulse considered as piece-wise constant in the SLR process. It is assumed that the length Δt of each rectangle is small enough such that the rotations induced by the RF pulse and gradient can be considered independently during this interval.

enough Δt , the rotation of the magnetization generated by the RF pulse and the gradient during this interval can be decomposed into two sequential rotations represented by matrices \mathbf{Q}^{RF} and \mathbf{Q}^G , respectively. In the RF part, \vec{B}_1 induces a rotation of angle

$$\phi = -\gamma \left| \vec{B}_1 \right| \Delta t \quad (3.29)$$

about the direction

$$\vec{n} = \frac{\gamma \Delta t}{|\phi|} (B_{1,x}, B_{1,y}, 0)^T \quad (3.30)$$

During the gradient evolution, the magnetization at position z is rotated about the z axis by an angle

$$- \gamma G_z z \Delta t \quad (3.31)$$

By inserting the previous expressions in relations (3.22) and (3.24), the \mathbf{Q}^{RF} and \mathbf{Q}^G matrices are given by

$$\mathbf{Q}^{RF} = \begin{pmatrix} \cos(\frac{\gamma |\vec{B}_1| \Delta t}{2}) & ie^{-iz\vec{B}_1} \sin(\frac{\gamma |\vec{B}_1| \Delta t}{2}) \\ ie^{iz\vec{B}_1} \sin(\frac{\gamma |\vec{B}_1| \Delta t}{2}) & \cos(\frac{\gamma |\vec{B}_1| \Delta t}{2}) \end{pmatrix} \quad (3.32)$$

$$\mathbf{Q}^G = \begin{pmatrix} e^{i\gamma G_z z \Delta t / 2} & 0 \\ 0 & e^{-i\gamma G_z z \Delta t / 2} \end{pmatrix} \quad (3.33)$$

The matrix \mathbf{Q}_j describing the rotations generated by the piece wise constant j^{th} segment of the RF and gradient waveforms can be written as

$$\mathbf{Q}_j = \mathbf{Q}_j^{RF} \mathbf{Q}_j^G = \begin{pmatrix} C_j & -S_j^* \\ S_j & C_j \end{pmatrix} \begin{pmatrix} p^{1/2} & 0 \\ 0 & p^{-1/2} \end{pmatrix} \quad (3.34)$$

where

$$\begin{aligned} C_j &= \cos(\gamma |\vec{B}_{1,j}| \Delta t / 2) \\ S_j &= ie^{iz\vec{B}_{1,j}} \sin(\gamma |\vec{B}_{1,j}| \Delta t / 2) \\ p &= e^{i\gamma G_z z \Delta t} \end{aligned} \quad (3.35)$$

Based on equations (3.25) and (3.26), the following recursion over the Cayleigh-Klein coefficients can be set

$$\begin{pmatrix} \alpha_j \\ \beta_j \end{pmatrix} = p^{1/2} \begin{pmatrix} C_j & -S_j^* \\ S_j & C_j \end{pmatrix} \begin{pmatrix} 1 & 0 \\ 0 & p^{-1} \end{pmatrix} \begin{pmatrix} \alpha_{j-1} \\ \beta_{j-1} \end{pmatrix} \quad (3.36)$$

Setting

$$\begin{aligned} \alpha_j &= p^{j/2} A_j \\ \beta_j &= p^{j/2} B_j \end{aligned} \quad (3.37)$$

the recursion becomes

$$\begin{pmatrix} A_j \\ B_j \end{pmatrix} = \begin{pmatrix} C_j & -S_j^* p^{-1} \\ S_j & C_j p^{-1} \end{pmatrix} \begin{pmatrix} A_{j-1} \\ B_{j-1} \end{pmatrix} \quad (3.38)$$

As at the beginning of the pulse ($j=0$) no rotation has yet been performed, the initial Cayleigh-Klein coefficients are obtained by considering $\phi = 0$ in equation (3.24)

$$\begin{pmatrix} \alpha_0 \\ \beta_0 \end{pmatrix} = \begin{pmatrix} 1 \\ 0 \end{pmatrix} \quad (3.39)$$

The first terms of the recursion are thus given by

$$\begin{aligned} \begin{pmatrix} A_1 \\ B_1 \end{pmatrix} &= \begin{pmatrix} C_1 \\ S_1 \end{pmatrix} \\ \begin{pmatrix} A_2 \\ B_2 \end{pmatrix} &= \begin{pmatrix} C_1 C_2 - S_1 S_2^* p^{-1} \\ C_1 S_2 + C_2 S_1 p^{-1} \end{pmatrix} \\ \begin{pmatrix} A_3 \\ B_3 \end{pmatrix} &= \begin{pmatrix} C_1 C_2 C_3 - (C_3 S_1 S_2^* + C_1 S_2 S_3^*) p^{-1} - C_2 S_1 S_3^* p^{-2} \\ C_1 C_2 S_3 - (S_1 S_2^* S_3 - C_1 C_3 S_2) p^{-1} + C_2 C_3 S_1 p^{-2} \end{pmatrix} \end{aligned} \quad (3.40)$$

After n intervals Δt , A and B can be expressed as polynomials of degree $n-1$

$$\begin{aligned} A_n(p) &= \sum_{j=0}^{n-1} a_j p^{-j} \\ B_n(p) &= \sum_{j=0}^{n-1} b_j p^{-j} \end{aligned} \quad (3.41)$$

These results show that the effect of the slice selective RF pulse on the magnetization can be expressed with two $(n-1)$ -order complex polynomials. The amplitude and phase of $\vec{B}_1(t)$ are provided by the different coefficients of the polynomials.

From a pulse design perspective, the goal would be to determine the amplitude and phase of the $\vec{B}_{1,j}$ s that produce the desired polynomials. Considering the design of a pulse inducing a $\pi/2$ rotation about the x axis, equation (3.24) implies that the ideal polynomial $B_I(p)$ is equal to $i\sqrt{2}/2$ for in-slice positions. For out-of-slice isochromats, since they should not be excited, $B_I(p) = 0$. Given this target, the amplitude and phase of each $\vec{B}_{1,j}$ are then optimized such that the resulting profile, $B_R(p)$, is in accordance with the idealized one, $B_I(p)$. Several tools can be used to design the polynomials according to the expected expressions. Among them, the Parks-McClellan algorithm providing satisfying results is used in [44] for the design of excitation, inversion and refocusing RF pulses.

The Shinnar-Le Roux algorithm making use of the spin domain version of the Bloch equations to reduce the product of 3×3 matrices describing the magnetization evolution into two $(n-1)$ -order polynomials provides an efficient way of designing RF pulses beyond the low tip angle regime. The spin domain framework will be considered again in section 6.1 where the design of k_T -point pulses at high tip angle will be described.

3.2 RF pulse design to correct B_1^+ inhomogeneity

RF pulse design was first proposed to establish well performing slice-selective RF pulses in the low (small tip angle approximation) and high (Shinnar-Le Roux algorithm) flip angle regimes. In this section, different techniques of pulse design proposed to correct the inhomogeneous B_1^+ distribution observed at high field strength will be described.

The transmit magnetic field B_1^+ is the component of B_1 that rotates in the transverse plane in the clockwise sens. For an RF coil in the circularly polarized configuration (cf. section 2.4.3) the B_1 and B_1^+ fields are identical whereas in the case of a linearly polarized B_1 field, only the component rotating clockwise corresponds to B_1^+ . The wavelength λ of the B_1^+ field can be calculated using the formula

$$\lambda f_0 = c/n \quad (3.42)$$

where c is the speed of light, n the refractive index of the medium and f_0 the Larmor frequency. It was shown in section 2.2.1.2 that f_0 is equal to γB_0 which is about 297MHz for 1H atoms at 7T. Larmor frequencies of 64 and 128MHz are respectively observed at 1.5 and 3T. The associated wavelength in the air ($n^{air} \approx 1$) are presented in the following table

B_0 [T]	f_0 [MHz]	λ [m]
1.5	64	4.68
3	128	2.34
7	297	1.01

Figure 3.3 presents a comparison of the wavelengths at different field strengths in respect to the human head. When the coil is loaded with a subject, the B_1^+ field propagates through a medium with $n > 1$. In biological tissues, refractive indexes can be calculated via

$$n(\omega) = \sqrt{\epsilon_r(\omega)} \quad (3.43)$$

where ϵ_r is the material's relative permittivity and ω shows the frequency dependency. For frequencies in the MHz range, $\epsilon_r = 52, 73$ and 84 were respectively reported in the WM, GM and CSF [48]. According to these numbers, an approximative wavelength can be calculated at different field strengths for the brain tissues

B_0 [T]	λ [m]		
	GM	WM	CSF
1.5	0.65	0.55	0.51
3	0.33	0.28	0.25
7	0.14	0.12	0.11

For wavelengths comparable to or smaller than the sample size as it occurs at 7T, the interaction between the transmit field and the tissues (of which dielectric properties vary from

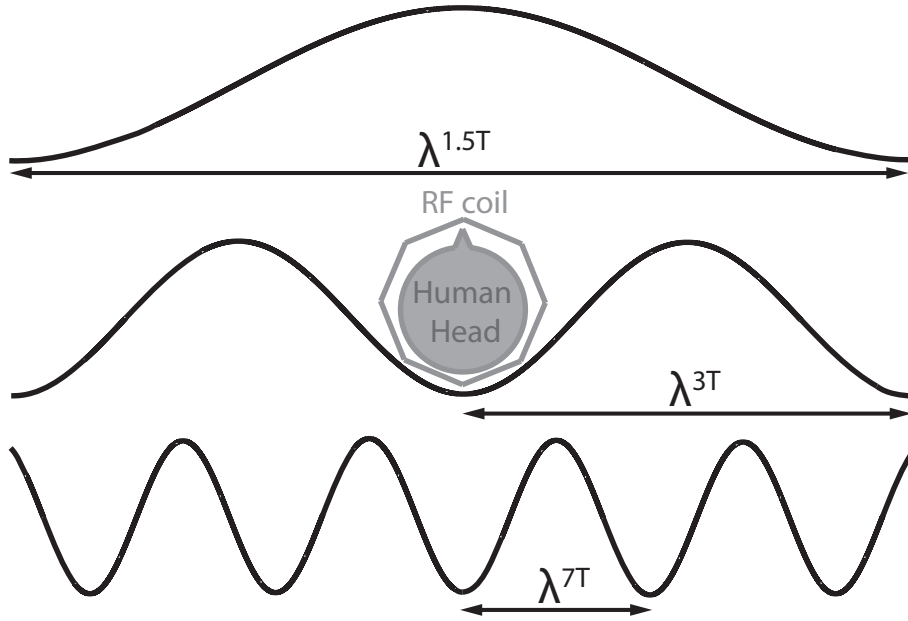


Figure 3.3: Pictorial comparison of the size of the human head with the wavelengths at different field strengths. In this illustration the waveforms were scaled in respect to the head by considering air as the propagating material ($n^{\text{air}} = 1$). It should be noted that when the propagation occurs throughout tissues ($n^{\text{issues}} > 1$), the wavelength at 7T becomes even smaller than the head size.

one to the other) becomes strong enough to make the B_1^+ distribution position dependent. Such an inhomogeneous B_1^+ profile across the sample is an essential source of error for image interpretation.

In general, pulse design techniques addressing the B_1^+ inhomogeneity issue are based on the knowledge of the B_1^+ distribution across the sample which is measured using an appropriate mapping technique. The concept of B_1^+ -mapping will be extensively discussed in chapter 4.

3.2.1 B_1^+ -mapping and the unit transformation

It was chosen in this thesis to consider the magnitude of the B_1^+ field as a multiplicative factor of a nominal flip angle α^{nom} . This means that for an RF pulse of flip angle α^{nom} , if $|B_1^+(\vec{r}_i)| = 0.5$, the actual flip angle that will be applied at position \vec{r}_i is equal to $0.5 \cdot \alpha^{\text{nom}}$. In other works [49, 50], expressing B_1^+ maps in $\mu\text{T}/V$ or Gauss units is preferred. This section explains how B_1^+ expressed as a multiplicative factor of α^{nom} can be transformed into $\mu\text{T}/V$ units.

Starting from equation (2.30), the flip angle α (in radians) generated by a hard pulse of duration T and amplitude B_1 is given by

$$\alpha = 2\pi\gamma B_1 T \quad (3.44)$$

At the beginning of an MR experiment, the reference RF voltage V is calibrated such that a $500\mu\text{s}$ hard pulse generates a $\pi/2$ rotation. Plugging those numbers in the previous equation and dividing by the reference voltage provides

$$\frac{500}{\gamma V} \left[\frac{T}{V} \right] = B_1 \quad (3.45)$$

This relationship indicates to how much T/V or $\mu T/V$ a value of $B_1^+ = 1$ corresponds. Multiplying a B_1^+ map expressed as multiplicative values of α^{nom} by the left member of the last equation thus provides a B_1^+ profile with $\mu T/V$ units.

3.2.2 Spokes and k_T -points

Based on the STA approximation, RF pulse design techniques were developed to correct the B_1^+ inhomogeneity occurring at high field strength. Slice selective RF pulses exciting specific $k_x - k_y$ segments and known under the name of "spokes" [29] or "fast- k_z " [30] were first proposed to perform an homogeneous excitation in a two-dimensional field of view. Following the same formalism, k_T -point pulses [36] exciting optimized k_x , k_y and k_z positions were introduced to obtain a corrected three-dimensional excitation profile.

The most common methodology behind spoke and k_T -point pulse designs will be described hereafter.

3.2.2.1 Spokes

As mentioned earlier, the design of RF pulses correcting B_1^+ inhomogeneities requires the knowledge of the B_1^+ profile over the sample. Several methodologies used to perform B_1^+ -mapping will be described in chapter 4. For now, it can be assumed that the transmit field profile $\vec{B}_1^+(\vec{r})$, also referred to as the transmit sensitivity of the coil, $S(\vec{r})$, is known. As explained in the previous section, $\vec{B}_1^+(\vec{r})$ or $S(\vec{r})$ can be expressed as a multiplicative factor of the expected flip angle α^{nom} . To have a better description of the spin system, this spatial quantity (which is complex) must be taken into account in equations (3.16) and (3.17) as a term multiplying $\gamma B_{1,xy}(t)$

$$\begin{aligned} M_{xy}(t, \vec{r}) &= iM_0 \int_0^t S(\vec{r}) \gamma B_{1,xy}(\tau) e^{-2\pi i \vec{k}(\tau) \cdot \vec{r}} d\tau \\ d(x, y) &= iM_0 \sum_{t=1}^T S(x, y) \gamma B_{1,xy}(t) e^{-2\pi i (k_x(t)x + k_y(t)y)} \end{aligned} \quad (3.46)$$

A spoke pulse [29] in its whole can be seen as a series of slice selective pulses applied at different k-space locations such that the resulting excitation profile is as uniform as possible. When using the STA regime for the design of spoke pulses, the Fourier relationship between

the RF waveforms and $M_r(t, \vec{r})$ can be considered. The slice selectivity part can thus be obtained using sinc pulses coupled with appropriate G_z gradients (Fig. 3.4a). Relation (3.15)

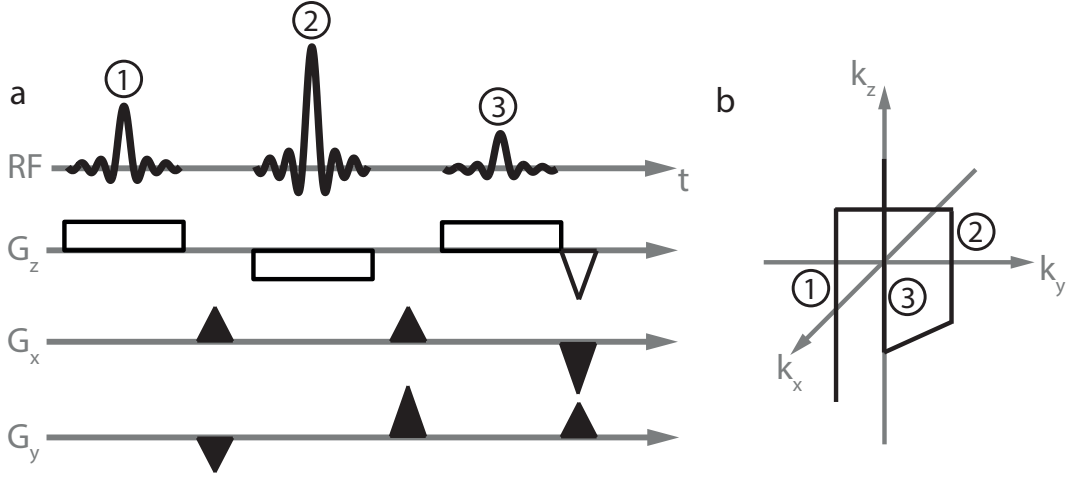


Figure 3.4: (a) Set of sinc sub-pulses and gradients defining a spoke RF pulse. Each sinc sub-pulse and G_z gradient pair defines a slice-selective excitation of a $k_x - k_y$ position. The G_x and G_y gradient blips are used to move from one optimized $k_x - k_y$ location to the next. (b) Excited k -space trajectory characterizing the spoke pulse in (a). Note that the trajectory ends at k -space center.

implies that applying G_z for a certain duration corresponds to exciting a straight line (spoke) along k_z (Fig. 3.4b). The different sinc pulses in a spoke pulse are applied with optimized amplitudes and phases at specific (k_x, k_y) positions defining a weighted k -space trajectory. The challenge in spoke design thus consists in finding the optimal amplitudes and phases of the different RF pulses as well as the k -space positions where they should be applied in order to produce an homogeneous excitation pattern over the sample.

When designing a pulse with N spokes the discretized equation in (3.46) can be rewritten as

$$d(x, y) = iM_0 \sum_{n=1}^N S(x, y) \gamma \beta(n) e^{-2\pi i(k_x(n)x + k_y(n)y)} \quad (3.47)$$

where the $(k_x(n), k_y(n))$ corresponds to the position of the n^{th} spoke ($n \in [1, N]$) and $\beta(n)$ represents the amplitude and phase of the n^{th} sinc pulse. Writing the previous equation in the same way as in (3.18), the following optimization problem can be considered

$$d = \underset{\vec{k}, \beta}{\operatorname{argmin}} \left\{ \left\| |A(\vec{k})\beta| - d \right\|_2^2 + \lambda \|\beta\|_2^2 \right\} \quad (3.48)$$

where d is an $M \times 1$ column vector corresponding to the targeted excitation profile for the M voxels belonging to the 3D mask inside which the optimization is performed. β is an $N \times 1$ column vector and A is an $M \times N$ matrix of which elements are given by:

$$A_{m,n} = S(x_m, y_m) e^{-2\pi i(k_x(n)x_m + k_y(n)y_m)} \quad (3.49)$$

with (x_m, y_m) defining the position of pixel m ($m \in [1, M]$). The Lagrangian multiplier λ in equation (3.48) is introduced to constrain the amount of power deposited in the sample. The part into curved brackets in equation (3.48) defines the cost function to minimize. It will be explained in section 3.3.3 why the magnitude of the designed excitation profile represented by the $|A\beta|$ term in equation (3.48) was considered.

Both \vec{k} and β variables are involved in the optimization problem. Determining the k-space positions of the spokes is usually the cumbersome part of the process since this cannot be performed by solving a linear problem. Several methods have been proposed to choose the \vec{k} vector associated with the most homogeneous excitation profile :

(a) The simplest approach is based on the calculation of the inverse Fourier transform of the targeted profile. The N k-space positions in the Fourier domain with the largest magnitudes are selected for the placement of the spokes.

(b) Another method is to use the sequential optimal selection of spokes (SOLO) algorithm [35]. Starting from an empty set, the algorithm goes through a 2D discretized k-space grid defining the k_x and k_y possibilities and finds the position minimizing the cost function. Since the B_1^+ variations observed at high field strengths remain in the low frequency domain, the size of the visited grid can be restricted to a small portion of the entire k-space.

At the n^{th} iteration, the algorithm optimizes a new spoke position while discarding the $n-1$ previously optimized ones from the grid. After N steps, the entire k-space trajectory is known and the problem given in equation (3.48) is reduced to the optimization of the β vector.

3.2.2.2 k_T -points

To extend the B_1^+ inhomogeneity correction to three-dimensional volumes, k_T -point pulses can be designed. The term k_T refers to the transmission k-space. It was shown that a spoke pulse excites a 2D weighted trajectory in the (k_x, k_y) space. In the same way, a k_T -point pulse excites a 3D trajectory in the (k_x, k_y, k_z) space. As they are exciting a 3D volume, non-selective hard sub-pulses are used in a k_T -point pulse (Fig. 3.5a). Gradient blips are introduced in the z direction since k_z positions now represent an optimization parameter. The set of sub-pulses and gradient blips defines a weighted three-dimensional k-space trajectory (Fig. 3.5b) optimized to produce the desired excitation pattern.

Taking the third dimension into account, equation (3.47) can be rewritten as

$$d(x, y, z) = iM_0 \sum_{n=1}^N S(x, y, z) \gamma \beta(n) e^{-2\pi i(k_x(n)x + k_y(n)y + k_z(n)z)} \quad (3.50)$$

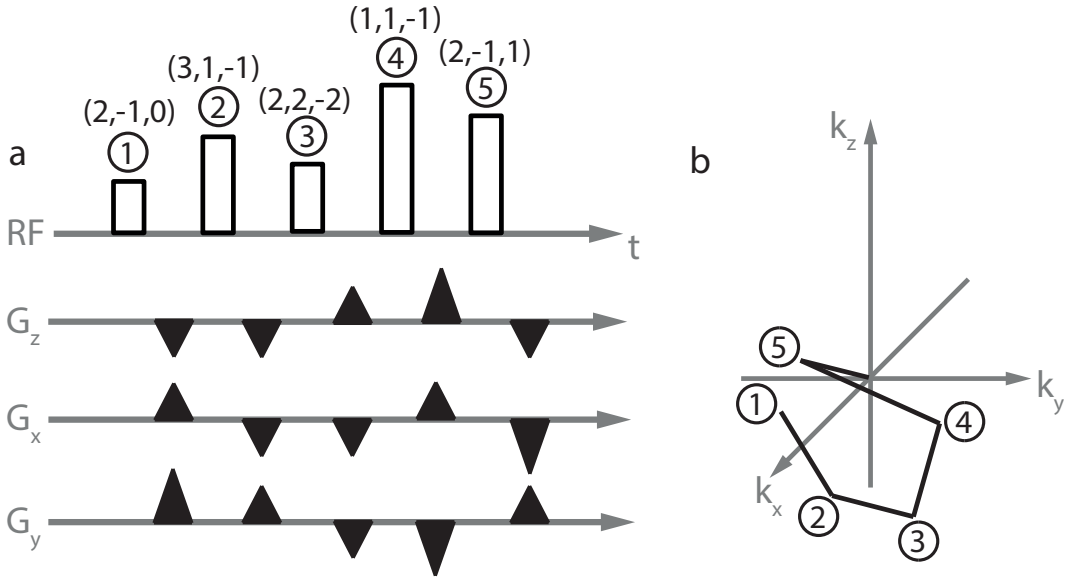


Figure 3.5: (a) Set of hard sub-pulses and gradient blips defining a k_T -point RF pulse. The sub-pulses indicate the amount of RF energy deposited at each location of the k -space trajectory defined by the gradient blips. (b) Excited k -space trajectory characterizing the k_T -point pulse in (a). Note that the trajectory ends at k -space center.

The form of the optimization problem presented in (3.48) remains unchanged but determining the optimal k -space positions becomes more demanding since the possibilities for \vec{k} now extend over a 3D space. The techniques presented for the determination of the spoke positions (inverse Fourier transform, SOLO algorithm) can also be applied to find the optimal k_T -point positions.

3.3 Parallel transmission

Parallel transmission (PTx) was roughly described in section 2.4.3.1 where the PTx system was presented. The current section starts with the introduction of the superposition principle which is central in PTx. From it, the STA approximation formalism will be extended to PTx such that the design of spoke and k_T -point pulses via a linear system of equations remains valid for a multichannel system.

For PTx applications, the knowledge of the transmit sensitivities generated by the different array elements $B_{1,c}^+(\vec{r})$ is fundamental. The methodology used in this thesis for the acquisition of the $B_{1,c}^+(\vec{r})$ distributions will thus be presented.

As described at the beginning of section 3.2, one of the main issues with high field MRI is the inhomogeneous distribution of the B_1^+ field. In the early days of PTx, multichannel transmit coils were developed such that the amplitude and phase of each element can be adjusted in order to correct for the B_1^+ inhomogeneity. This method called RF shimming [51, 52] will

also be introduced. After that, an evaluation of the impact of volume vs slice based RF shimming on the reduction of the B_1^+ inhomogeneity across the brain at 7T will be presented. The major breakthrough in PTx happened when transmit SENSE [38] was proposed. A new degree of freedom is provided by this technique where, instead of modifying the amplitude and phase of the transmitting elements (while applying identical waveforms), the entire time course of the RF pulses is designed for each channel. As it offers the framework for the design of RF pulses providing an excellent B_1^+ inhomogeneity compensation at high field strengths (cf. chapter 5), the transmit SENSE technique will be described at the end of the current section.

3.3.1 Superposition principle

The current section starts with the introduction of the superposition principle which is central in PTx.

In PTx, the superposition principle implies that the profile of the transmit magnetic field produced by an array with C transmitting channels is given by

$$B_1^+(\vec{r}) = \sum_{c=1}^C B_{1,c}^+(\vec{r}) \quad (3.51)$$

where the sum is done over the complex individual $B_{1,c}^+(\vec{r})$ profiles ($c \in [1, C]$) generated by the different array elements. Figure 3.6 shows the results for the PTx system with C=8 channels used in this thesis.

The superposition principle plays a central role in every PTx applications. This can be illustrated by considering again equation (3.16) established in the STA regime

$$M_{xy}(T, \vec{r}) = iM_0 B_1^+(\vec{r}) \int_0^T \gamma b_1(t) e^{-2\pi i \vec{k}(t) \cdot \vec{r}} dt \quad (3.52)$$

where the inhomogeneity in the transmit magnetic field characteristic at high B_0 strength was taken into account by adding the coil sensitivity $B_1^+(\vec{r})$ term. As a reminder, this equation implies that the excited transverse magnetization profile results from a k-space trajectory weighted by an RF waveform $b_1(t)$. Now if each array element applies its own waveform $b_{1,c}(t)$ such that it weights the k-space trajectory in a specific way, C different transverse magnetization profiles $M_{xy,c}(T, \vec{r})$ are generated. From the superposition principle, the magnetization excited by the entire array is given by

$$M_{xy}(T, \vec{r}) = \sum_{c=1}^C M_{xy,c}(T, \vec{r}) = i\gamma M_0 \sum_{c=1}^C B_{1,c}^+(\vec{r}) \int_0^T b_{1,c}(t) e^{-2\pi i \vec{k}(t) \cdot \vec{r}} dt \quad (3.53)$$

where $B_{1,c}^+(\vec{r})$ are the sensitivities of the different array elements.

The previous expression was first presented by Grissom [37] and subsequently used for the

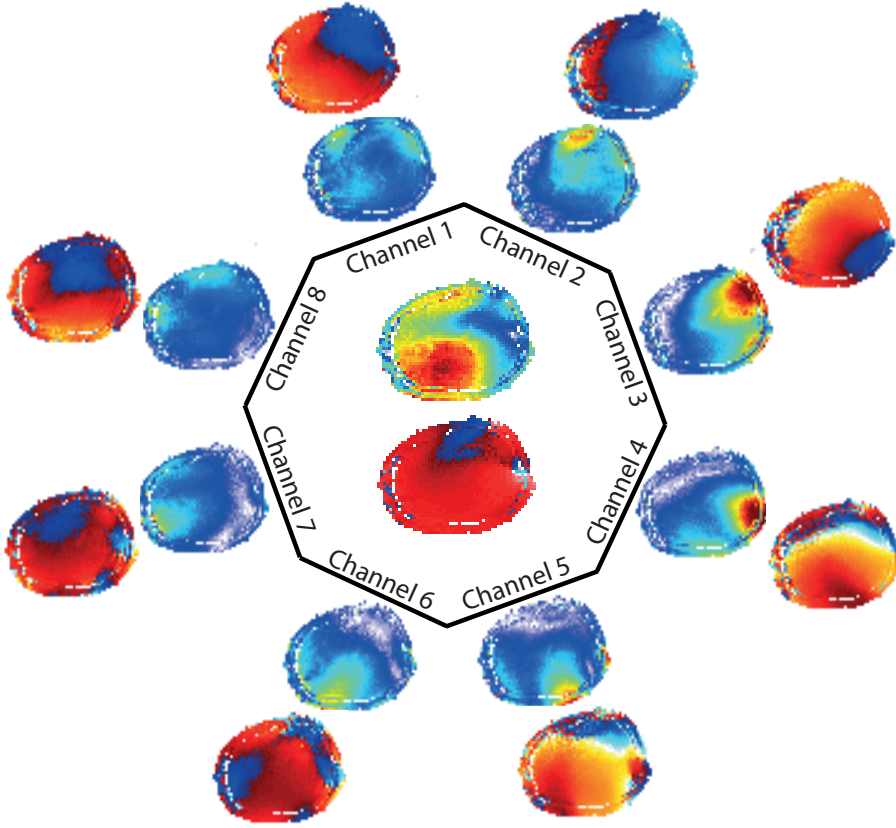


Figure 3.6: Illustration of the superposition principle in PTx for an eight channel transmit-receive octahedral array. The central magnitude and phase profiles of the B_1^+ field are obtained by summing the complex distributions generated by the different array elements. The inner circle out of the array presents the amplitudes of the individual $B_{1,c}^+$ profiles while their phases are shown on the outer circle. The colors in phase maps correspond to a $[-\pi, \pi]$ interval. For the magnitude profiles the significance of the scale used will be described in chapter 4. The methodology used to obtain the individual $B_{1,c}^+$ distributions will be described in the next section.

design of spokes and k_T -points on parallel transmit systems [29, 35, 36]. As will be shown in chapter 5, equation (3.53) will be considered for the design of k_T -point pulses used in a TSE sequence in order to improve the quality of T_2 -weighted images at 7T.

3.3.2 Time efficient methods for B_1^+ -mapping

As mentioned earlier, the knowledge of the transmit sensitivities generated by the different array elements $B_{1,c}^+(\vec{r})$ is required for PTx applications. In this thesis, the methodology used to measure the B_1^+ field generated by each transmitter was mainly based on the approach proposed in [33]. Quantitative B_1^+ profiles provided by the SA2RAGE sequence were thus combined with relative B_1^+ maps acquired with a FLASH sequence in order to get rid of the image parameters not related to the B_1^+ field. As explained in chapter 4, the SA2RAGE sequence provides the distribution of the B_1^+ field over the region of interest. A SA2RAGE acquisition with every array elements transmitting thus generates the B_1^+ profile resulting

from the superposition of all individual fields

$$B_{1,SA2RAGEAll}^+ = \sum_{k=1}^C \left| \vec{B}_{1,k}^+(\vec{r}) \right| e^{i\phi_k^+(\vec{r})} \quad (3.54)$$

where the k index is used to refer to the different transmitters and $\phi_k^+(\vec{r})$ corresponds to the phase of the transmit magnetic field $\angle \vec{B}_{1,k}^+(\vec{r})$ for the k^{th} element.

A FLASH (Fast Low Angle SHots) sequence corresponds to a train of identical RF pulses with low flip angle α .

A simple analytical expression for the signal throughout the sequence can be established if only the longitudinal magnetization survives from one RF pulse to the other. To fulfill this criterion, strong dephasing gradients applied between the pulses after the signal encoding step are combined with RF spoiling such that the remaining transverse magnetization averages out to zero. Another option would be to use a gap between the pulses much larger than T_2 which is not time efficient.

When several RF pulses of flip angle α are applied in succession, at some point, a steady state magnetization, $m_{z,ss}$ is reached. This means that before the pulse n, the magnetization retrieves the value it had before pulse n-1. After an RF pulse α^{nom} , the longitudinal and transverse magnetization become

$$\begin{aligned} M_z(O^+) &= m_{z,ss} \cdot \cos(\alpha^{nom} |B_1^+(\vec{r})|) \\ M_{xy}(O^+) &= m_{z,ss} \cdot \sin(\alpha^{nom} |B_1^+(\vec{r})|) \cdot e^{i\phi^+(\vec{r})} \end{aligned} \quad (3.55)$$

The fact that the inhomogeneous B_1^+ field increases or lowers the nominal value of the flip angle was considered. The phase of the B_1^+ field $\phi^+(\vec{r})$ was also taken into account.

Defining the period between two pulses as TR^{FLASH} and considering equation (2.35), the longitudinal magnetization before the next RF pulse is

$$M_z(TR^{FLASH}) = M_0 + (m_{z,ss} \cdot \cos(\alpha^{nom} |B_1^+(\vec{r})|) - M_0) e^{-TR^{FLASH}/T_1} = m_{z,ss} \quad (3.56)$$

The last equality was set by considering that \vec{M} comes back to the steady state at the end of the TR^{FLASH} period. Isolating $m_{z,ss}$ from the last equation provides

$$m_{z,ss} = M_0 \frac{1 - e^{-TR^{FLASH}/T_1}}{1 - \cos(\alpha^{nom} |B_1^+(\vec{r})|) e^{-TR^{FLASH}/T_1}} \quad (3.57)$$

Considering equation (3.55), the echo signal S occurring at time TE after each RF pulse can be written as

$$S(TE) = M_0 \frac{\sin(\alpha^{nom} |B_1^+(\vec{r})|) (1 - e^{-TR^{FLASH}/T_1})}{1 - \cos(\alpha^{nom} |B_1^+(\vec{r})|) e^{-TR^{FLASH}/T_1}} e^{i\phi^+(\vec{r})} |B_1^-(\vec{r})| e^{i\phi^-(\vec{r})} e^{-TE/T_2^*} \quad (3.58)$$

where the receive sensitivity of the coil, characterized by the term $|B_1^-(\vec{r})| e^{i\phi^-(\vec{r})}$ was taken into account. In the last expression, the T_2^* decay during the TE period was also considered. In general, the arrays used in PTx are used for both transmission and reception. This implies that the C array elements play the role of transmitters and receivers. Hereafter, the k index will be kept to refer to the different transmitters, whereas j will be used for the receivers. Therefore, the signal recorded by the j^{th} receiver when the k^{th} transmitter sent an RF waveform, $S_{k,j}$, can be expressed as

$$S_{k,j} = M_0 \frac{\sin\left(\alpha^{nom} \left| B_{1,k}^+(\vec{r}) \right| \right) \left(1 - e^{-TR^{FLASH}/T_1} \right)}{1 - \cos\left(\alpha^{nom} \left| B_{1,k}^+(\vec{r}) \right| \right) e^{-TR^{FLASH}/T_1}} e^{i\phi_k^+(\vec{r})} \left| B_{1,j}^-(\vec{r}) \right| e^{i\phi_j^-(\vec{r})} e^{-TE/T_2^*} \quad (3.59)$$

If α^{nom} is in the low tip angle regime, the previous equation becomes

$$S_{k,j} \approx M_0 \cdot \alpha^{nom} \left| B_{1,k}^+(\vec{r}) \right| e^{i\phi_k^+(\vec{r})} \left| B_{1,j}^-(\vec{r}) \right| e^{i\phi_j^-(\vec{r})} e^{-TE/T_2^*} \quad (3.60)$$

When only transmitter k is active, the sum over the signals acquired by the different receivers is

$$FLASH^k = \sum_{j=1}^C S_{k,j} = M_0 \cdot e^{-TE/T_2^*} \cdot \alpha^{nom} \left| B_{1,k}^+(\vec{r}) \right| e^{i\phi_k^+(\vec{r})} \sum_{j=1}^C \left| B_{1,j}^-(\vec{r}) \right| e^{i\phi_j^-(\vec{r})} \quad (3.61)$$

On the other hand, if all transmitters are active, the sum over the receivers becomes

$$FLASH^{All} = \sum_{j=1}^C \sum_{k=1}^C S_{k,j} = M_0 \cdot e^{-TE/T_2^*} \cdot \alpha^{nom} \sum_{k=1}^C \left| B_{1,k}^+(\vec{r}) \right| e^{i\phi_k^+(\vec{r})} \sum_{j=1}^C \left| B_{1,j}^-(\vec{r}) \right| e^{i\phi_j^-(\vec{r})} \quad (3.62)$$

Combining the two last equations allows the suppression of several terms and particularly the receive sensitivity of the array $B_1^-(\vec{r})$

$$\frac{FLASH^k}{FLASH^{All}} = \frac{\left| B_{1,k}^+(\vec{r}) \right| e^{i\phi_k^+(\vec{r})}}{\sum_{k=1}^C \left| B_{1,k}^+(\vec{r}) \right| e^{i\phi_k^+(\vec{r})}} \quad (3.63)$$

By mixing this last result with equation (3.54), the B_1^+ field generated by the k^{th} transmitter can be obtained

$$B_{1,SA2RAGE}^{+All} \frac{FLASH^k}{FLASH^{All}} = \left| B_{1,k}^+(\vec{r}) \right| e^{i\phi_k^+(\vec{r})} \quad (3.64)$$

In summary, the individual B_1^+ profiles of the different array elements can be calculated from one SA2RAGE acquisition with every transmitters active and C+1 FLASH measurements: one with every transmitters active and C where the elements are transmitting one by one. It could be thought that performing C SA2RAGE acquisition with only one transmitter active at a time would represent an easier way of acquiring the individual B_1^+ profiles of the

array elements. The advantage of the presented methodology is that the acquisition of C FLASH 3D images can be done in a few seconds whereas several minutes would be necessary for C SA2RAGE measurements.

The individual profiles displayed on figure 3.6 were not obtained by acquiring the C FLASH images with only one element active, but C modes were excited instead, following the interferometry technique proposed in [53]. A mode is a specific configuration of the array transmitters. For example, the CP mode corresponds to the configuration where all transmitters are active with a phase shift of $2\pi/C$ existing from one to the next. The mode considered for the mapping of the individual B_1^+ profiles is named "AllBut1,m" and corresponds to the configuration where all array elements are active, but transmitter m which is off. When acquiring $FLASH^{AllBut1,m}$ instead of $FLASH^k$, the result of equation (3.64) becomes $\vec{B}_{1,m}^+(\vec{r})$ which is from the principle of superposition, the sum over the $\vec{B}_{1,k}^+(\vec{r})$ profiles, for which $k \neq m$. If the measurements of the C Allbut1,m modes ($m \in [1,C]$) are performed, the individual distributions $\vec{B}_{1,k}^+(\vec{r})$ and those of the modes $\vec{B}_{1,m}^+(\vec{r})$ are linked via the system of equations

$$\mathbf{B}_{1,m}^+ = A\mathbf{B}_{1,k}^+ \quad (3.65)$$

where the C components of $\mathbf{B}_{1,m}^+$ are the $\vec{B}_{1,m}^+(\vec{r})$ profiles and $\mathbf{B}_{1,k}^+$ contains the individual $\vec{B}_{1,k}^+(\vec{r})$. The previous equation is not only valid for the AllBut1 mode, but for any configuration of the array, as long as the A matrix is correctly adapted. For the AllBut1,m configuration, the A matrix takes the form

$$A^{C \times C} = \text{Ones}^{C \times C} - I^{C \times C} \quad (3.66)$$

where $\text{Ones}^{C \times C}$ is a matrix with C lines and C columns of ones whereas $I^{C \times C}$ is the identity matrix. If a phase combination generating signal coherence in the brain center and avoiding severe destructive interferences was considered, phase terms were included in the A matrix. From equation (3.65), the individual B_1^+ profiles can be calculated using

$$\mathbf{B}_{1,k}^+ = A^{-1}\mathbf{B}_{1,m}^+ \quad (3.67)$$

Figure 3.7 shows the $B_{1,m}^+$ distributions of the different AllBut1,m modes acquired for a particular subject and the associated individual profiles $B_{1,k}^+$ obtained by using equation (3.67). When the individual profiles are acquired with only one active element at a time, noisy regions are observed far from the transmitter locations where the B_1^+ field is low. This is because the B_1^+ field cannot be measured precisely under a certain threshold (cf. chapter 4). As shown on figure 3.7, the advantage of using the AllBut1,m mode is that the resulting $\vec{B}_{1,m}^+$ do not contain any region under the threshold. From such profiles, equation (3.67) provides individual distributions with well defined regions of low B_1^+ field (Fig. 3.7).

Of course, a higher voltage could be used when transmitting with only one transmitter at a time in order to generate a higher B_1^+ field in the critical areas. This would be a bad option

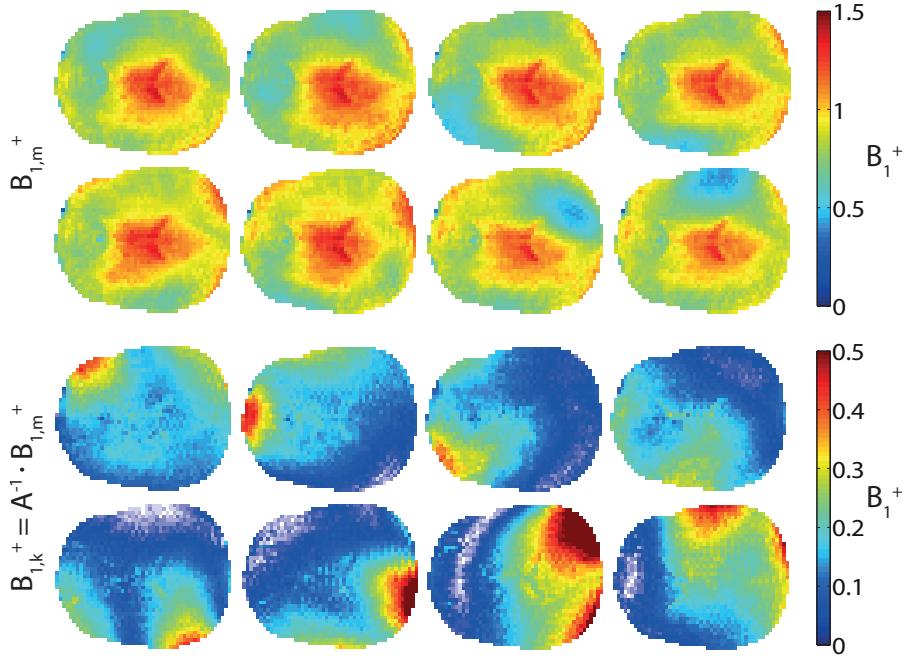


Figure 3.7: B_1^+ profiles of the different AllBut1,m modes (top two rows) and the individual distributions (bottom rows) calculated using equation (3.67). For the sake of simplicity, only the magnitude maps of B_1^+ are presented here.

since the SAR would increase and because the accuracy and precision of quantitative B_1^+ mapping is only guaranteed under a given maximal threshold (cf. chapter 4).

It should be noted that a large number of configurations can be used to obtain the individual profiles of the array elements. This was investigated more intensively in [54].

3.3.3 RF Shimming

The idea of RF or B_1^+ shimming [55] is to optimize the amplitude and phase of each array element in order to make the B_1^+ distribution as homogeneous as possible over the region of interest. A complex number $x_k = |x_k|e^{i\phi_k}$ is attributed to transmitter k ($k \in [1, C]$) to describe its amplitude $|x_k|$ and phase ϕ_k . From the principle of superposition, the B_1^+ field generated at position \vec{r}_p is given by

$$\sum_{k=1}^C B_{1,k}^+(\vec{r}_p) |x_k| e^{i\phi_k} = b(\vec{r}_p) \quad (3.68)$$

A similar equation can be written for the P voxels belonging to the region where the B_1^+ inhomogeneity correction is desired. Defining \mathbf{x} as the vector of which components are the

amplitudes and phases of the different array elements

$$\mathbf{x} = \begin{bmatrix} |x_1|e^{i\phi_1} \\ \vdots \\ |x_C|e^{i\phi_C} \end{bmatrix} \quad (3.69)$$

and M as a matrix with the C columns corresponding to the $B_{1,k}^+$ profiles of the transmitters and the P lines associated with the voxel positions, their product is a P by 1 vector with complex components containing the magnitudes and phases of the total B_1^+ field generated by the array over the region of interest

$$M\mathbf{x} = \mathbf{b} \quad (3.70)$$

The \mathbf{x} vector can thus be optimized such that the targeted field represented by \mathbf{b} is generated. This can be done by calculating M^+ , the Moore-Penrose pseudo inverse [56] of M (as M is generally not a squared matrix). From the previous relation, the optimized set of amplitudes and phases of the array elements is calculated using

$$\mathbf{x} = M^+\mathbf{b} \quad (3.71)$$

This expression corresponds to the solution of the conventional Least Squares (LS) problem

$$\mathbf{x} = \min \left\{ \|M\mathbf{x} - \mathbf{b}\|_2^2 \right\} \quad (3.72)$$

As in many imaging applications, only the magnitude of images is of interest while the phase profile is relatively unimportant as long as it is slowly varying from one voxel to the other [32], the magnitude profile of the B_1^+ field can be improved at a cost of a less uniform phase profile. Mathematically, this corresponds to finding a solution to the Magnitude Least Squares (MLS) problem

$$\mathbf{x} = \min \left\{ \left\| |M\mathbf{x}| - \mathbf{b} \right\|_2^2 \right\} \quad (3.73)$$

The non-convexity of the MLS optimization implies that a global minimum is not guaranteed. Therefore, the solution found (local minimum) highly depends on the starting conditions. An approach where the best solution is selected from optimizations performed with several starting conditions could be considered but was not attempted in this thesis.

In order to limit the amplitudes of the different array elements to help maintaining the power deposition within the SAR limits, a Tikhonov regularization term λ can be introduced in the previous expression

$$\mathbf{x} = \min \left\{ \left\| |M\mathbf{x}| - \mathbf{b} \right\|_2^2 + \lambda \|\mathbf{x}\|_2^2 \right\} \quad (3.74)$$

The λ parameter can be increased in order to reduce the amount of power deposited on the sample at a cost of a worse homogeneity in the optimized B_1^+ distribution.

The optimizations shown in expression (3.48) and (3.74) present similarities although the variables involved correspond to different entities. This implies that the methodology developed for RF shimming can also be partially used in pulse design. The approach presented here to solve the MLS problem in RF shimming will thus be considered again for the design of k_T -point pulses in the STA regime (cf. chapter 5).

As solving the MLS problem cannot rely on the Moore-Penrose pseudo inverse of M , the iterative phase exchange method proposed in [57] was used. Although several iterations need to be calculated with the phase exchange technique, the operations involved are quite simple and a solution can be found in less than a second.

Figure 3.8 shows the improvement provided by RF shimming on a B_1^+ profile obtained at 7T by transmitting with the same amplitude for all array elements and a phase combination calculated such that the B_1^+ field adds up constructively in the brain center. The target in this

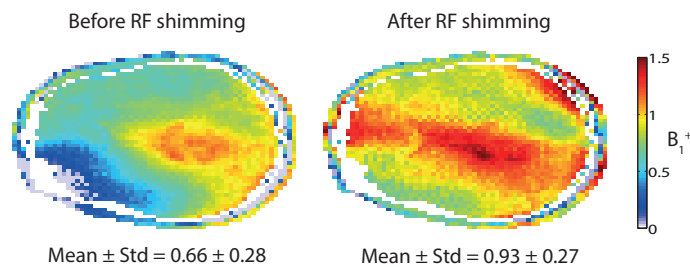


Figure 3.8: B_1^+ profiles across the brain before and after RF shimming. The mean and standard deviation of B_1^+ presented below each map were calculated over the entire brain. The profile on the right shows the characteristic bright spot in the brain center remaining after RF shimming at ultra high field.

optimization was to obtain a uniform profile with $B_1^+ = 1$ for all voxels. In expression (3.74), the vector \mathbf{b} representing the target was thus chosen as having all its components equal to one.

When comparing the ratios std/mean over the brain, a significant improvement of 32% was obtained after RF shimming. This result has to be interpreted carefully since it was calculated from only one subject and also because the result before shimming is highly inhomogeneous.

It can be observed on the map obtained after RF shimming that an intense spot remains in the brain center. This residual inhomogeneity that was also reported by other groups [36, 58] cannot be corrected by using RF shimming as it was described in the current section.

In general, the degree of B_1^+ homogeneity across the brain obtained by performing RF shimming at ultra high field is not sufficient for imaging applications.

In order to improve the results obtained with the standard RF shimming process, a methodology where the optimization of the amplitudes and phases of the array elements is performed on a slab by slab basis, is presented in the next section.

3.3.3.1 Volume vs. slab-based RF shimming

Material and methods

A 7T parallel transmit system (Siemens) equipped with an eight channel transmit-receive RF coil (Rapid biomedical, Germany) was used for the experiment.

Unlike what was presented in section 3.3.2, for this work, the B_1^+ profiles of the array elements were obtained by performing eight SA2RAGE acquisitions of the AllBut1,m modes (no FLASH measurements involved). The individual $\vec{B}_{1,k}^+(\vec{r})$ profiles of the different transmitters were then calculated using equation (3.67).

The following protocol was used for the SA2RAGE sequence: $TR_{SA2RAGE} = 2.4s$, $TR_{flash} = 3ms$, $TD_1 = 104ms$, $TD_2 = 1.8s$, $\alpha_1 = 4^\circ$, $\alpha_2 = 11^\circ$, $n_{PE1} = 64$, $T_1 = 1.5s$.

RF shimming was performed by solving either the LS or the MLS problem presented in expressions (3.72) and (3.73). The novelty brought to standard RF shimming is that instead of optimizing a single set of amplitudes and phases for a thick slab covering the entire brain, different \vec{x} vectors are calculated for several sub-slabs of thickness d (Fig. 3.9). Reducing

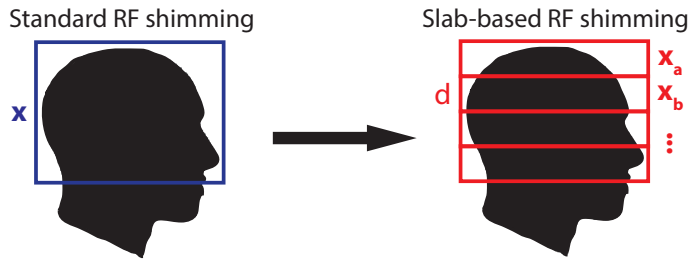


Figure 3.9: Slab based RF shimming consists in subdividing the original large slab (blue) covering the entire brain into several sub-slabs of reduced thickness d (red) for which multiple \vec{x} vectors are calculated.

d implies that the number of slabs needs to be higher in order to perform RF shimming over the same region of interest. The idea is thus to observe if the B_1^+ homogeneity can be improved over the brain by increasing the number of sub-slabs for which \vec{x} vectors are optimized.

Four subjects were scanned and RF shimming was performed over a region of interest (mask) covering the whole brain but with different number of sub-slabs : 1 ($d=60mm$), 2 ($d=30mm$), 4 ($d=15mm$) and 12 ($d=5mm$). In each case, the B_1^+ homogeneity was evaluated by calculating the full width at half maximum (FWHM) of the B_1^+ distribution across the brain.

Results and discussion

Figure 3.10 shows the B_1^+ distributions simulated across the brain when the number of sub-slabs considered in RF shimming is varied. On those results for a particular subject, it can be seen that increasing the number of sub-slabs and therefore the set of optimized amplitudes and phases, tightens the B_1^+ distribution over the region of interest where RF shimming was performed.

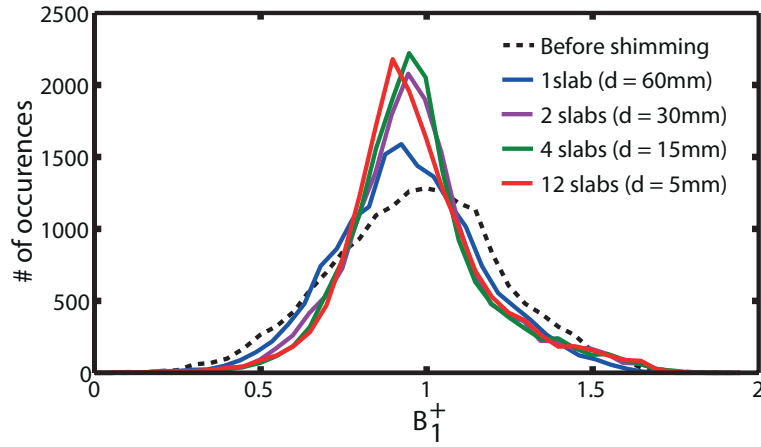


Figure 3.10: Histograms corresponding to the B_1^+ distributions over a 60mm thick region of interest for a particular subject when RF shimming is performed with the MLS optimization. The different histograms were obtained by varying the number of sub-slabs. The dashed line represents the distribution before RF shimming.

The results averaged over the four different subjects are presented in the following table for both LS and MLS optimizations

# of sub-slabs (d [mm])	FWHM of the B_1^+ distribution over the brain	
	Least Squares (LS)	Magnitude Least Squares (MLS)
1 (60)	0.37	0.38
2 (30)	0.32	0.31
4 (15)	0.32	0.30
12 (5)	0.32	0.30

As expected, MLS outperforms the LS optimization. Slab-based RF shimming combined with an MLS optimization thus offers a 21% improvement over the standard RF shimming (one slab). The table also shows that the highest B_1^+ inhomogeneity correction occurs when the number of sub-slabs is increased from one to two. For higher values, the improvement is hardly noticeable.

It should be noted here that the data presented correspond to simulations based on the acquired B_1^+ profiles of the individual transmitters. Those results should be verified experimentally by programming a sequence applying different sets of amplitudes and phases to the parallel transmit array depending on the slab position.

Conclusion

It was demonstrated that the B_1^+ homogeneity across the brain obtained with the standard RF shimming process can be further improved by designing several sets of amplitudes and phases for an eight channel array, depending on the position of the excited magnetization. The proposed methodology could be useful in 2D imaging applications such as DTI and might benefit from systems with a higher number of transmitting elements.

3.3.4 Transmit SENSE and spatial domain method for the design of RF pulses in PTx

The concept of transmit SENSE proposed by Katscher in [38] follows the SENSE principle [59] used in parallel imaging.

In a few words, the idea of SENSE is to accelerate the data acquisition by undersampling the reception k-space. The missing data reconstruction is then performed based on the knowledge of the individual sensitivities of the multiple receive coils.

It was shown in section 3.2.2 that in the low tip angle regime, RF pulses such as spokes and k_T -points can be designed to produce a weighted k-space trajectory representing a specific magnetization profile. In analogy with SENSE, this trajectory in the excitation k-space can be shortened by taking advantage of the knowledge of the spatially varying $\vec{B}_{1,k}^+(\vec{r})$ sensitivities of several transmitting coils. The magnetization profile can be maintained since PTx enables independent weightings of the shortened trajectory by the different transmitters.

In transmit SENSE, the mathematical description for the RF pulse design was performed in the spatial frequency domain. An equivalent approach was proposed by Grissom et al. [37] in the spatial domain. The fundamental relationship proposed in their work and used in this thesis to design k_T -point pulses in the STA regime was derived in section 3.3.1

$$M_{xy}(T, \vec{r}) = \sum_{c=1}^C M_{xy,c}(T, \vec{r}) = i\gamma M_0 \int_0^T \left(\sum_{c=1}^C B_{1,c}^+(\vec{r}) b_{1,c}(t) \right) e^{-2\pi i \vec{k}(t) \cdot \vec{r}} dt \quad (3.75)$$

The interpretation of this equation was that the total transverse magnetization excited within the sample corresponds to the sum over the magnetization profiles generated by the different array transmitters (superposition principle). Another interpretation is that $M_{xy}(T, \vec{r})$ corresponds to the k-space trajectory visited with a field given by the sum over the coil profiles $B_{1,c}^+(\vec{r})$ individually weighted by the RF waveforms $b_{1,c}(t)$.

The extra degree of freedom given by $B_{1,c}^+(\vec{r})$ and $b_{1,c}(t)$ allows the k-space trajectory to be shortened and hence the designed RF pulses can have a reduced sensitivity to T_2^* decay and B_0 inhomogeneities (larger bandwidth). Alternatively, the length of the k-space trajectory can be maintained such that a higher fidelity in the desired magnetization profile is obtained.

The flexibility afforded by PTx makes RF pulse design particularly adapted for the correction of the B_1^+ inhomogeneity at high field.

To design N k_T -point pulses in the STA regime using PTx, the discretized version of equation (3.75) can be considered

$$d(x, y, z) = i\gamma M_0 \sum_{c=1}^C \sum_{n=1}^N B_{1,c}^+(x, y, z) b_{1,c}(n) e^{-2\pi i (k_x(n)x + k_y(n)y + k_z(n)z)} \quad (3.76)$$

Similarly as for equation (3.17), the previous relation can be rewritten as a system of equations

$$\mathbf{d} = A\mathbf{b} \quad (3.77)$$

where \mathbf{d} is an $M \times 1$ column vector representing the transverse magnetization in the region of interest containing M voxels. A is now an $M \times (C \cdot N)$ matrix of which elements are given by

$$A_m^{(n-1)C+c} = i\gamma M_0 B_{1,c}^+(x_m, y_m, z_m) e^{-2\pi i(k_x(n)x_m + k_y(n)y_m + k_z(n)z_m)} \quad (3.78)$$

The vector \mathbf{b} has $C \cdot N$ components containing the complex weights of the N k_T -point sub-pulses for the C transmitters. By considering again the MLS approach and a Lagrangian multiplier to constrain the amount of deposited RF power, the following optimization problem comes out

$$d = \underset{\vec{k}, \beta}{\operatorname{argmin}} \left\{ \left\| |A(\vec{k})\beta| - d \right\|_2^2 + \lambda \|\beta\|_2^2 \right\} \quad (3.79)$$

A modified version of the SOLO algorithm was developed to determine the k_T -point positions whereas the sub-pulse amplitudes and phases were optimized using the phase exchange method (cf. chapter 5).

Considering $\vec{k} = \vec{0}$, $\gamma M_0 = 1$ and the RF waveforms being continuously applied for the different transmitters, equation (3.75) becomes identical to (3.68). RF shimming can thus be interpreted as a particular weighting of the k -space center by the different array elements.

4

B_1^+ -mapping with the SA2RAGE sequence

Adapted from:

Florent Eggenschwiler, Tobias Kober, Arthur W. Magill, Rolf Gruetter and José P. Marques
SA2RAGE: A new sequence for fast B_1^+ -mapping
Magnetic Resonance in Medicine, 67, p.1609-1619, 2012

4.1 SA2RAGE sequence

It was explained in section 3.2 that when dealing with high strengths ($\geq 3T$) of the B_0 field, the transmit magnetic field B_1^+ becomes position dependent due to wavelength effects. The inhomogeneous B_1^+ distribution across the sample is an essential source of error for image interpretation. Measuring the B_1^+ field is thus necessary to identify possible artifacts and to correct them.

It was also mentioned that when designing RF pulses to correct for the B_1^+ inhomogeneity, the knowledge of the B_1^+ profile or coil sensitivity was required, cf. equations (3.47) and (3.50). When presenting PTx applications such as RF shimming or transmit SENSE, it was shown that the acquisition of the individual B_1^+ profiles of the array elements was fundamental for subsequent optimizations, cf. equations (3.68) and (3.76). In section 3.3.2, the methodology used to obtain the B_1^+ distribution generated by each transmitter of a parallel transmit array was described. The process is based on the combination of FLASH and SA2RAGE acquisitions.

An analytical description for the FLASH sequence was presented in section 3.3.2. The SA2RAGE sequence, more complex, will be described extensively in this chapter.

4.1.1 Introduction

Several approaches have been developed in the past 20 years to determine the distribution of the B_1^+ field. The most straightforward implementation is the double-angle method (DAM), which calculates B_1^+ from the ratio of two images acquired by using flip angles α_1 and $\alpha_2 = 2\alpha_1$ and a very long repetition time [60].

Another approach relies on a sequence made of three RF pulses ($\alpha, 2\alpha, \alpha$) in order to generate both a spin echo and a stimulated echo signal, which encode the transmit magnetic field information [61, 62].

Recently, a technique dubbed actual flip angle imaging has been introduced where two images are acquired after excitations with the same flip angle α but different repetition times TR_1 and TR_2 [63]. An appropriate choice of TR_1 and TR_2 removes the T_1 -sensitivity of the ratio between the two signals, which therefore only depends on B_1^+ and TR_2/TR_1 .

Another method uses the 180° signal null to build a flip angle map [64]. An innovative approach consists in the measurement of B_1^+ from the phase of the MR signal [65, 66].

Recently, with the availability of higher magnetic fields (implying increased B_1^+ inhomogeneity) and multiple transmit channels, B_1^+ measurements have become increasingly important, and many new methodologies have been proposed [34, 49, 53, 67–71].

One of the main challenges for any B_1^+ -mapping strategy to be used in the context of high static magnetic fields and parallel transmission is the range in which the measured B_1^+ is accurate and precise. A B_1^+ -mapping methodology should have a large range where the assumptions made to calculate B_1^+ are valid, and the B_1^+ calculation should in that range

be well conditioned (i.e the measured B_1^+ field should not be too sensitive to noise on the original images). To illustrate the importance of the large range of accuracy needed for B_1^+ -mapping techniques, at 7T, the conventional circularly polarized mode (used to combine the phases of the different transmit elements) can generate B_1^+ values inside the human head that vary 4-fold, from 0.4 to 1.6 of the nominal flip angle [18, 72].

When using localized arrays for transmission, in which case the RF field of each coil has to be mapped, the range of B_1^+ values is even greater (with regions distal to the coil having very low B_1^+ amplitudes).

The impact of the local coils on the range of accuracy required when performing the B_1^+ -mapping can be somewhat reduced by using recently proposed interferometry techniques [53, 54]. As described in section 3.3.2, this is achieved through the measurement of the B_1^+ field generated by a combination of coils rather than by one coil at a time. Such methods, as well as B_1^+ -shimming and transmit SENSE methods, require the B_1^+ -mapping technique to be sensitive to the phase of B_1^+ , which is not the case when using approaches that rely on the image phase to encode the B_1^+ amplitude [65, 66], or techniques where the B_1^+ of one specific channel is measured with the signal acquired by all channels [71].

Often, the effect of T_1 relaxation and B_1^+ inhomogeneity on signal are intertwined, and some techniques effectively measure these two quantities simultaneously [53, 67, 68, 73], which impacts on the signal to noise ratio (SNR) efficiency of the method, or have to rely on very long repetition times to guarantee full longitudinal relaxation, at the cost of an increased measurement time.

One approach proposed to overcome the need of prohibitively long repetition times in the DAM is to use saturation pulses [74]. Such an approach is difficult to implement at high fields, due to the high B_1^+ inhomogeneity. Furthermore, as the static magnetic field increases, the energy associated with a similar RF pulse increases quadratically with the reference frequency and hence specific absorption rate (SAR) considerations become increasingly important, effectively limiting the power of RF pulse amplitudes and slew rate of a given sequence or implying an increase of the repetition times used. Hence, a sequence for fast B_1^+ -mapping to be used at high static magnetic fields should be mostly based on low flip angle excitations. Given the large B_1^+ variations over the body it is important to be able to perform the mapping over the entire volume either via three-dimensional (3D) sampling or interleaved multislice. Multislice-based methods have the disadvantage that their precision can depend on the quality of the slice selection profile, which varies as large flip angles are applied.

In this thesis, a novel scheme named saturation prepared with 2 rapid Gradient Echoes (SA2RAGE) is proposed. This sequence allows the 3D B_1^+ -mapping of a human brain in under a minute with high precision over a large range of B_1^+ values. This method combines pulses with high and low flip angles in order to quickly measure the B_1^+ field with low SAR and is demonstrated in phantoms and for in vivo studies at 7T.

4.1.2 Methods

The proposed sequence SA2RAGE (Fig 4.1) can either be seen as a fast saturation recovery sequence with two different delay times, or as two images acquired in a turbo flash manner separated by a saturation pulse. The images acquired just after a saturation pulse

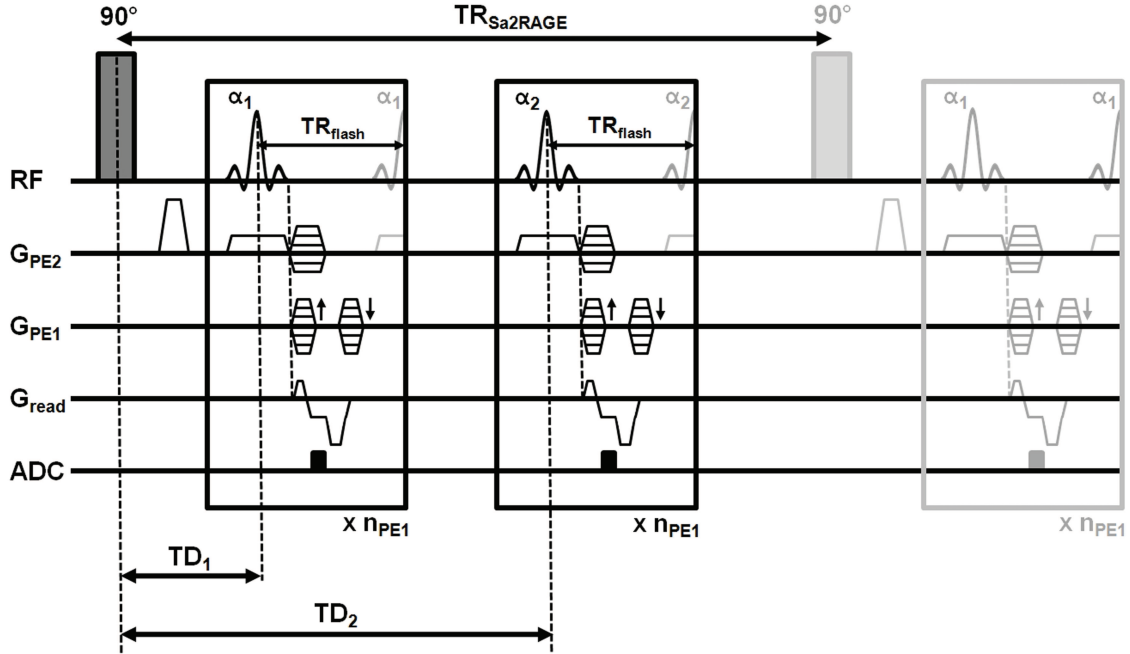


Figure 4.1: SA2RAGE sequence. A 90° RF saturation pulse is followed by two gradient echo blocks. The excitation pulses of low flip angles α_1 and α_2 within the gradient recalled echo (GRE) blocks are separated by a short repetition time TR_{flash} . Each readout gradient is followed by a spoiling gradient. A strong crusher gradient is also applied in the second phase encoding direction (PE2) after the saturation pulse. During each block, all n_{PE1} phase encoding lines of the second dimension are acquired. The sequence is repeated n_{PE2} times in order to acquire all third dimension k-space planes. Each GRE block was RF spoiled so that the assumption of no transverse magnetization prior to the following excitation can be considered valid (cf. Appendix 4.1.6).

and before the following one were named $SA2RAGE_1$ and $SA2RAGE_2$, respectively. To reduce T_1 -sensitivity, the first delay time (TD_1) was minimized while the second (TD_2) was maximized, making the ratio between the two acquired signals $SA2RAGE_1/SA2RAGE_2 = SA2RAGE_{ratio}$ mostly dependent on the saturation pulse performance. The predicted steady-state $SA2RAGE_{ratio}$ for several B_1^+ values was numerically calculated by solving the Bloch equations (see Appendix 4.1.6). The observed signal was considered to arise from the point where the center of k-space was acquired [18]. Both the saturation pulse and the GRE acquisitions were gradient spoiled (see Fig 4.1). Furthermore an RF spoiling with a 50° phase increment [75], was used within each GRE block. A lookup table between $SA2RAGE_{ratio}$ and B_1^+ values was then established from the numerical calculations (cf. Fig 4.2a). To guarantee a large range of accuracy on the B_1^+ estimation without compromising the total acquisition time, simulations were performed to determine the optimum parameters of the

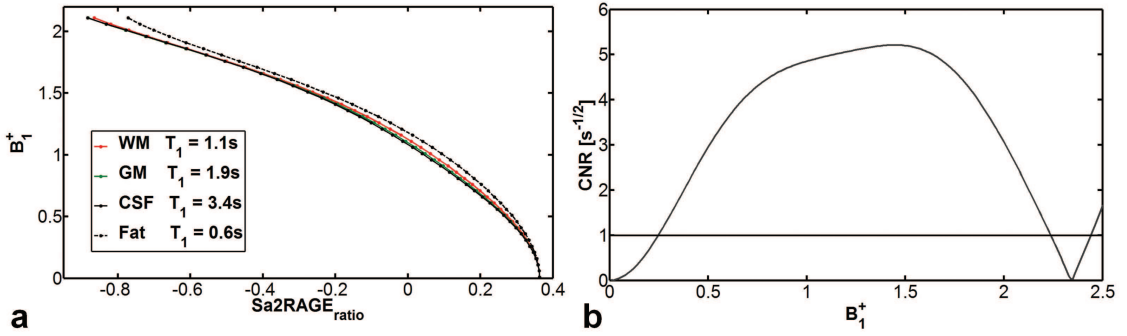


Figure 4.2: a: Dependence of B_1^+ on $SA2RAGE_{ratio}$ for protocol A ($TR_{SA2RAGE}/TD_2 = 2.4/1.8s$, $\alpha_1/\alpha_2 = 4^\circ/11^\circ$, $n_{PE1} = 64$) and different brain tissues (cerebrospinal fluids - CSF, grey matter - GM, white matter - WM and fat whose T_1 's belong to the interval 0.6-3.4s). The B_1^+ values are presented as relative multiplicative factor of the expected B_1^+ field. b: CNR curve corresponding to the optimum parameters of the SA2RAGE sequence. The horizontal line represents $CNR_{threshold}$ and allows the visualization of the interval inside which B_1^+ can be measured above an acceptable noise level.

SA2RAGE sequence.

The contrast-to-noise ratio per unit of time (CNR) of the estimated $B_{1,i}^+$ in respect to a neighbouring $B_{1,i+1}^+$ amplitude was defined as

$$CNR_{B_{1,i}^+} = \frac{(B_{1,i+1}^+ - B_{1,i}^+)}{\sqrt{\sigma_{B_{1,i+1}^+}^2 + \sigma_{B_{1,i}^+}^2}} \frac{1}{\sqrt{TR_{SA2RAGE}}} \quad (4.1)$$

where $B_{1,i}^+$ and $B_{1,i+1}^+$ represent two sequential B_1^+ values. The noise of the $B_{1,i}^+$, $\sigma_{B_{1,i}^+}^2$, was calculated via error propagation of the noise in the measurement of the $SA2RAGE_1$ and $SA2RAGE_2$ signals, into the $SA2RAGE_{ratio}$ and subsequently arising from the lookup table interpolation

$$\begin{aligned} \sigma_{B_{1,i}^+}^2 &= \left| \frac{\partial B_1^+}{\partial SA2RAGE_{ratio}} \Big|_{B_1^+ = B_{1,i}^+} \right|^2 \sigma_{SA2RAGE_{ratio}}^2 \\ &= \left| \frac{\partial B_1^+}{\partial SA2RAGE_{ratio}} \Big|_{B_1^+ = B_{1,i}^+} \right|^2 \frac{SA2RAGE_1^2 + SA2RAGE_2^2}{SA2RAGE_2^4} \sigma^2 \end{aligned} \quad (4.2)$$

The first term, corresponding to the noise amplification due to the interpolation, was numerically calculated from the lookup table of $SA2RAGE_{ratio}$ as a function of the transmit field. The second term, corresponding to the noise propagation from the original images into $SA2RAGE_{ratio}$, is analytically calculated via error propagation theory. As the acquisition of each image was performed under the same conditions (acquisition bandwidth and resolution), their noise was assumed to be identical, i.e., $\sigma_{SA2RAGE_1} = \sigma_{SA2RAGE_2} = \sigma$.

For each set of sequence parameters, CNR was computed for values of relative B_1^+ varying from 0.01 to 2.51 (in steps of 0.025), creating a CNR curve as a function of B_1^+ (cf. equation 4.1) that represents the ability to distinguish consecutive B_1^+ values in the presence of

noise on the original images. A threshold CNR value ($CNR_{threshold}$) was then experimentally derived. Subsequently, B_1^+ related to CNR values higher than this threshold were deemed as being accurately estimated. For the sake of simplicity, σ was set such that the value of $CNR_{threshold}$ corresponds to one (Fig. 4.2b), meaning that above this threshold a change of relative B_1^+ of 0.025 can be measured.

Given the widespread range of B_1^+ values found at high fields, simulations were performed with the aim to maximize the width of CNR curve over $CNR_{threshold}$. To reduce the number of variables to evaluate, the following assumptions were made: (a) the number of excitations per GRE module (n_{PE_1}) was set to 64 and TR_{Flash} to 2.9ms; (b) TD_1 was kept at a minimum value (given the above mentioned settings of n_{PE_1} and TR_{Flash}) of 101 ms; (c) $T_1 = 1.5$ s was considered for all in vivo experiments (this value corresponds to the average T_1 in the brain). Concerning in vitro measurements, $T_1 = 0.8$ s was used for the experiments conducted with an oil phantom whereas an average $T_1 = 1.5$ s was considered when using an agar gel head phantom. The parameters varied were: (i) the repetition time $TR_{SA2RAGE}$ (from 1.5 to 3.5s in steps of 0.1s); (ii) TD_2 (from 1.3 to 3.4s in steps of 0.1s); (iii) α_1 and α_2 (varied independently from 1-10° and 1-20°, respectively).

The SA2RAGE sequence was subsequently improved in terms of T_1 -insensitivity by allowing the minimal value of TD_1 and n_{PE_1} to be further reduced. The center of k-space can be acquired earlier when either partial Fourier or parallel imaging acceleration (GRAPPA) [76] is applied in the phase encoding direction (Fig 4.1) leading to the possibility to choose TD_1 significantly smaller than 101 ms. These modifications were evaluated via numerical simulations and in vivo measurements.

In vitro and in vivo scans were performed on a Siemens 7T parallel transmit (PTx) system (Siemens Healthcare, Germany) equipped with a custom-designed 8-channel transmit-receive array coil (Rapid Biomedical, Germany). The experimental protocol was approved by local ethics committee, and one healthy subject providing informed consent was scanned. For subject's safety, simulations of the RF coil were performed and the worst case scenario (sum of in phase electric fields over the whole brain) implied that the maximum power delivered by each coil element was limited to 0.9 W/10 s and 0.3W/6 min.

The $SA2RAGE_{ratio}$ signal (computed by division of the complex images $SA2RAGE_1$ and $SA2RAGE_2$) was acquired with the sequence parameters optimized above and using a matrix size of 64x64x16 and nominal resolution of $3x3x5mm^3$. The GRE excitation pulses were slab-selective, while the saturation was a hard pulse. The specific sequence parameters used will be given throughout the results section. B_1^+ values were computed using a lookup table created as described in the Appendix 4.1.6 using the specific sequence parameters.

To demonstrate the linearity of the B_1^+ estimated by SA2RAGE with the effective B_1^+ applied, the reference voltage was varied from 10 to 190 V in 19 steps. This experiment was conducted with the agar gel head phantom (dimensions: 15 cm left-right; 18 cm anterior-posterior; 21 cm top-bottom) whose geometric and electric properties created inhomogeneities significantly bigger than those found in the human head. The average estimated B_1^+ in two

different regions of interest was measured in order to have enough points in the low and high transmit field regimes, respectively. For comparison, the B_1^+ field was also mapped using the DAM with an echo planar imaging (EPI) (TR/TE = 30s/15ms, two averages, matrix size = 64x64x16). The nominal flip angles α_1 and α_2 used for the DAM method were 60° and 120° , respectively, and the same variation of the reference voltage was performed. To ensure that the same region was selected for both the DAM and SA2RAGE methods, one EPI- 60° image was coregistered to an SA2RAGE₂ image using FSL [77]. The obtained transition matrix was subsequently applied to all the B_1^+ maps calculated with the DAM method. To be able to estimate the interference between B_1^+ maps of different coils, it is fundamental to know both magnitude and phase of B_1^+ . The phase of the transmit field was assumed to be simply equal to that of the second SA2RAGE image, although it also includes B_0 field inhomogeneities and reception B_1^- phase contributions, as these are the same for all the measured maps their contribution to the interference can be neglected. $\vec{B}_1^+(\vec{r})$ was therefore assumed to be equal to $|\vec{B}_1^+(\vec{r})| e^{i\phi(\vec{r})}$, where $\phi(\vec{r})$ is the phase of SA2RAGE₂ and $|\vec{B}_1^+(\vec{r})|$ is calculated from the lookup table.

To demonstrate the phase sensitivity of the SA2RAGE sequence, eight different modes were excited (cf. AllBut1,m configuration in section 3.3.2). Individual coil B_1^+ maps were then computed by matrix inversion [53] and compared with B_1^+ maps acquired with single coil excitations (transmission on only one coil at a time).

4.1.3 Results

The maps presented in Figure 4.3 show the variation of CNR_{width} , as a function of two flip angles, TR and TD_2 . CNR_{width} was defined as the width of the CNR curve above $CNR_{threshold}$

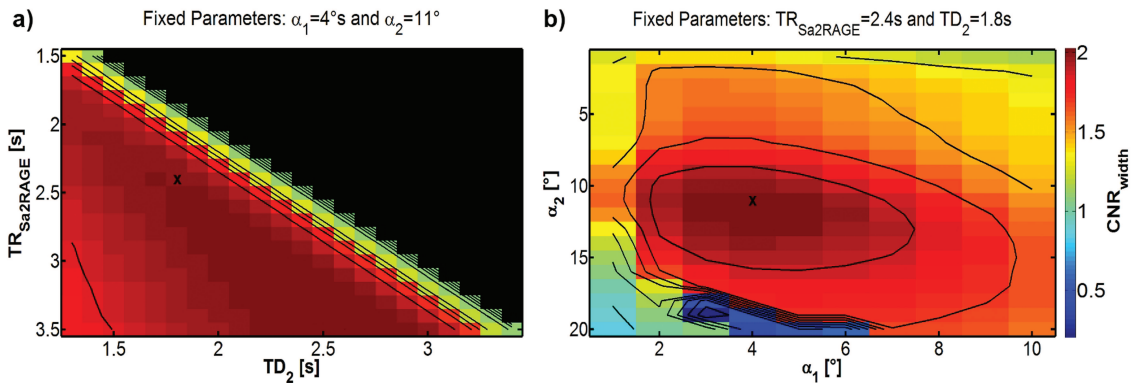


Figure 4.3: Maps of CNR_{width} , defined as the width of the CNR curve above $CNR_{threshold}$, as a function of $TR_{SA2RAGE}$ and TD_2 (a); α_1 and α_2 (b). The contour lines represent isolines of CNR_{width} at 10% intervals of the maximum CNR_{width} achieved. The parameters considered optimal for the SA2RAGE sequence are represented by crosses. The black area in (a) corresponds to the forbidden region of the parameter space (TD_2 must be smaller than $TR_{SA2RAGE} - n_{aft} \cdot TR_{flash}$ ($n_{aft} = 32$)).

(Fig. 4.2b). The parameters that maximize CNR_{width} were $TD_2 = 2.6$ s and $TR_{SA2RAGE} = 3.5$

s.

Given that CNR_{width} is a slowly varying function, and that for the sought applications the speed of the methodology is a priority the parameters $TD_2 = 1.8$ s and $TR_{SA2RAGE} = 2.4$ s were chosen and will be used afterwards, because it provides a substantial improvement in terms of acquisition time at a low cost of the CNR_{width} value.

The contrast-to-noise optimization thus led to the following optimal parameters for the SA2RAGE sequence: $TR_{SA2RAGE}/TD_1/TD_2 = 2.4$ s/0.101 s/1.8 s; $\alpha_1/\alpha_2 = 4^\circ/11^\circ$. This protocol (defined as-protocol A-for future references) provided a large range of precision for the B_1^+ estimations (from 0.25 to 2.25 times the nominal flip angle, see Fig. 4.2b). As TD_1 cannot be decreased indefinitely due to the duration of the gradient echo train, the $SA2RAGE_{ratio}$ depends not only on B_1^+ but also on the different T_1 s. Although this deviation is hardly noticeable in Fig. 4.2a for the different brain tissues, it can potentially cause a systematic error on the B_1^+ values measured (cf. Figure 4.4a).

The importance of using TD_1 as short as possible is illustrated in Figure 4.4b where sig-

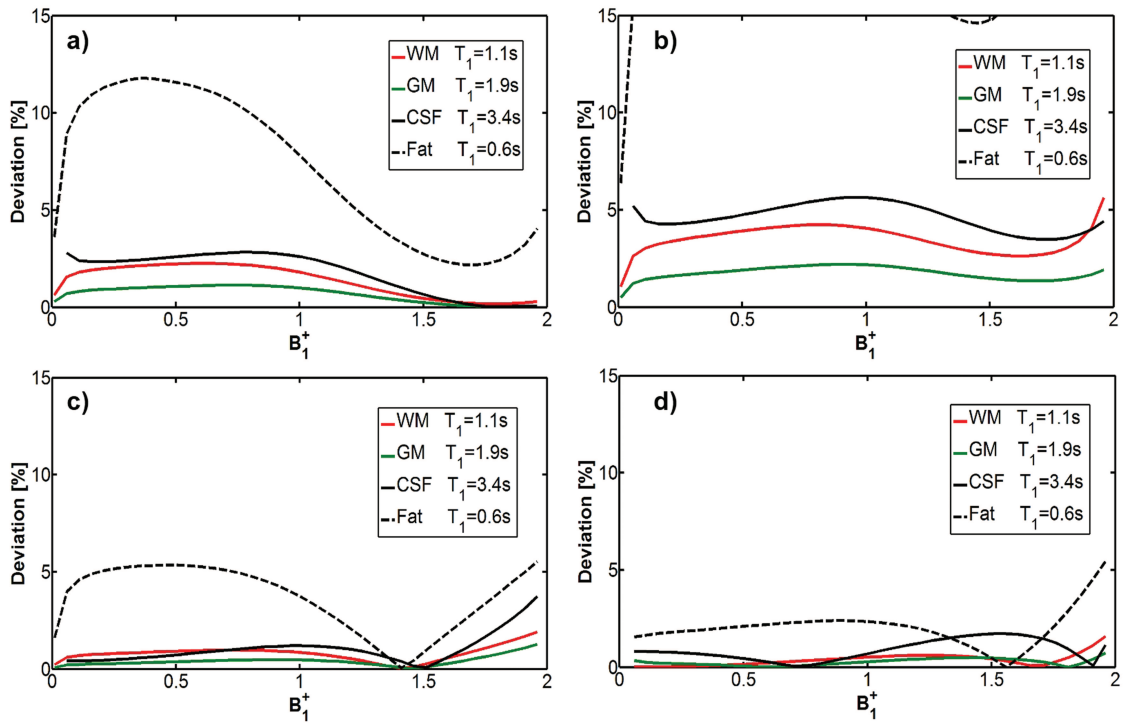


Figure 4.4: Plots representing the error introduced on the estimated B_1^+ maps as a function of the B_1^+ intensity for CSF, GM, WM and fat at 7T by considering an average $T_1 = 1.5$ s. The sequence parameters for all the simulations are ($TR_{SA2RAGE}/TD_2 = 2.4/1.8$ s, $\alpha_1/\alpha_2 = 4^\circ/11^\circ$) while TD_1 was varied in the four plots by considering the following acquisitions: (a) Full k-space acquisition (Protocol A: $TD_1 = 101$ ms); (b) Full k-space acquisition with $TD_1 = 200$ ms; (c) 6/8 partial Fourier (Protocol B: $TD_1 = 56$ ms); (d) 6/8 partial Fourier + GRAPPA (Protocol C: $TD_1 = 39$ ms).

nificantly higher deviation curves are observed when $TD_1 = 200$ ms is considered. The use of 6/8 partial Fourier encoding in the phase direction implies that the center of k-space was acquired after 16 steps instead of 32 ($n_{PE1} = 64$) allowing a decrease of TD_1 to 56 ms (proto-

col B). A supplementary reduction of TD_1 was achieved with the additional use of GRAPPA (acceleration factor = 2) in the same encoding direction making the minimum available $TD_1 = 39$ ms (Protocol C).

The impact of such changes on the sensitivity to T_1 variations is illustrated in Figure 4.4c and d, respectively. When using protocol C, the errors introduced in WM/GM/CSF B_1^+ were estimated to be smaller than 1.6% (Fig. 4.4d) for a wide range of B_1^+ values (from 0.06 to 1.96) when compared with the 2.8% in the case of protocol A (Fig. 4.4a).

It should be noted from Figure 4.4c and d that B_1^+ -mapping is made possible even for body regions containing tissues with short T_1 values such as fat (important in the case of abdominal applications) when using either Protocol B or C. This observation reinforces the relevance of using short TD_1 values to achieve T_1 insensitivity.

Figure 4.5a shows the linearity of the measured B_1^+ values with the amplitude of the RF voltage in the region of interest of high B_1^+ intensity compared with the rest of the phantom. The

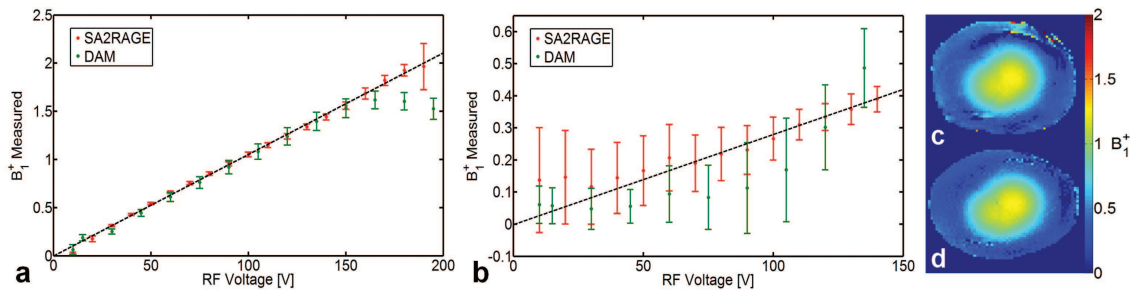


Figure 4.5: Mean values and standard deviations of B_1^+ calculated using the SA2RAGE and the DAM on a ROI ($5 \times 5 \times 4$ pixels) located on different areas of an agar gel phantom as a function of the transmit reference RF voltage: (a) region with a relatively high B_1^+ intensity in respect to the remaining phantom - bright spot (b) region with low B_1^+ intensity in respect to the remaining phantom. For comparison purposes, an axial view of the B_1^+ maps obtained with (c) the DAM and (d) the SA2RAGE sequence at 120 V are shown. The scan times were 1 min 30 s and 38 s for the DAM (two measurements alternating the readout polarity were acquired to remove ghosting artifacts [78]) and the SA2RAGE sequence respectively.

estimates obtained using the SA2RAGE sequence and the DAM are in good agreement over a large range. Divergence from linearity and a significant increase in the observed standard deviation of the measured values is noticeable at B_1^+ greater than 1.7, with the larger errors being observed for the DAM method. This increased deviation from linearity in the DAM data can be attributed to slice profile issues associated with the two-dimensional nature of the DAM method that become more noticeable as the "double angle" pulse approaches 180° and the sum of the signal excited over the slice deviates from $\sin(\alpha)$.

On the other end of the B_1^+ intensity spectrum, as shown in Figure 4.5b (where B_1^+ values were measured in a region of lower B_1^+ intensity), it is possible to observe the increased noise at low B_1^+ values as anticipated by the left side of the CNR curve (Fig. 4.2b).

It should also be noted that in this regime, the SA2RAGE sequence outperformed the DAM both in terms of linearity and noise behavior. It is also noteworthy that the DAM, despite the usage of an EPI readout, took 2.5 times longer than the SA2RAGE acquisition. Figure 4.5c

and d illustrates the agreement between the two mapping methods when measuring B_1^+ values up to 1.5.

Figure 4.6 presents the two images provided by the SA2RAGE sequence when three different protocols are used (a-f). The expected spatial pattern with a central bright spot can be

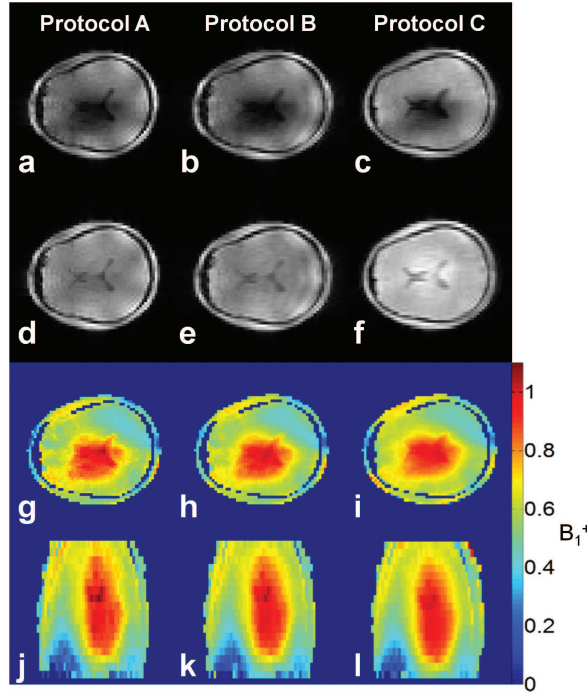


Figure 4.6: Axial views of the two 3D $64 \times 64 \times 20$ images ($4 \times 4 \times 5$ mm³ resolution) provided by the SA2RAGE sequence in 48 s with the following parameters $TR_{SA2RAGE}/TD_2 = 2.4/1.8$ s, $\alpha_1/\alpha_2 = 4^\circ/11^\circ$. The different columns represent the following different protocols used: first column: Full k -space acquisition (Protocol A: $TD_1 = 101$ ms); second column: 6/8 partial Fourier (Protocol B: $TD_1 = 56$ ms); third column: 6/8 partial Fourier + GRAPPA (Protocol C: $TD_1 = 39$ ms). The first (a-c) and second (d-f) rows present SA2RAGE₁ and SA2RAGE₂ images respectively, while the third (g-i) and fourth (j-l) rows present the corresponding B_1^+ maps in the transverse and coronal planes respectively.

observed on the corresponding brain B_1^+ maps (g-l).

The reduced sensitivity to T_1 variations from protocol A to C was evident on such in vivo B_1^+ maps; in figure 4.6g, it is possible to visualize residual contrast between different brain tissues, such as gray and white matter in the anterior part of the brain, whereas it is virtually vanished in figure 4.6i.

Figure 4.7 displays B_1^+ maps with the transmit magnetic field produced by the different coils of the 8-channel transmit-receive array acquired using the parallel transmission system; it shows the good spatial agreement between the two methodologies used (top: measurement of the B_1^+ maps of the individual coils; middle row: B_1^+ maps of the individual coils calculated using the interferometry technique). This result demonstrates the phase sensitivity of the sequence, because the system of equations describing the interference between the different array elements can be resolved properly only with the knowledge of the phases of the B_1^+ maps before matrix inversion. Moreover, the interferometry approach to map indi-

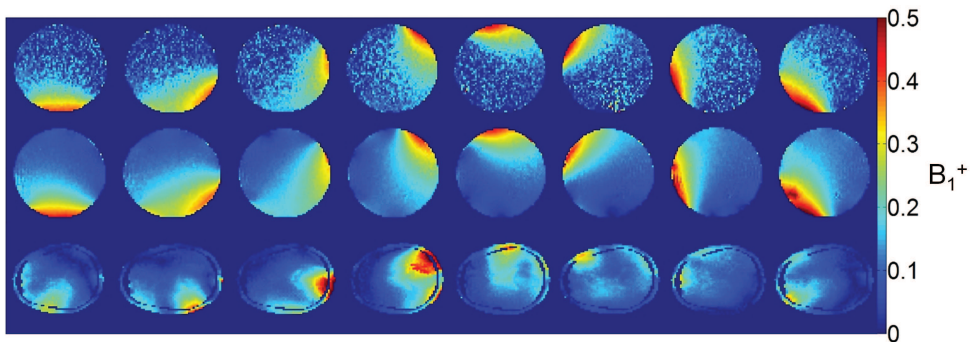


Figure 4.7: Axial views ($z = 8$) of $64 \times 64 \times 16$ pixel images corresponding to the B_1^+ profiles produced by each individual coil on an oil phantom (top and middle row) and on a human head (bottom row). On the top row only one activated coil was measured at a time. On the middle and bottom rows, the B_1^+ map of each array element was measured by means of interferometry using all but one coils active. The scan time for each image was 38 s ($TR_{SA2RAGE} = 2.4$ s).

vidual coils clearly results in a lower noise level present in the coil profiles acquired with the SA2RAGE method.

Bottom row in Figure 4.7 shows the B_1^+ maps of the individual coils calculated using the interferometry method on a volunteer with the total acquisition time of ≈ 5 min without exceeding the SAR constraints mentioned in the methods section.

4.1.4 Discussion

A new sequence to map the transmit magnetic field in a 3D manner was introduced in this work. Its short acquisition time and low SAR characteristics as well as its wide range of accuracy make it a valuable tool to quantitatively map the transmit field B_1^+ in vivo at high fields.

It should be highlighted that the short acquisition times needed to obtain the B_1^+ maps in this work did not rely on EPI readouts. Such readouts, as used to accelerate the DAM, pose serious limitations in vivo because of their high sensitivity to physiological noise (due to the inherently longer TE), which will affect the precision of the calculated transmit field.

The limiting factor in terms of acquisition time of the current B_1^+ map calculation is the number of repetitions performed and used to encode the different slices. The lookup table created to estimate the B_1^+ field relies on the assumption that the steady state is achieved (cf. Appendix 4.1.6); it is interesting to note that the B_1^+ estimation converges to that of the steady state extremely quickly. This observation was made via simulations considering the process of driving the magnetization from fully relaxed through various repetitions of the SA2RAGE sequence towards steady state. During the second repetition, the estimated B_1^+ field had a maximum deviation from the steady state estimation of 3% (at the third repetition, the maximum deviation was already under 0.4%). This observation implies that the SA2RAGE method could be used for 3D acquisitions with as few as 4 to 8 repetitions, which would bring the total time to acquire a 3D B_1^+ map down to 9.5 or 19 s, respectively.

Another important assumption of the lookup table is that the signal of each image is fully described by the intensity of the echo corresponding to the central k-space plane. As the local B_1^+ increases, the higher the flip angles are and hence the intensity between the different k-space lines will change more rapidly, increasing the point spread function weighing in the phase encoding direction. This effect could be responsible for the deviation from the linear relation in the SA2RAGE sequence visible for high B_1^+ values (Fig. 4.5a). However, it should be noted that the deviation for high nominal B_1^+ values was smaller than the one observed with the DAM method. Reducing the number of excitations and the duration of the GRE block will mitigate possible consequences to the point spread function stemming from both saturation and T_1 relaxation.

One last assumption of the SA2RAGE sequence is that the signal is ideally spoiled throughout the GRE readout periods. Deviations from ideal spoiling are expected to be observable at high B_1^+ values, with the effective flip angle of the second GRE block being as high as 22° (for a $B_1^+ = 2$). The validity of this assumption is extensively evaluated and confirmed through simulations, calibration studies, and in vivo data acquisitions in Appendix 4.1.7.

As discussed in the introduction, many B_1^+ -mapping techniques are sensitive to the varying T_1 values found in different tissues and this dependence can be mitigated by either using long repetition times or designing the mapping method in such a way that both B_1^+ and T_1 values are measured. As shown in figure 4.4a, c, and d, for the typical T_1 values found in the human brain, the optimal parameters make the estimate of the transmit field virtually insensitive to variations in the longitudinal relaxation times (<3 and $<1.7\%$, respectively). With the insensitivity to T_1 achieved by using parallel imaging (Fig. 4.4d), it is possible to state that this B_1^+ -mapping scheme could find applications also in the domain of abdominal imaging. Moreover, it is possible to further reduce the sensitivity to T_1 by decreasing the TD_1 time. Such a reduction could be achieved in several ways: either by reducing the number of phase encoding steps (by further parallel imaging acceleration or decreasing the resolution), or by increasing the number of phase-encoded lines per excitation (and hence reducing the number of time consuming slab-selective excitation pulses). In case the whole sensitive volume of the coil is to be acquired, the slab-selective pulses can be replaced by shorter hard pulses, which will also contribute to the reduction of TD_1 .

One other approach to reduce the T_1 sensitivity of the SA2RAGE sequence, by reducing TD_1 , would be to use a centric phase encoding. Such an approach was not pursued due to the significantly increased blurring on the phase encoding direction when compared with that introduced by linear phase encoding [79, 80]. While the blurring might be rather benign at the center of the image (as the B_1^+ map is not expected to present fast spatial variations), at the edges, this effect would be more pronounced. Furthermore, the amount of blurring would be B_1^+ dependent, increasing with increasing B_1^+ values which accentuate the PSF via

the increased signal saturation $\cos^n(\alpha |B_1^+|)$ and via the faster longitudinal recovery

$$(1 - 2\cos(\frac{\pi}{2} |B_1^+|))e^{-TD/T_1} \quad (4.3)$$

4.1.5 Conclusions

The SA2RAGE sequence can be used to accurately and quantitatively map the B_1^+ field within a 3D volume in less than 30 s. The wide range of validity experimentally observed from $B_1^+ = 0.2 - 2.0$ should also be noted. The accuracy of the SA2RAGE and insensitivity to the range of T_1 values observed in the brain ($< 3\%$) is acceptable for most B_1^+ -mapping applications and was shown to be further improvable by using partial Fourier sampling schemes. SA2RAGE is thus a promising tool for fast and accurate B_1^+ -mapping, of particular interest for applications using multichannel transmission. In our current implementation it is possible to obtain B_1^+ maps online, making it an important tool during the scan setup process.

4.1.6 Appendix A

The SA2RAGE sequence is characterized simply by three types of periods that affect the longitudinal magnetization in the following way:

- (a) Longitudinal magnetization is saturated by means of an hard pulse, meaning that

$$M_{z,sat}(M_z(0), B_1^+) = M_z(0)\cos(\frac{\pi}{2} |B_1^+|) \quad (4.4)$$

- (b) During the GRE blocks of n RF pulses with constant flip angles α , separated by an interval TR , the longitudinal magnetization evolves in the following way [81]

$$M_{z,nRF}(M_z(0), T_1, n, TR, \alpha B_1^+) = M_z(0) \left(\cos(\alpha |B_1^+|) e^{-TR/T_1} \right)^n + M_0(1 - e^{-TR/T_1}) \frac{1 - (\cos(\alpha |B_1^+|) e^{-TR/T_1})^n}{1 - \cos(\alpha |B_1^+|) e^{-TR/T_1}} \quad (4.5)$$

where $M_z(0)$ is the longitudinal magnetization at the start of the RF free periods.

- (c) During the periods with no RF pulses, the longitudinal magnetization relaxes freely towards equilibrium following the conventional T_1 relaxation expression

$$M_{z,ORF}(M_z(0), T_1, t) = M_z(0)e^{-t/T_1} + M_0(1 - e^{-t/T_1}) \quad (4.6)$$

A full account of the signal resulting from the SA2RAGE sequence has to take into account the steady state condition. This implies that the longitudinal magnetization before successive saturations, $m_{z,ss}$, has to be the same. Between two successive saturations, the $m_{z,ss}$,

undergoes first one saturation (a), followed by recovery for a period TA (c), a first GRE block (b), a free recovery for a period TB (c), a second GRE block (b), and a final recovery for a period TC (c) by the end of which it should be back to its initial value. Mathematically, it is equivalent to solve the following composite equation

$$\begin{aligned}
 m_{z,ss} = & \\
 & M_{z,orf}(M_{z,nrf}(M_{z,orf}(M_{z,nrf}(M_{z,tmp}, T_1, n, TR, \alpha_1 B_1^+), T_1, TB), T_1, n, TR, \alpha_2 B_1^+), T_1, TC) \\
 & M_{z,tmp} = M_{z,orf}(M_{z,sat}(m_{z,ss}, B_1^+), T_1, TA)
 \end{aligned} \tag{4.7}$$

where TA, TB, and TC are the delays in between the saturation and the start of the first GRE block, between the two GRE blocks and from the end of the second GRE block to the saturation pulse, respectively. Solving this equation for $m_{z,ss}$ results in the following steady state

$$\begin{aligned}
 m_{z,ss} = & M_0 \\
 & \frac{\left[TMP \cdot (\cos(\alpha_2 |B_1^+|)E1)^n + (1 - E1) \frac{1 - (\cos(\alpha_2 |B_1^+|)E1)^n}{1 - \cos(\alpha_2 |B_1^+|)E1} \right] EC + (1 - EC)}{1 - \cos(\frac{\pi}{2} |B_1^+|)(\cos(\alpha_1 |B_1^+|)\cos(\alpha_2 |B_1^+|))^n e^{-TR_{SA2RAGE}/T_1}} \\
 TMP = & \left(\left((1 - EA)(\cos(\alpha_1 |B_1^+|)E1)^n + (1 - E1) \frac{1 - (\cos(\alpha_1 |B_1^+|)E1)^n}{1 - \cos(\alpha_1 |B_1^+|)E1} \right) EB + (1 - EB) \right)
 \end{aligned} \tag{4.8}$$

where $E1 = e^{-TR/T_1}$, $EA = e^{-TA/T_1}$, $EB = e^{-TB/T_1}$, and $EC = e^{-TC/T_1}$. Once the steady state condition is known, the signal for each of the images can be expressed as

$$\begin{aligned}
 SA2RAGE_1 = & \\
 & B_1^- e^{-TE/T_2^*} e^{-i\Delta\omega TE} M_0 \sin(\alpha_1 |B_1^+|) \\
 & \left[\left(\frac{\cos(\frac{\pi}{2} |B_1^+|) m_{z,ss}}{M_0} EA + (1 - EA) \right) (\cos(\alpha_1 |B_1^+|)E1)^{n_{bef}} + (1 - E1) \frac{1 - (\cos(\alpha_1 |B_1^+|)E1)^{n_{bef}}}{1 - \cos(\alpha_1 |B_1^+|)E1} \right] \\
 SA2RAGE_2 = & \\
 & B_1^- e^{-TE/T_2^*} e^{-i\Delta\omega TE} M_0 \sin(\alpha_2 |B_1^+|) \\
 & \left[\frac{\frac{m_{z,ss}}{M_0} - (1 - EC)}{EC(\cos(\alpha_2 |B_1^+|)E1)^{n_{aft}}} - (1 - E1) \frac{1 - (\cos(\alpha_2 |B_1^+|)E1)^{n_{aft}} - 1}{1 - \cos(\alpha_2 |B_1^+|)E1} \right]
 \end{aligned} \tag{4.9}$$

where n_{bef} and n_{aft} stand for the number of phase encoding steps before and after the k-space center is excited (in the case of full k-space coverage $n_{bef} = n/2 - 1$ and $n_{aft} = n/2$). From equation (4.9), it is clear that when combining the two different images to generate

the SA2RAGE ratio image the dependence in M_0 , T_2^* , and $\Delta\omega$ will disappear, whereas only B_1^+ and T_1 dependences will remain. The lookup tables from which B_1^+ values were subsequently computed were based on the ratio between $SA2RAGE_1$ and $SA2RAGE_2$ as described in equation (4.9).

To understand the general trends of the SA2RAGE ratio to a first order, consider: the low flip angle regime (where $\sin(\alpha |B_1^+|) \approx \alpha |B_1^+|$ and $\cos(\alpha |B_1^+|) \approx 1$); EA = E1 = EC = 1. The ratio between the two images will thus be simply given by

$$\frac{\alpha_1}{\alpha_2} \cos\left(\frac{\pi}{2} |B_1^+|\right) \quad (4.10)$$

meaning that either positive or negative values of the ratio are observed when the relative B_1^+ amplitude is smaller or bigger than one, respectively.

4.1.7 Appendix B

Equations (4.4-4.9) are valid only if the transverse magnetization before each excitation or saturation in the SA2RAGE sequence can be neglected. This approximation can only be done if an efficient gradient and RF spoiling scheme is applied. In order to determine the most suitable scheme, simulations considering gradient spoiling after each excitation pulse (cf. Fig. 4.1) as well as RF spoiling were performed for the SA2RAGE sequence as described in Ref. [75]. Simulations were performed considering an average $T_1 = 1.5$ s and an average $T_2 = 100$ ms. It should be noted that this T_2 , in the context of brain imaging at 7T, is rather large (T_2^* values in white and grey matter vary from 18-33 ms [82]). Such a long T_2 was chosen so that an upper bound of the problem could be estimated.

The magnetization (M_x , M_y , M_z) at the very beginning of the sequence was considered as being fully relaxed ($M_x = 0$, $M_y = 0$, $M_z = 1$). The transverse magnetization was only ignored after the saturation pulse, which is followed by a strong crusher gradient (Fig. 4.1) different from the crushers applied after each readout gradient.

Within each GRE block, the effects of the excitation pulses of flip angles α_1 (and α_2) were taken into account via a matrix formalism simulating a rotation of the magnetization (M_x , M_y , M_z) by a flip angle $|B_1^+| \cdot \alpha_1$ ($|B_1^+| \cdot \alpha_2$ for the second GRE block) around an axis defined by the phase ϕ of the RF spoiling scheme. This phase increases from the n^{th} excitation pulse of the GRE block to the $n^{\text{th}} + 1$ according to [83]: $\phi_{n+1} - \phi_n = n\Delta\Phi$ ($n \in [1, n_{PE1}]$). T_1 and T_2 relaxations were also simulated between each excitation pulse. The spoiling gradient applied after each readout gradient was taken into account by considering a rotation of the magnetization vector around the z axis by an angle Ω . Note that Ω was varied from 4° to 360° in steps of 4° in order to simulate different isochromats.

This SA2RAGE simulation was repeated for three TRs in order to reach the steady-state. At the end of the simulation, the sum over all isochromats was performed for each phase encoding step to obtain a macroscopic value for the magnetization. The simulation was re-

peated for $\Delta\Phi$ values ranging from 0° to 180° in steps of 0.1° , and for B_1^+ values varying from 0.01 to 2.11.

Two different methodologies were used to evaluate the optimum RF spoiling scheme. In the first methodology, the $SA2RAGE_{ratio}$ was calculated considering the k-space centre excitation for the simulated range of B_1^+ , and for each specific $\Delta\Phi$. The different lookup tables were then compared with the analytical one resulting from equation (4.4-4.9). In the second methodology, the RF spoiling was evaluated by considering, for each RF spoiling phase increment, the sum over the simulated B_1^+ values and all the 64-phase encoding steps of the square difference between the simulated $SA2RAGE_2$ signal and the analytical expression. While the first methodology favors RF spoiling schemes that provide a good result at the k-space centre (although this might be dependent on the T_2 value and number of phase encoding steps), the second methodology favors a scheme with less fluctuations over all the phase encoding steps. These two metrics produce different patterns (Fig. 4.8a). For the first methodology, the ideal RF spoiling scheme was found to be $\Delta\Phi = 139.8^\circ$, while the second methodology had an optimum RF spoiling phase increment of 137.5° .

It should be noted that the RF phase spoiling patterns obtained with the second methodology are in close agreement with those of conventional GRE sequence (cf. Fig. 1 of Ref. [75]), the actual flip angle imaging sequence (cf. Fig. 2 of Ref. [84]) and the steady state preparation (cf. Fig. 9 of Ref. [85]).

Three different RF spoiling increments were evaluated from a theoretical, an experimental calibration and human application perspectives. The three evaluated RF spoiling phase increments were: 50° (the standard Siemens RF spoiling phase increment, originally suggested by Preibisch et al. [75] and used throughout the article); 139.8° (to optimize the $SA2RAGE_{ratio}$ accuracy-Methodology 1) and 137.5° (to optimize the stability of $SA2RAGE_2$ over the various phase encoding steps-Methodology 2).

In terms of theoretical $SA2RAGE_{ratio}$ fidelity, figure 4.8b shows the expected trend, with the RF spoiling phase with the best match being that obtained using Methodology 1, but with very satisfactory results being obtained using the two remaining phase increments (although very different results are observed in the absence of RF spoiling). It is also clear that, by reducing the amplitude of the flip angle used in the second readout from 11° to 6° , the importance to use an appropriate phase cycling is significantly reduced, with all methods showing acceptable results.

Figure 4.8(d-f) demonstrates that the fluctuations observed throughout the GRE train increase with the increase of the B_1^+ value (which increases the effective flip angle) and are minimized for a phase increment of 137.5° as expected from the simulations (Fig. 4.8a). Such fluctuations can be significantly reduced by selecting a protocol with smaller flip angles (Fig. 4.8(g-i)). Note that these fluctuations are calculated considering a $T_2 = 100\text{ms}$, which is likely to represent a worst case scenario in the context of high field imaging.

Figure 4.9 shows calibration curves obtained in a phantom experiment (identical to that described for Fig. 4.5) for the protocol with the large flip angle ($\alpha_2 = 11^\circ$, Fig. 4.9a) and for

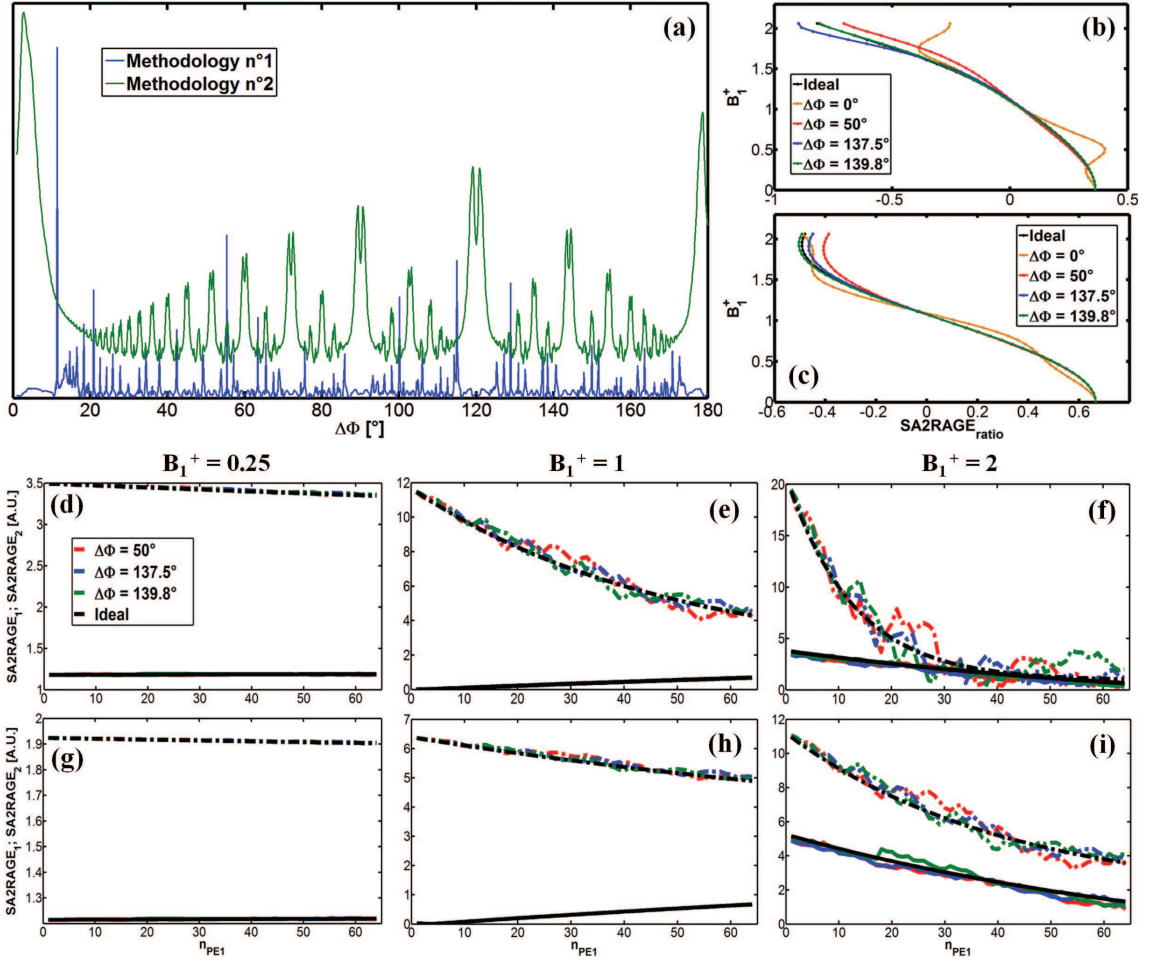


Figure 4.8: *a*: Plot showing the deviation from the ideally spoiled SA2RAGE sequence (using Protocol A) as a function of the RF spoiling phase increment. Deviation was computed considering the norm of the difference between ideal and simulated SA2RAGE_{ratio} (Methodology 1) and the sum of the squared difference between the ideal and simulated SA2RAGE₂ over all phase encoding steps and B_1^+ values (Methodology 2). SA2RAGE lookup tables simulated for different RF spoiling phase increments and ideally spoiled using: *(b)* protocol A and *(c)* a smaller flip angle protocol ($\alpha_2 = 6^\circ$ and otherwise equivalent to protocol A). Plots showing the magnitude of the signal of SA2RAGE₁ (full lines) and SA2RAGE₂ (dashed lines) as a function of the phase encoding steps for a B_1^+ of 0.25 (*d,g*), 1 (*e,h*), and 2 (*f,i*) for protocol A (*d,e,f*) and the small flip angle protocol (*g,h,i*).

the protocol with small flip angle ($\alpha_2 = 6^\circ$, Fig. 4.9b) using the three evaluated RF spoiling phase increments. No significant differences are observable between the various RF spoiling methodologies. Nevertheless, it should be noted that the differences observed for high reference voltages (and hence B_1^+ values) was in agreement with the behaviour predicted by the simulations (cf. Fig. 4.8b). The RF spoiling schemes with 50° and 137.5° underestimate and overestimate B_1^+ values measured with the ideal spoiling and the 139.8° phase increment. Furthermore, using the SA2RAGE sequence with $\alpha_2 = 6^\circ$ implies a shortening of the range over which B_1^+ can be accurately measured (more than 20% loss in CNR_{width} if α_2 is reduced from 11° to 6° as can be seen in figure 4.3b and from the earlier deviation from linearity in

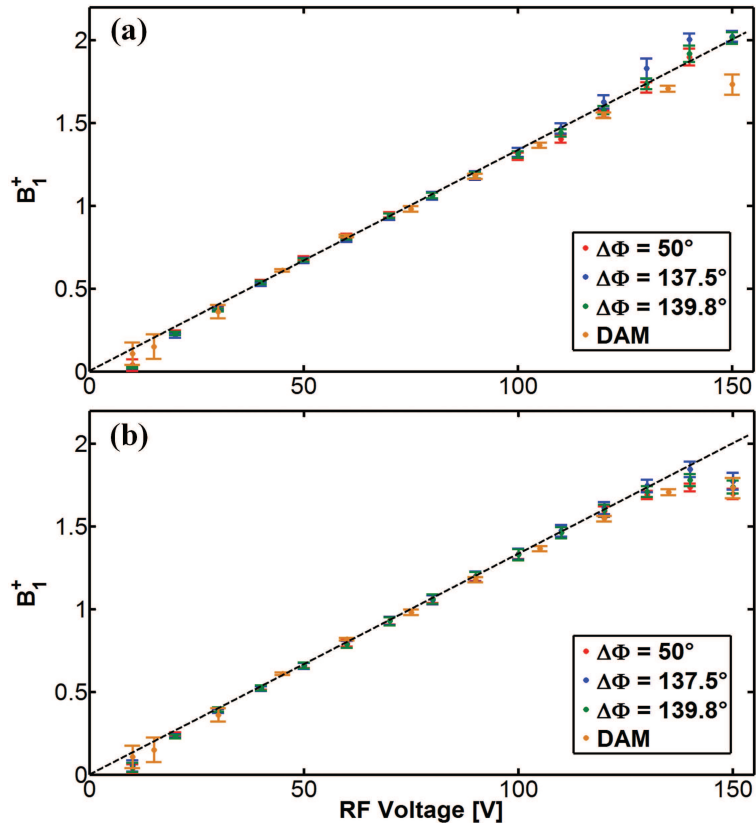


Figure 4.9: Mean values and standard deviations of B_1^+ calculated using the SA2RAGE sequence on a ROI (5x5x4 pixels) of an agar gel phantom as a function of the transmit RF voltage using (a) protocol A and (b) the small flip angle variation of protocol A ($\alpha_2 = 6^\circ$). The different colours correspond to different RF spoiling phase increments (50° , 137.5° , and 139.8°).

figure 4.9b than in figure 4.9a).

Figure 4.10 shows in vivo B_1^+ maps obtained with different RF spoiling phase increments. The differences between the tested RF spoiling increments are minor (cf. Fig. 4.10(b-d)), while using no RF spoiling introduced significant errors on the estimated values (cf. Fig. 4.10a). Again, the need to use RF spoiling decreases significantly as α_2 is made smaller (the bottom rows of figures 4.9 and 4.10 were obtained with $\alpha_2 = 6^\circ$, implying that for a relative $B_1^+ = 2$, the effective $\alpha_2 = 12^\circ$). Note that the in vivo B_1^+ map obtained in the absence of RF spoiling with small flip angles (Fig. 4.10e) closely resembles the B_1^+ maps obtained using the optimized RF spoiling schemes.

This appendix demonstrates both the importance of using an appropriate RF spoiling to obtain accurate B_1^+ values, but also that a large number of possible choices exist that have a small impact on the outcome of the measured B_1^+ . It should be noted that the three spoiling options evaluated are close to optimal in both evaluated metrics.

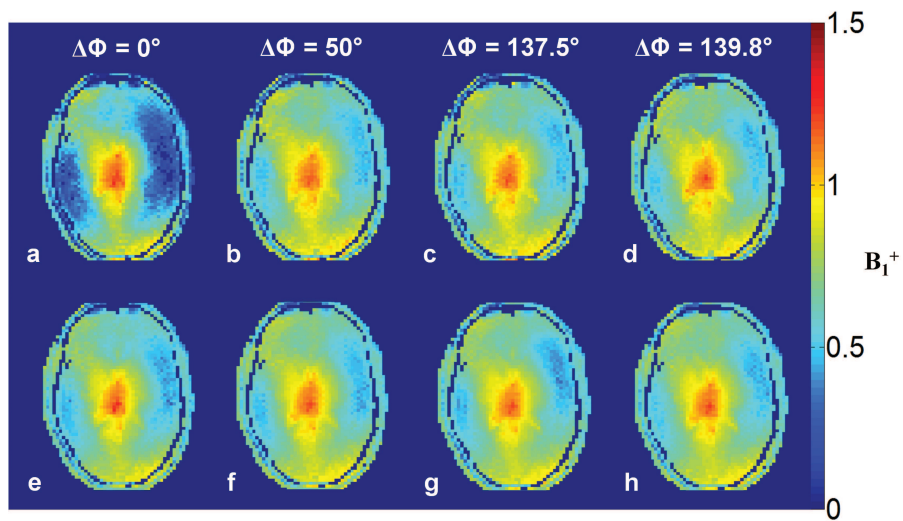


Figure 4.10: Axial views of 3D *in vivo* B_1^+ maps ($4 \times 4 \times 5 \text{ mm}^3$ resolution, $64 \times 64 \times 20$ matrix) calculated by the SA2RAGE sequence in 48s with the following parameters: $TR_{SA2RAGE}/TD_2 = 2.4/1.8\text{s}$, $\alpha_1/\alpha_2 = 4^\circ/11^\circ$ (top) and $\alpha_1/\alpha_2 = 4^\circ/6^\circ$ (bottom). Each column is related to a specific RF spoiling phase increment $\Delta\Phi$: $\Delta\Phi = 0^\circ$ (a,e); $\Delta\Phi = 50^\circ$ (b,f); $\Delta\Phi = 137.5^\circ$ (c,g); $\Delta\Phi = 139.8^\circ$ (d,h).

5

T_2 -weighted imaging with static k_T -points

Adapted from:

Florent Eggenschwiler, Kieran R. O'Brien, Rolf Gruetter and José P. Marques
Improving T_2 -weighted imaging at high field through the use of k_T -points
Magnetic Resonance in Medicine, 71, p.1478-1488, 2014

In this chapter, k_T -points designed in the small tip angle regime will be used to improve the T_2 -weighted images generated by a TSE sequence with variable flip angles. This methodology is referred to as a static k_T -points design since a single k_T -point pulse is designed for all the pulses of the sequence. Although the sub-pulse amplitudes in a k_T -point pulse are scaled according to the flip angle to reach, their ratios remain constant from one pulse to the next.

5.1 Improvement in T_2 -weighted imaging through the use of k_T -points

5.1.1 Introduction

T_2 -weighted imaging is a widely used MRI technique for the diagnosis of brain diseases involving gray and white matter lesions such as multiple sclerosis (MS).

T_2 -weighted imaging should benefit from the increased signal-to-noise ratio (SNR) available at high field strengths ($B_0 \geq 3\text{T}$) to allow higher spatial resolution acquisitions and hence better visualization of small brain structures. However, as explained in section 3.2 the distribution of the transmit magnetic field B_1^+ becomes non-uniform when moving towards ultra-high field. This spatial B_1^+ inhomogeneity gives rise not only to variations in signal intensity for a given tissue across the brain, but more importantly, to different degrees of T_1 or T_2 contrast between two tissues as has been shown in literature [86–88]. In particular, FLAIR imaging [87, 88], which is one of the most efficient techniques for highlighting contrast between GM and WM, and DIR imaging [86], which is widely used for GM visualization in MS, could be significantly improved by correcting the non-uniform B_1^+ profile observed at 7T and its propagation into the signal evolution of the involved turbo spin echo (TSE) sequence.

Adiabatic pulses have long been proposed as a means to reduce the sensitivity to transmit field inhomogeneities. It was shown that they can flip/invert/refocus the magnetization as expected even in the presence of substantial B_1^+ inhomogeneities [89]. Unfortunately, adiabatic pulses result in a much larger specific absorption rate (SAR) than amplitude modulated RF pulses. This limitation becomes even more prominent at higher field strengths.

PTx described in section 3.3 provides a new degree of freedom that can be utilized to mitigate B_1^+ inhomogeneity. The simplest methodology to take advantage of such hardware is to perform RF-shimming (cf. section 3.3.3) which has been used in the context of T_2 -weighted imaging at 3T to reduce the B_1^+ field inhomogeneity by using either global or varying RF-shimming combinations throughout a turbo spin echo train [90].

As explained in section 3.2.2, another promising method for B_1^+ inhomogeneity correction consists of designing short RF pulses applied at different locations in k-space and with different RF amplitudes. An even higher flexibility for the B_1^+ correction can be reached by combining this approach with PTx [38, 91], which allows the design of independent weightings of the k-space trajectory for each transmit channel of the array coil (cf. section 3.3.4).

Promising results have previously shown that RF pulses can be designed to produce a homogeneous excitation profile across a 2D FOV [29, 30, 33, 92] and equivalently in 3D, k_T -points were shown to provide highly homogenous excitation [36] and inversion profiles throughout the entire brain, giving rise to high quality T_1 -weighted images at 7T [93].

The aim of this article is to demonstrate that k_T -points can be used to significantly improve the homogeneity observed in non-selective 3D T_2 -weighted imaging at 7T. The T_2 -weighted images were acquired with a commercially available variable flip angle TSE sequence known as the Sampling Perfection with Application optimized Contrasts using different flip angle Evolutions (SPACE) sequence [94]. This sequence optimizes the signal evolution of the flip angle train for specified T_1/T_2 relaxation times and allows longer RF-pulse trains to be utilised.

At high field strengths, the inhomogeneous B_1^+ distribution makes the expected signal evolution of a specific tissue position dependent, leading to contrast variations throughout the image. The SPACE sequence's non-selective hard pulses were replaced by k_T -point pulses designed based on the subject's acquired B_1^+ map to improve the excitation profile homogeneity and remove the spatial dependent contrast in T_2 -weighted images.

Herein we show that the use of k_T -point pulses for both excitation and refocusing of the signal on a single channel transmit system and a parallel-transmit system can improve the T_2 -weighted imaging quality.

5.1.2 Methods

K_T -points and RF pulse design

The k_T -points were designed by making use of the STA approximation, which allows the three dimensional excitation profile after an RF pulse to be written as a Fourier transform expression involving a weighted k-space trajectory (cf. section 3.1.1).

Based on the transmit sensitivity of the RF coil transmitting in CP mode (single channel system) or of each transmit coil element (PTx system), the positions and weights of N k_T -points were optimized in order to obtain the most homogeneous excitation profile, by considering equation (3.79).

To find the N k_T -point locations, a modified version of the SOLO algorithm was implemented. The first k_T -point was fixed at $\vec{k} = \vec{0}$ and the subsequent k_T -points were searched on a 3D grid covering the following k-space locations: $k_x \in [-3\Delta k_x; +3\Delta k_x]$, $k_y \in [-3\Delta k_y; +3\Delta k_y]$, $k_z \in [-2\Delta k_z; +2\Delta k_z]$, where the grid steps $\Delta k_{x,y,z} = 1/FOV_{x,y,z}$. This set of low spatial frequencies was selected because only smooth variations in the brain's B_1^+ profiles are observed at 7T. For each k_T -point to be added, the SOLO algorithm fixes the previously determined k_T -points and evaluates each of the remaining positions of the grid. For each trial, the amplitudes and phases of the RF sub-pulses related to the involved k-space locations are optimized according to the local phase-exchange method [57]. The k-space location providing the excitation profile the closest to the targeted one is kept and the next algorithm

iteration begins. The algorithm stops when all the N desired k_T -points are found.

The optimization was performed for the voxels belonging to a 3D mask designed by applying BET (Brain Extraction Toolbox, www.fmrib.ox.ac.uk) on a GRE image used to calculate the coil transmit sensitivity.

When designing k_T -points on the PTx system, one particular set of RF weights was optimized for each coil element and Lagrangian multipliers, λ , were introduced to penalize the amount of RF power deposited, taking into account the fact that different channels had different forward and reflected power which made the SAR constraint to be channel dependent. A first estimation of the per channel sequence power was obtained from the RF power monitoring units of the PTx system when running the sequence with a short TR, low-resolution and without k_T -point pulse. Based on those values, the power per channel of the desired protocol with k_T -point pulses was calculated for each coil element. As long as all the computed power per channel values were not below a pre-computed threshold, the sub-pulses were redesigned by iteratively increasing the Lagrangian multipliers related to elements exceeding the limit.

The resulting k_T -point pulse consists of a set of RF sub-pulses and gradient blips corresponding to the weighted k-space trajectory designed by the SOLO algorithm. This k_T -point pulse is then used to replace the non-selective hard pulses in the TSE sequence in order to correct the effects of the B_1^+ -inhomogeneity in the resulting T_2 -weighted images.

K_T -point implementation and evaluation

The SOLO algorithm, being based on the STA approximation, has no information regarding the order in which the different k-space locations should be visited. Given that the TSE sequence uses pulses with flip angles beyond the range for which the STA approximation is valid, two types of sub-pulse sets were designed to replace the original pulses of the TSE sequence (Fig. 5.1a).

The first approach consisted in creating pulses with N sub-pulses corresponding to the N k-space positions found by the SOLO algorithm, similarly to what is usually presented in literature [29, 31, 35, 36]. Half of the sub-pulses were applied before the sub-pulse at $\mathbf{k} = \mathbf{0}$ and the remaining were applied after it (Fig. 5.1b). Since it contains most of the RF energy, the sub-pulse exciting k-space center was fixed at half of the RF pulse duration in order to guarantee a refocusing of the signal halfway through the duration separating the refocusing pulses of the TSE sequence. Such a k_T -point pulse made of N sub-pulses corresponds to the fastest way of exciting the optimized k-space trajectory and will be referred to as a "short k_T -point pulse".

In the second approach, the sub-pulse exciting the $\mathbf{k} = \mathbf{0}$ position was also forced at the centre of the trajectory for the same reason as for the short k_T -point pulse, and the remaining sub-pulses were split around it with their durations halved (Fig. 5.1c). In this way, the optimized k-space trajectory is visited twice with a total of $2N-1$ sub-pulses applied for an N k_T -point design. Halving the duration of the sub-pulses applied at $\mathbf{k} \neq \mathbf{0}$ locations was

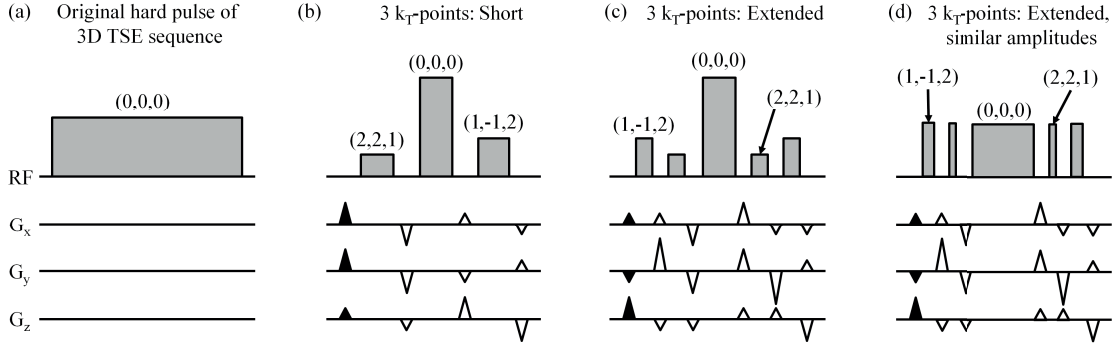


Figure 5.1: Types of RF pulse shapes for which performance analysis of the TSE sequence was realized. *a:* Original hard pulse exciting the k -space center position. *b:* Short k_T -point pulse exciting the k -space trajectory defined by: $k_1 = (2, 2, 1)^T \cdot 1/\text{FOV}$; $k_2 = (0, 0, 0)^T \cdot 1/\text{FOV}$; $k_3 = (1, -1, 2)^T \cdot 1/\text{FOV}$, with $\text{FOV} = (\text{FOV}_x, \text{FOV}_y, \text{FOV}_z)^T \text{ mm}^3$. The positions k_1 and k_3 were arbitrarily chosen for the example purpose. The large central pulse is applied at $\mathbf{k} = \mathbf{0}$. Other sub-pulses correspond to the other k -space positions found by the SOLO algorithm. *c:* Extended k_T -point pulse exciting the same trajectory as for the short k_T -point pulse. For both short and extended k_T -point pulses, CPMG conditions are fulfilled since each positive gradient blip is compensated by a negative one. *d:* Same extended k_T -point pulse as in (c) with reshaped sub-pulse amplitudes and durations in order to minimize the pulse SAR. Having the sub-pulse amplitudes similar across the whole pulse makes the energy deposition more efficient.

performed so that the excitation profile can be kept close to the one resulting from the STA approximation for longer by reducing the rotation associated with each sub-pulse, while allowing most of the energy to be delivered in the centre of the RF pulse and hence have the refocusing of the MR signal still at the centre of the echo spacing. As its duration is increased in respect to the short k_T -point pulse and its excitation profile should be closer to the STA approximation in a larger range of flip-angles, this pulse will be referred to as an "extended k_T -point pulse".

In TSE sequences, several types of echoes (Hahn echo, stimulated echo, etc.) arise from multiple refocusing mechanisms. It is fundamental that the phases of simultaneously acquired echoes are coherent in order to avoid SNR degradation and image artefacts. To ensure that the multiple echoes of the TSE sequence occur at the desired time points with phase consistency, the CPMG conditions (cf. section 2.3.4.2) must be fulfilled throughout the entire train of flip angles. It was also shown in section 2.3.4.2 that the gradient moments between two successive RF pulses of the sequence have to be balanced. Hence, gradient blips (solid triangles in figure 5.1b and c) were added for each type of pulse at the start in order to fulfill this property. This ensures that the k -space trajectory is correctly visited according to the backwards time-relationship given in equation (3.15) stating that the k -space trajectory always finishes at $\mathbf{k} = \mathbf{0}$, but also that it starts from the $\mathbf{k} = \mathbf{0}$ position (only relevant for the refocusing pulses). Having a gradient blip before applying any RF waveform in the k_T -point pulse may look irrational at first sight but it is important not to forget that transverse magnetization exists between the refocusing pulses.

Triangular gradient blips with 300 T/m/s slew rate were used in this work. Given that the k_T -point locations correspond to low spatial frequencies, the gradient blip durations were

of 50-150 μ s.

To determine the best strategy between short and extended k_T -point pulses, Bloch simulations of the excitation profiles provided by both methods were performed for a range of flip angles going from 45° to 120° which encompasses the range of RF pulses applied in the TSE sequence. For those simulations, equilibrium initial magnetization $M = (M_x, M_y, M_z)^T = (0, 0, 1)^T$ was assumed. The excitation profiles $e(\vec{r})$ were calculated in the following way

$$e(\vec{r}) = \tan^{-1} \left(\frac{M_{xy}(\vec{r})}{M_z(\vec{r})} \right) \frac{1}{\alpha^{nom}} e^{i\angle M_{xy}(\vec{r})} \quad (5.1)$$

such that $|e(\vec{r})|$ represents a multiplicative factor of a nominal flip angle α^{nom} . M_{xy} and M_z correspond to the states of transverse and longitudinal magnetizations at the end of the pulse.

To further evaluate the different k_T -point implementations and their similarity to the STA regime, full Bloch simulations were additionally calculated for 5 different subjects and 4 types of k_T -point pulses: short N (N k_T -points - N sub-pulses, Fig. 5.1b); extended N (N k_T -points - 2N-1 sub-pulses, Fig. 5.1c); short 2N-1 (2N-1 k_T -points - 2N-1 sub-pulses); extended N asymmetric (N k_T -points - 2N-1 sub-pulses with the $\mathbf{k} = \mathbf{0}$ sub-pulse applied at the end of the waveform).

The third waveform (short 2N-1) was introduced to guarantee that the improvements observed were not simply due to the increased number of sub-pulses, but by effectively reducing their tip angle.

The last waveform was analysed to determine if having a certain form of symmetry was an important feature when designing a single set of k_T -points for the excitation and refocusing pulses of the sequence (even if frequency evaluation was not considered during the RF pulse).

The deviation between full Bloch equation profile and the excitation profile resulting from the STA approximation, $STA(\vec{r})$ was calculated as

$$\left\| \frac{e(\vec{r}) - STA(\vec{r})}{STA(\vec{r})} \right\|_1 \quad (5.2)$$

for different flip-angles (10° to 120° in steps of 10°). All the possible arrangements of the sub-pulses applied at $\mathbf{k} \neq \mathbf{0}$ locations for each of the 5 different subjects were considered in this analysis.

Turbo spin echo sequence simulation with Spatially Resolved Extended Phase Graph

To evaluate the impact of introducing k_T -points in the TSE sequence, the signal throughout the sequence was simulated using the phase-graph formalism (description presented in section 2.2.6). This methodology presents the advantage that it describes the full Bloch equations with a relatively low computational demand.

The B_1^+ profile and the designed k_T -points were taken into account in the signal calculation, which means that each flip angle of the TSE sequence becomes position dependent. A similar model, the Spatially Resolved Extended Phase Graph (SR-EPG), which considers spatially varying flip angles throughout a TSE sequence was proposed in [90]. Full Bloch simulations of the magnetization evolution throughout the TSE sequence were thus performed by using this model.

To ensure that the magnetization reaches the steady-state, the sequence was simulated over $5 \cdot TR$ periods. The signal acquired at time TE was calculated for 5 subjects for the case of : (a) hard pulses (Fig. 5.1a); (b) short 3 k_T -point pulses (Fig. 5.1b); (c) extended 3 k_T -point pulses (Fig. 5.1c); (d) short 5 k_T -point pulses; (e) extended 3 k_T -point asymmetric pulses.

The deviation from the theoretical EPG signal (assuming perfectly homogeneous B_1^+ field) was computed similarly to what was described in the previous section.

Experimental setup

In-vivo scans were performed on a Siemens 7T scanner (Siemens Healthcare, Germany) with parallel transmission capabilities and equipped with a head gradient insert (maximum gradient amplitude and slew rate of 80 mT/m and 333 T/m/s respectively). A 32 channel coil (Nova Medical, USA) was used when transmitting RF signals in combined mode (single channel system) whereas a custom-designed eight channel transmit-receive array coil (RAPID Biomedical, Germany) was used for parallel transmission (PTx system).

The experimental protocol was approved by local ethics committee and two healthy subjects providing informed consent were scanned. For subject's safety, simulations of the eight channel transmit-receive array were performed for the use of PTx system and the worst case scenario (sum of in phase electric fields over the whole brain) implied that the maximum power delivered by each coil element was limited to 0.9W/10s and 0.3W/6min.

B_1^+ -mapping protocol

When using the single channel system, the transmit sensitivity profile was obtained by acquiring an absolute B_1^+ map of the subject's brain using the SA2RAGE sequence presented in chapter 4 with the following parameters: TR = 2.4s, TE = 1.35 ms, $TD_1 = 50$ ms, $TD_2 = 1800$ ms, $\alpha_1 = 4^\circ$, $\alpha_2 = 11^\circ$, $3.2 \times 3.2 \times 4.0$ mm³ resolution and a $64 \times 64 \times 48$ matrix size acquired with sagittal orientation (acquisition time of 1min28s).

With the PTx system, the transmit sensitivity profiles of every array elements were required. To find those profiles, the methodology presented in section 3.3.2 was used. The SA2RAGE acquisition was performed with the same protocol as that used for the single channel system and array elements transmitting with channel phases defined such that constructive interferences occur at the brain center. FLASH images were acquired with a protocol equivalent to the SA2RAGE sequence in terms of echo time, resolution and bandwidth (remaining parameters TR = 3.5s, $\alpha_1 = 1^\circ$, acquisition time 11s). The FLASH acquisitions were performed with a phase configuration identical to the one used for the SA2RAGE sequence.

Turbo spin echo protocol

Replacing the original hard pulses of the TSE sequence with variable flip angles by sets of sub-pulses and gradients blips increases the SAR of the sequence, which is especially problematic when using the PTx system for which the SAR limits are more restrictive. As a consequence, the duration of these pulses had to be longer than would have been necessary using simple hard pulses. This inherently affected the echo spacing (and hence echo time) of the sequence and the calculation of the flip angle train. To keep the comparison simple and limited to the change of the homogeneity of the excitation profile, and not to echo times and different flip angle trains, the same pulse length was used with and without k_T -points. While this might have affected the maximum signal and contrast achieved by the TSE sequence when using hard pulses, it should not have affected the homogeneity of the contrast throughout the brain.

The following protocols were used in the different systems

- (i) single channel system: TR = 1s, TE = 313ms, echo train length (ETL) = 120, echo spacing (ES) = 5.68ms, RF duration (RF_{Dur}) = 2.11ms, resolution = $0.8 \times 0.8 \times 0.8 \text{ mm}^3$, matrix size = $320 \times 320 \times 208$ and 4 k_T -points per RF pulse (total acquisition time 4min15s);
- (ii) PTx system: TR = 6s, TE = 460ms, ETL = 120, ES = 7.66ms, RF_{Dur} = 3.08ms, resolution = $0.75 \times 0.75 \times 0.85 \text{ mm}^3$, matrix size = $256 \times 256 \times 176$ and 3 k_T -points per RF pulse (total acquisition time 13min08s).

As the role of the first refocusing pulses is mainly to lead the magnetization towards steady-state and the signal associated with them has much higher amplitude than that of the steady-state, the echoes occurring at the beginning of the refocusing train were not used for image reconstruction. For the protocols used on the single channel and PTx systems, 15 and 20 echoes were respectively discarded at the beginning of the train.

On both systems, a standard TSE image with identical parameters and non-selective hard pulses of the same duration as the k_T -point pulses was also acquired for comparison.

Data processing

To focus on the improvement provided by k_T -points in terms of contrast and signal homogeneity, bias field correction was subsequently applied to the anatomical images acquired on the single channel system, in order to remove the signal variations related to the highly non-uniform reception profile $B_1^-(\vec{r})$ of the 32 channel coil. The bias field correction was performed using FAST (FMRIB's Automated Segmentation Tool, www.fmrib.ox.ac.uk) which calculates a smooth profile, mainly corresponding to $B_1^-(\vec{r})$ [95].

This processing step was not applied on images acquired on the PTx system since an acceptable homogeneity was observed for the B_1^- profile of the eight channel array coil. The SPACE images resulting from this correction were visually compared with the uncorrected

ones.

5.1.3 Results

k_T -point implementation and evaluation

Designing the k_T -point pulses based on the B_1^+ profiles resulting from the SA2RAGE acquisition (Fig. 5.2a), leads to the STA approximation maps (Fig. 5.2b) that were compared with the full Bloch simulations of the excitation profiles related to the short and extended k_T -point pulses (Fig. 5.2 c and d), performed for different flip angles.

The simulated magnitude and phase of the excitation profiles $e(\vec{r})$ after the pulse, given by

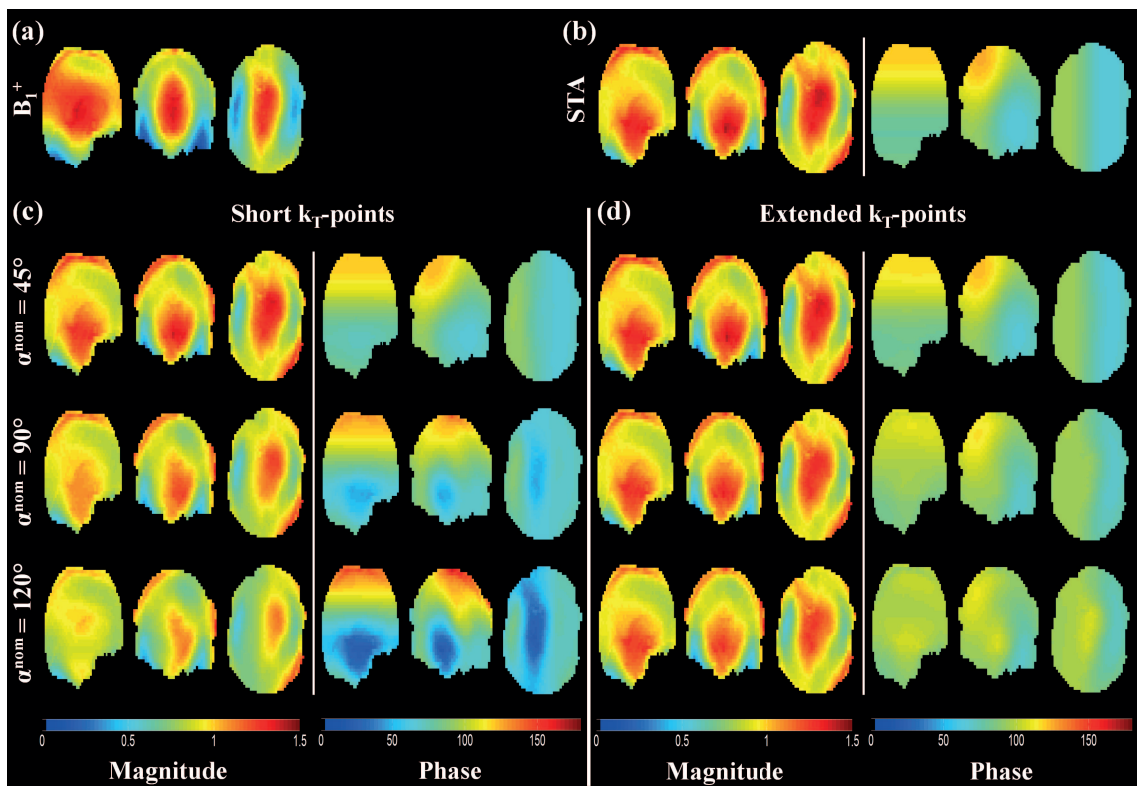


Figure 5.2: *a:* B_1^+ profiles of a particular subject acquired using the SA2RAGE sequence. *b:* Magnitude and phase of the excitation profile expected from the STA approximation. Alternatively, excitation profiles calculated by full Bloch simulations of (c) short k_T -point (Fig. 5.1b) and (d) extended k_T -point (Fig. 5.1c) pulses related to the design of 3 k_T -points in the single channel system, performed based on the B_1^+ profiles in (a). The range of flip angles simulated in c and d roughly corresponds to the one used for the train of refocusing pulses in the TSE sequence.

equation (5.1) are displayed for each type of pulse. Figure 5.2c shows that both magnitude and phase of the excitation profiles involving a short k_T -point pulse start to diverge from the STA approximation solution when simulating large flip angles ($> 60^\circ$). This observation can be explained by the fact that such flip angles are out of the regime where the STA approximation holds, as described in [37, 40]. However with an extended k_T -point pulse,

Fig. 5.2d demonstrates that the excitation profiles remain remarkably close to the STA approximation solution even when simulating flip angles as high as 120° .

Figure 5.3 shows SR-EPG simulations of the TSE sequence for both types of k_T -point pulses considered (Fig. 5.3 b and c). For comparison, the profiles simulated without k_T -point are

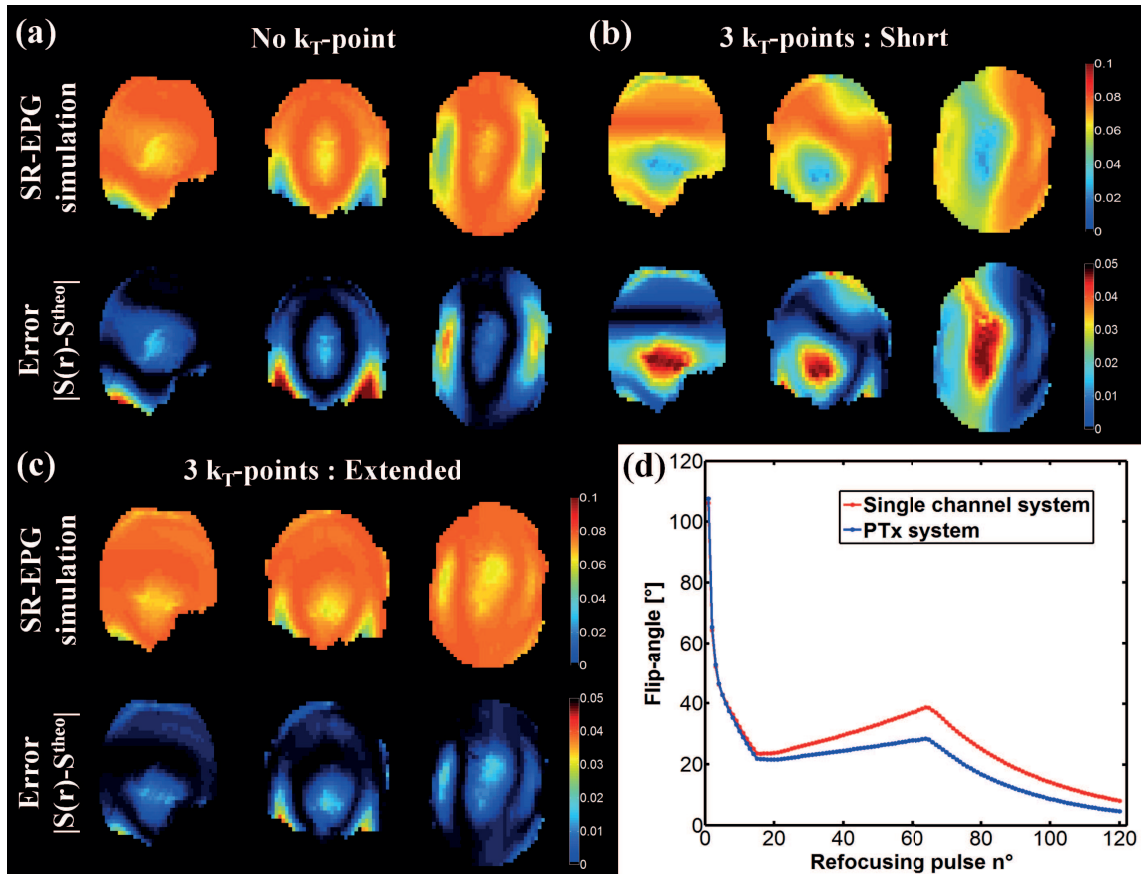


Figure 5.3: Signal coming from the central k -space acquisition calculated with SR-EPG simulations of the TSE sequence for a particular subject. The signal maps calculated by using (b) short (Fig. 5.1b) and (c) extended (Fig. 5.1c) 3 k_T -point pulses in the sequence were compared with the profiles simulated without k_T -point (a). The second row in a, b and c displays the profiles of the absolute value of the difference between images of the first row $S(\mathbf{r})$ and the theoretical signal at k -space center S^{theo} calculated assuming a perfectly homogeneous B_1^+ distribution across the brain. d: Flip angle train for the TSE sequence when using the protocols presented in the methods section for the single channel system (red curve) and for the PTx system (blue curve).

also displayed (Fig. 5.3a). The sequence parameters presented in the methods section for the single channel system were used for those simulations.

On figure 5.3 a-c, the first row shows the TSE signal for a tissue of $T_1/T_2=1.5\text{s}/75\text{ms}$ simulated after the 55th refocusing pulse (k -space center) for each voxel within the region of interest. On the second row, the difference between the profiles of the first row and the theoretical signal at k -space center calculated with the standard extended phase graph simulation (assuming a perfectly homogeneous B_1^+ distribution) is presented.

The flip angle values for the train of refocusing RF pulses throughout the TSE sequence

corresponding to the protocol used for the single channel (red curve) and PTx (blue curve) systems are presented on figure 5.3d.

The profiles displayed on figure 5.3 confirm the higher quality of the results obtained when using an extended k_T -point pulse. Comparing the mean of the error maps of both types of pulses (cf. second row of figure 5.3 a-c) it is possible to conclude that the extended k_T -point pulse outperforms the short k_T -point pulse by more than 60% in terms of signal homogeneity obtained in the final image. This difference is mainly due to high flip angles of the refocusing pulses present at the beginning of the train (cf. Fig. 5.3d) where the deviation from the STA varies significantly depending on which pulse is used (cf. last row of Fig 5.2 c and d). Moreover, the severe phase variation observed between the last two rows of Fig. 5.2c, means that when using short k_T -point pulses in the TSE sequence, for many voxels, the CPMG conditions are violated between the excitation and refocusing pulses and between high flip angle refocusing pulses. This phase discrepancy leads to a higher inhomogeneity (Fig. 5.3b) of the signal maps than that obtained when using standard hard pulses (Fig. 5.3a), especially in regions exhibiting large variations in the phase profiles of figure 5.2c.

The high stability in the phase profiles of the extended k_T -point pulse (Fig. 5.2d) suggests that the validity of CPMG conditions is extended up to a larger flip angle range as is supported by SR-EPG simulations (Fig. 5.3c).

To further support the results of figure 5.2, the deviations from the STA regime of four different k_T -point waveforms are displayed on figure 5.4a. Comparing the curves related to

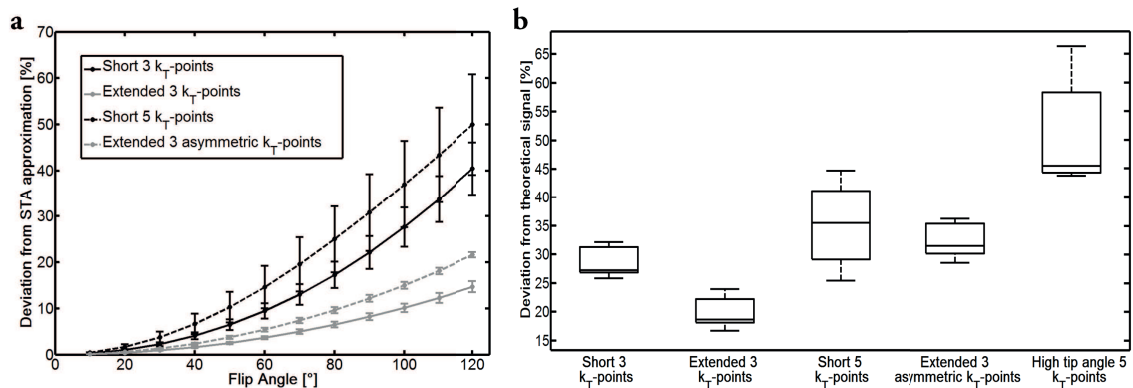


Figure 5.4: a: Plot of the deviation between the excitation profile corresponding to full Bloch simulations of an RF pulse and the excitation profile of the STA approximation as a function of the flip angle. Four different pulses are shown: a short 3 k_T -point pulse (solid black); an extended 3 k_T -point pulse (solid grey); a short 5 k_T -point pulse (dashed black); an extended asymmetric 3 k_T -point pulse (dashed grey). For each type, all the configurations of the sub-pulses corresponding to off-centered k -space positions were simulated for 5 different subjects. Each point represents the average and standard deviation (given by error bars) over the subjects and sub-pulse configurations. b: Box-and-whisker diagrams of the deviation between the theoretical signal and the SR-EPG simulations for 5 different subjects. On the x-axis the different tested pulse configurations are shown. Additionally to the four trajectories and waveforms in (a), the results for a pulse designed based on the extended 3 k_T -point pulse, and optimized on the high tip angle regime to offer homogeneous 60° excitation are shown.

short and extended k_T -point pulses in figure 5.4a clearly confirms that the excitation profile

stays closer to that of the STA approximation when exciting with the extended k-space trajectory. The same conclusion can be arrived at by comparing the curves corresponding to the extended 3 k_T -point pulse and the short 5 k_T -point pulse, which are both pulses made of 5 sub-pulses. This observation suggests that the improvement is not due simply to the number of sub-pulses of the k_T -point waveforms but to effectively reducing the rotation associated with each sub-pulse.

Figure 5.4b emphasizes that extended k_T -point pulses perform better than short k_T -point pulses not only for excitation but also when used as refocusing pulses. The deviation between the theoretical signal profile (perfectly homogeneous B_1^+) and the one simulated by considering k_T -points is smaller for an extended 3 k_T -point pulse than for a short 5 k_T -point pulse, despite the fact that the latter provides a more homogenous excitation profile in the STA regime.

The extended 3 k_T -point waveform with the sub-pulse associated to $\mathbf{k} = \mathbf{0}$ position applied at the end showed acceptable excitation properties (Fig. 5.4a) but was worse than both the short and extended 3 k_T -point pulses on the SR-EPG simulations (Fig. 5.4b). This shows that having the large sub-pulse exciting the k-space center in the middle of the RF shape is important not only from an echo formation point of view, but also to guarantee a better refocusing capability of the k_T -point pulse.

Finally, a k_T -point waveform was designed in the high tip angle regime [40, 96, 97] using a gradient descent method over the Bloch simulations, starting from the extended 3 k_T -point solution. An homogeneous excitation profile was targeted for a 60° flip angle (roughly corresponding to the average flip angle of the first ramp of the echo train in figure 5.3d) and the k-space trajectory was kept the same as for the extended 3 k_T -point pulse (optimization of the sub-pulses only).

Although the excitation profile homogeneity of the high tip angle RF shape outperformed the one of the extended 3 k_T -point pulse by 30% in terms of std/mean, figure 5.4b shows that using such a pulse to replace the pulses of the TSE sequence had the worst outcome in terms of TSE signal homogeneity. This can be explained by the fact that homogeneity in the excitation profile obtained for a 60° k_T -point pulse (which is optimal) rapidly deteriorates for other flip angle values.

The set of sub-pulses and gradients used to replace the original hard pulses of the TSE sequence on the single channel system are displayed in figure 5.1d (example with $N = 3$). The sub-pulses in figure 5.1c were distributed over the predefined total pulse duration (RF_{Dur}) in a way minimizing the SAR of the k_T -point pulse. A 29% SAR drop was observed when comparing the pulses of figure 5.1 c and d.

The sub-pulse amplitudes were finally weighted according to the flip angles of the excitation pulse and the refocusing pulse train (cf. Fig. 5.3d). This was also performed on the PTx system, where one specific set of sub-pulses was designed for each array element.

On the single channel and PTx systems the use of k_T -points respectively comes at the cost of an 8 and 3 fold increase in global SAR when compared to a hard pulse with the same total

duration meaning that the RF pulse used had to be adapted to have a length respectively ~ 3 and ~ 2 times bigger than that would be possible when using standard hard pulses.

Excitation profiles and TSE images

Excitation profiles simulated with and without 4 k_T -points for the single channel system are presented in the first row of figure 5.5. The corresponding TSE images are displayed on the

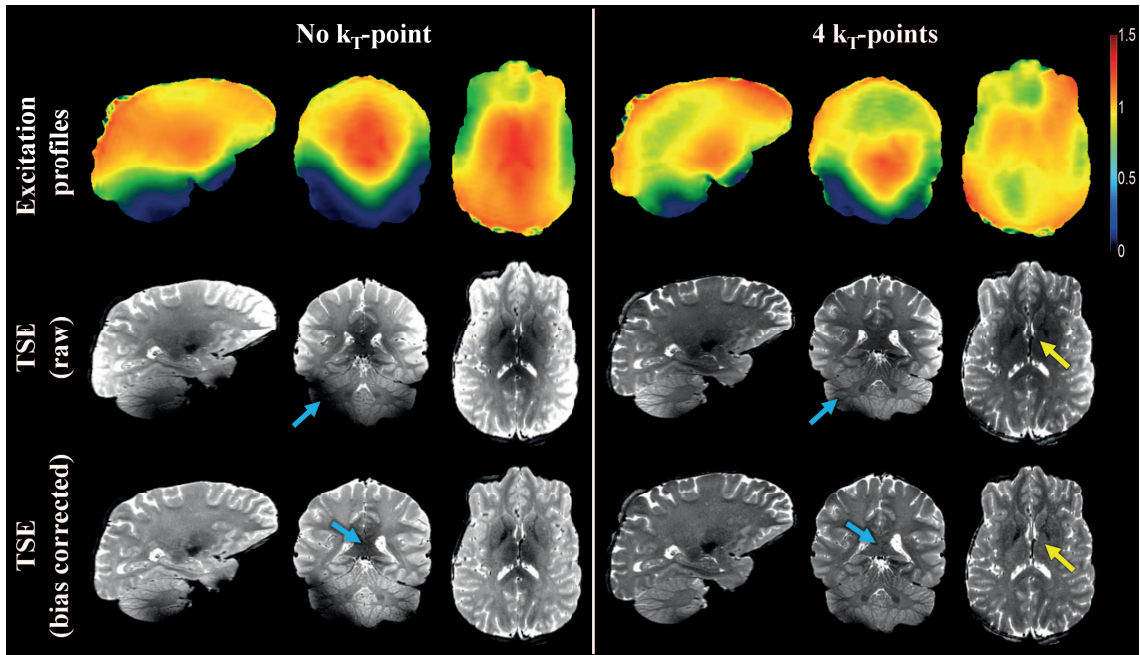


Figure 5.5: Excitation profiles and TSE images obtained with (right columns) and without (left columns) the use of 4 k_T -points on the single channel system. The k_T -points were designed to correct the inhomogeneous excitation profile measured at 7T using the SA2RAGE sequence. The second row shows raw TSE images that subsequently underwent bias field correction (third row) using FAST. Blue arrows highlight areas where signal homogeneity was highly improved. Yellow arrows emphasize the fact that residual signal variations observed on images acquired using k_T -points are dominated by the receive field non-uniformity.

following rows. The second row presents the raw TSE images, whereas the third one shows TSE profiles subjected to bias field correction. Using 4 k_T -points improves the predicted excitation profile homogeneity which leads to less signal variation for a given tissue across the brain. Considerable improvement occurs in the cerebellum and in the central brain region (blue arrows) both prior to and post bias field corrections.

The darker region still observable in the brain center when 4 k_T -points are used (yellow arrows) is significantly reduced when using bias field correction demonstrating that it is most likely to be due to the receive coil profiles (B_1^-). On the other hand, the contrast observed in this region (close to the thalamus) in the absence of k_T -point, remains even after bias field correction. This region of low intensity is correlated with regions of high B_1^+ field and not to anatomical contrast (as can be observed by its extension to the corpus callosum).

Some dark areas still persist on the bias field corrected images of the right columns. Those

regions are correlated with the remaining low intensity regions of the corrected excitation profile.

Figure 5.6 shows the results obtained on the PTx system (8 channels) when 3 k_T -points are designed.

Blue arrows point out regions that are severely affected by the inhomogeneity in the orig-

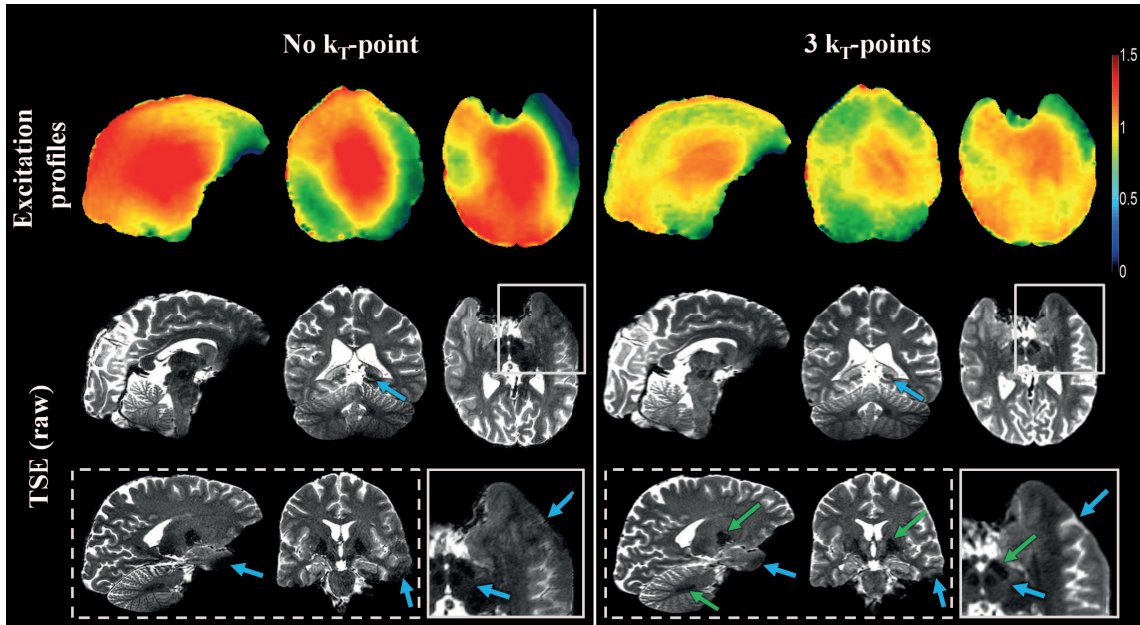


Figure 5.6: Excitation profiles and TSE images obtained without (left columns) and with (right columns) the use of 3 k_T -points on the PTx system. Raw TSE images are presented in the second and third rows. Solid boxes: Zooms over the top-right area of the axial profiles presented in the second row. Improved GM-WM contrast is clearly observed in the temporal lobe in the inset corresponding to the anatomical image acquired by using 3 k_T -points. Dashed boxes: Sagittal and coronal views of the raw TSE images for slices different from the ones presented in the second row. Blue arrows highlight brain parts for which signal homogeneity was highly improved whereas green arrows point out the fact that structures known to be iron rich are clearly distinguishable on the TSE images acquired using k_T -points.

inal excitation profile and for which the improvement provided by the k_T -points is most relevant. On the middle row the arrows highlight the intensity asymmetry between the left and right hippocampus observed in the absence of k_T -point and corrected after using k_T -points. In the bottom row, a magnified view over the top-right area of the axial slices through the temporal lobe highlights the lack of contrast between grey and white matter which is recovered by designing 3 k_T -points (blue arrows). Also the signal intensity in the white matter surrounding the red nucleus and substantia nigra is significantly increased with the proposed methodology.

Throughout the TSE images acquired with k_T -points it is possible to observe that regions of low intensity reflect (as expected) structures known to be iron rich such as the dentate nucleus in the cerebellum, the red nucleus and substantia nigra in the brain stem, subthalamic nuclei and the globus pallidus (green arrows). On the other hand, in the absence of k_T -point regions of low intensity can also be attributed to the high and low nominal B_1^+ values visible

on the excitation profiles.

5.1.4 Discussion

This study shows that T_2 -weighted images, known to be highly affected by the inhomogeneous distribution of the B_1^+ field observed at 7T [86–88], can be considerably improved by replacing the original hard pulses of a TSE sequence with variable flip angles by k_T -point pulses. It was also demonstrated that exciting the optimized k-space trajectory multiple times with a reduced rotation associated to the sub-pulses applied at the off-centre k-space locations, extends the validity of the STA approximation up to flip angles as high as 120° . The comparison of short and extended k_T -point pulses was performed according to their excitation properties (transfer of M_z towards M_{xy}) in figures 5.2 and 5.4a. The same examination could also be conducted for the other transfer pathways, e.g. refocusing (M_{xy} towards M_{xy}^* , where M_{xy}^* is the complex conjugate of M_{xy}). This was implicitly done when simulating the signal using the SR-EPG framework, cf. figures 5.3 and 5.4b, which takes all the transfer pathways into account.

The homogeneity observed for the TSE profiles resulting from the use of extended k_T -point pulses thus means that this type of pulse is better suited for all transfer pathways (excitation and refocusing). From the previous discussion it can be concluded that: the design of a single set of k_T -points for the pulses of a TSE sequence highly benefits from exciting the optimized k-space trajectory twice (with the RF energy of the sub-pulses applied at off-center k_T -points halved). It should be emphasized though that, independently of the argument of echo formation at the centre of the echo spacing (the SR-EPG did not consider frequency evolution during the RF pulses), symmetry in the extended k_T -point waveforms (large sub-pulse in the center of the RF shape) provides a higher degree of homogeneity in the signal calculated (Fig. 5.4b).

The only cost of the extended k_T -point pulse is in the length of the RF pulse (due to the increased number of gradient blips) that was 9 and 5% longer for the single and pTx systems respectively.

Designing 4 k_T -points on the single channel system already provided a high degree of homogeneity on the anatomical images (Fig. 5.5). However, some areas exhibit low signal even after bias field correction. Those areas are highly correlated with the remaining low intensity regions of the excitation profile.

To further improve the excitation profile homogeneity, the number of designed k_T -points could be increased. However, to sufficiently correct those low intensity regions, a large number of k_T -points would be needed (data not shown), which would be prohibitive due to both SAR and pulse length limitations.

Another approach to obtain a higher homogeneity of the excitation profile when using the single transmit system would be the combination of the proposed method with the use of

highly dielectric pads positioned close to the cerebellum [98, 99] which can significantly improve the available B_1^+ field in this region. Furthermore, such a methodology that increases the strength of the B_1^+ field in regions where it is currently virtually absent will have a positive impact in terms of SAR (as it will decrease the amplitude of the various sub-pulses).

Designing k_T -points combined with parallel transmission further improved the homogeneity of the excitation profile throughout the brain and consequently the quality of TSE images (Fig. 5.6). Despite the fact that different RF coils and subjects were used, it can be nevertheless observed that the excitation profiles obtained with the PTx system outperformed those of the single channel system even when using a smaller number of k_T -points and despite the need to use regularization parameters to minimize the delivered power. Note that due to higher SAR restrictions on the PTx system, a less SAR-intensive protocol of the TSE sequence (lower refocusing pulses; cf. Fig. 5.3d) and a 6-fold longer repetition time were used. In the future, using methodologies recently proposed to monitor the local SAR deposition based on various body models [27, 100], and additionally incorporate the design of the k_T -point waveform [101] and different regularization parameters for the different channels [102] should allow the SAR limits to be relaxed, and more efficient protocols to be used.

Although B_0 -shimming was performed on both single channel and PTx systems to reduce the B_0 inhomogeneity effects, TSE images acquired using k_T -points are still affected by the residual B_0 non-uniformity, for example in figure 5.5 where a darker signal is observed in the frontal lobe region. This effect is more pronounced on the images acquired with the PTx system due to the reduced bandwidth of the 3.08ms RF-pulses used throughout the sequence. Such artifacts could be minimized either by designing shorter k_T -point pulses (at the cost of an SAR increase), or by mapping the B_0 field distribution across the brain and considering it in the pulse designing procedure [37, 103].

Another source of errors in the RF-pulse design process can arise from the inaccuracy of the B_1^+ maps used. Indeed, the precision with which the transmit field is measured decreases on low B_1^+ regions [104]. On the single channel system, this limitation can be overcome by increasing the B_1^+ field on those regions, either with the use of a higher RF voltage or, as mentioned earlier, with the utilization of highly dielectric pads [99].

On the PTx system, the B_1^+ maps related to individual coil elements were calculated by combining an absolute B_1^+ measurement with eight individual relative B_1^+ maps (obtained from different modes via matrix inversion, cf. section 5.1.2). The limitation of this approach is that inaccuracies in regions with low values in the quantitative B_1^+ maps will be amplified when the low B_1^+ values are of destructive interference origin (the ratio of FLASH images for various channels in equation (3.64) is greater than one). This can significantly affect the individual coil profiles. A possible solution would be to repeat the B_1^+ -mapping procedure (both quantitative and relative measurements) by using a phase combination such that constructive interferences occur at the regions presenting low values on the first absolute B_1^+ acquisition. A matrix inversion taking both datasets into account would thus provide individual B_1^+ profiles with improved quality.

It is hence possible that the inhomogeneity on some regions was not corrected to its full capacity because the B_1^+ field used in the pulse design algorithm was not accurately measured (for example, in the temporal lobe).

In this paper, a single set of N k_T -points was optimized for all the RF pulses of the TSE sequence and the STA approximation was used throughout although pulses as high as 120° were used in the protocols. The next step for improving further the quality of T_2 -weighted imaging will be to design separate k_T -points for the excitation and for the refocusing pulses, the ultimate goal being to optimize a k_T -point waveform for each pulse of the TSE sequence. To this end, the methodology presented in [90] would be of particular interest since instead of optimizing the excitation profile, it directly models and optimizes the signal throughout the TSE sequence with the SR-EPG framework. As in this framework all transitions are already described by a full Bloch equation formalism, the outcome will not be sensitive to deviation from the STA regime which could further improve the quality of the resulting T_2 -weighted images. More importantly, such an increase of the degrees of freedom could allow the usage of shorter and less SAR intensive k_T -point pulses affording the use of more efficient protocols.

5.1.5 Conclusions

We conclude that replacing the original hard pulses of the TSE sequence by one set of sub-pulses exciting an optimized k-space trajectory provides T_2 -weighted images of high quality in terms of signal and contrast homogeneity. Combining this methodology with parallel transmission gives access to anatomical images largely devoid of artefacts resulting from the common B_1^+ inhomogeneity at 7T.

6

K_T -point design in the HTA regime & T_2 -weighted imaging with dynamic k_T -points

This chapter starts by presenting a methodology developed to extend the optimization of k_T -points beyond the STA regime.

In the previous chapter, it was shown that the signal and contrast inhomogeneities observed in T_2 -weighted imaging at 7T can be corrected by designing a single k_T -point pulse in the STA regime and use it to replace the original hard pulses of a TSE sequence with variable flip angles (static k_T -points). The other goal of the current chapter is to demonstrate that T_2 -weighted images can be further improved by considering the SR-EPG formalism to design specific k_T -points for each pulse of the TSE sequence (dynamic k_T -points).

6.1 K_T -points described by Cayleigh-Klein coefficients

6.1.1 Introduction

The use of k_T -points is promising for the correction of the inhomogeneous B_1^+ distribution resulting from the short wavelength present at high field strengths ($B_0 \geq 3T$). The k_T -point design was first proposed in the small tip-angle (STA) regime and was then extended to large tip-angles [93] using the optimal control approach [40] which is highly demanding in terms of computation resources. A faster methodology would be highly desirable, especially when combining k_T -points with a turbo spin echo (TSE) sequences with variable flip angles for which several high tip-angle k_T -points have to be designed (cf. section 6.2). This section presents a new approach for designing high tip-angle k_T -point pulses based on a linearization of the Bloch equations and the usage of symbolic notation to accelerate the computation when the optimization has to be performed for a large number of voxels.

6.1.2 Methods

When designing a high tip angle k_T -point, a first estimation of the N k_T -point positions and weightings was performed in the STA regime using the SOLO algorithm.

It was shown in chapter 5 that exciting the k-space trajectory defined by the optimized k_T -points in a symmetric way: the $k=0$ position forced at the center of the trajectory and the remaining k_T -points symmetrically split around it with their amplitudes halved (Fig. 6.1), offers a large range of validity to the STA approximation and hence a good starting point for further optimizations. A symmetric k_T -point pulse is made of a set of N RF sub-pulses (SP) and $3(N+1)$ gradient waveforms defined by the k_x , k_y and k_z positions of the k_T -points. Considering the spin domain version of the Bloch equations introduced in section 3.1.2, the

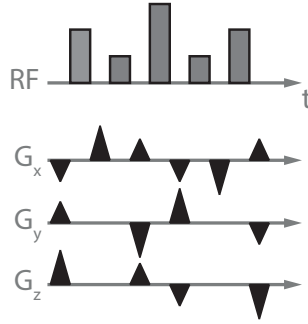


Figure 6.1: Set of symmetric sub-pulses and gradients ($N=5$ k_T -points) used as a starting point for the design of high tip angle k_T -point pulses.

states of the magnetization before and after a k_T -point pulse are linked by the system of equations (3.28). The Cayley-Klein parameters α and β are given by

$$\begin{pmatrix} \alpha \\ \beta \end{pmatrix} = Q^{Tot} \cdot \begin{pmatrix} 1 \\ 0 \end{pmatrix} \quad (6.1)$$

with

$$Q^{Tot} = Q^{G,N+1} \cdot Q^{RF,N} \cdot \dots \cdot Q^{G,2} \cdot Q^{RF,1} \cdot Q^{G,1} \quad (6.2)$$

describing the succession of RF sub-pulses and gradient waveforms applied during the k_T -point pulse. As a reminder, each Q matrix has the form

$$\begin{pmatrix} a & -b^* \\ b & a^* \end{pmatrix} \quad (6.3)$$

where

$$\begin{aligned} a &= \cos(\phi/2) - in_z \sin(\phi/2) \\ b &= -i(n_x + in_y) \sin(\phi/2) \end{aligned} \quad (6.4)$$

describe a rotation through an angle ϕ about a vector $\vec{n}=(n_x, n_y, n_z)^T$. In this specific problem, α and β coefficients are functions of the amplitudes and phases of the k_T -point weights as well as their k_x, k_y, k_z positions. Since the pulse is made of N sub-pulses and $3(N+1)$ gradient blips, $N_P = 2N+3(N+1)$ parameters can be optimized in order to obtain the desired magnetization distribution. The factor 2 comes from the fact that the amplitude and phase of each sub-pulse can be optimized.

The optimization of the pulse parameters P_i ($i \in [1, N_P]$) was done by using a linear extension of the targeted coefficients α_{aim} and β_{aim}

$$\begin{aligned}\alpha_{aim} &\approx \alpha + \frac{\partial \alpha}{\partial P} \Delta P \\ \beta_{aim} &\approx \beta + \frac{\partial \beta}{\partial P} \Delta P\end{aligned}\quad (6.5)$$

where ΔP is a vector containing the updates of each parameter P_i . The partial derivatives in respect to parameter P_i , $\partial(\cdot)/\partial P_i$ can be calculated efficiently using the Jacobis's method

$$\begin{aligned}\begin{pmatrix} \frac{\partial \alpha}{\partial P_i} \\ \frac{\partial \beta}{\partial P_i} \end{pmatrix} &= Q^{G,N+1} \cdot Q^{RF,N} \cdot \dots \cdot \frac{\partial Q^{RF,i}}{\partial P_i} \cdot \dots \cdot Q^{RF,1} \cdot Q^{G,1} \begin{pmatrix} 1 \\ 0 \end{pmatrix} \\ \begin{pmatrix} \frac{\partial \alpha}{\partial P_i} \\ \frac{\partial \beta}{\partial P_i} \end{pmatrix} &= Q^{G,N+1} \cdot Q^{RF,N} \cdot \dots \cdot \frac{\partial Q^{G,i}}{\partial P_i} \cdot \dots \cdot Q^{RF,1} \cdot Q^{G,1} \begin{pmatrix} 1 \\ 0 \end{pmatrix}\end{aligned}\quad (6.6)$$

where the first equation is used if P_i corresponds to the amplitude or the phase of a sub-pulse whereas the second gives the derivative when the parameter is associated with the k -space positions k_x, k_y and k_z .

For any specific number of sub-pulses, $\alpha, \beta, \partial \alpha / \partial P$ and $\partial \beta / \partial P$ can be evaluated symbolically using MATLAB, stored as functions and then calculated for every voxels with small matrix operations, without the need of expensive loops.

Excitation optimization

Given an initial magnetization $M_z = 1$, optimizing a 90° excitation pulse consists of making the " $-2\alpha^* \beta$ " term of the matrix in equation (3.28) homogeneous across the brain. The targeted profile $M_{xy,aim} = -2\alpha_{aim}^* \beta_{aim}$ and the profile corresponding to the starting symmetric k_T -point pulse are displayed in figure 6.2. The goal is thus to iteratively bring $M_{xy,c}$ as close as possible to $M_{xy,aim}$. The difference between $M_{xy,aim}$ and a current solution $M_{xy,c} = -2\alpha_c^* \beta_c$ can be written as:

$$M_{xy,aim} - M_{xy,c} = -2\alpha_{aim}^* \beta_{aim}^* + 2\alpha_c^* \beta_c^* = -2 \left(\alpha_c^* + \frac{\partial \alpha_c^*}{\partial P} \Delta P \right) \left(\beta_c + \frac{\partial \beta_c}{\partial P} \Delta P \right) + 2\alpha_c^* \beta_c^* \quad (6.7)$$

Developing the parenthesis product and neglecting the second order terms, the result be-

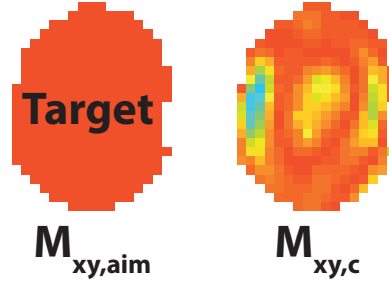


Figure 6.2: Left: targeted M_{xy} profile when an excitation pulse is designed. Right: M_{xy} profile of the symmetric k_T -point pulse designed in the STA regime and used as a starting point in the optimization process.

comes

$$M_{xy,aim} - M_{xy,c} \approx \underbrace{-2 \left(\alpha_c^* \frac{\partial \beta_c^*}{\partial P} + \beta_c \frac{\partial \alpha_c^*}{\partial P} \right)}_{A_{M,N_p}} \Delta P \quad (6.8)$$

As $\partial()/\partial P$ contains the derivatives in respect to the N_p parameters, their evaluation at all voxel positions gives rise to the $M \times N_p$ matrix A . Note that for a given number of k_T -point sub-pulses, $\partial()/\partial P_i$ is an analytical function that can be precalculated using equation (6.6). Expression (6.8) corresponds to a linear system of equations for which a solution ΔP can be found using the pseudo-inverse method

$$\Delta P = \text{pinv}(A) \cdot (M_{xy,aim} - M_{xy,c}) \quad (6.9)$$

The set of parameters is then updated following

$$P^{c+1} = P^c + \Delta P \quad (6.10)$$

where P^c represents every parameters P_i at iteration c . A full Bloch simulation of the M_{xy} profile (evaluation of $-2\alpha^*\beta$) is then performed with the new set of parameters, defining an updated $M_{xy,c}$ map closer to the target $M_{xy,aim}$. In practice, this can be simply done using prestored analytical functions calculated from equations (6.1) and (6.2). The procedure is repeated until a stopping criterion is reached.

The workflow presented in figure 6.3 summarizes how the different parameters are optimized in order to bring the magnetization as close as possible to the desired distribution across the region of interest.

Other Optimizations Again according to the matrix in equation (3.28), inversion and re-focusing k_T -point pulses were optimized by considering the terms $\alpha\alpha^* - \beta\beta^*$ (transfer of M_z into $-M_z$) and $-(\beta^*)^2$ (transfer of M_{xy} into M_{xy}^*), respectively.

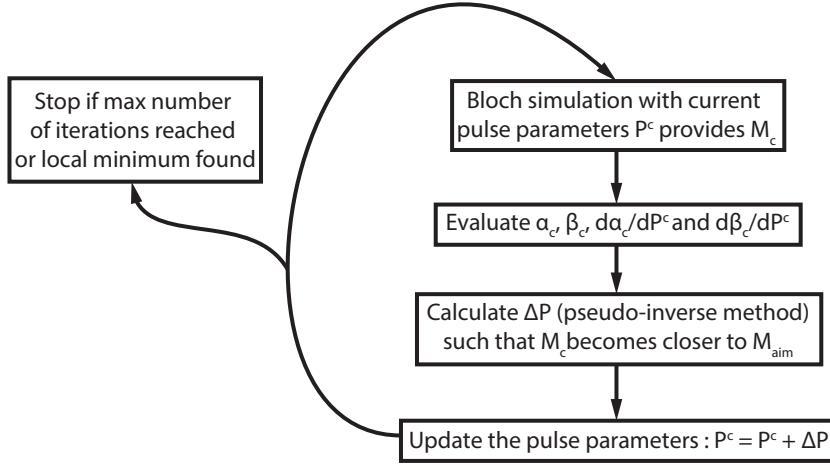


Figure 6.3: Overview of the methodology used to design k_T -point pulses in the high tip angle regime.

Proof of principle For each type of pulse designed, 4 optimizations were performed:

- (1) Sub-pulse amplitudes and phases only (SP)
- (2) SP and k_T -point positions (SP + k_x, k_y, k_z)
- (3) SP with a gradient descent (GD) algorithm used to determine the parameter updates ΔP where numerical differentiations are involved (SP^{GD})
- (4) SP + k_x, k_y, k_z using the GD algorithm ($[SP + k_x, k_y, k_z]^{GD}$)

For the excitation, refocusing and inversion optimizations, the results over three subjects were compared in terms of the homogeneity obtained in the final M_{xy} , M_{xy}^* and M_z profiles. Aspects such as the deviation from target in respect to iterations and convergence speed were also considered in the evaluation of the proposed method.

A 90° excitation pulse and a 180° inversion pulse both made of 5 k_T -points were designed using optimizations (1-4) for 3 different subjects. In the same way, a 180° refocusing pulse made of 7 k_T -points was calculated.

When designing the pulses, the iterative procedure was stopped if the magnetization ($M_{xy,c}$, $M_{z,c}$ or $M_{xy,c}^*$) at iteration $c+1$ was not closer to $M_{xy,aim}$, $M_{z,aim}$ or $M_{xy,aim}^*$ than the magnetization at step c (local minimum found) or if the maximum of 50 iterations was exceeded.

When the matrix in equation (6.3) corresponds to a sub-pulse, the angle ϕ and the vector \vec{n} in equation (6.4) depend on the amplitude and phase of the \vec{B}_1^+ distribution over the brain

as

$$\begin{aligned} \phi^i(\vec{r}) &= \phi^{nom} \cdot \left| \vec{B}_1^+(\vec{r}) \right| \cdot \left| RF^i \right| \\ \vec{n}(\vec{r}) &= \begin{pmatrix} \cos[\angle RF^i + \angle \vec{B}_1^+(\vec{r})] \\ \sin[\angle RF^i + \angle \vec{B}_1^+(\vec{r})] \\ 0 \end{pmatrix} \end{aligned} \quad (6.11)$$

where RF^i is a complex number containing the amplitude and phase of the sub-pulse $n^{\circ}i$ and ϕ^{nom} is the desired flip angle for the entire k_T -point pulse.

In-vivo B_1^+ maps acquired using the SA2RAGE sequence (chapter 4) on a 7T Siemens system were used in the current study.

6.1.3 Results and discussion

For the excitation k_T -point pulse, the profiles of M_{xy} resulting from optimizations (1-4) are compared on figure 6.4 with the case associated to the symmetric k_T -point pulse designed in the STA regime (first column). In this case, optimizing both SP and k_x, k_y, k_z provides the

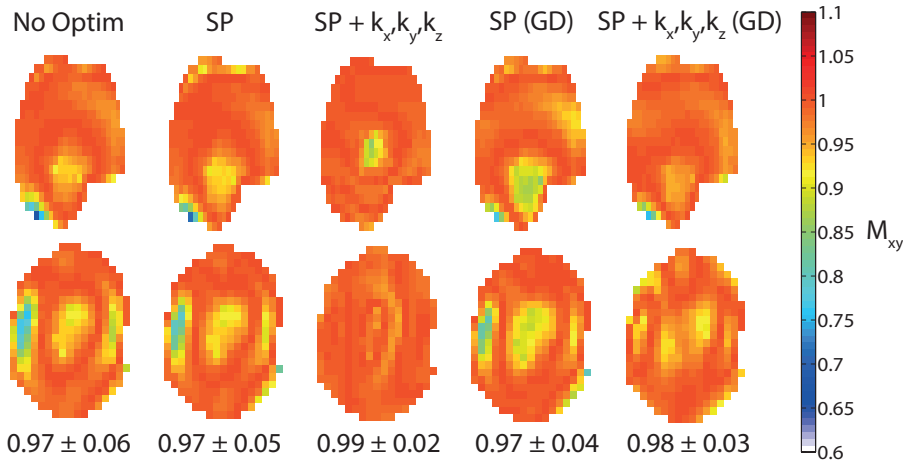


Figure 6.4: Profiles of the transverse magnetization M_{xy} at the end of a $5k_T$ -point excitation pulse. The first column shows the profile associated to the symmetric k_T -point calculated in the STA regime and used as a starting point for subsequent optimizations. The profiles presented in the remaining columns result from the different optimizations (1-4). Mean \pm std across the brain are presented below each profile. An 86% improvement is found when comparing the ratio $std/mean$ for the maps obtained on the first and third columns.

distributions with the higher homogeneity (third and fifth columns).

Curves showing the deviation between the magnetization profile at iteration c , $M_{xy,c}$ and the target, $M_{xy,aim}$ over all three subjects are displayed on figure 6.5. For every subjects, it is obvious that optimizing both SP and k_x, k_y, k_z leads to a smaller deviation. This was expected since the possibility of varying the k_T -point positions consists in an additional degree of freedom for the optimizations. It can also be observed that the proposed methodology

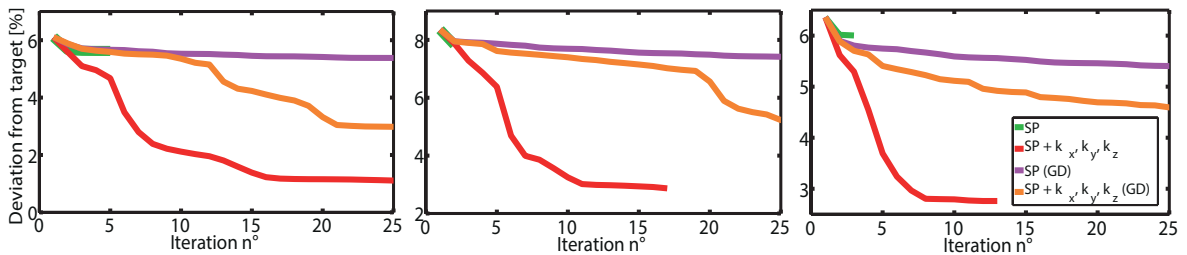


Figure 6.5: Curves showing the evolution of the deviation between $M_{xy,c}$ and $M_{xy,aim}$ for the different optimizations performed as a function of the iterations. Each graph is related to one subject.

outperforms the gradient descent algorithm in terms of both convergence speed (less iterations required to reach the same deviation value) and homogeneity obtained for the M_{xy} profiles.

For the inversion k_T -point pulse, the best solutions were provided by optimizations (1) and (4), i.e. when considering SP only with the proposed method and SP + k_x , k_y , k_z with the gradient descent algorithm (Fig. 6.6). The curves showing the deviation from the target of

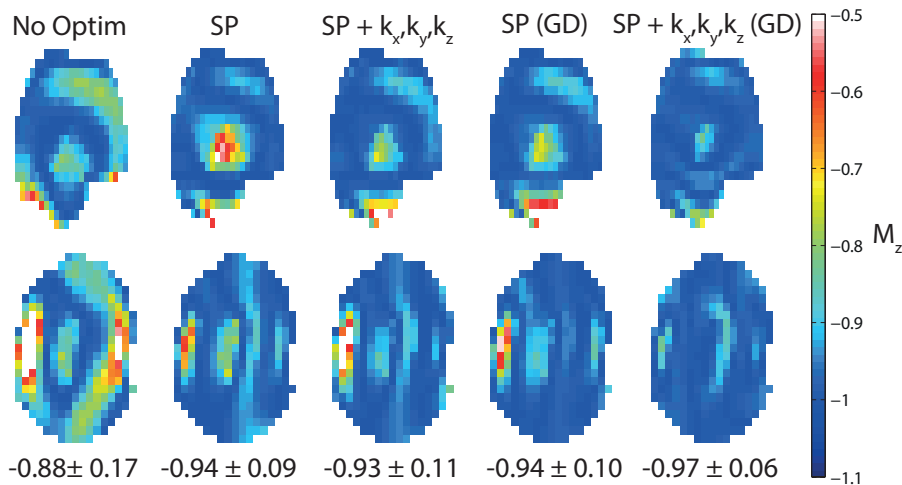


Figure 6.6: Profiles of the longitudinal magnetization M_z at the end of a $5k_T$ -point inversion pulse. A 63% improvement is found when comparing the ratio $std/mean$ for the maps obtained on the first and fifth columns.

having $M_z = -1$ throughout the brain as a function of iterations for each subject are displayed on figure 6.7. Those results confirm that the best solutions are found using optimizations (1) and (4). The fact that the M_z profiles obtained when considering SP only outperform those found by optimizing SP and k_x , k_y , k_z is a limitation of the proposed methodology. This happens when the curve corresponding to optimization (2) stops earlier than (1), meaning that a local minimum has been reached earlier when considering SP and k_x , k_y , k_z (cf. stopping criterion on figure 6.3).

Even if the proposed methodology is more affected by local minima than the gradient descent algorithm, it remains faster in terms of convergence speed, characterized by the steep-

ness of the curves in figure 6.7.

For the refocusing pulse, the results provided by the gradient descent algorithm are slightly

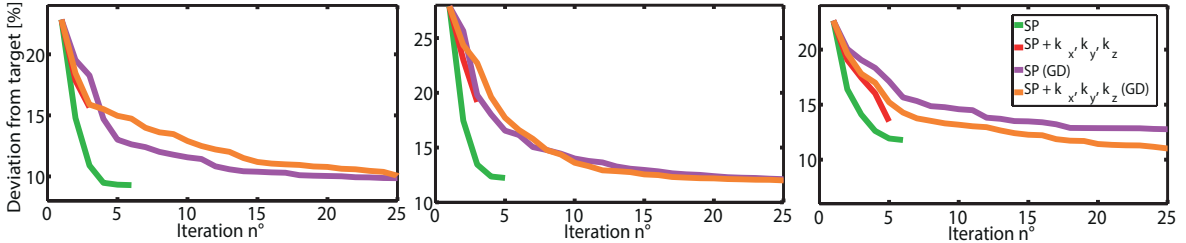


Figure 6.7: Curves showing the evolution of the deviation between $M_{z,c}$ and $M_{z,aim}$ for the different optimizations performed as a function of the iterations.

better than those found with the proposed methodology (Fig. 6.8) where the issue of reaching local minima happens again when considering SP and k_x, k_y, k_z (Fig. 6.9).

On a standalone PC, the $5k_T$ -point excitation and refocusing pulses were designed in less

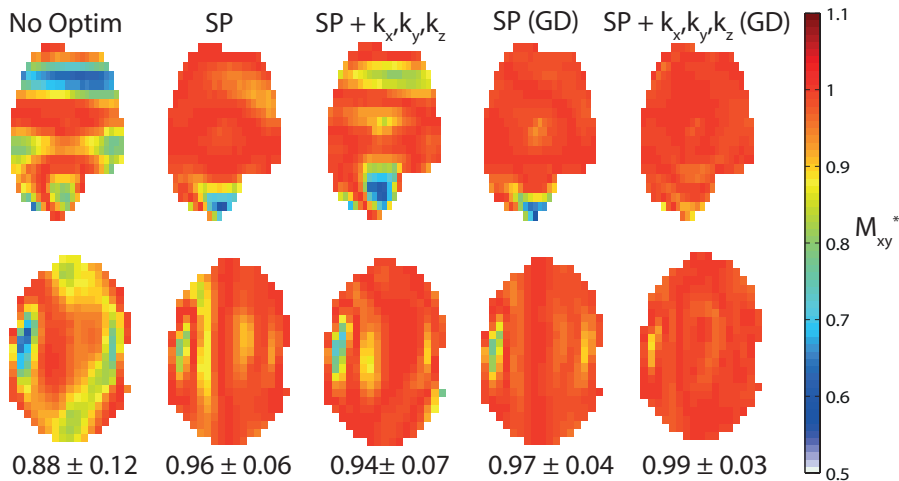


Figure 6.8: Profiles of the transverse magnetization M_{xy}^* at the end of a $7k_T$ -point refocusing pulse. A 73% improvement is found when comparing the ratio $std/mean$ for the maps obtained on the first and fifth columns.

than one minute with optimizations (1) and (2) whereas the design of the $7k_T$ point refocusing pulse took 5min.

6.1.4 Conclusion

High tip-angle excitation, inversion and refocusing k_T -point pulses were designed by iteratively using a linear form of the Bloch equations.

Although affected by local minima, the proposed methodology provides reasonably homogeneous magnetization profiles for the three types of pulses investigated. Moreover it generally outperforms the gradient descent algorithm in terms of convergence speed, i.e.

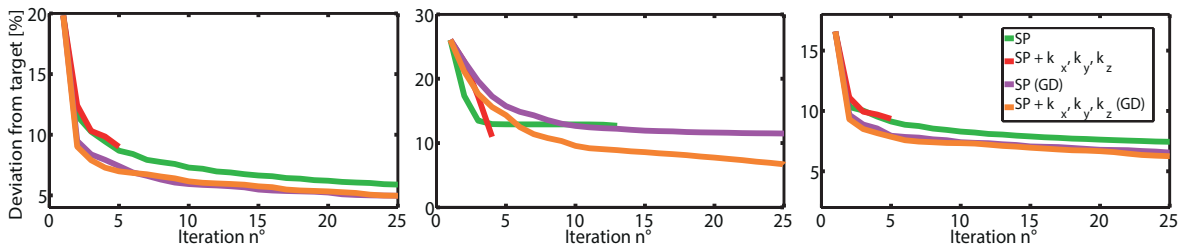


Figure 6.9: Curves showing the evolution of the deviation between $M_{xy,c}^*$ and $M_{xy,aim}^*$ for the different optimizations performed as a function of the iterations.

less iterations are required to reach a satisfactory solution, at least for the iterations where the highest percentage of improvement occurs. As it relies on symbolically precomputed matrices, each iteration is computed faster than an iteration of the gradient descent.

Even if the whole calculation of the pulse parameters was always performed in less than 5mins, the procedure could be made faster by reducing the number of voxels involved in the optimizations. For example, instead of considering every voxels inside the brain, a randomly distributed subset could be selected.

The presented methodology could be easily extended to parallel transmission, which would provide another degree of freedom to the optimization process and be adapted to have an SAR regularization term.

6.2 Dynamic k_T -points: a new concept to improve T_2 -weighted imaging at high field

6.2.1 Introduction

T_2 -weighted imaging plays a crucial role in the detection of brain diseases involving GM and WM lesions such as multiple sclerosis [105, 106], Alzheimer disease [107] and cancers [108].

Nowadays, sequences involving a turbo spin echo train are widely used to obtain T_2 -weighted images in a clinically acceptable amount of time. As explained in section 3.2, at ultra-high field, the RF wavelength becomes smaller than the typical sample size leading to an inhomogeneous distribution of the B_1^+ field over the brain. Images resulting from TSE sequences are highly affected by this artifact since the non-uniform B_1^+ profile propagates throughout the train of RF pulses. However, sequences involving a TSE readout such as FLAIR and DIR are nowadays very frequently used in clinical routines. To go clinical at high field, such sequences should rely on a TSE train where the effect of the inhomogeneous B_1^+ profile has been substantially reduced.

In chapter 5, high quality whole brain T_2 -weighted imaging was achieved by replacing the original hard pulses of a TSE sequence with k_T -point pulses. For both single and parallel

transmit systems, a single k_T -point pulse was designed in the STA regime with a uniform excitation profile as a target. Each pulse of the TSE sequence with variable flip angle was then replaced by the set of optimized sub-pulses, with fixed amplitude and phase relationships between the sub-pulses. This configuration will be referred to as a static k_T -point design in the current chapter.

Instead of searching for the most uniform excitation profile, another approach making use of PTx was recently introduced in [90] in which the signal throughout the TSE sequence was directly optimized. The spatially varying B_1^+ profiles of the different transmitters is taken into account in the methodology by considering a spatially resolved extended phase graph (SR-EPG) providing a simulation of all the states of the magnetization across the sequence for each voxel in the brain. The inverse problem of computing specific amplitudes and phases of the different array elements for every pulses leading to the expected signal response for all the echoes throughout the sequence was proposed, taking advantage of the extra degree of freedom provided by PTx. Since the amplitude and phase relationships between the different array elements vary from one pulse to the next, this methodology was presented as a "dynamic" RF shimming.

The aim of this article is to demonstrate that T_2 -weighted imaging can be further improved by designing a specific k_T -point pulse for each pulse of a TSE sequence with variable flip angles. The design of individual k_T -points for the different pulses of a TSE sequence was already proposed in [109] where the rotation matrix describing the effect of each k_T -point pulse was optimized. In the methodology presented here, the magnetization across the TSE sequence is simulated and optimized by using the SR-EPG framework. In order to obtain a targeted signal across the sequence, all the magnetization states have to be taken into account in the optimization process and therefore the STA approximation used in chapter 5 to design the k_T -points cannot be considered anymore. Instead, the adjustable sub-pulses of all the k_T -point pulses of the sequence are optimized according to a cost function comparing the theoretical signal over several echoes and the one simulated thanks to the SR-EPG formalism. In agreement with the concept of dynamic RF shimming proposed in [90] having variable k_T -point pulses throughout the sequence will be referred to as a dynamic k_T -point design.

As in chapter 5, the SPACE sequence was used to perform T_2 -weighted imaging acquisitions.

6.2.2 Methods

Design of dynamic k_T -points

As explained in section 2.3.4.2, a TSE sequence with a train of modulated flip-angles can be used to establish a static pseudo-steady state of the magnetization and then maintain it

throughout a large number of echoes such that image artifacts are minimized. According to this, the flip-angle values $[\alpha_1^{nom}, \dots, \alpha_{ETL}^{nom}]$ were predefined depending on the parameters of the sequence and specified T_1/T_2 relaxation times. Knowing the flip-angle train, the expected echo signal across the sequence $S^{theo} = [S_1^{theo}, \dots, S_{ETL}^{theo}]$ was simulated (Fig. 6.10a) using a forward EPG formalism [21]. Given that the transmit magnetic field profile $B_1^+(\vec{r})$ varies

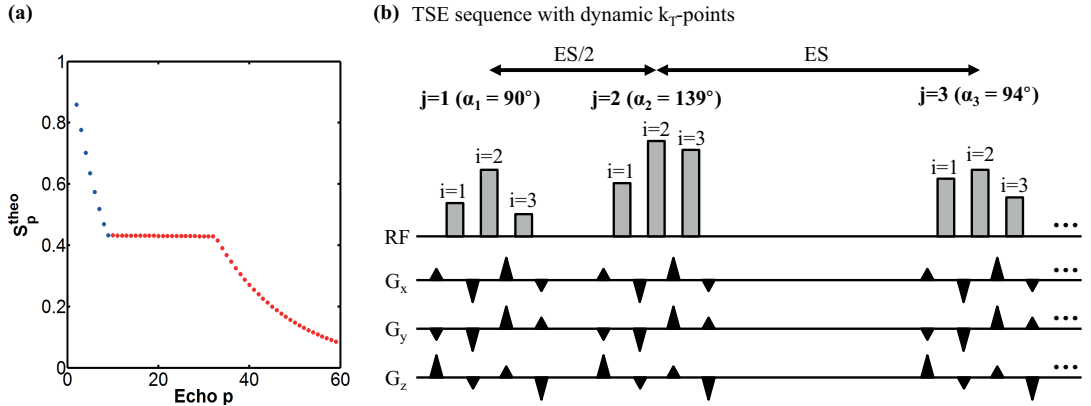


Figure 6.10: *a:* Signal at each echo of the TSE sequence simulated for the described protocol ($ETL = 57$) and assuming no B_1^+ inhomogeneity. Blue dots correspond to echoes associated with pulses bringing the magnetization into static pseudo-steady state which is maintained for the subsequent echoes (represented by red dots). *b:* TSE sequence with dynamic k_T -points. Example with $N = 3$ sub-pulses (identified by index i) for each k_T -point pulse (identified by index j). To fulfil the CPMG conditions, the gap between the excitation pulse ($j=1$) and the first refocusing pulse ($j=2$) is two times shorter than between the refocusing pulses themselves. The set of gradient blips is identical for all k_T -point pulses since the visited k -space trajectory is kept unchanged from one pulse to the next.

throughout space at 7T, each flip-angle α_j in the train also becomes position dependent

$$\alpha_j(\vec{r}) = B_1^+(\vec{r}) \cdot \alpha_j^{nom} \quad (6.12)$$

As mentioned previously, this inhomogeneity leads to signal and contrast variation since the signal at each echo becomes spatially varying. To correct for that, the original hard pulses of the sequence were replaced by k_T -point pulses of which shapes are optimized such that the signal distribution for echoes throughout the sequence stays close to the theoretical value S^{theo} for all voxels belonging to the region of interest, Ω .

For the sake of maintaining the computational demand of the optimization problem in a reasonable range, a single k -space trajectory was determined for all the k_T -point pulses of the sequence. This means that the set of gradient blips making transitions from one k -space position to the next will remain the same for all the pulses of the refocusing train. Those k_T -point positions were determined by designing a k_T -point pulse in the STA regime using the

modified version of the SOLO algorithm fed with the subject-specific B_1^+ profile. Although the design of a k_T -point pulse in this framework seeks for a homogeneous excitation profile, it was shown in chapter 5 that the k-space trajectory found also performs reliably for the refocusing pulses.

The dynamic k_T -point design consists in optimizing the amplitudes $A_{i,j}$ and phases $\phi_{i,j}$ of sub-pulse i ($i=1-N$) belonging to the j^{th} k_T -point pulse ($j=0$ -ETL), where N corresponds to the number of sub-pulses per k_T -point pulse (Fig. 6.10b) and ETL represents the echo train length of the TSE sequence.

Using the SR-EPG, the echo signal throughout all the voxels $S_p(\vec{r})$ can be simulated after each pulse p . The set of echoes for a sequence of ETL pulses was defined as $S(\vec{r}) = [S_1(\vec{r}), \dots, S_{ETL}(\vec{r})]$ and is a function of the B_1^+ signal profile as well as the $A_{i,j}$ and $\phi_{i,j}$ of the k_T -point pulses in the train. The sub-pulse amplitudes and phases were thus optimized in order to minimize the difference $\|S_{EOI}(\vec{r}) - S_{EOI}^{theo}\|$ where EOI refers to the echoes of interest, i.e. echoes involved in the optimization process.

A gradient descent algorithm with a least squares (LS) cost function was used to determine the $A_{i,j}$ and $\phi_{i,j}$ providing the best match between $S_{EOI}(\vec{r})$ and S_{EOI}^{theo} .

Again regarding the complexity of the optimization problem, the procedure of finding the $A_{i,j}$ and $\phi_{i,j}$ for the pulses of the TSE sequence was split into two parts:

- (a) The first task was to calculate simultaneously $A_{i,j}$ and $\phi_{i,j}$ ($j = 0$ - EOI_1) at each iteration of the gradient descent algorithm for all the pulses belonging to the ramp bringing the magnetization into static pseudo-steady state such that the difference between $S_{EOI_1}(\vec{r})$ and $S_{EOI_1}^{theo}$ is minimized. With the set of sequence parameters used, EOI_1 was set to 10 (shown in figure 6.10a as the blue echoes).

The average phase over the EOI was calculated at iteration k and used as a target at iteration $k+1$. This ensured a smooth phase transition from one echo to the next, significantly improving the quality of the acquired T_2 -weighted images.

- (b) In the second part, each k_T -point pulse was optimized independently and consequently $EOI_2 = 1$. The goal at this point was to maintain the signal homogeneity achieved at the end of the first optimization for the remaining echoes of the sequence. The gradient algorithm was thus used ETL- EOI_1 times in order to determine the amplitudes and phases of the pulses corresponding to echoes belonging to the red part of figure 6.10a. Once the sub-pulses of the p^{th} k_T -point pulse were found, the SR-EPG states after it were calculated since they are needed to perform the optimization of the pulse $p+1$. Each time the gradient descent algorithm was used, the amplitudes and phases of the previously optimized k_T -point pulse were considered as an initial guess.

Experimental setup

In-vivo scans were performed on a Siemens MAGNETOM 7T scanner (Siemens Healthcare,

Germany) equipped with a head gradient insert (maximum gradient amplitude and slew rate of 333 T/m/s and 80 mT/m respectively). A 32 channel coil (Nova Medical, USA) was used for image acquisition.

The experimental protocol was approved by local ethics committee and two healthy subjects providing informed consent were scanned.

To avoid having the area typically observed at 7T presenting very low B_1^+ intensity across the cerebellum, dielectric pads [98, 99] were placed below the top part of the neck for both subjects such that the average B_1^+ field increases in this region.

B_1^+ -mapping protocol

The transmit sensitivity profile $B_1^+(\vec{r})$ was obtained by acquiring an absolute B_1^+ map of the subject's brain using the SA2RAGE sequence with the following parameters: TR = 2.4s, TE = 1.35 ms, $TD_1 = 50\text{ms}$, $TD_2 = 1800\text{ms}$, $\alpha_1 = 4^\circ$, $\alpha_2 = 11^\circ$, $3.2 \times 3.2 \times 4.0 \text{ mm}^3$ resolution and a $64 \times 64 \times 48$ matrix size acquired with sagittal orientation (acquisition time of 1min28s).

Randomly chosen voxels in ROI

The region of interest Ω where a signal matching S^{theo} is desired was determined from a coarse segmentation of the brain achieved by a simple non-rigid registration step. In particular, a manual mask of the brain was codified in a homebuilt MRI template corresponding to the second image acquired by the SA2RAGE sequence ($SA2RAGE_2$) on a healthy subject. This template is deformed and aligned to the patient reference volume by estimating a free-form diffeomorphic displacement field using a fast multi-resolution iterative scheme that maximizes the local correlation between the template and the incoming scan. The mask is therefore also automatically deformed to adapt to the reference volume, thus providing a subject-specific mask.

Because the computation time required for the calculation of dynamic k_T -point pulses is proportional to the number of voxels involved, the option of randomly using a subset of N_{vox} voxels belonging to the mask was investigated. The aim of this analysis was to find a tradeoff between the computation time and the deviation made in respect to the solution obtained when considering all voxels in the mask.

Dynamic k_T -point evaluation

The SR-EPG framework was subsequently used to simulate the signal throughout the TSE sequence when it is made of:

- (i) standard hard pulses
- (ii) static k_T -point pulses
- (iii) dynamic k_T -point pulses.

When using the SR-EPG to calculate the evolution of the magnetization states, the sequence was simulated over 5·TR periods to ensure that the magnetization reaches the steady-state. The quality of each approach was evaluated in terms of signal fidelity by calculating the following quantity throughout the entire sequence

$$DEV_p = \frac{\left\| |S_p(\vec{r})| - |S_p^{theo}| \right\|}{\left\| S_p^{theo} \right\|} \quad (6.13)$$

where p belongs to [1; ETL] and refers to the echo number.

Another signal homogeneity assessment was performed by computing the standard deviation $STDev_p$ throughout each $S_p(\vec{r})$ map. In this way, only the inhomogeneity and not the deviation from the desired echo train is evaluated.

In (ii) and (iii), $N=3$ and 5 k_T -points were used for each sequence pulse.

To support simulations, TSE images acquired with 3 k_T -point pulses designed statically and dynamically were compared with images acquired with standard hard pulses (no k_T -point). To highlight the regions with large signal change, maps of the difference between images acquired without and with k_T -points named $D^{static}(\vec{r})$ and $D^{dynamic}(\vec{r})$ were calculated. In order to test the quality of the predictions provided by SR-EPG simulations, signal profiles at k-space center (k_0) were calculated for a TSE sequence without k_T -points, $S_{k_0}^{no-k_T}(\vec{r})$, as well as with static, $S_{k_0}^{static}(\vec{r})$, and dynamic, $S_{k_0}^{dynamic}(\vec{r})$, k_T -points. For both subjects, the differences between the simulated and measured signals without and with k_T -points were compared.

Turbo spin echo protocol

Replacing the original hard pulses of the TSE sequence with variable flip angles by sets of sub-pulses and gradients blips increases the SAR of the sequence. A trade-off between the SAR constraints and the highest GM-WM contrast was thus considered to establish the optimal sequence parameters. The following protocol was used for the acquisition of T_2 -weighted images: TR = 2s, TE = 100ms, ETL = 57, echo spacing (ES) = 4.16ms, RF_{Dur} = 1.40ms, resolution = $0.85 \times 0.85 \times 0.85 \text{ mm}^3$, matrix size = $256 \times 256 \times 176$ and 3 k_T -points per RF pulse (total acquisition time 6min30s). As for the acquisitions of TSE images with static k_T -points performed in chapter 5 on the single channel system, 15 echoes were discarded at the beginning of the train in order to minimize artifacts.

When compared to the acquisition performed on the single channel system in chapter 5, a shorter value of ES could be used for the sequence with dynamic k_T -points since the number of sub-pulses per RF pulse was reduced (three instead of four).

A standard TSE image with identical parameters and non-selective hard pulses of the same duration as the k_T -point pulses was also acquired for comparison.

Data processing

As explained in chapter 5 bias field correction was subsequently applied to the anatomical images in order to remove the signal variations related to the highly non-uniform reception profile $B_1^-(\vec{r})$ of the 32 channel coil.

6.2.3 Results

Randomly chosen voxels in ROI

The consequence of reducing the number of voxels selected for the optimization of the TSE pulses was investigated in [90] where decimated regular grids comprising every m^{th} voxel in each spatial dimension were used in simulations.

In this work, a reduced number of voxels N_{vox} was randomly chosen in Ω . Depending on N_{vox} , the effects on the optimization speed and the deviation between the solutions $S^{All}(\vec{r})$ and $S^{N_{vox}}(\vec{r})$ obtained when optimizing dynamic k_T -points by considering respectively all and N_{vox} voxels in Ω were explored. $S^{All}(\vec{r})$ and $S^{N_{vox}}(\vec{r})$ are vectors whose components $S_c^{All}(\vec{r})$ and $S_c^{N_{vox}}(\vec{r})$ are the signal profiles simulated at each echo using the SR-EPG. The error E made in respect to the solution obtained when considering all voxels in Ω was calculated using the following expression

$$E = \frac{1}{ETL} \sum_{c=1}^{ETL} \frac{\left| \left| S_c^{All}(\vec{r}) \right| - \left| S_c^{N_{vox}}(\vec{r}) \right| \right|}{\left\| S_c^{All}(\vec{r}) \right\|} \quad (6.14)$$

As the voxels were randomly selected, $S^{N_{vox}}(\vec{r})$ was simulated 20 times such that the average and standard deviations of E can be established.

Figure 6.11a shows an example where $N_{vox} = 200$ voxels are selected out of the full mask (All = 4070). It can be observed on figure 6.11b that N_{vox} can be surprisingly small without a drastic error made regarding the solution found when considering all voxels in Ω . The box size becoming significantly larger when going from $N_{vox} = 200$ to 100, the acceptable threshold regarding the quality of the calculated solution was set to $N_{vox} = 200$. On the other hand, figure 6.11c illustrates how the time required to calculate the dynamic k_T -points evolves when lowering N_{vox} . Considering figure 6.11 b and c, $N_{vox} = 200$ was chosen for subsequent optimizations since this allows dynamic k_T -points to be designed as precisely as when considering all voxels in Ω in less than 5min.

Dynamic k_T -point evaluation

The curves presented in figure 6.12 a and b show the improvement provided by the dynamic k_T -points over the static k_T -point design and the approach without k_T -point in terms of both echo train fidelity (characterized by DEV_p) and homogeneity (characterized by $STDev_p$). It can be seen that the solution resulting from the use of 3 dynamic k_T -points is comparable to

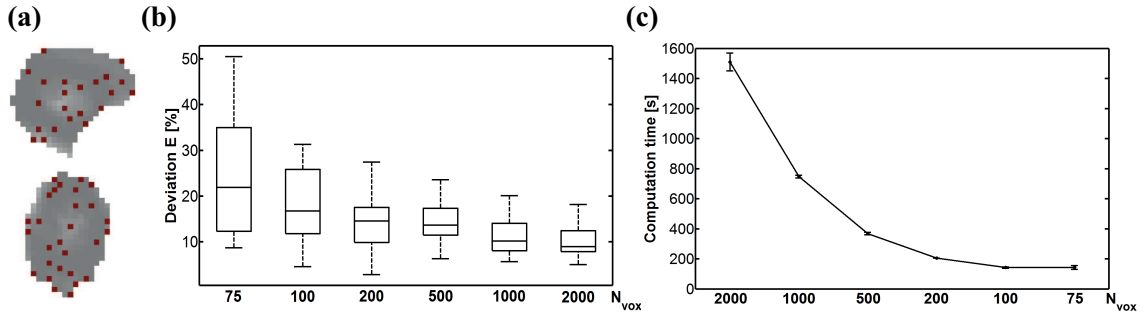


Figure 6.11: *a:* Sagittal and transversal views of a $64 \times 64 \times 48$ excitation profile downsampled to 4070 voxels. The red dots correspond to an example where $N_{vox} = 200$ voxels were randomly selected. *b:* Error between the solutions $S^{All}(\vec{r})$ and $S^{N_{vox}}(\vec{r})$ obtained when performing optimization of dynamic k_T -points ($N=3$) by considering respectively every and N_{vox} randomly chosen voxels in the region of interest Ω . The horizontal line on each box plot represents the median while the box edges correspond to the first and third quartiles. The whiskers extend up to the most extreme datapoints considered as not being outliers. *c:* Average time (over 20 simulations) required to perform the dynamic k_T -point optimization as a function of N_{vox} .

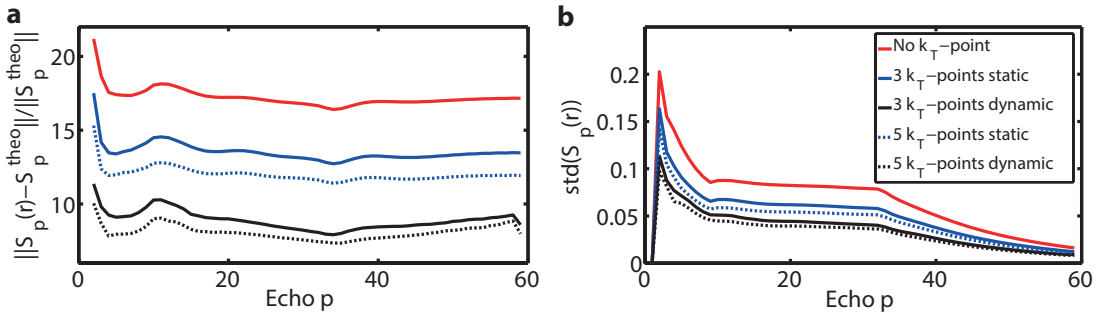


Figure 6.12: *a:* Echo train fidelity estimated by computing the percentage deviation DEV_p between sequence echoes $S_p(\vec{r})$ and theoretical signal S_p^{theo} (Fig. 6.10a) for different k_T -point configurations. *b:* Assessment of the signal homogeneity by evaluating the standard deviation $STDev_p$ throughout each echo map $S_p(\vec{r})$ for the different RF pulse designs.

the one obtained with 5 k_T -points in the static regime. Moreover, for the same k_T -point pulse duration and all the other parameters the same, the sequence designed with 3 dynamic k_T -points outperformed the one with 5 static k_T -points by more than 50% in terms of SAR. Despite the increased homogeneity obtained using a higher number of k_T -points, measured images were acquired using 3 k_T -points to keep the RF duration shorter than 1.5ms and within SAR limits.

Figure 6.13 shows that the differences $D^{static}(\vec{r})$ and $D^{dynamic}(\vec{r})$ calculated for the measured TSE images (Fig. 6.13 a,c,e,g) are in close agreement with those simulated using the SR-EPG $DSim^{static}(\vec{r})$ and $DSim^{dynamic}(\vec{r})$ (Fig. 6.13 b,d,f,h). This demonstrates that the state of the magnetization throughout the TSE sequence can be reliably understood with SR-EPG simulations, both when using static and dynamic k_T -points.

TSE images acquired with and without dynamic k_T -points are displayed in figure 6.14. High improvements in signal and contrast homogeneity are seen in the cerebellum, brain center

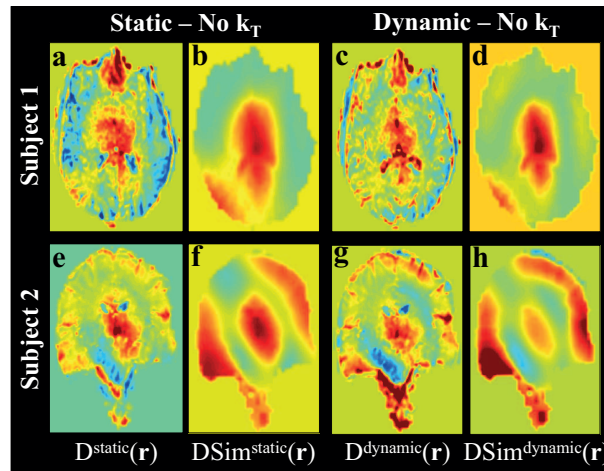


Figure 6.13: Difference between images - acquired without and with static k_T -points $D^{static}(\vec{r})$ (a,e) - acquired without and with dynamic k_T -points $D^{dynamic}(\vec{r})$ (c,g) - simulated without and with static k_T -points $DSim^{static}(\vec{r})$ (b,f) - simulated without and with dynamic k_T -points $DSim^{dynamic}(\vec{r})$ (d,h). a-d maps are associated to subject $n^{\circ}1$ and e-h maps to subject $n^{\circ}2$.

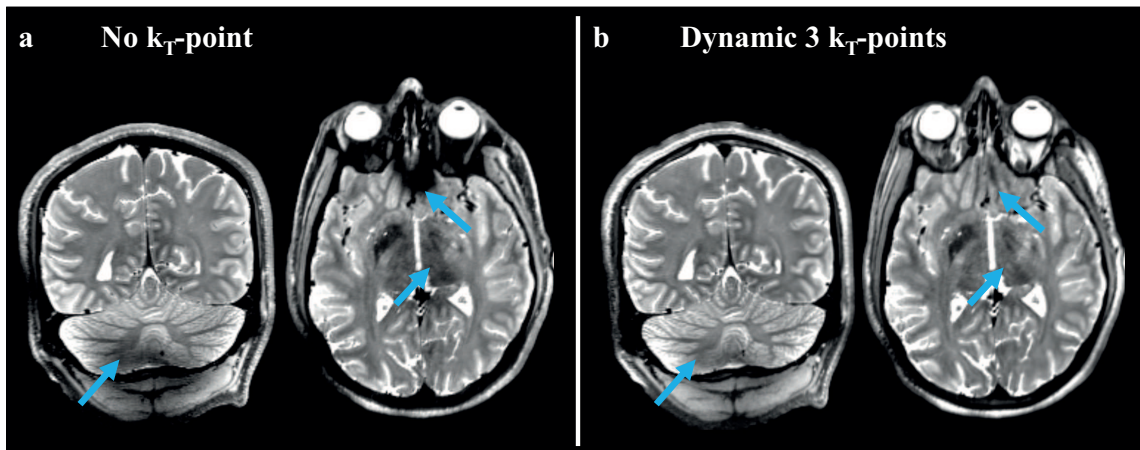


Figure 6.14: TSE images acquired without (a) and with dynamic 3 k_T -point pulses (b) for subject $n^{\circ}1$. Blue arrows highlight brain regions with noticeable improvements.

and over sinuses (blue arrows) when using dynamic k_T -points.

6.2.4 Discussion

The good agreement between simulations and experimental data demonstrates that including k_T -points in the SR-EPG formalism provides a new degree of freedom to control the magnetization distribution in a TSE sequence with variable flip angles leading to T_2 -weighted images with high level of signal and contrast homogeneity at 7T. It was also shown that dynamic k_T -points outperform the static ones in terms of T_2 -weighted image quality (Fig. 6.12 a and b).

Although they were not acquired with the same TSE sequence protocol, comparing anatomical images of figure 6.14 b with the ones presented in figure 5.6 shows that results almost as good (in terms of signal and contrast homogeneity) as the ones provided by parallel transmission and static 5 k_T -points can be reached on a single channel system by using dynamic 3 k_T -points. On the other hand, for the same number of k_T -points, dynamic k_T -points are usually more SAR demanding than statics are. Considering SAR limitations, a maximum number of 3 k_T -points was allowed in the dynamic design. A larger k_T -point pulse duration could be chosen to lower the sequence SAR but at a cost of a reduced RF bandwidth. Another option would be to introduce a regularization parameter in the dynamic k_T -point optimization process. This would penalize the SAR intensive sub-pulses with high amplitudes at a cost of a higher deviation of the sequence echoes in respect to the targeted values. In the design of dynamic k_T -points, the duration of the sub-pulses was fixed for all the k_T -points of the sequence. An option to significantly reduce the sequence SAR would be to follow the approach presented in chapter 5 where the duration of each sub-pulse was determined such that the RF power of the k_T -points is minimized. Therefore, by designing the dynamic k_T -points with the condition that all the sub-pulses of a k_T -point pulse have a constant amplitude (and different durations), a larger maximum number of k_T -points would be afforded in the optimization process.

When optimizing dynamic k_T -points, the B_0 inhomogeneity over the brain was not considered. However, it can be observed in figure 6.14 that the signal loss in the sinus region which is typically due to strong B_0 variations at 7T is fully recovered when acquiring the image by using dynamic k_T -points. The sub-pulse duration of the k_T -point pulses being shorter than the one of the hard pulses (0.3ms vs 1.4ms) means that their bandwidth is larger. As the duration of hard pulses could have been reduced, this improvement cannot be attributed to the k_T -point per se.

As demonstrated already in [90] for dynamic RF-shimming, it was shown in the current work that signal and contrast homogeneity resulting from the use of a TSE sequence made of dynamic k_T -points can be predicted from SR-EPG simulations (cf. Fig. 6.13). Such an understanding of the sequence also gives rise to new horizons towards further improvements in T_2 -weighted imaging. Among them, dynamic k_T -points combined with parallel transmission will be considered as a next stage since greater advantages are expected thanks to the increased number of degrees of freedom associated with the different transmit channels.

Another improvement would consist in designing dynamic k_T -points with different number of sub-pulses. In particular, having more k_T -points for pulses bringing the magnetization into static pseudo-steady state would help achieving a higher echo signal homogeneity which could be maintained with less k_T -points for the remaining pulses of the sequence. This would improve the T_2 -weighted image quality together with a SAR reduction, the overall number of k_T -points of the sequence being lowered.

The k-space trajectory visited by the dynamic k_T -points could also vary from one pulse of the sequence to the next. This extra degree of freedom could help obtaining better solutions

or allow sustaining the same image quality while using more efficient k_T -point pulses. As mentioned earlier, the gradient blips were kept constant from pulse to pulse to reduce the computation and sequence implementation complexity. Having them as part of the optimization process would thus require advanced resources such as parallel computation. In general, the proposed improvements would aim at increasing the degrees of freedom when optimizing the homogeneity, which should enable the usage of shorter and less SAR intensive k_T -points allowing more efficient protocols to be used.

6.2.5 Conclusions

This study demonstrates that replacing the original hard pulses of a TSE sequence with variable flip angles by dynamic k_T -point pulses allows T_2 -weighted images unaffected by the common B_1^+ inhomogeneity at 7T to be acquired.

It was concluded that dynamic k_T -points outperform static ones and led to T_2 -weighted images of high quality in terms of signal and contrast homogeneity even on a single channel transmit system.

From the similarity between simulated and acquired images it was further concluded that the SR-EPG combined with k_T -points is a very helpful tool to optimize and predict the state of the magnetization throughout a TSE sequence. This framework was used in a way such that the train of echoes matches a theoretical signal across the sequence but it could easily be extended to other targets like having only a specific number of echoes fitted or matching a predefined point spread function.

7

General Conclusion and outlook

7.1 Main conclusions

This thesis was dedicated to the measurement and correction of the inhomogeneous distribution of the B_1^+ field observed at 7T.

It was demonstrated that the B_1^+ field can be rapidly acquired in a three dimensional volume by using the implemented SA2RAGE sequence providing reliable B_1^+ measurements over a wide range of B_1^+ values. The fast and accurate B_1^+ -mapping technique presented was thus perfectly adapted for the measurements of all the B_1^+ distributions performed in the rest of the thesis, in particular for the acquisition of the individual B_1^+ profiles of the different array elements required for parallel transmission applications.

Regarding RF pulse design, it was demonstrated that magnetization profiles with high uniformity can be obtained by designing excitation, inversion and refocusing k_T -point pulses besides the small tip angle regime by using a linear form of the Bloch equations. Even if this methodology was not concretely applied in this thesis it could be used for the design of pulses in several types of sequence. For example, a well performing inversion k_T -point pulse could be designed as a preparation module in a FLAIR sequence. In the same way, a 90° pulse providing a very homogeneous excitation profile could be designed for a turbo spin echo sequence in order to obtain a reliable magnetization state before applying the train of refocusing pulses.

From the results presented in the two last chapters of this thesis, it can be concluded that the design of k_T -points to replace the original hard pulses of a turbo spin echo sequence provides very promising results for the acquisition of T_2 -weighted images unaffected by the inhomogeneous B_1^+ distribution observed at 7T. Anatomical images corrected from signal and contrast variations were obtained by combining the design of symmetric k_T -points in the small tip angle regime (static k_T -points) with parallel transmission.

It can be further concluded that using the SR-EPG framework, a better understanding of the TSE sequence is obtained by simulating the different echo profiles. Having access to the

magnetization states throughout the entire sequence allowed the optimization of several k_T -point pulses at a time to make the echo distributions as close as possible to a desired echo train (dynamic k_T -points). It was demonstrated that T_2 -weighted images of high quality in terms of signal and contrast homogeneity could even be acquired on a single channel transmit system by designing dynamic k_T -points for the TSE sequence.

Therefore, by designing k_T -point pulses for a turbo spin echo sequence with variable flip angles, T_2 -weighted anatomical images largely devoid of artifacts resulting from the common B_1^+ inhomogeneity at 7T could be acquired.

This methodology is thus promising for clinical applications at high field since by adding a preparation module to the TSE sequence made of k_T -points, FLAIR and DIR images unaffected by the B_1^+ inhomogeneity could be generated and would be of high interest for the study or diagnosis of brain diseases involving gray and white matter lesions such as multiple sclerosis and iron deposition such as Alzheimer disease.

7.2 Outlook

High tip angle k_T -points

When designing k_T -points in the high tip angle regime by considering a linearization of the Bloch equations, it was shown that the iterative process was sometimes stopped early due to the fact that a local minimum was reached. This happened when optimizing the k_T -point sub-pulses (SP) only or the SP and the k-space positions (k_x, k_y, k_z) but in general, a local minimum was not reached in either case. An approach alternating the optimizations of SP only and SP + k_x, k_y, k_z could be established in order to guarantee the convergence towards a better minimal solution.

Design of k_T -points for the TSE sequence

It was shown that the design of k_T -point pulses by using the SR-EPG framework represents a promising technique to obtain T_2 -weighted images unaffected by the B_1^+ inhomogeneity observed at ultra high field. In general, for both single channel and parallel transmit systems, the SAR of the TSE sequence increases when k_T -point pulses are designed for it. This implies that certain parameters such as TR or the k_T -point pulse duration cannot be reduced down to the desired value. Some modifications could further increase the degrees of freedom available, which should enable the use of shorter and less SAR intensive k_T -points allowing more efficient protocols to be used.

A first option would be to consider variable numbers of k_T -points throughout the train of flip angles. Indeed, pulses with more k_T -points could be designed for the part of the train

bringing the magnetization towards the pseudo steady-state in order to reach a uniform echo distribution at that point. Less k_T -points could be used for the remaining refocusing pulses since their role would be simply to maintain the homogeneity until the end of the sequence.

The design of the excitation pulse of the TSE sequence could benefit from the methodology presented for the optimization of k_T -points in the high tip angle regime. Given that with this approach, the k_x, k_y, k_z positions of the k_T -points can be optimized in addition to the sup-pulse amplitudes and phases, more degrees of freedom for the subsequent optimizations of the TSE sequence are provided by designing an excitation pulse with a large number of k_T -points. In addition to the extra degrees of freedom available, this approach should also provide an improved starting point for the optimization of the first RF pulses of the TSE sequence since a k-space trajectory favoring the excitation pathway would be specifically designed for the 90° pulse.

Another obvious improvement would be to combine the design of dynamic k_T -points with parallel transmission which would provide another degree of freedom to the optimization process. This could be performed at a cost of a higher computation demand. Moreover, due to the more constrained SAR limitations on the parallel transmit system, the RF power of the TSE sequence with dynamic k_T -points should be carefully controlled for example with SAR regularization terms in the optimization process or by using the approach proposed in [27] to relax the tight threshold defined by the worst case scenario.

Other applications

T_2 -mapping at high field strengths is still a topic under research since the different techniques proposed reported divergent T_2 measurements [110–112]. The ability to predict the magnetization states throughout the entire TSE sequence provided by the SR-EPG could be used to establish a T_2 -mapping procedure. According to the work presented in [16] for a static pseudo steady-state (SPSS) sequence, the main EPG states F_0 and $F_{\pm 1}$ can be combined in order to have a T_2 dependence. Simulations can thus be performed to build a lookup table linking the combinations of states with their associated T_2 -values. A similar lookup table could be calculated for the F_0 and $F_{\pm 1}$ states of the TSE sequence at each voxel position by using the SR-EPG. A T_2 map could then be extracted from the measurements of the F_0 and $F_{\pm 1}$ states. The main advantage with this approach is that the signal generated by TSE sequences is higher than for SPSS and therefore T_2 maps with increased SNR could potentially be obtained.

List of Symbols

Symbol	Description
B_0	Main magnetic field
ω_0	Larmor frequency
γ	Gyromagnetic ratio
h	Planck's constant
B_1	RF magnetic field
B_1^+	Component of B_1 rotating in the clockwise direction
B_{eff}	Effective magnetic field
\vec{G}, G_x, G_y, G_z	Magnetic field gradients
\vec{M}	Magnetization vector
n_+, n_-	Spin populations on states up and down (1H atom)
T	Temperature
T_1	Longitudinal relaxation time
T_2	Transverse relaxation time
T_2^*	Transverse relaxation time affected by B_0 non-uniformities
$\Delta B_0(\vec{r})$	B_0 field non-uniformities
α	Flip angle amplitude
Φ	Flip angle phase
k_T	Transmission k-space
\vec{S}	Nuclear spin
$\vec{\mu}$	Magnetic dipole moment
k_B	Boltzmann's constant
M_0	Magnetization at thermal equilibrium
ρ	Number of protons per unit volume
$\vec{e}_x, \vec{e}_y, \vec{e}_z$	Unit vectors in the lab frame
$\vec{e}_{x'}, \vec{e}_{y'}, \vec{e}_{z'}$	Unit vectors in the rotating frame
Φ_B	Magnetic field flux
ε	Electromotive force
$RX(\vec{r})$ or $B_1^-(\vec{r})$	Coil receive sensitivity
$S(\vec{r})$ or $B_1^+(\vec{r})$	Coil transmit sensitivity
F_n, F_{-n}, Z_n	Configuration states
$\Psi(\vec{r})$	Phase of an isochromat at position \vec{r}
k_x, k_y, k_z	Transmit or receive k-space coordinates

List of Symbols

Symbol	Description
$\Delta k_x, \Delta k_y$	K-space intervals
$k_{x,max}, k_{y,max}$	Coordinates of the largest k-space points acquired
W_{k_x}, W_{k_y}	Width of the acquired k-space in x and y directions
δ_x, δ_y	Spatial resolution in x and y directions
FOV_x, FOV_y	Field of view in x and y directions
TE_{eff}	Effective TE
RF_{Dur}	RF Duration
$G_{x,max}, G_{y,max}, G_{z,max}$	Highest gradient amplitudes that the MR system can achieve
\vec{E}	Electric field
$\sigma(\vec{r})$	Electric conductivity distribution
α, β	Cayleigh-Klein coefficients
λ	RF wavelength
c	Speed of light
n	Refractive index
ϵ_r	Relative permittivity
M_{xy}	Magnetization in the transverse plane
M_z	Longitudinal magnetization
$m_{z,SS}$	Steady-state longitudinal magnetization
TD_1, TD_2	Delay times in SA2RAGE sequence
$e(\vec{r})$	Excitation profile
α^{nom}	Nominal flip angle

List of Abbreviations

Acronym	Meaning
NMR	Nuclear Magnetic Resonance
MRI	Magnetic Resonance Imaging
fMRI	functional MRI
SNR	Signal to Noise Ratio
RF	Radio Frequency
TSE	Turbo Spin Echo
T	Tesla
G	Gauss
CW	Continuous-Wave
FID	Free Induction Decay
CSF	Cerebro Spinal Fluids
WM	White Matter
GM	Gray Matter
GE	Gradient Echo
SE	Spin Echo
HE	Hahn Echo
STE	STimulated Echo
EPG	Extended Phase Graph
FE	Frequency Encoding
PE	Phase Encoding
SS	Slice Selection
PD	Proton Density
FOV	Field Of View
TR	Repetition Time
TE	Echo Time
RARE	Rapid Acquisition with Relaxation Enhancement
FSE	Fast Spin Echo
TA	Acquisition Time
ETL	Echo Train Length
ES	Echo Spacing

Acronym	Meaning
CPMG	Carr Purcell Meiboom Gill
sPSS	static Pseudo Steady State
CP	Circularly Polarized
TALES	Transmit Antenna LLevel Sensor
LPF	Low Pass Filter
ADC	Analog to Digital Converter
PNS	Peripheral Nerve Stimulation
EPI	Echo Planar Imaging
SAR	Specific Absorption Rate
STA	Small Tip Angle
SOLO	Sequential Optimal seLection Of Spokes
PTx	Parallel Transmission
SENSE	SENSitivity Encoding
FLASH	Fast Low Angle SHots
LS	Least Squares
MLS	Magnitude Least Squares
FWHM	Full Width at Half Maximum
SA2RAGE	SAturation prepared with 2 RApid Gradient Echoes
DAM	Double Angle Method
CNR	Contrast to Noise Ratio
MS	Multiple Sclerosis
FLAIR	FLuid Attenuated Inversion Recovery
DIR	Double Inversion Recovery
SPACE	Sampling Perfection with Application optimized Contrasts using different flip angle Evolutions
SR-EPG	Spatially Resolved-Extended Phase Graph

- [1] F. Bloch, W. W. Hansen, and M. Packard. The nuclear induction experiment. *Phys. Rev.*, 70:474–485, 1946. 2.1
- [2] E. M. Purcell, H. C. Torrey, and R. V. Pound. Resonance absorption by nuclear magnetic moments in a solid. *Phys. Rev.*, 69:37–38, 1946. 2.1
- [3] N. Bloembergen, E. M. Purcell, and R. V. Pound. Relaxation effects in nuclear magnetic resonance absorption. *Phys. Rev.*, 73:679–712, 1948. 2.1
- [4] R. R. Ernst and W. A. Anderson. Application of fourier transform spectroscopy to magnetic resonance. *Review of Scientific Instruments*, 37:93–102, 1966. 2.1
- [5] W. P. Aue, E. Bartholdi, and R. R. Ernst. Two-dimensional spectroscopy. application to nuclear magnetic resonance. *The Journal of Chemical Physics*, 64(5):2229–2246, 1976. 2.1
- [6] Michael P. Williamson, Timothy F. Havel, and Kurt Wuthrich. Solution conformation of proteinase inhibitor {IIA} from bull seminal plasma by 1h nuclear magnetic resonance and distance geometry. *Journal of Molecular Biology*, 182(2):295 – 315, 1985. 2.1
- [7] P. C. Lauterbur. Image formation by induced local interactions: Examples employing nuclear magnetic resonance. *Nature*, pages 190–191, 1973. 2.1
- [8] Grannell PK Mansfield P. Nmr "diffraction" in solids? *J Phys C Solid State Phys*, 1973. 2.1
- [9] Mansfield P Garroway AN, Grannell PK. Image formation in nmr by a selective irradiative process. *J Phys C Solid State Phys*, 1974. 2.1
- [10] Raymond Damadian. Tumor detection by nuclear magnetic resonance. *Science*, 171:1151–1153, 1971. 2.1
- [11] Anil Kumar, Dieter Welti, and Richard R Ernst. Nmr fourier zeugmatography. *Journal of Magnetic Resonance (1969)*, 18(1):69 – 83, 1975. 2.1
- [12] W A Edelstein, J M S Hutchison, G Johnson, and T Redpath. Spin warp nmr imaging and applications to human whole-body imaging. *Physics in Medicine and Biology*, 25(4):751, 1980. 2.1
- [13] S Ogawa, T M Lee, A R Kay, and D W Tank. Brain magnetic resonance imaging with contrast dependent on blood oxygenation. *Proceedings of the National Academy of Sciences*, 87(24):9868–9872, 1990. 2.1
- [14] Jr. Pauli, W. Uber die gesetzmassigkeiten des anomalen zeemaneffektes. *Zeitschrift fur Physik*, 16:155–164, 1923. 2.2.1.1

- [15] E. L. Hahn. Spin echoes. *Phys. Rev.*, 80:580–594, Nov 1950. 2.2.5
- [16] Rahel Heule, Peter Bar, Christian Mirkes, Klaus Scheffler, Siegfried Trattnig, and Oliver Bieri. Triple-echo steady-state t2 relaxometry of the human brain at high to ultra-high fields. *NMR in Biomedicine*, 27(9):1037–1045, 2014. 2.3.4.1, 7.2
- [17] P.J. Wright, O.E. Mougin, J.J. Totman, A.M. Peters, M.J. Brookes, R. Coxon, P.E. Morris, M. Clemence, S.T. Francis, R.W. Bowtell, and P.A. Gowland. Water proton t1 measurements in brain tissue at 7, 3, and 1.5t using ir-epi, ir-tse, and mprage: results and optimization. *Magnetic Resonance Materials in Physics, Biology and Medicine*, 21(1-2):121–130, 2008.
- [18] Jose P. Marques, Tobias Kober, Gunnar Krueger, Wietske van der Zwaag, Pierre-Francois Van de Moortele, and Rolf Gruetter. Mp2rage, a self bias-field corrected sequence for improved segmentation and t1-mapping at high field. *NeuroImage*, 49(2):1271 – 1281, 2010. 2.3.4.1, 4.1.1, 4.1.2
- [19] H. Y. Carr and E. M. Purcell. Effects of diffusion on free precession in nuclear magnetic resonance experiments. *Phys. Rev.*, 94:630–638, 1954. 2.3.4.2
- [20] S. Meiboom and D. Gill. Modified spin-echo method for measuring nuclear relaxation times. *Review of Scientific Instruments*, 29:688–691, 1958. 2.3.4.2
- [21] J Hennig. Multiecho imaging sequences with low refocusing flip angles. *Journal of Magnetic Resonance (1969)*, 78(3):397 – 407, 1988. 2.3.4.2, 6.2.2
- [22] D.C. Alsop. The sensitivity of low flip angle rare imaging. *Magnetic Resonance in Medicine*, 37:176–184, 1997. 2.3.4.2
- [23] Juergen Hennig, Matthias Weigel, and Klaus Scheffler. Multiecho sequences with variable refocusing flip angles: Optimization of signal behavior using smooth transitions between pseudo steady states (traps). *Magnetic Resonance in Medicine*, 49(3):527–535, 2003. 2.3.4.2
- [24] Juergen Hennig, Matthias Weigel, and Klaus Scheffler. Calculation of flip angles for echo trains with predefined amplitudes with the extended phase graph (epg)-algorithm: Principles and applications to hyperecho and traps sequences. *Magnetic Resonance in Medicine*, 51(1):68–80, 2004.
- [25] Matthias Weigel and Juergen Hennig. Development and optimization of t2 weighted methods with reduced rf power deposition (hyperecho-tse) for magnetic resonance imaging. *Zeitschrift fur medizinische Physik*, 18(3):151–161, 2008. 2.3.4.2
- [26] E Kanal, J Gillen, J A Evans, D A Savitz, and F G Shellock. Survey of reproductive health among female mr workers. *Radiology*, 187(2):395–399, 1993. 2.5.1

- [27] Ingmar Graesslin, Hanno Homann, Sven Biederer, Peter Bornert, Kay Nehrke, Peter Vernickel, Giel Mens, Paul Harvey, and Ulrich Katscher. A specific absorption rate prediction concept for parallel transmission mr. *Magnetic Resonance in Medicine*, 68(5):1664–1674, 2012. 2.5.3, 5.1.4, 7.2
- [28] D.I Hoult. The solution of the bloch equations in the presence of a varying b1 field - an approach to selective pulse analysis. *Journal of Magnetic Resonance (1969)*, 35(1):69–86, 1979. 3.1
- [29] AC. Zelinski, L.L. Wald, K. Setsompop, V.K. Goyal, and E. Adalsteinsson. Sparsity-enforced slice-selective mri rf excitation pulse design. *Medical Imaging, IEEE Transactions on*, 27(9):1213–1229, Sept 2008. 3.1, 3.2.2, 3.2.2.1, 3.3.1, 5.1.1, 5.1.2
- [30] Suwit Saekho, Chun-yu Yip, Douglas C. Noll, Fernando E. Boada, and V. Andrew Stenger. Fast-kz three-dimensional tailored radiofrequency pulse for reduced b1 inhomogeneity. *Magnetic Resonance in Medicine*, 55(4):719–724, 2006. 3.2.2, 5.1.1
- [31] Kawin Setsompop, Vijayanand Alagappan, Borjan A. Gagoski, Andreas Potthast, Franz Hebrank, Ulrich Fontius, Franz Schmitt, L.L. Wald, and E. Adalsteinsson. Broadband slab selection with b1+ mitigation at 7t via parallel spectral-spatial excitation. *Magnetic Resonance in Medicine*, 61(2):493–500, 2009. 5.1.2
- [32] K. Setsompop, L.L. Wald, V. Alagappan, B.A. Gagoski, and E. Adalsteinsson. Magnitude least squares optimization for parallel radio frequency excitation design demonstrated at 7 tesla with eight channels. *Magnetic Resonance in Medicine*, 59(4):908–915, 2008. 3.3.3
- [33] Kawin Setsompop, Vijayanand Alagappan, Borjan Gagoski, Thomas Witzel, Jonathan Polimeni, Andreas Potthast, Franz Hebrank, Ulrich Fontius, Franz Schmitt, Lawrence L. Wald, and Elfar Adalsteinsson. Slice-selective rf pulses for in vivo b1+ inhomogeneity mitigation at 7 tesla using parallel rf excitation with a 16-element coil. *Magnetic Resonance in Medicine*, 60(6):1422–1432, 2008. 3.3.2, 5.1.1
- [34] Kawin Setsompop, Lawrence L. Wald, Vijayanand Alagappan, Borjan Gagoski, Franz Hebrank, Ulrich Fontius, Franz Schmitt, and Elfar Adalsteinsson. Parallel rf transmission with eight channels at 3 tesla. *Magnetic Resonance in Medicine*, 56(5):1163–1171, 2006. 4.1.1
- [35] Chao Ma, Dan Xu, Kevin F. King, and Zhi-Pei Liang. Joint design of spoke trajectories and rf pulses for parallel excitation. *Magnetic Resonance in Medicine*, 65(4):973–985, 2011. b, 3.3.1, 5.1.2
- [36] M. A. Cloos, N. Boulant, M. Luong, G. Ferrand, E. Giacomini, D. Le Bihan, and A. Amadon. kt-points: Short three-dimensional tailored rf pulses for flip-angle ho-

- mogenization over an extended volume. *Magnetic Resonance in Medicine*, 67(1):72–80, 2012. 3.2.2, 3.3.1, 3.3.3, 5.1.1, 5.1.2
- [37] William Grissom, Chun-yu Yip, Zhenghui Zhang, V. Andrew Stenger, Jeffrey A. Fessler, and Douglas C. Noll. Spatial domain method for the design of rf pulses in multicoil parallel excitation. *Magnetic Resonance in Medicine*, 56(3):620–629, 2006. 3.3.1, 3.3.4, 5.1.3, 5.1.4
- [38] Ulrich Katscher, Peter Bornert, Christoph Leussler, and Johan S. van den Brink. Transmit sense. *Magnetic Resonance in Medicine*, 49(1):144–150, 2003. 3.1, 3.3, 3.3.4, 5.1.1
- [39] John Pauly, Dwight Nishimura, and Albert Macovski. A k-space analysis of small-tip-angle excitation. *Journal of Magnetic Resonance (1969)*, 81(1):43 – 56, 1989. 3.1
- [40] Dan Xu, Kevin F. King, Yudong Zhu, Graeme C. McKinnon, and Zhi-Pei Liang. Designing multichannel, multidimensional, arbitrary flip angle rf pulses using an optimal control approach. *Magnetic Resonance in Medicine*, 59(3):547–560, 2008. 3.1, 5.1.3, 5.1.3, 6.1.1
- [41] D.J. Lurie. A systematic design procedure for selective pulses in nmr imaging. *Magnetic Resonance Imaging*, 3(3):235 – 243, 1985. 3.1
- [42] Steven Conolly, Dwight Nishimura, and A. Macovski. Optimal control solutions to the magnetic resonance selective excitation problem. *Medical Imaging, IEEE Transactions on*, 5(2):106–115, June 1986.
- [43] James B Murdoch, Arnold H Lent, and Margaret R Kritzer. Computer-optimized narrowband pulses for multislice imaging. *Journal of Magnetic Resonance (1969)*, 74(2):226 – 263, 1987.
- [44] J. Pauly, P. Le Roux, Dwight Nishimura, and A Macovski. Parameter relations for the shinnar-le roux selective excitation pulse design algorithm. *Medical Imaging, IEEE Transactions on*, 10(1):53–65, Mar 1991. 3.1, 3.1.2
- [45] Meir Shinnar and John S. Leigh. The application of spinors to pulse synthesis and analysis. *Magnetic Resonance in Medicine*, 12(1):93–98, 1989. 3.1.2
- [46] Gruppentheorie und ihre anwendungen auf die quantenmechanik der atomspektren. von e. wigner, 332 seiten, 12 abbildungen, f. vieweg u. sohn verlagsgesellschaft wiesbaden 1977. *Physik in unserer Zeit*, 10(2):66–67, 1979. 3.1.2
- [47] E. T. Jaynes. Matrix treatment of nuclear induction. *Phys. Rev.*, 98:1099–1105, May 1955. 3.1.2

- [48] Xiaotong Zhang, Shanan Zhu, and Bin He. Imaging electric properties of biological tissues by rf field mapping in mri. *Medical Imaging, IEEE Transactions on*, 29(2):474–481, Feb 2010. 3.2
- [49] Laura I. Sacolick, Florian Wiesinger, Ileana Hancu, and Mika W. Vogel. B1 mapping by bloch-siegert shift. *Magnetic Resonance in Medicine*, 63(5):1315–1322, 2010. 3.2.1, 4.1.1
- [50] O Ipek, A J E Raaijmakers, D W J Klomp, J J W Lagendijk, P R Luijten, and C A T van den Berg. Characterization of transceive surface element designs for 7 tesla magnetic resonance imaging of the prostate: radiative antenna and microstrip. *Physics in Medicine and Biology*, 57(2):343, 2012. 3.2.1
- [51] Gregor Adriany, Pierre-Francois Van de Moortele, Florian Wiesinger, Steen Moeller, John P. Strupp, Peter Andersen, Carl Snyder, Xiaoliang Zhang, Wei Chen, Klaas P. Pruessmann, Peter Boesiger, Tommy Vaughan, and Kamil Ugurbil. Transmit and receive transmission line arrays for 7 tesla parallel imaging. *Magnetic Resonance in Medicine*, 53(2):434–445, 2005. 3.3
- [52] Peter Ullmann, Sven Junge, Markus Wick, Frank Seifert, Wolfgang Ruhm, and Jurgen Hennig. Experimental analysis of parallel excitation using dedicated coil setups and simultaneous rf transmission on multiple channels. *Magnetic Resonance in Medicine*, 54(4):994–1001, 2005. 3.3
- [53] David O. Brunner and Klaas P. Pruessmann. B1+ interferometry for the calibration of rf transmitter arrays. *Magnetic Resonance in Medicine*, 61(6):1480–1488, 2009. 3.3.2, 4.1.1, 4.1.2
- [54] Shaihan J. Malik, David J. Larkman, and Joseph V. Hajnal. Optimal linear combinations of array elements for b1 mapping. *Magnetic Resonance in Medicine*, 62(4):902–909, 2009. 3.3.2, 4.1.1
- [55] David I. Hoult. Sensitivity and power deposition in a high-field imaging experiment. *Journal of Magnetic Resonance Imaging*, 12(1):46–67, 2000. 3.3.3
- [56] E. H. Moore. On the reciprocal of the general algebraic matrix. *Bulletin of the American Mathematical Society*, 26:394–395. 3.3.3
- [57] PW. Kassakian. Convex approximation and optimization with applications in magnitude filter design and radiation pattern synthesis. 2006. 3.3.3, 5.1.2
- [58] Weihua Mao, Michael B. Smith, and Christopher M. Collins. Exploring the limits of rf shimming for high-field mri of the human head. *Magnetic Resonance in Medicine*, 56(4):918–922, 2006. 3.3.3

- [59] Klaas P. Pruessmann, Markus Weiger, Markus B. Scheidegger, and Peter Boesiger. Sense: Sensitivity encoding for fast mri. *Magn Reson Med*, 42:952–962, 1999. 3.3.4
- [60] R. Stollberger and P. Wach. Imaging of the active b1 field in vivo. *Magnetic Resonance in Medicine*, 35(2):245–251, 1996. cited By (since 1996)149. 4.1.1
- [61] S. Akoka, F. Franconi, F. Seguin, and A. Le Pape. Radiofrequency map of an nmr coil by imaging. *Magnetic Resonance Imaging*, 11(3):437 – 441, 1993. 4.1.1
- [62] F. Jiru and U. Klose. Fast 3d radiofrequency field mapping using echo-planar imaging. *Magnetic Resonance in Medicine*, 56(6):1375–1379, 2006. 4.1.1
- [63] Vasily L. Yarnykh. Actual flip-angle imaging in the pulsed steady state: A method for rapid three-dimensional mapping of the transmitted radiofrequency field. *Magnetic Resonance in Medicine*, 57(1):192–200, 2007. 4.1.1
- [64] Nicholas G. Dowell and Paul S. Tofts. Fast, accurate, and precise mapping of the rf field in vivo using the 180 signal null. *Magnetic Resonance in Medicine*, 58(3):622–630, 2007. 4.1.1
- [65] C.H. Oh, S.K. Hilal, Z.H. Cho, and I.K. Mun. Radio frequency field intensity mapping using a composite spin-echo sequence. *Magnetic Resonance Imaging*, 8(1):21–25, 1990. 4.1.1
- [66] Glen R. Morrell. A phase-sensitive method of flip angle mapping. *Magnetic Resonance in Medicine*, 60(4):889–894, 2008. 4.1.1
- [67] Roman Fleysheer, Lazar Fleysheer, Songtao Liu, and Oded Gonen. Tritone: a radiofrequency field (b1)-insensitive t1 estimator for mri at high magnetic fields. *Magnetic Resonance Imaging*, 26(6):781 – 789, 2008. 4.1.1
- [68] Jung-Jiin Hsu, Greg Zaharchuk, and Gary H. Glover. Rapid methods for concurrent measurement of the rf-pulse flip angle and the longitudinal relaxation time. *Magnetic Resonance in Medicine*, 61(6):1319–1325, 2009. 4.1.1
- [69] Jinghua Wang, Maolin Qiu, Qing X. Yang, Michael B. Smith, and R. Todd Constable. Measurement and correction of transmitter and receiver induced nonuniformities in vivo. *Magnetic Resonance in Medicine*, 53(2):408–417, 2005.
- [70] Jinghua Wang, Weihua Mao, Maolin Qiu, Michael B. Smith, and R. Todd Constable. Factors influencing flip angle mapping in mri: Rf pulse shape, slice-select gradients, off-resonance excitation, and b0 inhomogeneities. *Magnetic Resonance in Medicine*, 56(2):463–468, 2006.

-
- [71] Sohae Chung, Daniel Kim, Elodie Breton, and Leon Axel. Rapid b1+ mapping using a preconditioning rf pulse with turboflash readout. *Magnetic Resonance in Medicine*, 64(2):439–446, 2010. 4.1.1
- [72] J.T. Vaughan, M. Garwood, C.M. Collins, W. Liu, L. DelaBarre, G. Adriany, P. Andersen, H. Merkle, R. Goebel, M.B. Smith, and K. Ugurbil. 7t vs. 4t: Rf power, homogeneity, and signal-to-noise comparison in head images. *Magnetic Resonance in Medicine*, 46(1):24–30, 2001. 4.1.1
- [73] Ralf Deichmann. Fast high-resolution t1 mapping of the human brain. *Magnetic Resonance in Medicine*, 54(1):20–27, 2005. 4.1.1
- [74] Charles H. Cunningham, John M. Pauly, and Krishna S. Nayak. Saturated double-angle method for rapid b1+ mapping. *Magnetic Resonance in Medicine*, 55(6):1326–1333, 2006. 4.1.1
- [75] C. Preibisch and R. Deichmann. Influence of rf spoiling on the stability and accuracy of t1 mapping based on spoiled flash with varying flip angles. *Magnetic Resonance in Medicine*, 61(1):125–135, 2009. 4.1.2, 4.1.7, 4.1.7
- [76] Mark A. Griswold, Peter M. Jakob, Robin M. Heidemann, Mathias Nittka, Vladimir Jellus, Jianmin Wang, Berthold Kiefer, and Axel Haase. Generalized autocalibrating partially parallel acquisitions (grappa). *Magnetic Resonance in Medicine*, 47(6):1202–1210, 2002. 4.1.2
- [77] Mark Jenkinson, Peter Bannister, Michael Brady, and Stephen Smith. Improved optimization for the robust and accurate linear registration and motion correction of brain images. *NeuroImage*, 17(2):825 – 841, 2002. 4.1.2
- [78] Wietske van der Zwaag, Jose P. Marques, Hongxia Lei, Nathalie Just, Tobias Kober, and Rolf Gruetter. Minimization of nyquist ghosting for echo-planar imaging at ultrahigh fields based on a "negative readout gradient" strategy. *Journal of Magnetic Resonance Imaging*, 30(5):1171–1178, 2009. 4.5
- [79] R. Deichmann, C.D. Good, O. Josephs, J. Ashburner, and R. Turner. Optimization of 3-d mp-rage sequences for structural brain imaging. *NeuroImage*, 12(1):112 – 127, 2000. 4.1.4
- [80] Tony Stoecker and N. Jon Shah. Mp-sage: A new mp-rage sequence with enhanced snr and cnr for brain imaging utilizing square-spiral phase encoding and variable flip angles. *Magnetic Resonance in Medicine*, 56(4):824–834, 2006. 4.1.4
- [81] R Deichmann and A Haase. Quantification of t1 values by snapshot-flash nmr imaging. *Journal of Magnetic Resonance (1969)*, 96(3):608 – 612, 1992. b

- [82] Andrew M. Peters, Matthew J. Brookes, Frank G. Hoogenraad, Penny A. Gowland, Susan T. Francis, Peter G. Morris, and Richard Bowtell. T2* measurements in human brain at 1.5, 3 and 7 t. *Magnetic Resonance Imaging*, 25(6):748 – 753, 2007. Proceedings of the International School on Magnetic Resonance and Brain Function. 4.1.7
- [83] Y. Zur, M. L. Wood, and L. J. Neuringer. Spoiling of transverse magnetization in steady-state sequences. *Magnetic Resonance in Medicine*, 21(2):251–263, 1991. 4.1.7
- [84] Vasily L. Yarnykh. Optimal radiofrequency and gradient spoiling for improved accuracy of t1 and b1 measurements using fast steady-state techniques. *Magnetic Resonance in Medicine*, 63(6):1610–1626, 2010. 4.1.7
- [85] Reed F. Busse and Stephen J. Riederer. Steady-state preparation for spoiled gradient echo imaging. *Magnetic Resonance in Medicine*, 45(4):653–661, 2001. 4.1.7
- [86] Guillaume Madelin, Niels Oesingmann, and Matilde Inglese. Double inversion recovery mri with fat suppression at 7 tesla: Initial experience. *Journal of Neuroimaging*, 20(1):87–92, 2010. 5.1.1, 5.1.4
- [87] Fredy Visser, Jaco J. M. Zwanenburg, Johannes M. Hoogduin, and Peter R. Luijten. High-resolution magnetization-prepared 3d-flair imaging at 7.0 tesla. *Magnetic Resonance in Medicine*, 64(1):194–202, 2010. 5.1.1
- [88] Jaco J.M. Zwanenburg, Jeroen Hendrikse, Fredy Visser, Taro Takahara, and Peter R. Luijten. Fluid attenuated inversion recovery (flair) mri at 7.0 tesla: comparison with 1.5 and 3.0 tesla. *European Radiology*, 20(4):915–922, 2010. 5.1.1, 5.1.4
- [89] Michael Garwood and Lance DelaBarre. The return of the frequency sweep: Designing adiabatic pulses for contemporary nmr. *Journal of Magnetic Resonance*, 153(2):155 – 177, 2001. 5.1.1
- [90] Shaihan J. Malik, Francesco Padormo, Anthony N. Price, and Joseph V. Hajnal. Spatially resolved extended phase graphs: Modeling and design of multipulse sequences with parallel transmission. *Magnetic Resonance in Medicine*, 68(5):1481–1494, 2012. 5.1.1, 5.1.2, 5.1.4, 6.2.1, 6.2.3, 6.2.4
- [91] Yudong Zhu. Parallel excitation with an array of transmit coils. *Magnetic Resonance in Medicine*, 51(4):775–784, 2004. 5.1.1
- [92] Kawin Setsompop, Vijayanand Alagappan, Adam C. Zelinski, Andreas Potthast, Ulrich Fontius, Franz Hebrank, Franz Schmitt, Lawrence L. Wald, and Elfar Adalsteinsson. High-flip-angle slice-selective parallel rf transmission with 8 channels at 7t. *Journal of Magnetic Resonance*, 195(1):76 – 84, 2008. 5.1.1

-
- [93] M.A. Cloos, N. Boulant, M. Luong, G. Ferrand, E. Giacomini, M.-F. Hang, C.J. Wiggins, D. Le Bihan, and A. Amadon. Parallel-transmission-enabled magnetization-prepared rapid gradient-echo t1-weighted imaging of the human brain at 7t. *NeuroImage*, 62(3):2140 – 2150, 2012. 5.1.1, 6.1.1
- [94] Mugler JP. Three-dimensional t2-weighted imaging of the brain using very long spin-echo trains. In *Proceedings of the 8th Annual Meeting of ISMRM, Denver, USA*, page 687, 2000. 5.1.1
- [95] Yongyue Zhang, M. Brady, and S. Smith. Segmentation of brain mr images through a hidden markov random field model and the expectation-maximization algorithm. *Medical Imaging, IEEE Transactions on*, 20(1):45–57, Jan 2001. 5.1.2
- [96] William A. Grissom, Chun-Yu Yip, Steven M. Wright, Jeffrey A. Fessler, and Douglas C. Noll. Additive angle method for fast large-tip-angle rf pulse design in parallel excitation. *Magnetic Resonance in Medicine*, 59(4):779–787, 2008. 5.1.3
- [97] John Pauly, Dwight Nishimura, and Albert Macovski. A linear class of large-tip-angle selective excitation pulses. *Journal of Magnetic Resonance (1969)*, 82(3):571 – 587, 1989. 5.1.3
- [98] W. M. Teeuwisse, W. M. Brink, K. N. Haines, and A. G. Webb. Simulations of high permittivity materials for 7 t neuroimaging and evaluation of a new barium titanate-based dielectric. *Magnetic Resonance in Medicine*, 67(4):912–918, 2012. 5.1.4, 6.2.2
- [99] Wouter M. Teeuwisse, Wyger M. Brink, and Andrew G. Webb. Quantitative assessment of the effects of high-permittivity pads in 7 tesla mri of the brain. *Magnetic Resonance in Medicine*, 67(5):1285–1293, 2012. 5.1.4, 6.2.2
- [100] Gabriele Eichfelder and Matthias Gebhardt. Local specific absorption rate control for parallel transmission by virtual observation points. *Magnetic Resonance in Medicine*, 66(5):1468–1476, 2011. 5.1.4
- [101] Joonsung Lee, Matthias Gebhardt, Lawrence L. Wald, and Elfar Adalsteinsson. Local sar in parallel transmission pulse design. *Magnetic Resonance in Medicine*, 67(6):1566–1578, 2012. 5.1.4
- [102] Martijn Anton Cloos, Michel Luong, Guillaume Ferrand, Alexis Amadon, Denis Le Bihan, and Nicolas Boulant. Local sar reduction in parallel excitation based on channel-dependent tikhonov parameters. *Journal of Magnetic Resonance Imaging*, 32(5):1209–1216, 2010. 5.1.4
- [103] David O. Brunner and Klaas P. Pruessmann. Optimal design of multiple-channel rf pulses under strict power and sar constraints. *Magnetic Resonance in Medicine*, 63(5):1280–1291, 2010. 5.1.4

- [104] Rolf Pohmann and Klaus Scheffler. A theoretical and experimental comparison of different techniques for b1 mapping at very high fields. *NMR in Biomedicine*, 26(3):265–275, 2013. 5.1.4
- [105] M.P. Wattjes, G.G. Lutterbey, J. Gieseke, F. Traeber, L. Klotz, S. Schmidt, and H.H. Schild. Double inversion recovery brain imaging at 3t: Diagnostic value in the detection of multiple sclerosis lesions. *American Journal of Neuroradiology*, 28(1):54–59, 2007. 6.2.1
- [106] C. Fellner, C. Menzel, F.A. Fellner, C. Ginthoer, N. Zorger, A. Schreyer, E.M. Jung, S. Feuerbach, and T. Finkenzeller. Blade in sagittal t2-weighted mr imaging of the cervical spine. *American Journal of Neuroradiology*, 31(4):674–681, 2010. 6.2.1
- [107] Lara Z. Diaz de Grenu, Julio Acosta-Cabronero, Joao M.S. Pereira, George Pengas, Guy B. Williams, and Peter J. Nestor. Mri detection of tissue pathology beyond atrophy in alzheimer’s disease: Introducing t2-vbm. *NeuroImage*, 56(4):1946 – 1953, 2011. 6.2.1
- [108] K. Thamburaj, V.V. Radhakrishnan, B. Thomas, S. Nair, and G. Menon. Intratumoral microhemorrhages on t2*-weighted gradient-echo imaging helps differentiate vestibular schwannoma from meningioma. *American Journal of Neuroradiology*, 29(3):552–557, 2008. 6.2.1
- [109] Aurelien Massire, Alexandre Vignaud, Benjamin Robert, Denis Le Bihan, Nicolas Boulant, and Alexis Amadon. Parallel-transmission-enabled three-dimensional t2-weighted imaging of the human brain at 7 tesla. *Magnetic Resonance in Medicine*, 2014. 6.2.1
- [110] Gaby S Pell, Regula S Briellmann, Anthony B Waites, David F Abbott, and Graeme D Jackson. Voxel-based relaxometry: a new approach for analysis of t2 relaxometry changes in epilepsy. *NeuroImage*, 21(2):707 – 713, 2004. 7.2
- [111] Sean C. L. Deoni, Terry M. Peters, and Brian K. Rutt. High-resolution t1 and t2 mapping of the brain in a clinically acceptable time with despot1 and despot2. *Magnetic Resonance in Medicine*, 53(1):237–241, 2005.
- [112] Oliver Bieri, Klaus Scheffler, Goetz H. Welsch, S. Trattnig, Tallal C. Mamsch, and Carl Ganter. Quantitative mapping of t2 using partial spoiling. *Magnetic Resonance in Medicine*, 66(2):410–418, 2011. 7.2

Peer-reviewed journal articles

1. **Florent Eggenschwiler**, Tobias Kober, Arthur W. Magill, Rolf Gruetter and José P. Marques *SA2RAGE: a new sequence for fast B_1^+ -mapping*, *Magnetic Resonance in Medicine*, 67, p.1609-1619, 2012
2. **Florent Eggenschwiler**, Kieran R. O'Brien, Rolf Gruetter and José P. Marques *Improving T_2 -weighted imaging at high field through the use of k_T -points*, *Magnetic Resonance in Medicine*, 71, p.1478-1488, 2013
3. Arthur, W. Magill, Benoît Schaller, **Florent Eggenschwiler**, Jose Marques and R. Gruetter, *A mechanically tuned 8-channel microstrip array for parallel transmission at 7 Tesla*, manuscript submitted to IEEE transactions on medical imaging, in press

Peer-reviewed abstracts at international conferences

1. **Florent Eggenschwiler**, Arthur W. Magill, Rolf Gruetter and José P. Marques *Sa2RAGE - A new sequence for rapid 3D B_1^+ -mapping with a wide sensitivity range*, Proc. ISMRM 18th Scientific Meeting, Stockholm, Sweden, 2010.
2. **Florent Eggenschwiler**, Arthur W. Magill, Tobias Kober, Rolf Gruetter and José P. Marques *Sa2RAGE sequence improvements and in-vivo brain RF-shimming at 7 Tesla*, Proc. ISMRM 19th Scientific Meeting, Montreal, Canada, 2011.
3. Mayur Narsudé, José P. Marques, **Florent Eggenschwiler** and Rolf Gruetter *Mapping Inversion Efficiencies of Adiabatic Pulses at 7T*, Proc. ISMRM 19th Scientific Meeting, Montreal, Canada, 2011.
4. **Florent Eggenschwiler**, José P. Marques and Rolf Gruetter *Slice-by-slice B_1^+ -shimming of the human head at 7T*, Proc. ESMRMB 28th Scientific Meeting, Leipzig, Germany, 2011.
5. **Florent Eggenschwiler**, Kieran R. O'Brien, José P. Marques and Rolf Gruetter *Improvement in T_2 -weighted imaging at 7T by using k_T -points*, Proc. ESMRMB 29th Scientific Meeting, Lisbon, Portugal, 2012.
6. José P. Marques, Tobias Kober, **Florent Eggenschwiler** and Rolf Gruetter *Exploring the complementarities of the MP2RAGE and the Sa2RAGE sequences-quantitative T_1 mapping*, Proc. ISMRM 20th Scientific Meeting, Melbourne, Australia, 2012.

7. **Florent Eggenschwiler**, Kieran R. O'Brien, Rolf Gruetter and José P. Marques *Improvement in T_2 -weighted imaging at 7T by using k_T -points*, Proc. ISMRM 21st Scientific Meeting, Salt Lake City, USA, 2013.
8. **Florent Eggenschwiler**, Rolf Gruetter and José P. Marques *Large tip angle k_T -points based on a linearization of the Bloch equations*, Proc. ISMRM 21st Scientific Meeting, Salt Lake City, USA, 2013.
9. **Florent Eggenschwiler**, Kieran R. O'Brien, Bénédicte Maréchal, Rolf Gruetter and José P. Marques *Dynamic k_T -points: a new concept to improve T_2 -weighted imaging at 7T*, Proc. ISMRM 22nd Scientific Meeting, Milan, Italy, 2014.
10. **Florent Eggenschwiler**, Kieran R. O'Brien, Danial Gallichan, Rolf Gruetter and José P. Marques *Highly dynamic k_T -points to minimize the B_1^+ inhomogeneity effects in T_2 -weighted imaging at 7T*, Proc. ISMRM 23rd Scientific Meeting, Toronto, Canada, 2015.

Florent Eggenschwiler

Date of birth: 18.11.1986

Place of birth: Delémont, Switzerland

Nationality: Swiss

Education

2010-2015 **Doctor in philosophy (PhD) in physics** done at the Center for Biomedical imaging (CIBM) of the Swiss Federal Institute of Technology (EPFL)
Thesis title : B_1^+ -mapping and B_1^+ inhomogeneity correction at high field

2005-2010 **Bachelor (BSc) and Master of Science (MSc) in physics**
Swiss Federal Institute of Technology (EPFL), Switzerland
Master thesis title : *Transmit magnetic field mapping and shimming at 7 Tesla*

2002-2005 **High-school (Gymnasium)**
Gymnasium of Porrentruy, Jura, Switzerland

Professional experience

2008-2015 Assistant of physics courses for first and second years EPFL Bachelor students and biomedical imaging courses for Master students

2003-2008 President of the Youth society of Rebeuvelier, Jura, Switzerland
Management of the society activities (meetings, events, journeys)

Technical Skills

Softwares MS-Office (Word, Excel, Powerpoint), Latex, Adobe Illustrator and Photoshop

Programming Matlab, C/C++, HTML/CSS, PHP/SQL

Language Skills

French Mother language

English Fluent (both written and spoken), C1 (European standard)

German Medium level, A2 (European standard)

Leisure activities

Football (1991-2011), running coach (2014-2015), ski mountaineering, guitar (2002-2013), motorbike.

Acknowledgments

Writing this last section of the thesis means that my time as a PhD student is close to an end. This also marks the end of an almost ten years story as an EPFL member. Such a nice adventure would not have been what it was without a fantastic group of people to whom I would like to express my appreciation.

I would like to start by transmitting my grateful thanks to Professor Rolf Gruetter who gave me the chance to do my PhD at CIBM. It was a pleasure to work in such an outstanding lab. Thank you so much for all the efforts you put for offering us the working conditions that we have here in Lausanne. I also appreciated having you reminding me sometimes to keep the confusing simulations aside and not to forget to think as the "old style" physicists do.

I also want to warmly thank my jury members Shaihan Malik, Oliver Bieri, Jean-Philippe Thiran, Georges Meylan and Rolf Gruetter for their very interesting questions, comments, remarks and suggestions regarding my thesis during the private defense.

I am not sure I will find the correct words to properly say thank you to the person who had a huge influence on all the accomplishments of this PhD, my very talented supervisor José Marques. I really learned a lot by your side, not only about MRI but also on how research should be conducted. Working with you sometimes made my life too easy since for each issue I had, I knew that I could simply move three offices further to get an answer. I like a lot the way you explain things (sometimes in a very funny way) and your capability to always find new directions where to search. As a PhD student, having a supervisor like you provides a really secure feeling. Thank you so much for this nice working atmosphere and for all your inputs, advices, support, guidance and encouragements during this thesis!

I also had the chance to collaborate with another very kind and talented scientist, Kieran O'Brien. Thank you for your tremendous help with the inclusion of the k_T -points in the crazy SPACE sequence. I really enjoyed working with you in the SPACE team for almost half of my PhD. Thanks also for having been so professional and for making sure you left me with all what I needed to finish the k_T -point project.

During these PhD years, it has been a pleasure to share an office with my preferred Indian guy, Mayur Narsudé. Thanks for the nice atmosphere we had in the office and sorry for all the sport stuff I brought a bit everywhere. I hope I will not leave too early such that we can organize some other drone sessions and photography nights!

I would like to express my appreciation to two very important persons who made my PhD life much easier, Lillian Vernacchio and Cédric Passerini. Lillian, thank you for your help with the administrative tasks, your efficiency makes everything very simple. Thanks also for being in good mood every morning and for the memorable bowling game at the last Christmas dinner! Cédric, I cannot count how many times I came to your office over those last years. I really appreciated your availability and all your help with my IT requests and issues.

I would like to express my gratitude to all the members of the CIBM 7T group for their com-

Acknowledgments

ments and suggestions during the 7T meetings and for all their help with the scanner, MR equipment, data analysis, programming and so on throughout my time in the lab.

I felt so lucky to be part of a lab with so many PhD students who entertained my everyday's life quite a lot. In particular, I would like to say thank you to the old ones (those who started before me); Benoît for all the running, football and after sport sessions and for your dynamism; Lali for saving me every time I forgot my CAMIPRO card. It was great to have both of you as office neighbours; Jessica for always having funny stories to tell and for being such a leader in the organization of many events (the ultimate Frisbee period was amazing); Tobi for making me laughing every Monday at discofit and for having introduced me to Rudy.

...and of course the newbies (those who started after me); Joao, that is sad we cannot continue the movie editing adventure, it was becoming better and better. I am going to miss "the voice" and the rush hours before the public defenses; Andrea, the Italian maestro. Thanks for your friendship and I hope you will teach me many more Italian recipes; Matthieu the ambassador, I still do not know if you are able to have a serious discussion! Thank you for all your jokes and for all the delicious French biscuits; Masoumeh my Persian teacher. "Kheily Mamnoon" for each time you waited for me late in the evening to catch the last metro.

My deep gratitude also go to the other PhD students: Ruud, Mélanie, Bernard, Rajika, Emine, Guillaume, Elise, Sarah, Jérémie, Yohan, Marta, Frédéric, Diana, Veronika and of course all the CIBM colleagues who made the atmosphere of the lab so enjoyable.

I had the great privilege to do my studies with an extremely talented physicist, Jean-Claude Jacot. Thank you JC for all what you taught me over those last ten years. Having you as a flatmate was like having a personal professor at home!

Of course I cannot forget my flatmates Jonas and Fred, those last six months with you were just unbelievable. Thank you for being so convenient in the weekdays and for maintaining the weekends so alive!

I truly appreciated interacting with the members of the UNIL-EPFL running club. I met amazing people there and each training was always an excellent way to completely free my mind for an hour or two. Thanks also to all the persons who shared many unforgivable sport events with me, in particular: my running buddies, Diego, Vincenzo, Juju, Pierre, Arnaud, Gael; the climbing team, Andrea, Matt, Pierre, Isa and my swimming coach Maya.

It is important for me to also acknowledge the people who took part, sometimes slightly and sometimes much more, in my PhD life: Pat, Laura, Sioux, Mylène, Tan's, Manu, Sarah, Fred, Chri, Urbs, Sylvette, Luc, Clara, Julien, Oli, Alex and Malika, Damien. Thank you so much my dear friends, this adventure would not have been so incredible without you!

Finally, I would like to express my deepest appreciation to my family members for their unconditional love, support and encouragements no matter what my decisions are. A huge thank you to my parents Christiane and Jean-Luc for all what you do for me, especially when I come back to visit you in the Jura where I feel like I am on holiday. Martine, thank you so much for always welcoming me cheerfully at the Pont-de-Cran and for making me

discover Belgium more and more. My lovely sister and brother Virginie and Loïc, I would like to spend so much more time with you! Thanks both of you for all your questions and interest for what I am doing and for making every moments we spend together so particular!

Ecole Polytechnique Fédérale de Lausanne

Florent Eggenschwiler

April 2015

"I cannot even imagine where I would be today were it not for that handful of friends who have given me a heart full of joy. Let's face it, friends make life a lot more fun."

C.R. Swindoll